This is to certify that the
dissertation entitled

SUBSTRATES FOR SURFACE-ENHANCED RAMAN SPECTROSCOPY

presented by

MUHAMMAD AJMAL KHAN

has been accepted towards fulfillment
of the requirements for the

PhD degree in Electrical Engineering

Major Professor's Signature

11/19/08

Date

SUBSTRATES FOR SURFACE-ENHANCED RAMAN SPECTROSCOPY

By

MUHAMMAD AJMAL KHAN

A DISSERTATION

Submitted to
Michigan State University
in partial fulfillment of requirements
for the degree of

DOCTOR OF PHILOSOPHY

Electrical Engineering

2008

ABSTRACT

SUBSTRATES FOR SURFACE-ENHANCED RAMAN SPECTROSCOPY

By

Muhammad Ajmal Khan

Surface enhanced Raman spectroscopy (SERS) utilizes surface plasmon resonance in metallic nanostructures to yield nearly a millionfold increase in the Raman signal of an analyte. The unprecedented sensitivity and specificity of SERS has great potential for applications in analytical chemistry and biological sensors. SERS is inherently a nanoscale phenomenon and recent advances in nanotechnology have generated an immense opportunity for the use of nanoparticles, nanowires and nanorods as substrates for SERS. This dissertation explores different aspects of utilizing bulk synthesized germanium oxide, zinc oxide nanowires, and metallic nanorods as substrates for SERS. It discusses the synthesis details and growth kinetics for the oxide nanowires and metallic nanorods. The germanium nanowire growth is carried out in a simple tube furnace chamber using two different temperature regimes - the traditionally high temperature synthesis and a novel low temperature synthesis. The high temperature synthesis (~850 °C) does not yield good control over length and diameter of the nanowires. The new low temperature synthesis technique overcomes these limitations by maintaining the source temperature at ~650 °C.

Zinc oxide nanowires are synthesized by thermal evaporation of zinc powder in an oxidizing environment. The as-synthesized bulk nanowires act as nanostructured template that is coated with a thin gold film to create a plasmon active surface for SERS

application. In addition metallic nanorods of aluminum, copper, and silver were synthesized on glass slides in an e-beam equipped physical vapor deposition system using oblique angle deposition technique. Structural and chemical compositional characterization of the SERS substrates was done using a scanning electron microscope, transmission electron microscope and energy dispersive X-ray spectroscopy (EDS). The SERS performance is evaluated using model analytes of 4-methylbenzenthiol, 1,2-benzenedithiol and trans-1,2-bis(4-pyridyl)ethylene. The substrates yield strong and unambiguous Raman spectra from just a monolayer or few femto moles of analyte. The Raman enhancement factors are computed by comparing the intensity of Raman signal from SERS substrate to that from the bulk analyte. The metallic nanorods substrates show a metal dependent SERS enhancement with silver yielding an order of magnitude stronger enhancement compared to other metals. The oxide nanowires based substrates show an average Raman enhancement factor of ~10^6 with good reproducibility of signal over the tested area. The dissertation puts in to perspective how noble metal coated germanium oxide and zinc oxide nanowires can be used as robust SERS platform for detection of trace levels of chemical species.

To my parents and family.

ACKNOWLEDGEMENTS

First of all, I would like to thank Almighty for granting me the honor of accomplishing this work. I would also like to thank my committee for their patience, guidance and understanding throughout the course of this research. I would like to specifically express my deep gratitude to my advisor, Prof. Timothy P. Hogan without whom none of the accomplishments documented in this dissertation would have been possible. He has always been an outstanding mentor and a great friend throughout my stay at Michigan State University.

On a personal note, I would like to express my most sincere gratitude to my parents, my parents-in-law, and my family whose love, prayers, and motivation are the biggest reason behind my success. I would also like to express my warmest appreciation and gratitude for my wife, whose passion, sacrifice and encouragement gave me the strength and inspiration to complete this work.

And finally I would like to express my gratitude and thanks to my long time friend and fellow researcher, Muhammad Farhan, for his support, dedication and encouragement that kept me focused during ups and downs of my stay in graduate school.

Financial support from the National Science Foundation is gratefully acknowledged.

TABLE OF CONTENTS

LIST OF TABLES x

LIST OF FIGURES xi

Chapter 1: Introduction 1
1.1 Raman spectroscopy 1
1.2 Limitations of conventional Raman spectroscopy 2
1.3 Surface enhanced Raman spectroscopy 3
1.4 Common SERS substrates 6
1.5 Major challenge for SERS 7
1.6 SERS from Nanowires : Motivation for this work 8
1.7 Organization of this dissertation 11

Chapter 2: Theory of Raman Scattering 12
2.1 Classical theory of Raman scattering 13
2.2 Quantum mechanical theory of Raman scattering 20
2.3 Surface enhanced Raman scattering 25
2.3.1 Electromagnetic mechanism 25
2.3.2 The chemical enhancement 47
2.4 Ordinary Raman spectra and SERS spectra 48

Chapter 3: Experimental Set up 50
3.1 Oxide nanowire synthesis set up 50
3.2 Silver nanorods synthesis set up 53
3.3 Raman spectroscopy set up 55
3.3.1 Laser spot size determination 59
3.3.2 Raman system calibration 60

Chapter 4: Germanium Oxide Nanowires based SERS Substrates 63
4.1 Nanowire synthesis 64
4.1.1 Reviews of past efforts 64
4.1.2 Our synthesis technique 65
4.1.3 Characterization of nanowires 67
4.2 Nanowire growth kinetics 71
4.2.1 Oxidation of germanium 71
4.2.2 Stability of germanium oxides 73
4.2.3 Growth model 74
4.2.4 Synthesis temperature profile 83
4.2.5 Synthesis pressure profile 84
4.3 Factors affecting growth of nanowires 87
4.3.1 Role of gold catalyst 87
4.3.2 Effect of growth time on length of nanowires 100
4.3.3 Effect of oxygen flow rate 101
4.3.4 Effect of synthesis temperature 103

4.3.5 Effect of background gas 104
4.3.6 Effect of background gas pressure 107
4.4 Raman characterization of GeO_2 nanowires 109
4.4.1 Experimental parameters 110
4.4.2 Raman spectra of GeO_2 nanowires 110
4.4.3 Gold coating of GeO_2 nanowires 112
4.5 Evaluation of SERS substrate 120
4.5.1 SERS of rhodamine and nile blue 121
4.5.2 SERS of thiols 130
4.6 Conclusion 159

Chapter 5: Low Temperature Synthesized GeO_2 Nanowires based Substrates for SERS 161
5.1 Limitation of high temperature nanowire synthesis 162
5.2 Low temperature Synthesis of nanowires 167
5.3 Nanowire growth kinetics 172
5.3.1 Oxidation of germanium 172
5.3.2 Growth kinetics 174
5.3.3 Synthesis temperature profile 180
5.3.4 Pressure profile 181
5.4 Factors affecting NWs synthesis 182
5.4.1 Effect of gold film thickness 183
5.4.2 Effect of growth time on length of nanowires 195
5.4.3 Effect of oxygen flow rate 197
5.4.4 Effect of background gas flow rate 200
5.4.5 Effect of temperature 201
5.4.6 Background gas type 203
5.4.7 Effect of background gas pressure 209
5.5 Raman characterization of GeO_2 nanowires 210
5.5.1 Raman spectra of substrate 210
5.5.2 Gold coating of GeO_2 nanowires 213
5.6 SERS evaluation of substrates 217
5.6.1 Detection of 4-MBT 218
5.6.2 Detection of 1,2-BDT 228
5.7 Conclusion 232

Chapter 6: Zinc Oxide Nanowires based SERS Substrates 234
6.1 Zinc oxide nanowires synthesis 234
6.2 ZnO nanowires growth model 242
6.3 Raman characterization of ZnO nanowires 248
6.3.1 Raman Characterization of NWs 249
6.3.2 Gold coating of ZnO nanowires 250
6.4 SERS study of ZnO nanowires substrate 252
6.5 Detection of R6G probe molecule 252
6.6 Detection of nile blue 254
6.7 Detection using thiols 256

6.7.1 Gold coating thickness study 257
6.7.2 SERS for 4-MBT 261
6.7.3 SERS for 1,2-BDT 271
6.8 Conclusion 274

Chapter 7: Metallic Nanorods based SERS Substrates 276
7.1 Oblique angle deposition 276
7.2 Metallic nanorods synthesis 277
7.3 Oblique angle deposition kinetics 287
7.3.1 Incident flux angle 288
7.3.2 Temperature 288
7.3.3 Rate of deposition 289
7.4 Raman characterization of substrates 289
7.5 Detection of nile blue 291
7.6 Detection of MBT 294
7.7 Detection of BDT 307
7.8 Conclusion 309

Chapter 8: Conclusions and Future Work 310
8.1 Conclusion 310
8.2 Future work 315

Appendix A: Operation of EzRaman-L system 317
A.1 Introduction 317
A.2 Procedure 317
A.3 Sample mounting 317
A.4 Acquiring Spectra 318
A.5 Shutdown 319
A.6 System Calibration 319

References 320

LIST OF TABLES

Table 3-1. Isopropyl alcohol Raman peaks and wavenumbers. 61

Table 4-1. SERS EF for common substrates. 145

Table 4-2. Raman band assignment for 4-MBT. 148

Table 4-3. Raman peak assignment for BPE 152

Table 4-4. Raman band assignment for 1,2-BDT. 155

Table 7-1. Depolarization factors for some common geometries. 302

LIST OF FIGURES

Figure 2-1. Pictorial representation of Rayleigh and Raman scattering[47]..... 17

Figure 2-2. Three modes of vibrations of CO_2 molecule[3]..... 19

Figure 2-3. Schematic illustration of plasmon oscillation for sphere showing electron distortion in response to electric field [72]..... 27

Figure 2-4. Energy flux (Poynting vector) around a metal nanoparticles under plane wave excitation for two frequencies[77]- away from resonance and at plasmon resonance..... 33

Figure 2-5. Effect of radiation damping for different aspect ratio of gold nanorods. Also shown is the resonant wavelength for each aspect ratio..... 44

Figure 2-6. Light interaction with metal nanospheres dimmers[73]. Analyte molecule is shown by small green filled circle in between two particles..... 45

Figure 2-7. Calculated Raman enhancement factors at the junction of 60 nm diameter dimmers for 497 nm excitation[39]..... 46

Figure 3-1. Photograph of nanowire synthesis set up..... 52

Figure 3-2. Quartz support plate with typical sample layout (A top view)..... 52

Figure 3-3. Physical vapor deposition systems for metallic nanorods synthesis..... 54

Figure 3-4. Schematic of oblique angle deposition of silver nanorods using e-beam evaporation. (a) Normal angle deposition. (b) Oblique angle deposition..... 55

Figure 3-5. Raman system set up..... 56

Figure 3-6. Raman system optical fiber head and sample stage..... 57

Figure 3-7. Knife edge method for determining laser beam diameter..... 60

Figure 3-8. Reference Raman spectra of Isopropanol, t_{acc}= 20 s..... 61

Figure 4-1. Schematic of germanium dioxide nanowire synthesis..... 67

Figure 4-2. SEM image of GeO_2 nanowires on different samples of Si..... 68

Figure 4-3. EDS spectrum and quantification results for GeO_2 nanowires..... 69

Figure 4-4. TEM image showing gold at tip and EDS spectra for two regions of nanowire and the diffraction pattern. 70

Figure 4-5. Vapor pressure of GeO at different temperatures. 76

Figure 4-6. Formation of cloudy reactants after introducing oxygen into the quartz tube. 77

Figure 4-7. Spherical particles and GeO_2 NWs. 78

Figure 4-8. Faceted germanium oxide particles with NWs. 78

Figure 4-9. GeO_2 particles on Au coated Si substrate after typical synthesis run. 82

Figure 4-10. Plot showing GeO_2 stability as function of temperature and the hydrogen to water vapors pressure ratio[112]. 83

Figure 4-11. Tube furnace typical temperature profile during nanowire synthesis. 84

Figure 4-12. Typical pressure profile during NW synthesis. 86

Figure 4-13. GeO_2 NWs on Si(100) partially coated with 7 nm Au film. 88

Figure 4-14. GeO_2 NW showing particle at tip. 89

Figure 4-15. SEM image and particle size distribution for 3 nm Au film. 90

Figure 4-16. SEM image and particle size distribution for 7 nm Au film. 91

Figure 4-17. SEM image and particle size distribution for 15 nm Au film. 92

Figure 4-18. SEM image and particle size distribution for 21 nm Au film. 93

Figure 4-19. SEM image and particle size distribution for 28 nm Au film. 94

Figure 4-20. Mean particle size distributions after annealing different thickness Au films. Error bars indicate standard deviation from mean. 95

Figure 4-21. GeO_2 NW diameter distribution for 3 nm Au film. 96

Figure 4-22. GeO_2 NW diameter distribution for 7 nm Au film. 97

Figure 4-23. GeO_2 NW diameter distribution for 15 nm Au film. 97

Figure 4-24. Mean diameters of GeO_2 NWs and annealed Au film particles. 98

Figure 4-25. A faceted GeO_2 whisker. 99

Figure 4-26. Cross-section of substrate showing long NWs extending from substrate. 101

Figure 4-27. Effect of oxygen concentration on NW synthesis. In all cases, the total flow rate (background + oxidation mix) was 100 sccm. 102

Figure 4-28. GeO_2 NWs synthesized at different temperatures (a) 865 °C (b) 840 °C (d) 830 °C (d) 800 °C (e) 765 °C..... 104

Figure 4-29. SEM image of GeO_2 NWs synthesized using N_2 as background gas..... 106

Figure 4-30. SEM image of GeO_2 NWs synthesized using Ar as background gas..... 106

Figure 4-31. GeO_2 NWs diameters for different background gases..... 107

Figure 4-32. Effect of background gas pressure on NW synthesis..... 108

Figure 4-33. White GeO_2 coating at the end of quartz tube. 109

Figure 4-34. (a) Raman spectra for two phases of GeO_2. Reproduced with permission from ref [114]. (b) Raman spectra of GeO_2 nanowires on Silicon substrate, t_{acc}=15 s.. 111

Figure 4-35. Raman spectra of 21 nm Au coated GeO_2 NWs, t_{acc}=15 s. Also shown are spectra for uncoated NWs..... 112

Figure 4-36. Raman spectra of 15 nm Au coated GeO_2 NWs, t_{acc}=5 s. Also shown is the spectra for uncoated NWs..... 113

Figure 4-37. Raman spectra for bare silicon wafer and after coating with ~21nm gold. 114

Figure 4-38. Variation of 520 cm^{-1} Raman peak intensity with Au film thickness..... 115

Figure 4-39. Raman spectra of 10nm e-beam high purity gold coated GeO_2 nanowires, t_{acc}=5 s. Also shown is the spectra from an uncoated part of the sample..... 116

Figure 4-40. Successive Raman spectra from same point on sample for 21 nm Au coated GeO_2 NW sample dried in a desiccator for 36 hr..... 117

Figure 4-41. Effect of ~21nm gold coated GeO_2 nanowires at 146 °C, t_{acc}=5 s. Insert shows room temperature Raman spectra..... 119

Figure 4-42. TEM image of 21 nm Au coated GeO_2 NW. Insert shows another NW with larger Au particles..... 120

Figure 4-43. Chemical structure and ordinary Raman spectra of R6G with 785 nm excitation..... 122

Figure 4-44. Raman spectra of 2μM R6G in DI water for 14nm gold coated GeO_2 nanowires. Bulk solution spectrum of same concentration is also shown, t_{acc}=15 s. Bulk spectrum is ×10 times the value to show features..... 123

Figure 4-45. Raman spectra of 3 μM R6G in ethanol for 21 nm gold coated GeO_2 nanowires. Also shown is the ordinary Raman spectra of 3 μM ethanolic R6G bulk solution, t_{acc}=15 s. 124

Figure 4-46. Raman spectra of 3 μM R6G in ethanol from GeO_2 nanowire substrate decorated with 60 nm gold colloidal. Also shown is the baseline corrected spectra, t_{acc}= 15 s..... 125

Figure 4-47. (a) Nile blue molecular structure. SERS spectra of NB with 531 nm excitation[124]..... 127

Figure 4-48. SERS spectra of 21 nm Au film coated GeO_2 NWs before and after application of 2 μL of 10 μM NB, t_{acc}= 15 s. Baseline corrected spectra of NB is also shown..... 128

Figure 4-49. SERS spectra from 2 μL of 10 μM ethanolic NB along a line from GeO_2 NWs, t_{acc}= 5 s..... 128

Figure 4-50. Raman spectrum of spectra of 15 nm Ag coated GeO_2 nanowire substrate before and after applying 2.73 μM Nile blue in ethanol, t_{acc}= 5 s..... 129

Figure 4-51. Chemical structures Raman ethylene analytes..... 131

Figure 4-52. Effect of Au thickness on SERS spectra..... 132

Figure 4-53. SERS from 1mM BDT for 20 min soak..... 133

Figure 4-54. Effect of gold coating age on SERS from 1mM MBT..... 134

Figure 4-55. SEM image of GeO_2 NW substrate after 12 hr soak in 1mM MBT..... 135

Figure 4-56. Chemical structure and ordinary Raman spectrum of 4-MBT..... 136

Figure 4-57. (a) SERS spectra of a SAM of 4-MBT. Also shown is the Raman spectra of substrate before formation of SAM, t_{acc}=15 s for both spectra. (b) SERS spectra of a SAM of 4-MBT from 5 adjacent points 250 μm apart, t_{acc}= 5 s..... 138

Figure 4-58. 4-MBT 1068 cm^{-1} Raman peak intensity distribution for randomly chosen area on substrate, t_{acc}= 5 s..... 139

Figure 4-59. Possible structures of 4-MBT SAM on Au(111)[130]. Open circles are gold atoms and solid circles represent sulfur head group of 4-MBT. 140

Figure 4-60. Ordinary Raman spectra of 4-MBT and polystyrene, t_{acc}= 5 s. 143

Figure 4-61. (a) EF correction for cylindrical excitation volume assumption. (b) DFOV estimation using two Raman bands of solid 4-MBT crystals. 144

Figure 4-62. SERS spectra of a SAM of 4-MBT on Klarite chip from 5 different points, t_{acc}= 5 s. 146

Figure 4-63. 4-MBT 1068 cm^{-1} Raman peak intensity distribution for randomly chosen area on Klarite chip, t_{acc}= 5 s. 147

Figure 4-64. Chemical structure and ordinary Raman spectrum of BPE 149

Figure 4-65. SERS spectra of 0.83 μM BPE from Au coated GeO_2 NWs, t_{acc}= 15 s. .. 150

Figure 4-66. SERS spectra of 0.83 μM BPE from different points on substrate, t_{acc}= 5 s. 151

Figure 4-67. BPE 1190 cm^{-1} Raman peak intensity distribution for randomly chosen area on substrate, t_{acc}= 5 s. 151

Figure 4-68. Ordinary Raman spectra of 1,2-BDT in liquid state. Also show is the chemical structure of molecule. 153

Figure 4-69. SERS spectra of self-assembled monolayer of 1,2-BDT from Au coated GeO_2 nanowires, t_{acc}= 15 s. 154

Figure 4-70. SERS spectra from 1mM BDT along line on substrate. 156

Figure 4-71. Area map of 1028 cm^{-1} Raman peak of 1,2-BDT, t_{acc}=5 s. 157

Figure 4-72. Molecular structure of 1,2-BDT and formation of SAM on Au(111) face[126]. 157

Figure 4-73. Optical image of laser illumination of Si wafer (left) and GeO_2 NWs substrate (right). 159

Figure 5-1. SEM image of GeO_2 NW substrate 164

Figure 5-2. SEM image of cracked GeO_2 film on Si substrate during nanowire synthesis. 164

Figure 5-3. EDS elemental map for top right corner of cavity in **Figure 5-2**. 165

Figure 5-4. SEM image showing non-uniformity of the film on the substrate. 166

Figure 5-5. SEM image of substrate showing different morphologies of GeO_2 particles and NWs 166

Figure 5-6. Schematic of low temperature synthesis of germanium dioxide nanowire. 168

Figure 5-7. SEM image of GeO_2 nanowires on Si at 400-500 °C 168

Figure 5-8. EDS spectrum and quantification results for GeO_2 nanowires. 169

Figure 5-9. TEM image showing dark catalyst particle at tip. Right image shows a dark spherical particle probably broken during sample preparation. 170

Figure 5-10. Different morphology of low temperature GeO_2 NWs. 171

Figure 5-11. Rate of Ge oxidation versus oxygen pressure at 550 °C [98] 175

Figure 5-12. Plot showing GeO_2 stability as function of temperature and the hydrogen to water vapors pressure ratio[112] 180

Figure 5-13. Tube furnace typical spatial temperature profile during nanowire synthesis. 181

Figure 5-14. Typical pressure profile during NW synthesis. 182

Figure 5-15. GeO_2 NWs on Si(100) that has patterned Au film (No gold was coated in the dark "X" pattern). Right image shows close up of the red circled area of left image. 184

Figure 5-16. GeO_2 NW showing particle at tip. 184

Figure 5-17. SEM image and particle size distribution for 3 nm Au film. 186

Figure 5-18. SEM image and particle size distribution for 7 nm Au film. 187

Figure 5-19. SEM image and particle size distribution for 15 nm Au film. 188

Figure 5-20. SEM image and particle size distribution for 21 nm Au film. 189

Figure 5-21. SEM image and particle size distribution for 28 nm Au film. 190

Figure 5-22. Mean particle size distribution for different initial Au film thickness at 500 °C. Error bars indicate standard deviation from mean. 191

Figure 5-23. GeO_2 NW diameter distribution for 7 nm Au film. 192

Figure 5-24. GeO_2 NW diameter distribution for 14 nm Au film. 193

Figure 5-25. GeO_2 NW diameter distribution for 21 nm Au film. 193

Figure 5-26. Mean diameters of GeO_2 NWs and annealed Au film particles. 195

Figure 5-27. Effects of growth time on the length of the NWs. 196

Figure 5-28. Length of NWs versus growth time. 197

Figure 5-29. Effect of oxygen concentration on NW synthesis. 198

Figure 5-30. Elemental composition of the sample surfaces after growth for different oxygen concentrations. 199

Figure 5-31. Effect of background gas flow rate on NWs synthesis. 201

Figure 5-32. GeO_2 NW growth at different temperatures. 202

Figure 5-33. SEM images of GeO_2 NWs synthesized using Ar as background gas..... 203

Figure 5-34. SEM image of GeO_2 NWs synthesized using N_2 as background gas. 204

Figure 5-35. GeO_2 NWs diameters for different background gases. 205

Figure 5-36. Island like growth of NWs for 7 nm Au coated Si substrate with N_2 as background gas. 206

Figure 5-37. Island like growth of NWs for 7 nm Au coated Si substrate with Ar as the background gas. 207

Figure 5-38. GeO_2 NWs found at higher temperature region of furnace on 7 nm Au coated Si substrate..... 208

Figure 5-39. GeO_2 NWs found at higher temperature region of furnace on 15 nm Au coated Si substrate..... 208

Figure 5-40. NW synthesis at a background gas pressure of 1.1 Torr. 209

Figure 5-41. NW synthesis at a background gas pressure of 6 Torr shows location dependent growth. 210

Figure 5-42. Raman spectra of GeO_2 NWs of different diameters, t_{acc}=15 s. 211

Figure 5-43. Raman spectra for two different morphologies of NWs. Insert shows SEM image showing circular islands on uniform background. 212

Figure 5-44. Raman spectra of bare and 12 nm Au coated GeO_2 NWs, t_{acc}=15 s. 214

Figure 5-45. Raman spectra of Au coated GeO_2 NWs of average diameter 108 nm, t_{acc}=15 s. 215

Figure 5-46. Raman spectra of Au coated GeO_2 NWs of average diameter 120 nm, t_{acc}=15 s. 216

Figure 5-47. SEM images of substrate before (left) and after (right) 12 hr soak in 1 mM methanolic MBT. 217

Figure 5-48. Chemical structures of 4-MBT and 1,2-BDT used as Raman analytes. ... 217

Figure 5-49. SERS spectra of SAM of 4-MBT on 108 nm dia NWs, t_{acc}=15 s. 219

Figure 5-50. Successive spectra from substrate points spaced 250 μm along a line, t_{acc}=15 s.. 219

Figure 5-51. Effect of Au coating thickness on SERS activity of substrate having 108 nm mean diameter NWs. 221

Figure 5-52. Effect of Au coating thickness on SERS activity of substrate having 108 nm mean diameter NWs. Also shown is spectra (along the *x*-axis) from a flat Si(100) with 55 nm Au coating that was soaked in 1mM MBT along with the NWs. 221

Figure 5-53. Variation of 1068 cm^{-1} Raman peak intensity of 4-MBT with Au film thickness. 222

Figure 5-54. SERS spectra of SAM of 4-MBT for different Au film thickness on GeO_2 NWs with 108 nm mean diameter. 222

Figure 5-55. Variation of Raman intensity with Au film thickness for different diameters of NWs. 223

Figure 5-56. Variation of Raman EF with length of GeO_2 NWs coated with 40 nm thick Au film. 224

Figure 5-57. Spatial map of SERS intensity for 1068 cm^{-1} peak of 4-MBT. 225

Figure 5-58. Ordinary Raman spectra of 4-MBT and polystyrene. 228

Figure 5-59. SERS spectra of SAM of 1,2-BDT on 108 nm diameter NWs, t_{acc} = 15 s. 229

Figure 5-60. SERS spectra of SAM of 1,2-BDT from different points on substrate. 229

Figure 5-61. Spatial map of SERS intensity for 1028 cm^{-1} peak of 1,2-BDT, t_{acc}=5 s. 230

Figure 6-1. Experimental set up for ZnO nanowire synthesis. 237

Figure 6-2. Zinc oxide nanowires on Si 100 substrate using Au as catalyst..... 237

Figure 6-3. Diameter distribution of ZnO NWs..... 238

Figure 6-4. ZnO nanowires on source powder..... 238

Figure 6-5. ZnO NWs found in uncoated area of Si wafer..... 239

Figure 6-6. EDS spectrum and quantization results for ZnO nanowires..... 240

Figure 6-7. Different morphologies of ZnO nanostructures. (a) Nanocombs. (b) Nanorods. (c) Nanowhisker. (d) Nanocages. (e) Flowers. (f) Hexagonal rods..... 241

Figure 6-8. Probing structures under ZnO NWs..... 245

Figure 6-9. NWs on catalyst coated (left) and uncoated (right) substrates..... 245

Figure 6-10. ZnO nanostructures in low temperature region on gold coated silicon..... 248

Figure 6-11. Raman spectra of Zinc oxide nanowires on alumina and silicon substrates showing characteristic peak at 437cm^{-1}, t_{acc}=20 s..... 249

Figure 6-12. Raman spectra of 21nm gold coated ZnO nanowires on Si 100 substrate, t_{acc}=15 s. Insert shows the SEM image of substrate..... 251

Figure 6-13. Raman spectra of ZnO combs on Si100, t_{acc}=15 s. Insert shows SEM image of the substrate..... 251

Figure 6-14. Ordinary Raman spectra of 3 μM ethanolic solution of R6G showing only the ethanol peaks..... 253

Figure 6-15. Raman spectra of 3 μM R6G from 21 nm Au coated ZnO nanowires synthesized on Si(100) substrate..... 253

Figure 6-16. Raman spectra of ZnO nanowire. (a) Before adding NB. (b) After adding NB..... 255

Figure 6-17. Raman spectra of 2.73 μM ethanolic NB from ZnO nanowires coated with 60 nm gold colloidal at two locations, t_{acc}=15 s..... 256

Figure 6-18. Effect of gold coating thickness of SERS from SAM of 1,2-BDT on ZnO NWs, t_{acc}=15 s..... 258

Figure 6-19. Effect of gold coating thickness of SERS from SAM of BDT on ZnO NWs, t_{acc}=15 s..... 258

Figure 6-20. Effect of gold coating thickness of SERS from SAM of 4-MBT on ZnO NWs, t_{acc}=15 s. 260

Figure 6-21. Effect of gold coating thickness of SERS from SAM of MBT on ZnO NWs, t_{acc}=15 s. 260

Figure 6-22. ZnO NWs substrate. (a) Before 4-MBT soak. (b) After 12 hr soak in 1 mM MBT. 261

Figure 6-23. SERS spectra of a SAM of 4-MBT from 5 adjacent points 250 μm apart, t_{acc}= 15 s. 262

Figure 6-24. 4-MBT 1068 cm^{-1} Raman peak intensity distribution for randomly chosen area on substrate, t_{acc}= 5 s. 263

Figure 6-25. Ordinary Raman spectra of 4-MBT and polystyrene, t_{acc}= 5 s. 266

Figure 6-26. SEM image of two typical morphologies of ZnO NWs. (a) Randomly oriented. (b) Partially aligned. Scale bar is 2 μm in both images. 267

Figure 6-27. Comparison of SERS signal from random and partially aligned ZnO NWs for SAM of 4-MBT, t_{acc}=15 s. 268

Figure 6-28. SERS from SAM of 4-MBT for (a) randomly distributed NWs, t_{acc}=15 s. (b) Partially aligned NWs, t_{acc}=15 s. 269

Figure 6-29. Cross-section for ZnO nanowires. (a) Randomly distributed. (b) Partially aligned. 270

Figure 6-30. ZnO nanoparticles in low temperature region of reactor and SERS spectra of SAM of MBT after gold coating of particles, t_{acc}=5 s. 271

Figure 6-31. SERS spectra of self-assembled monolayer of 1,2-BDT from Au coated ZnO nanowires, t_{acc}= 15 s. Also shown is spectra before analyte application. 272

Figure 6-32. Successive SERS spectra from 1mM BDT along a line on substrate, t_{acc}=15 s 273

Figure 6-33. Area map of 1028 cm^{-1} Raman peak of 1,2-BDT, t_{acc}=5 s for each point. 273

Figure 7-1. (a) OAD experimental set up schematic. (b) Optical image of Silver nanorods substrate (c) Optical image of copper nanorods substrate. 278

Figure 7-2. SEM images of nanorods synthesized on glass substrate. (a) Aluminum nanorods. (b) Copper nanorods. (c) Silver nanorods. (d) Silver nanorods showing shadowing effect. 280

Figure 7-3. Aluminum NRs diameter and length distribution. 281

Figure 7-4. Copper NRs diameter and length distribution. 282

Figure 7-5. Silver NRs diameter and length distribution. 283

Figure 7-6. EDS spectra and quantization results for aluminum nanorods substrate. ... 284

Figure 7-7. EDS spectra and quantization results for copper nanorods substrate 285

Figure 7-8. EDS spectra and quantization results for silver nanorods substrate 286

Figure 7-9. Silver nanorods that grew on sample clips (clips made of steel). 287

Figure 7-10. Raman spectra of silver nanorods, t_{acc} = 5 s. Insert shows SEM image of silver nanorods. 290

Figure 7-11. Raman spectra of smooth silver film and glass slide, t_{acc} =5 s. 290

Figure 7-12. Raman spectra of copper and silver tipped aluminum nanorods, t_{acc} 5 s.. 291

Figure 7-13. SERS spectra from Ag nanorods substrates before and after applying 3 μL of 5 μM ethanolic NB, t_{acc} 15 s. Insert shows ordinary Raman spectra of 170 mM NB in ethanol with only weak 582 cm^{-1} peak identifiable. 292

Figure 7-14. SERS spectra from Ag nanorods substrate from different spots for 5 μM ethanolic NB, t_{acc}= 5 s. 293

Figure 7-16. Raman spectra from silver tipped aluminum nanorods before and after application of 100 μM 4-MBT, t_{acc}= 15 s. 295

Figure 7-17. MBT SAM spectra before and after soaking aluminum nanorods in 0.1 mM methanolic for 14 hrs, t_{acc}= 5 s. 295

Figure 7-18. 4-MBT 1071 cm^{-1} Raman peak intensity distribution from silver tipped aluminum nanorods for randomly chosen area on substrate, t_{acc}= 5 s 296

Figure 7-19. Raman spectra from copper nanorods before and after formation of SAM of MBT, t_{acc}= 15 s. 297

Figure 7-20. Raman spectra of from Silver nanorods substrate before and after formation of SAM of 4-MBT, t_{acc}= 15 s. 298

Figure 7-21. 4-MBT 1068 cm^{-1} Raman peak intensity distribution for a randomly chosen area on a silver nanorods substrate, t_{acc}= 5 s. 298

Figure 7-22. (a) Optical constants of silver as function of incident wavelength[76]. Circles correspond to laser wavelength used in this work. (b) Theoretical enhancement factor for an isolated silver nanorod as function of aspect ratio. 304

Figure 7-23. (a) Optical constants of copper as function of incident wavelength[76]. Circles correspond to laser wavelength used in this work. (b) Theoretical enhancement factor for an isolated copper nanorod as function of aspect ratio. 306

Figure 7-24. Raman spectra of aluminum nanorods before and after application of formation of SAM of 1,2-BDT, t_{acc}= 15 s. 307

Figure 7-25. Raman spectra of silver nanorods before and after application of 20 μM 1,2-BDT, t_{acc}= 15 s. 308

Images in this dissertation are presented in color.

Chapter 1: Introduction

1.1 Raman spectroscopy

The understanding and control of interaction between light and matter has always been an area of active research due to its potential applications in many fields of science and technology. Vibrational spectroscopic techniques have been extensively employed to study this interaction and have played a major role in extending our understanding of structure, bonding, and reactivity in all phases of matter. The main techniques to detect molecular vibrations are based on the processes of infrared (IR) absorption and Raman scattering. These are widely used to provide information on chemical structure of matter, identify substances using their characteristic spectral patterns, and to determine quantitatively or semi-quantitatively the amount of substance in a sample. Samples can be examined in a whole range of physical states; for example, as solids, liquids or vapors, in hot or cold states, in bulk, as microscopic particles, or as surface layers.

Raman spectrum is considered as the optical fingerprint of chemicals and bimolecules as it represents the vibrational frequencies of functional chemical bonds in molecules[1]. Raman spectroscopy offers a number of advantages due to its ability to examine samples inside glass containers without any special preparation and in the presence of common solvents like water. Being a completely non-detructive and non-intrusive technique, it permits the detection and identification of unknown species in any phase. As an optical technique it has high resolution (1 cm^{-1}) and immunity to the presence of an ambient gas phase. On the more fundamental side, it provides spectra complementary to those obtained by either infrared absorption or electron energy loss

spectroscopy[2]. Raman scattering depends upon the change in the molecular polarizability during a molecular vibration, while infrared absorption depends upon the change in the dipole moment. High resolution, wide spectral range, high sensitivity, complementary selection rules, and high spatial resolution make Raman spectroscopy an ideal probe for surface sciences. It also finds its usage in a wide variety of fields including examination and identification of inorganics, minerals, art, archaeology, polymers, emulsions etc. Raman scattering is extensively employed in biological, pharmaceutical and forensic applications to study physical structures of the live cells, and for plant control and reaction following[3].

1.2 Limitations of conventional Raman spectroscopy

Despite its numerous advantages, conventional Raman scattering is less widely used than infrared absorption. The major shortcoming of the technique is its extremely small scattering cross section as compared to the Rayleigh or elastic scattering. Typical Raman scattering cross sections of molecules are in the range of $\sim 10^{-29}$ cm^2 whereas typical Rayleigh scattering cross sections are $\sim 10^{-26}$ cm^2 [4]. The scattering cross section of a particle is defined by relating the rate of photons striking a molecule to the rate of scattering in all directions and can be viewed as an area presented by a molecule for the scattering of incident photons[4]. Thus it might appear that the application of such an intrinsically inefficient process to the detection of trace amount of species would not be very productive. In addition to low signal intensity, Raman spectroscopy is also plagued by fluorescence[5]. Fluorescence is a strong light emission from the sample (including sample impurities) or its surrounding. These broadband fluorescence signals can be of much higher intensity than the Raman signals and may altogether obscure the Raman

spectra (typical fluorescence cross sections of molecules is ~ 10^{-19} cm^2)[4]. It is estimated that at least 40% of the samples used in Raman spectroscopy suffer from some degree of fluorescence. Techniques such as time resolved spectroscopy, excitation using deep ultraviolet (UV) and metal fluorescence quenching have been studied to tackle fluorescence problem but each has its associated problems like sample degradation from UV irradiation, spectra perturbation by metal etc. The chance of an unknown sample exhibiting fluorescence is strongly dependent on the wavelength of the laser used for excitation. Typical laser wavelengths are 780 nm, 633 nm, 532 nm, and 473 nm, although others are common. Fluorescence from the sample or its surrounding can be significantly reduced by moving the excitation all the way to the near infrared (for example, 785 nm will yield considerably less fluorescence than 532 nm). But on the other hand the efficiency of Raman scattering is proportional to $1/\lambda^4$, so there is a decrease in enhancement as the excitation laser wavelength becomes longer. Hence a balance needs be maintained between enhancements from shorter wavelength versus accompanying fluorescence. Near-infrared (IR) laser excitation greatly reduces the number of samples prone to fluorescence and allows higher laser powers to be used without photodecomposition. This makes Near-IR excitation a natural choice for the study of fluorescent prone samples but the low sensitivity due to small scattering cross-section remains a major problem limiting the widespread application of Raman spectroscopy.

1.3 Surface enhanced Raman spectroscopy

The observation of Surface-Enhanced Raman Spectroscopy (SERS) by Fleishchman *et al.* in 1974 reinvigorated interest in Raman scattering as a powerful

analytical tool[6]. The Raman signals from pyridine molecules adsorbed on the electrochemically roughened silver electrode were found to be over a millionfold stronger than their corresponding surface densities. The initial enthusiasm following the discovery of SERS lasted for over a decade and many theories were proposed to explain the strong enhancement observed from rough surfaces and colloidal aggregates. Today, it is generally agreed that the SERS arises from two mechanisms – an electromagnetic enhancement and a chemical charge transfer effect. In electromagnetic enhancement model, the analyte located in the close proximity to the metal interacts with the incident laser light through the excitation of surface plasmons in metal[7]. The metal can be in the form of a thin rough film with nanoscale features or in the form of aqueous colloidal nanoparticles. Silver, gold and copper are the common metals employed due to their strong SERS activity. In the theory of chemical enhancement, the analyte chemically bonds to the metal and excitation is through the transfer of electrons from metal to molecule and back to metal again[8]. There is evidence for both mechanisms contributing to SERS but it is difficult to isolate one from the other in actual measurement. However, it is widely accepted that electromagnetic enhancement plays a more dominant role than the chemical enhancement. The work in SERS reached a plateau about ten years ago but became reinvigorated again by the reports of Kneipp and coworkers[9-13] and Nie and coworkers[14-18] of single molecule detection. Both independently and simultaneously demonstrated that under favorable circumstances it is possible to detect single molecule based on its SERS spectra. The reported enhancement factors are of the order of 10^{14} with an effective Raman cross-section of 10^{-16} cm^2/molecule at near-infrared non-resonant excitation for molecules in colloidal silver solution[19].

The discovery of SERS has offered an unprecedented sensitivity and selectivity to Raman spectroscopy. Identifying molecules at very low concentrations is critical for many analytical applications such as forensics, medical diagnostics, drug discovery, and chemical development. This giant enhancement of Raman signal offers the potential of developing an ultrasensitive sensing platform based on SERS with molecular (especially bimolecular) identification capabilities. SERS is an attractive tool for biomedical applications because it has several advantages over competing optical techniques. Some of these advantages are: (i) minimal sample preparation; (ii) potential for remote sampling through fiber optics; (iii) fast analysis; (iv) weak Raman scattering of hydroxyl group. This implies that water and silica do not manifest themselves as serious sources of background noise. Thus biological samples in aqueous media can be analyzed without any interference from water or glass containers. As a result, a number of biological applications using SERS have been reported. Kneipp has demonstrated SERS nanoprobes utilizing gold nanoparticles for probing intrinsic chemical environment in living cells[20]. Yonzon *e. al.* reported a SERS based blood-glucose sensor that can be used for real-time continuous sensing[21]. The sensor utilized a mixed self-assembled monolayer (SAM) of decanethiol (DT) and mercaptohexanol (MH) on silver film over nanospheres (AgFON). The purpose of SAM was to protect oxidation of silver and to provide for the binding of analyte of interest to the AgFON. The silver nanospheres based SERS was able to efficiently detect and quantify glucose in physiological concentration range in the presence of interfering analytes and in bovine plasma. The sensor showed temporal stability for at least 10 days in bovine plasma, making it a potential candidate for implantable sensing. Similarly Vo-Dinh and coworkers have successfully demonstrated

SERS based gene probes for the detection of HIV DNA, p53 cancer gene, and hyperspectral imaging of Raman dye-labeled silver nanoparticles in single cells[22, 23]. Alak and Vo-Dinh were the first to demonstrate trace level detection of organophosphorus chemical agents using SERS[24]. Since then, SERS has also been applied for the detection of chemical agents like cyanide, VX, Sarin etc., and their hydrolysis products in water[25]. Many researchers have reported successful detection of trace amount of bacillus anthracis (anthrax) spores using SERS[26-29]. SERS has also been utilized to detect common bacteria like E. coli that cause intestinal and extra-intestinal infections[30].

1.4 Common SERS substrates

The initial observation of SERS was from metal electrodes roughened by oxidation-reduction cycles. Later SERS was also reported from silver and gold colloidal nanoparticles. Currently the colloidals are one of the most widely used substrates for SERS due to the ease of preparation. However, the techniques exploiting colloids or roughened surfaces prevent the control of the spacing and periodicity of the features. This leads to the random and strong variations in the SERS signal from these substrates that limit their widespread use for analytical applications. Numerous efforts have been devoted to the search for a homogeneous, repeatable, and mass producible SERS substrate that can yield enormous enhancement factors observed in random "hot spots". Various forms of nanostructures have been explored to enhance SERS effects, such as rough metallic surfaces by chemical etching[31], silver films on TiO_2[32], colloidal silver nanoparticles[15], silver nanoparticle arrays fabricated by nanosphere lithography[33],

electro-deposition of silver on silver films at high potential[34], aligned monolayer of silver nanowires[35] and aligned silver nanorods by oblique angle deposition[36, 37]. However, many of these methods are either expensive or time consuming, and it is not easy to make reproducible substrates of the correct surface morphology to provide maximum SERS enhancements. Assembling metal nanostructures synthesized by a bottom-up approach, such as by Langmuir- Blodgett films or by casting metal colloids onto surfaces, can achieve quasi-regular arrays of metallic nanoparticles or nanowires with small separation. However, most of the bottom-up approaches usually require a monolayer coating of surfactants for dispersion during synthesis. This added surfactant can interfere with the Raman signal of the analyte. Other techniques, such as nanosphere lithography (NSL) uses self assembled and close-packed nanospheres as the lift-off layer for evaporated Raman active metal (usually Ag or Au)[38]. This technique also fails to provide the necessary nanometer-scale gaps between metallic nanostructures formed between nanospheres following lift-off.

1.5 Major challenge for SERS

The discovery of SERS effect promised to expand the applications of Raman for the detection of very low concentrations of molecules. The potential of SERS has been demonstrated by single molecule detection. However, until very recently, the common SERS substrates (typically colloids or roughened surfaces) gave highly variable signals and severely limited acceptance of SERS as a viable analytical technique. As a result, the dream of an ultra-sensitive field deployable robust SERS sensor is still far from reality. All the giant Raman enhancement demonstrations reported have come from few hotspots

on the substrate[15]. In the study of SERS from silver (Ag) nanocrsytal aggregates, Jiang and coworkers noted that the hotspots are mostly compact, nonfractal aggregates of Ag nanoparticles and only fewer than 1% of the aggregates give detectable SERS activity[39]. The hotspots yielding high SERS activity are interspersed with large areas of little or no enhancement. This leaves the analyst with the tedious task of manually exploring the surface of the substrate for these hotspots and subsequent detection of analyte. Mostly these hot spots result from natural and uncontrollable aggregation of nano-particles at random locations on substrate that make the SERS measurement highly erratic. The lack of reproducibility has effectively limited SERS to the research laboratory. A way around this problem is engineering substrates that have uniform morphology imitating such hotspots. The difficulty of fabricating such substrates can be gauged from the order of dimensions needed for reasonable SERS enhancement. Both the theoretical and experimental studies suggest that a separation of less than 5 nm between aggregated nanoparticles is necessary for strong SERS enhancement[39]. But this scale of controlled separation is far beyond the resolution of any scalable top-down fabrication approach[40]. Today main issue facing the SERS community is fabrication of a robust, economical and scalable substrate that can provide high sensitivity with good uniformity and repeatability over large area.

1.6 SERS from Nanowires : Motivation for this work

SERS has the potential to greatly enhance our current capability of trace chemical analysis. This can have significant impact on early medical diagnosis and treatment. Also it can be an effective tool in monitoring the food supply chain against viral and bacterial

contaminations. At the same time, the ability to detect chemical and nerve agents will help fight the threat of bio-terrorism. However, the full potential of SERS can be only realized after developing techniques for economical fabrication of a homogenous SERS substrate. This research has been motivated by the desire to fabricate an economical and reproducible SERS substrate based on different types of nanowires and nanorods. The terms nanowire and nanorod are often used interchangeably to denote high aspect ratio (AR) nanostructures. In this dissertation, the term nanowire is used to denote the nanostructures having lengths much larger than diameter (*i.e.*, $AR = \frac{length}{diamter} >> 1$). The nanorods are also high aspect ratio nanostructures but their aspect ratio is less compared to nanowires ($typically\ AR \leq 10$). The use of these high aspect ratio nanostructures such as nanowires and nanorods for SERS has several advantages. These include:

1. The high aspect ratio of these nanostructures yields strong electric field enhancement.
2. The surface properties of these nanostructures are highly reproducible and well defined as compared to colloidal systems.
3. The synthesized nanowires/nanorods offer many unique features (sharp vertices, noncircular cross-sections, inter-wire coupling) that may lead to larger field enhancement factors, offering higher sensitivity under optimal conditions[41, 42].
4. High density of nanowires/nanorods means close interaction between adjacent nanowires and hence strong inter-wire coupling, which enables SERS to manifest for a broad selection of excitation sources.

5. The nanowires/nanorods can readily be used for molecular detection either in air or in aqueous solution environment.
6. The semiconducting nanowires of zinc oxide and germanium dioxide are high refractive index materials, which can provide strong light confinement for improved SERS effect.

The major contribution of this dissertation to the field of SERS is an attempt to investigate oxide nanowire based substrates for potential use in detection of chemicals using Raman spectroscopy. This includes both the fabrication and characterization of the nanowire substrate for application as SERS platforms. It deals with bulk synthesized semiconducting nanowires of germanium oxide and zinc oxide to yield SERS. The germanium oxide nanowires were initially synthesized at high temperature (~850 °C). Subsequently a novel low temperature (~650 °C) synthesis was developed to achieve better control over the parameter of substrates. The as-synthesized oxide nanowires are not Raman active since only noble metals yield appreciable SERS. Gold coating of the nanowires has been employed as SERS active interface to support surface plasmons. Selection of gold is based on its chemical inertness, compatibility with biological systems and good optical properties for near IR laser excitation. The chemical functionality can be easily added to the gold coated substrates by exploiting well-established surface chemistry protocols. The coating of SERS substrates with ligand molecules having specific terminal groups is extremely effective to boost the selectivity of the SERS substrate. This functionalization of SERS substrates is particularly useful in the case of complex molecules such as proteins or for molecules with low affinity to metal. The

comparison of SERS performance of nanowires with that of commercially available Klarite chip showed a stronger enhancement from nanowires. The dissertation also investigates synthesis of aluminum and copper nanorods using well-established oblique angle deposition technique. The SERS performance of theses quasi-aligned nanorods is evaluated using model molecules and compared with those of commonly employed silver nanorods.

1.7 Organization of this dissertation

This dissertation is organized into 7 chapters. The dissertation begins with an introduction to the theory of Raman scattering and SERS in chapter 2. The experimental set up for the preparation of SERS substrates and their Raman characterization is described in chapter 3. Synthesis and Raman studies of high temperature fabricated germanium oxide nanowires is presented in chapter 4. Results of Raman analysis using low temperature germanium oxide, zinc oxide, and silver nanorods are presented in chapter 5, 6, and 7 respectively. Finally chapter 8 presents a summary of results and outlines some future tasks.

Chapter 2: Theory of Raman Scattering

When monochromatic radiation scattered from a system such as gas, liquid or solids is analyzed, most of the light has same frequency (hence wavelength) but some fraction is found to have different frequency than the incident light. Such scattering of light with a change of frequency is known as Raman scattering, after Indian scientist C. V. Raman who, with K. S. Krishnan, first observed this phenomenon in 1928[43]. The elastic scattering from scattering centers like molecules that are very small compared to the wavelength of incident radiation is called Rayleigh scattering. Another type of elastic scattering from larger objects (size greater than wavelength of incident radiation) like a dust particle is also possible and is referred as Mie scattering[44]. Often the term Rayleigh scattering is used to represent both Rayleigh and Mie elastic scattering[45]. Inelastic scattering originating from the Doppler effect with a very small frequency change (wavenumber change of the order of 0.1 cm^{-1}) can also exist. This type of scattering, predicted by Brillouin in 1922 and experimentally verified by Gross in 1930, is called Brillouin scattering[46]. However, due to very small wavenumber change, Brillouin scattering is not separable from the incident radiation under the experimental conditions used for Raman spectroscopy.

Light scattering arises from the dipole moments induced in molecules by the incident field, through the polarizability of the electrons. Polarizability is the ability of the electron cloud to be distorted by the electric field of the incident radiation. The more polarizable a molecule is, the more the electron clouds of its bonds are distorted by the incident radiation. The electric field of the radiation interacts with the electron cloud of

the bonds of molecule in the sample and this induces a temporary dipole moment in the bond[47]. The molecular bond emits the scattered light (Rayleigh or Raman scattered) as it relaxes to a low energy unexcited state. Rayleigh scattering is a result of static polarizability whereas Raman scattering follows from the modulation of polarization by electronic, vibrational or rotational motions[45]. Rayleigh scattering, being at the frequency of the incident radiation, does not convey any useful information but Raman scattering provides information about the vibrational states of the molecule.

2.1 Classical theory of Raman scattering

A simple classical model based on electromagnetic theory of radiation can be used to gain insight into the light scattering phenomena. Consider a laser beam illuminating the sample at frequency ν_0 with corresponding amplitude of electric field given by

$$E = E_0 \cos(2\pi\nu_0 t) \tag{2.1}$$

The electric field can induce a dipole moment μ in the molecule according to

$$\mu = \alpha E \tag{2.2}$$

where α is the polarizability of the molecule. At a molecule's equilibrium nuclei geometry, the polarizability has certain value, α_0. As the molecule vibrates, the distance

between nuclei changes from that of equilibrium. At some distance, Δr, away from the equilibrium position, the instantaneous polarizability is given by

$$\alpha = \alpha_0 + \left(\frac{\partial \alpha}{\partial r}\right)\Delta r \qquad (2.3)$$

Here the derivative term represents the change in the polarizability of the molecule with change in position. Suppose the molecule is vibrating or rotating in some sinusoidal manner with maximum displacement of $r_{\max}$, then Δr can be expressed in terms of vibrational frequency ν_m as

$$\Delta r = r_{\max} \cos(2\pi \nu_m t) \qquad (2.4)$$

Inserting equation (2.4) into equation (2.3) gives

$$\alpha = \alpha_0 + r_{\max}\left(\frac{\partial \alpha}{\partial r}\right)\cos(2\pi \nu_m t) \qquad (2.5)$$

Substituting the value of α and E from equation (2.5) and (2.1) respectively into (2.2), the time dependence of the dipole moment becomes

$$\mu = \alpha_0 E_0 \left[1 + r_{\max} \left(\frac{\partial \alpha}{\partial r} \right) \cos(2\pi \nu_m t) \right] \cos(2\pi \nu_0 t)$$
$$= \alpha_0 E_0 \cos(2\pi \nu_0 t) + \frac{1}{2} E_0 r_{\max} \left(\frac{\partial \alpha}{\partial r} \right) \cos(2\pi(\nu_0 + \nu_m)t) \qquad (2.6)$$
$$+ \frac{1}{2} E_0 r_{\max} \left(\frac{\partial \alpha}{\partial r} \right) \cos(2\pi(\nu_0 - \nu_m)t)$$

The final form of equation (2.6) shows that the scattered light has been modulated by the oscillating polarizability. The first term in the above equation corresponds to the Rayleigh scattering at the unshifted frequency. The second term with higher frequency, $\nu_0 + \nu_m$, is the anti-Stokes Raman scattering and third term with lower frequency, $\nu_0 - \nu_m$, is the Stokes Raman scattering. This simple classical treatment also provides a selection rule for Raman scattering: the molecular polarizability must change as a function of nuclear motion during a vibration for that vibration mode to be Raman active[2]. However, it is deficient in that it does not take into account the quantized nature of vibrations and lacks any information about intensities of scattering. Quantum theory on the other hand is able to better explain the relationship between molecular properties and Raman scattering. Nonetheless a simple insight into Raman scattering can be gained using a simple classical model of the wave nature of light.

Figure 2-1 shows a pictorial representation of the Rayleigh and Raman scattering. The states marked 0, 1, 2 etc., are different vibrational states (vibronic states) of the ground electronic state. The incident light considered as an oscillating dipole interacts with the molecule and polarizes the cloud of electrons. This transfers the energy of the light into the molecule, which is promoted to a higher energy virtual state as, indicated by upward arrows in **Figure 2-1**. This interaction can be considered as the formation of a

very short-lived 'complex' between the light and the electrons in the molecule[3]. This high-energy state, often called virtual state, has different electron geometry compared to the ground state and is characterized by the fact that the nuclei have not moved appreciably. This virtual state is a real state of the transitory 'complex' formed between light and molecule. This is an unstable state and energy is released almost simultaneously in the form of scattered radiation as annotated by the bold downward arrow in **Figure 2-1**. A word about the virtual state: since it has different electron geometry than the static state and the nuclei have not moved to reach a new equilibrium state to fit distorted electron arrangement, this state does not correspond to any of the electronic states of the molecule. The laser defines the extent of the distortion of electron cloud and the energy of the virtual state. As a result, this process is not quantized and the energy of the molecule can assume any of an infinite number of states depending on the frequency of radiation of the source. The Rayleigh scattering is the most intense form of scattering and is essentially an elastic process. This happens when the electron cloud relaxes without any nuclear motion. The Raman scattering (Stokes and anti-Stokes) happens when light and electrons interact and the nuclei begin to move at the same time. Since nuclei are much heavier than electrons, there is appreciable change in the energy of the molecule. If the molecules start with a ground state and finally relaxes to an excited ground state, then it has effectively absorbed the energy difference between two states. The scattered radiation is of longer wavelength than the excitation wavelength and the process is termed Stokes Raman scattering.

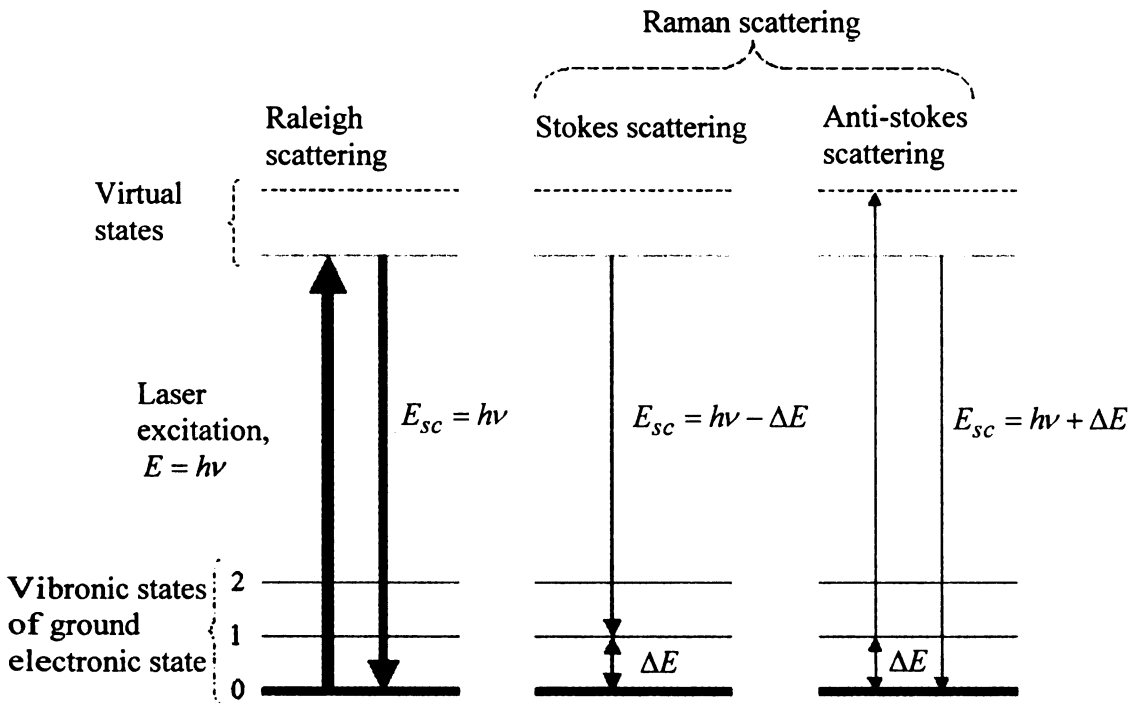

Figure 2-1. Pictorial representation of Rayleigh and Raman scattering[47].

On the other hand, if the molecule was initially in an excited state and makes a transition to ground state, the scattered radiation is of shorter wavelength and the process is called Anti-Stokes Raman scattering. At room temperature, most molecules are likely to be in their lowest energy electronic state or ground state '0' represented by bold horizontal line. Thus the intensity of Stokes Raman scattering will be much higher than the anti-Stokes scattering. The ratio of the Stokes and anti-Stokes Raman scatterings depends upon the population of molecules in the ground and excited state. This can be calculated using Boltzmann's equation

$$\frac{N_{ex}}{N_0} = \frac{g_{ex}}{g_0} \exp\left[\frac{-(E_{ex} - E_0)}{kT}\right] \qquad (2.7)$$

where

N_{ex} is the number of molecules in the excited vibrational energy level,

N_0 is the number of molecules in the ground vibrational energy level,

g is the degeneracy of the energy levels,

$E_{ex} - E_0$ is the difference in energy between the excited and the ground state,

k is the Boltzmann's constant (1.3807×10^{-23} JK^{-1}).

The intensity of Anti-Stokes band is expected to increase with increasing temperature as a larger fraction of a target molecules are expected to be in the first vibrationally excited states under such circumstance. It may be worth reiterating the fundamental differences between Raman scattering and the IR absorption. Although the Raman scattering and the IR absorption of a molecule are dependent upon the same vibrational modes, they arise from processes that are inherently different. The selection rule for IR absorption requires that the dipole moment must change for a molecular vibration to be IR active. Raman scattering on the other hand, involves a momentary distortion of the electron distribution of a bond in a molecule, which is then followed by reemission of the radiation as the bond returns to one of its ground electronic states. The homo-nuclear molecules such as nitrogen or oxygen provide a good example to illustrate this difference. These molecules do not possess any dipole moment in equilibrium position or under bond stretching vibration. Thus the bonds of homo-nuclear molecules are not infrared active as no dipole moment can be induced by the incident radiation. However, these bonds are Raman active since the polarizability of the bond between the

atoms in such a molecule varies periodically. The polarizability of the bond changes in phase with the stretching vibrations, reaching a maximum at the greatest separation and a minimum at the closest approach of the two nuclei.

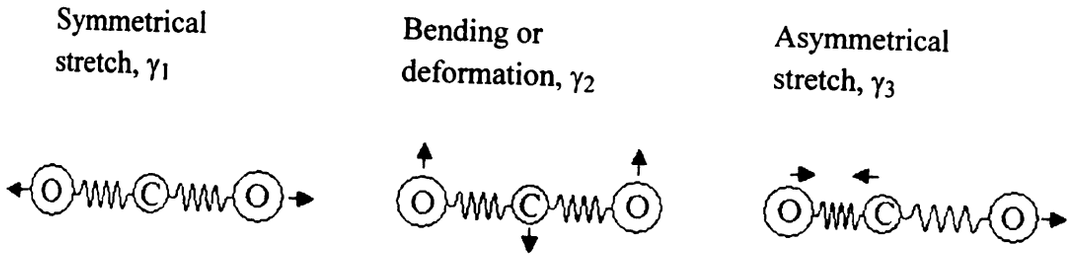

Figure 2-2. Three modes of vibrations of CO_2 molecule[3].

Figure 2-2 shows the three vibrational modes of CO_2. The symmetric stretches of CO_2 molecule are Raman active because polarizability clearly changes during the vibration. However, symmetric stretching is infrared inactive since there is no change in dipole. On the other hand, the asymmetric stretches in the molecule are Raman inactive because there is no change in the polarizability of the molecule. Since bond polarizability are additive, the polarizability change due to compression of one C=O bond is cancelled by the stretching of the other C=O bond. The asymmetric stretch is infrared active because when one of the oxygen atoms moves toward the carbon and other away from it. This results in a change in dipole moment, as there is a net change in charge distribution. Similar arguments apply to the bending vibration, which is IR active but Raman inactive.

The intensity of the Stokes Raman scattering is given by [3]

$$I = Kl\alpha^2\omega \qquad (2.8)$$

where K consists of constants such as speed of light, I is the laser power, ω is the frequency of incident radiation and α is the polarizability of the electrons in the molecule. This suggests that higher laser power and shorter wavelength will yield higher Raman intensities. But the problem of sample degradation, photodecomposition and fluorescence puts an upper limit on practically usable laser power and wavelength. The intensity has quadratic dependence upon the polarizability of the molecule. The polarizability is a function of the shape and size of the molecule. It usually varies with spatial direction and is independent of the permanent dipole moment (if present) in a molecule. It is an anisotropic property of a molecule and hence the scattered Raman intensity shows a dependence upon the direction and polarization of the incident and scattered radiation. Therefore, polarizability is often expressed as a tensor to take into account the possible variation in polarization. The polarizability is calculated quantum mechanically by perturbation theory or by time dependent theory.

2.2 Quantum mechanical theory of Raman scattering

In quantum mechanics, the Raman scattering is explained by the Kramers Heisenberg Dirac (KHD) equation derived by Krammers and Heisenberg[48], and Dirac[49]. The scattering process is described as an excitation to a virtual state (lower in energy than a real electronic transition) with nearly coincident de-excitation to a different vibronic state of ground electronics state. The difference in energy between two vibronic states manifests as a change in the wavelength of the scattered radiation. The scattering event occurs in 10^{-14} seconds or less. The KHD expression describing the molecular polarizability tensor for the transition from ground state to final state is given by[3]

$$\left(\alpha_{\rho\sigma}\right)_{GF} = \sum_{I}\left(\frac{\langle F|r_\rho|I\rangle\langle I|r_\sigma|G\rangle}{\hbar\omega_{GI} - \hbar\omega_L - i\Gamma_I} + \frac{\langle I|r_\rho|G\rangle\langle F|r_\sigma|I\rangle}{\hbar\omega_{IF} + \hbar\omega_L - i\Gamma_I}\right) \qquad (2.9)$$

Here G is the ground vibronic state, I is the intermediate state (a vibronic state of the excited electronics state) and F is the final vibronic state of ground state, $\left(\alpha_{\rho\sigma}\right)_{GF}$ is the molecular polarizability tensor component for transition $G \rightarrow F$, and ρ and σ are the incident and scattered polarization directions. The operator r is the electric dipole operator, $\hbar\omega_L$ is the incident photon energy, ω_{GI} is the angular frequency of transition $I \rightarrow G$, $\hbar$ represents $h/2\pi$ where h is Planck's constant and Γ_I is the natural linewidth of the intermediate state. The summation $\sum_I$ is over all vibronic states of the molecules due to non-specific nature of scattering. The numerator in equation (2.9) uses 'bra' and 'ket' (<| and |>) nomenclature for integrals to simplify the expression. In the integral $< I|r_\sigma|G >$, the $|G>$ is a wave function to represent ground vibronic state of the ground electronics state. The operator r_σ operating on $|G>$ and subsequent multiplication by excited state $<I|$ mixes the two states to describe the distorted electron configuration in the virtual state. This describes in part the excitation process (transition from ground vibronic state to an intermediate state). A similar scattering process described by $< F|r_\rho|I >$ leaves the molecule in the final state $|F>$. Since molecule can be in an excited vibronic state to start with, a second term in added in equation (2.9) that mixes the excited and ground in a similar way. It may be emphasized that the mixing of states (vibronic, excited and ground) employed in the KHD approximation models the virtual state of the molecule at the instant it had captured light. In the denominator of equation

(2.9), the $i\Gamma_I$ term relates to the life time of excited state and is small in energy compared to $\hbar\omega_L$ and $\hbar\omega_{GI}$. This term keeps the expression from blowing up when the laser energy approaches the energy difference between ground and the excited electronic state. It is obvious from the denominators of equation (2.9) that the second term plays smaller role in describing the polarization process and can be neglected.

The KHD expression models all possible transition from a ground state to a final state and it is very difficult to directly compute polarizability from basic electronic structure or even interpret spectra from KHD relation[50]. The KHD equation can be simplified by splitting states into electronic and vibrational components using the Born-Openheimer approximation. In this approximation, one can separate the total wave function (Ψ) into electronic (θ), vibrational (Φ) and rotational (r) components as

$$\Psi = \theta(r,R).\Phi(R).r(R) \tag{2.10}$$

where r and R are the electronic and nuclear co-ordinates respectively. The separation works because the time scales for electronic transitions (10^{-13} sec or less) are much smaller as compared to vibrational transitions (10^{-9} sec)[3]. Although rotational effects can be seen in gas phase Raman, these are relatively weak and can be neglected. The splitting up of the wave functions allows for the integrals of KHD expression to be split up as

$$\langle I|r_\sigma|G\rangle = \langle \theta_I.\Phi_I|r_\sigma|\theta_G.\Phi_G\rangle = \underbrace{\langle\theta_I|r_\sigma|\theta_G\rangle}_{electronic}\underbrace{\langle\Phi_I|r_\sigma|\Phi_G\rangle}_{vibronic} \tag{2.11}$$

No appreciable nuclear movement can occur during Raman scattering due to extremely small time scale of Raman scattering. Thus the electronic part of the wave function can be written as

$$M_{IG}(R) = \langle \theta_I | r_\sigma | \theta_G \rangle \tag{2.12}$$

Since nuclei will change position during vibrational transition, the electronic dipole matrix elements $M_{IG}(R)$ of equation (2.12) are varying functions of nuclear co-ordinates R. Thus movement M_{IG} can be expanded about the equilibrium position R_0 using Taylor series as

$$M_{IG}(R) = M_{IG}(R_0) + \left[\frac{\delta M_{IG}}{\delta R_\varepsilon}\right]_{R_0} R_\varepsilon + higher\ order\ terms \tag{2.13}$$

where R_ε is the normal mode co-ordinate operator of vibration mode ε. Similar expressions are valid for each of the $3N$ - 6 possible normal co-ordinates. Normal co-ordinates of a molecule make use of the natural directions of bonds and are those co-ordinates in which all atoms vibrating go through the center of gravity of the molecule at the same time. The energy of a molecule can be divided into a number of different parts or 'degrees of freedom'. Three of these degrees of freedom describe translation and another three describe rotation except linear molecules, which have only two possible rotations. Thus for a molecule of N atoms, the number of vibration degrees of freedom is

$3N$ -6 degrees or $3N$ -5 in the case of linear molecules. Substituting the Taylor series expansion into Born-Openheimer modified KHD expression yields

$$\left(\alpha_{\rho\sigma}\right)_{GF} = \overbrace{M_{IG}^2(R_o)\sum_I \frac{\left\langle \Phi_{R_F} \middle| \Phi_{R_I} \right\rangle \left\langle \Phi_{R_I} \middle| \Phi_{R_F} \right\rangle}{\hbar\omega_{GI} - \hbar\omega_L - i\Gamma_I}}^{(A-term)} + M_{IG}(R_o)M'_{IG}(R_o)\times$$
$$\underbrace{\sum_I \frac{\left\langle \Phi_{R_F} \middle| R_\varepsilon \middle| \Phi_{R_I} \right\rangle \left\langle \Phi_{R_I} \middle| \Phi_{R_G} \right\rangle + \left\langle \Phi_{R_F} \middle| \Phi_{R_I} \right\rangle \left\langle \Phi_{R_I} \middle| R_\varepsilon \middle| \Phi_{R_G} \right\rangle}{\hbar\omega_{IF} + \hbar\omega_L - i\Gamma_I}}_{(B-term)}$$

(2.14)

Here M and M' correspond to the zeroth order and 1st order terms in the Taylor series expansion of equation (2.13). The A-term is known as the Franck Condon term or the Albrechts A-term and describes the summation of the matrix elements coupling all vibrational states of a molecule. The contribution from A-term of equation (2.14) is zero due to "closure theorem", which demonstrates that when all vibrational wave functions are multiplied together, the final answer is zero[3]. It therefore does not contribute towards Raman scattering but only the Rayleigh scattering. The co-ordinate operator, R_ε *in* the B-term (also known as the Herzberg Teller term or the Albrechts B-term) describes the effect of movement along the molecular axis during vibration and appears because correction terms M' has been multiplied with the vibrational states. An important feature of this operator is that the integral will only have finite values when there is one quantum of energy difference between initial and final states. Thus the B-term describes the Raman scattering and, due to the existence of the operator, no overtones are available from this term (overtones are observed only if higher order terms from Taylor expansion

are utilized). It also follows from the product of integrals in the B-term that only symmetric vibrations will be Raman active.

2.3 Surface enhanced Raman scattering

Surface enhanced Raman scattering is a phenomenon which is observed when a molecule is adsorbed onto, or is close to a roughened metal surface[6]. Originally the enhancement was observed on silver but since then a wide range of metal surfaces has been used including noble, alkali and transition metals. However, silver, gold and copper are the commonly used metals since these have absorption maxima in the visible region and hence give the greatest enhancement in signal[51]. Many models were reported in the early days of SERS to explain the enhancement and the mechanisms that cause enhancements in SERS are still under debate. However, it is generally agreed that there are two main mechanisms that contribute to SERS and each provides varying degree of enhancement in parallel, i.e., multiplicatively[52-54]. These are the electromagnetic enhancement[54] and a charge transfer or chemical enhancement[8]. There is evidence that both these mechanisms affect the SERS enhancement and it is more appropriate to consider SERS arising from a combination of the two effects.

2.3.1 Electromagnetic mechanism

The electromagnetic enhancement stems from the special optical properties of noble metals to support surface plasmons. Plasmons are the collective oscillations of free electrons and, if oscillations are restricted to the surface of the conductor, then these are known as a surface plasmon. The first observation of the existence of surface plasmons

dates back to 1902 when Wood reported a sharp decrease in the reflectivity of diffraction grating at certain frequency that excited surface plasmons[55]. The surface plasmons are associated with an enhanced electric field at the surface and interaction of this enhanced field with the molecule constitutes the electromagnetic enhancement mechanism. On flat metal surfaces, surface plasmon excitation is prohibited by momentum conservation in the plane of the surface[56] and hence atomically flat metal surfaces do not show significant SERS activity[52, 53]. The momentum conservation rule does not hold for the rough surfaces and surface plasmons can be excited[56]. Surface plasmons interact with the incident light as determined by their dipole (and higher multipole) transition moments[39]. Moskovits was the first to suggest that the huge enhancement observed in SERS was due to excitation of surface plasmons[7]. Creighton *et al.* compared the wavelengths corresponding to the Mie extinction maximum for silver (or gold) aqueous sol particles and Raman enhancement for pyridine molecules adsorbed on these particles[57]. The sharp Raman enhancement at Mie extinction maximum was observed and it was concluded that surface plasmon excitation is the underlying mechanism for SERS. The electromagnetic enhancement models were simultaneously enunciated by Gestren *et al.*[58-61] and MeCall *et al.*[62, 63], and expanded upon by Kerker *et al.*[64-71]. The common geometries treated in these models include isolated sphere, isolated spheroid, interacting spheres, nitrating spheroid, rough surfaces, hemispherical bumps, and gratings[51]. In the first such model, Moskovits treated the rough metal surface as metal spheres placed on top of a flat metal surface. The simplest form of this model is a single isolated metal sphere, which explains, at least qualitatively, most of the physics behind other more complicated systems like rough surfaces or colloidals.

2.3.1.1 Isolated single metal sphere

For a small isolated sphere of radius R with a complex wavelength dependent dielectric constant $\varepsilon(\lambda) = \varepsilon'(\lambda) + i\varepsilon''(\lambda)$ that is illuminated by a plane wave (wavelength larger than the size of the particle), the sphere will develop an internal polarization, $P(r)$, oscillating coherently with the incident field E_0. This is schematically illustrated in **Figure 2-3**.

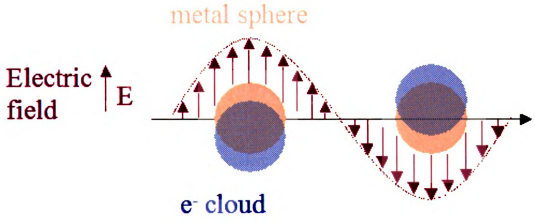

Figure 2-3. Schematic illustration of plasmon oscillation for sphere showing electron distortion in response to electric field [72].

Polarization $P(r)$, also known as optical current, is the dipole moment per unit volume. The internal polarization of the sphere creates an external (outside the sphere) EM field which can be represented by the field of a point dipole p located at the center of the sphere as[39]

$$p = 4\pi\varepsilon_0\varepsilon_m\left(\frac{\varepsilon-\varepsilon_m}{\varepsilon+2\varepsilon_m}\right)R^3E_0 \tag{2.15}$$

where ε_0 is the permittivity of free space and ε_m is the dielectric constant of media surrounding the sphere. In the electrostatic limit (radius of particle much smaller than wavelength) without retardation, $P(r)$ is related to the local internal electric field $E_{in}(r)$ and the incident field E_0 by[39]

$$\begin{aligned} P(r) &= \varepsilon_0(\varepsilon-\varepsilon_m)E_{in}(r) \\ &= 3\varepsilon_0\varepsilon_m\left(\frac{\varepsilon-\varepsilon_m}{\varepsilon+2\varepsilon_m}\right)E_0 \end{aligned} \tag{2.16}$$

Here P and $E_{in}(r)$ are independent of R within the isolated sphere. The net electric field at the surface remains constant as an increase in p is balanced by the increase in radius of sphere. The EM field outside the particle is due to the incident field and the polarized sphere. It is maximum at the surface of the sphere along the particle axis (defined as the incident electric field direction) and is given by

$$\begin{aligned} E_{surf} &= \frac{3\varepsilon}{\varepsilon+2\varepsilon_m}E_0 \\ &= gE_0 \qquad where\ g = \frac{3\varepsilon}{\varepsilon+2\varepsilon_m} \end{aligned} \tag{2.17}$$

This expression is independent of R as discussed above. The equation (2.17) has a pole at the dipole plasmon resonance, which is defined as the wavelength for which the real part of the complex dielectric constant ε' approaches -2. At the plasmon resonance, the electric field at the surface will become very large as real parts of denominator of equation (2.17) cancel each other (ε_m =1 for air) and magnitude of E_{surf} depends upon imaginary part of sphere's dielectric constant ε'', which is relatively small at plasmon wavelength for noble metals. In fact, the best SERS metal, silver, has the smallest ε'' and therefore yields the highest enhancement. Gold and copper have the next lowest values for ε'' in that order and their SERS enhancement factors reflect this. At plasmon resonance, $g >> 1$ and as a result $E_{surf} >> E_0$. The adsorbed molecule on the sphere surface will experience a very large field E_{surf} and will yield an enhanced Raman scattering signal. Quantitatively, the Raman intensity is proportional to the square of the electric field i.e., $I_{SERS} \propto E^2 \; or \; I_{SERS} \propto g^2$. Generally Raman scattered radiation frequency is not largely different from the excitation radiation and it also lies within the plasmon enhancement region. This means that the sphere will also enhance the scattered radiation field in exactly the same way ie, $I_{scattered} \propto {E_{scattered}}^2 \propto g'^2$ where g' is the enhancement of scattered field. The 'SERS enhancement', G , is defined as the ratio of the Raman scattered intensity in the presence of the sphere to its value in the absence of the sphere as [73]

$$G = \left| \frac{\alpha_R}{\alpha_{R_0}} \right| |gg'|^2 \qquad (2.18)$$

where α_{R_0} is the Raman polarizability of the isolated molecule. Normally $g \approx g'$ and the enhancement factor shows a fourth power dependence on the enhanced local field. This fourth power dependence is the key to the inordinate SERS enhancement. For silver, $g \approx 30$ at 400 nm but still provides a Raman enhancement of $G \approx 8\times10^5$, assuming no change in Raman polarizability of the molecule upon adsorption on the particle[73]. Neglecting the effect of particle size on its dielectric constant ε, the expression for g (constant relating dielectric constants in equation (2.17)) suggests constant SERS enhancement is independent of metal particle size. However, the dimension of the metal particle cannot be larger than the wavelength of light, nor can it be smaller than the average molecule size. The upper bound is due to the excitation of higher order multipoles (these modes, unlike dipole, are non-radiative and hence inefficient Raman scatterers) when the excitation light wavelength approaches the metal particle size. The lower bound arises from increased electron scattering (reduction in its conductivity) from the particle surface since the particle dimension approaches the electron mean free path[66]. At a given wavelength, the local field intensity near the metal sphere surface is related to the induced dipole moment ***p***, which also determines the sphere absorption (σ_{abs}) and Rayleigh cross-sections (σ_{sca}). For a metal particle diameter less than the wavelength of the incident light, the cross-sections are [39]

$$\sigma_{abs} = \frac{8\pi R^3 \sqrt{\varepsilon_m}}{\lambda}\left|\mathrm{Im}\left(\frac{\varepsilon-\varepsilon_m}{\varepsilon+2\varepsilon_m}\right)\right| = \frac{2\pi}{\lambda\varepsilon_0\sqrt{\varepsilon_m}}\left|\mathrm{Im}\frac{p}{E_0}\right| \qquad (2.19)$$

and

$$\sigma_{sca} = \frac{128\pi^5 R^6 \varepsilon_m^2}{3\lambda^4}\left|\frac{\varepsilon - \varepsilon_m}{\varepsilon + 2\varepsilon_m}\right|^2 = \frac{8\pi^3}{3\lambda^4 \varepsilon_0^2}\frac{p}{E_0} \tag{2.20}$$

It is obvious from equations (2.19) and (2.20) that a plasmon creates the same resonant peak (pole at $\varepsilon = -2\varepsilon_m$) in both cross-sections, as well as in local field intensity given by equation (2.17). However, the two cross-sections scale differently with the particle size and for small particles $\sigma_{abs} \propto R^3$ dominates whereas for large particles $\sigma_{sca} \propto R^6$ is dominant. This means that the nanostructures in the range 5-100 nm are expected to be good SERS substrates with exact size dependent upon wavelength and the metal used[73]. For example, the highest Raman enhancement for single silver spheres was calculated to be for particles with 40-50 nm diameter at ~425 nm excitation wavelength[74, 75]. Another important parameter affecting the quality of SERS is the width of plasmon resonance, which depends upon the electronic scattering rate and the metal interband transitions. For example, the wavelength dependent dielectric function of a Drude metal is given by

$$\varepsilon(\lambda) = \varepsilon_b(\lambda) + 1 - \frac{\omega_p^2}{\omega^2 + i\omega\gamma} \tag{2.21}$$

where ε_b is the contributions of interband transitions to the metal dielectric function, ω_p is the metal plasmon resonance and γ is the electronic scattering rate which is inversely

proportional to electron mean free path (or metal's DC conductivity). The polarizability of this sphere in vacuum is

$$\alpha = \frac{\varepsilon - 1}{\varepsilon + 2} R^3 \tag{2.22}$$

Substituting equation (2.21) into (2.22) yields[73]

$$\alpha = \frac{R^3(\varepsilon_b \omega^2 - \omega_p^2) + i\omega\varepsilon_b}{((\varepsilon_b + 3)\omega^2 - \omega_p^2) + i\omega\gamma(\varepsilon_b + 3)} \tag{2.23}$$

The pole of equation (2.23) is located at $\omega_R = \frac{\omega_p}{\sqrt{\varepsilon_b + 3}}$ and the width of this resonance is given by $\gamma(\varepsilon_b + 3)$ [73]. Now it is easy to see why only noble metals give good SERS enhancement. A larger γ value due to poor conductivity of a given metal (for example, transition metals) results in increased plasmon width and reduced SERS enhancement. Similarly a large contribution to dielectric constant (ε_b) from interband transitions also widens the resonance width and decreases Raman enhancement. This precisely explains why SERS enhancement of silver exceeds gold, which in turn exceeds that of copper. For example, the dielectric constants for thin films of silver, gold, and copper for 3.25 eV excitation light were found to be $-3.4720 + i0.1864, -1.6049 + i5.444$, and $-2.4131 + i5.4397$ respectively[76]. The small imaginary part of dielectric constant for silver as compared to gold and copper is

the main reason for high SERS activity of silver. The dipolar plasmon resonance frequency ω_R is also affected by the interband contributions to the dielectric constant for metal. Although the plasmon resonance frequency for noble metals ($\omega_p \approx 9$ eV) lies in UV region of the spectrum, ω_R is still located in visible or near visible region for Cu, Ag and Au due to varying contributions from ε_b. The plasmon resonance is pictorially depicted in **Figure 2-4**. When the particle is irradiated by a plane wave with frequency far from resonance, it does not interact significantly with the radiation. At plasmon resonance, the particle strongly interacts with incident light and the quality of resonance is dependent upon particle size, material and incident wavelength through factors like ε (which includes ε_b), γ, ε_m etc.

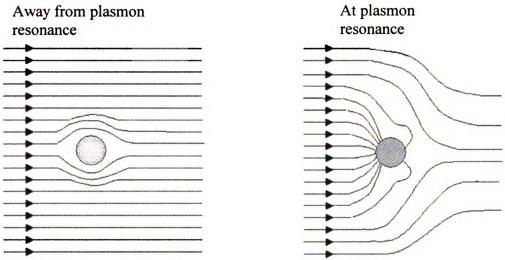

Figure 2-4. Energy flux (Poynting vector) around a metal nanoparticles under plane wave excitation for two frequencies[77]- away from resonance and at plasmon resonance.

2.3.1.2 A spheroid body in dielectric medium

The isolated spherical particle model is useful to provide a basic understanding of EM enhancement mechanism underlying SERS but is not sufficient to accurately describe real substrates. The real particles mostly consist of irregular shaped particles arranged in different geometries. Many a times the individual particles can be well approximated as ellipsoids and result in better analysis than using simple spherical particle. For example a nanowire can be approximated as prolate spheroid with high aspect ratio. The particle plasmon resonance wavelength is also dependent upon its shape and it is useful to get a brief review of the theory behind SERS enhancement for such shapes. The distribution of electric field around a particle of arbitrary shape can be calculated from Mie theory but the solution becomes quite involved even for simple shapes. The problem can be simplified if particle dimensions are small compared to the wavelength of laser and this assumption is made in following analysis.

Consider a spheroid with principal axes of length $2l_a$, $2l_b$, $2l_c$ having dielectric function ε_2 and placed in medium of dielectric constant ε_1. The spheroid is subject to an external field E_0 of frequency ω_0 applied along one of the principal axes. The potential inside the body by solving Laplace's equation in ellipsoidal harmonics is given by[78]

$$\phi_2 = -\frac{x(E_0)_x}{1+\frac{\varepsilon_2-\varepsilon_1}{\varepsilon_1}A_a} - \frac{y(E_0)_y}{1+\frac{\varepsilon_2-\varepsilon_1}{\varepsilon_1}A_b} - \frac{z(E_0)_z}{1+\frac{\varepsilon_2-\varepsilon_1}{\varepsilon_1}A_c} \tag{2.24}$$

where A_β is the depolarization factor given by

$$A_\beta = \frac{l_a l_b l_c}{2} \int_0^\infty \frac{ds}{(s+\beta^2)\left\{(s+l_a^2)(s+l_b^2)(s+l_c^2)\right\}^{1/2}}, \qquad (\beta = a,b,c)$$

The depolarization factors always satisfy $\sum A_\beta = 1$. For sphere, it is $A_a = A_b = A_c = 1/3$. For a prolate spheroid with $a:b = 3:1$, $A_a = 0.1087$; $A_b = 0.4456$.

The electric field inside ellipsoid can be found be taking gradient $E_{ins,\beta} = -\nabla\phi_2$ and is given by

$$E_{ins,\beta}(\omega_0) = \left\{1+\left[\varepsilon(\omega_0)-1\right]A_\beta\right\}^{-1} E_{0,\beta}(\omega_0) \qquad (2.25)$$

The electric field inside the particle is uniform and can be smaller or greater than applied field depending upon value dielectric constant. For dielectric such as quartz, $\varepsilon(\omega)$ is real and >1.0. This means that the field inside a dielectric is in phase, parallel to, and smaller in magnitude than applied field. On the other hand, metals have large number of free carriers that is associated with a complex dielectric function. Semiconductors can also have extra carriers excited by light and, to some extent, behave as metals. The complex dielectric constant of metals (and semiconductors) can have real part ($\varepsilon_1(\omega_0)$ that is negative and less than unity. Hence, the field inside can be larger and parallel or anti-parallel to the applied field. The possibility of supporting larger field than the applied field is the main source behind electromagnetic enhancement from metals. This also explains why only a selected set of metals (silver, gold and copper) yield strong SERS

effect. It is easy to see from equation (2.25) that maximum of internal field occurs when the real part of denominator vanishes

$$1+(\varepsilon_1(\omega_{sp})-1)A_\beta = 0$$
$$\varepsilon_1(\omega_{sp}) = 1-\frac{1}{A_\beta} \tag{2.26}$$

The frequency (ω_{sp}) is the surface plasmon frequency and corresponds to optical excitation frequency that causes resonance or excitation of surface plasmons in particle. This relationship also shows how the surface plasmon resonance frequency can be tuned by changing geometry of the particle. For a spherical particle with $A_\alpha = 1$ and we get standard condition of $\varepsilon_1(\omega_{sp}) = -2$. Although the dielectric constant of metals is a function of particle size, but for larger particles bulk constants can be used for simplicity. The laser wavelength used is also typically tied with the experimental set up. Then the knowledge of optical constant of SERS metal at the laser wavelength can be used in conjunction with equation (2.26) to determine a particle geometry that will yield resonance for the given excitation. It is important to mention that the condition of equation (2.26) correspond to the excitation of lowest order particle plasmon and is represented by a dipolar distribution of surface charge oscillating at ω_{sp}. The field just outside the tip of the axis α of spheroid can be calculated by using continuity of normal component of electric flux ($D_{out,\beta} = D_{ins,\beta} \Rightarrow \varepsilon_{out}E_{out,\beta} = \varepsilon_{ins}E_{ins,\beta}$) and is given by

$$E_{out,\beta}(\omega) = \frac{\varepsilon(\omega)}{1+(\varepsilon(\omega)-1)A_\beta} E_{0,\beta}(\omega) \tag{2.27}$$

The enhancement of electric field experienced by a molecule adsorbed just on the tip of the spheroid is given by

$$f(\omega) = \frac{\varepsilon(\omega)}{1+(\varepsilon(\omega)-1)A_\beta} \tag{2.28}$$

The molecule absorbed at the tip of the spheroid experiences an enhanced electric field compared to the incident field and this field results in polarization of the molecule. The total field experienced by the molecule will be a sum of incident field and field of the plasmons generated on the surface of the metal particle. The field at the site of the molecule can be calculated by replacing metal particle with an equivalent particle dipole P_e located at particle center. The dipole moment of spheroid is given by

$$P_{e,\alpha}(\omega_0) = V\alpha_{e,\beta\beta}(\omega_0)E_{0,\beta}(\omega_0) \tag{2.29}$$

Here V is particle volume and $\alpha_{e,\beta\beta}(\omega_0)$ is diagonal element of particle susceptibility tensor. This tensor element can be calculated by relating dipole moment with the field using relation

$$E + 4\pi \frac{P}{V} = \varepsilon E$$
$$P = \frac{V}{4\pi}(\varepsilon - 1)E \tag{2.30}$$

Equation (2.30) re-written for the case of polarized particle yields

$$\begin{aligned} P_{e,\beta}(\omega_0) &= \frac{V}{4\pi}(\varepsilon(\omega_0) - 1)E_{ins,\beta}(\omega_0) \\ &= \frac{V}{4\pi}\frac{\varepsilon(\omega_0) - 1}{1 + (\varepsilon(\omega_0) - 1)A_\beta}E_{0,\beta}(\omega_0) \end{aligned} \tag{2.31}$$

From equations (2.29) and (2.31), we find expression for susceptibility as

$$\alpha_{e,\beta\beta} = \frac{1}{4\pi}\frac{\varepsilon(\omega_0) - 1}{1 + (\varepsilon(\omega_0) - 1)A_\beta} \tag{2.32}$$

The molecule adsorbed at the tip of spheroid (at a distance l_β from center) will experience a field due to an equivalent dipole at the center of the particle

$$E_{dip,\beta}(\omega_0) = \frac{2P_{e,\beta}(\omega_0)}{{l_\beta}^3} \tag{2.33}$$

The adsorbed molecule is polarized by this dipole field and develops a dipole moment $\mu_{mol} = \alpha_{mol}E_{dip,\beta}(\omega_0)$. The vibrational motion of the nuclei modulates the

molecular polarizability α_{mol} and hence the dipole moment contains a component oscillating at the Raman frequency ω_R

$$\mu_\beta(\omega_R) = \alpha_{R,\beta\beta} E_{dip,\beta}(\omega_0) \tag{2.34}$$

Here the details of Raman scattering has been cast into phenomenological Raman polarizability α_R.

The metal particle is also subjected to Raman radiation, which polarizes it and this particle acts as antenna to amplify Raman signal. Analogous to incident radiation, the molecular field also produces a field at the center of metal particle given by

$$E_{mol,\beta}(\omega_R) = \frac{2\mu_\beta(\omega_R)}{l_\beta{}^3} \tag{2.35}$$

This field acts exactly like incident laser field (except at frequency ω_R) and produces a dipole moment in metal particle

$$P_\beta(\omega_R) = V\alpha_{e,\beta}(\omega_R) E_{mol,\beta}(\omega_R) \tag{2.36}$$

Inserting expressions for $\alpha_{e,\beta}(\omega_R)$ and $E_{mol,\beta}(\omega_R)$ into equation (2.36), one gets

$$P_\beta(\omega_R) = \left(\frac{V}{2\pi l_\beta{}^3}\right)^2 \frac{\varepsilon(\omega_0)-1}{1+(\varepsilon(\omega_0)-1)A_\beta} \frac{\varepsilon(\omega_R)-1}{1+(\varepsilon(\omega_R)-1)A_\beta} \alpha_{R,\beta\beta}(\omega_R) E_{0,\beta}(\omega_0) \tag{2.37}$$

The Raman dipole of the isolated molecule excited by incident field E_0 along direction β is given by

$$\mu_\beta(\omega_R) = \alpha_{R,\beta\beta} E_{0,\beta}(\omega_0) \tag{2.38}$$

Comparing equation (2.37) and (2.38), we see that relative to Raman dipole of an isolated molecule subject to same external field, the particle dipole is enhanced by the product $f_{pd}(\omega_R) f_{pd}(\omega_0)$ of local field enhancement factors at the Raman and incident frequencies.

$$f_{pd}(\omega) = \frac{V}{2\pi l_\beta{}^3} \frac{\varepsilon(\omega)-1}{1+(\varepsilon(\omega)-1)A_\beta} \tag{2.39}$$

Here the subscript *pd* shows point dipole approximation.

2.3.1.3 Correction for radiation damping

The analysis of the interaction of metal particle with the laser presented thus far has been under electrostatic approximation; i.e., the field was assumed to be constant

across the particle dimension d ($k_0 d << 1$, with $k_0 = \omega_0 c$). This approach doesn't take into account radiative losses, which are proportional to the square of particle dipole and hence of the volume. The dipole is expected to decrease in magnitude in reaction to its own radiation. This can be modeled as first order correction to the electrostatic approximation. A radiation reaction field E_r is defined such that the work per unit time done by this field on the particle dipole equals the power radiated by dipole[74]. In other words, the radiation reaction field tends to reduce the dipole in accordance with power radiated. This leads to the definition

$$E_r = i\frac{1}{3}(2k^3)P \tag{2.40}$$

This ration reaction field is 90° out of phase with the dipole and the metal particle experiences the external field as well as its own radiation field. The size of dipole is determined by self consistently from

$$P_\beta(\omega_0) = V\alpha_{e,\beta\beta}(\omega_0)\left[E_{0,\beta}(\omega_0) + i\frac{1}{3}(2k^3)P_\beta(\omega_0)\right] \tag{2.41}$$

Rearranging

$$\begin{aligned} P_\beta(\omega_0) &= \frac{V\alpha_{e,\beta\beta}(\omega_0)}{1 - i\frac{1}{3}(2k_0{}^3)V\alpha_{e,\beta\beta}(\omega_0)} E_{0,\beta}(\omega_0) \\ &= V\alpha_{eff,\beta\beta}(\omega_0)E_{0,\beta}(\omega_0) \end{aligned} \tag{2.42}$$

where $\alpha_{eff,\beta\beta}(\omega_0) = \dfrac{\alpha_{e,\beta\beta}(\omega_0)}{1 - i\frac{1}{3}(2k_0{}^3)V\alpha_{e,\beta\beta}(\omega_0)}$. The correction term in denominator of effective susceptibility expression dominates near particle resonance and limits the effective polarizability $V\alpha_{eff}$ to the order of a cubic wavelength $\lambda_0{}^3$. Now we can find field enhancement just outside the spheroid using this effective susceptibility.

$$E_{out,\beta}(\omega_0) = \varepsilon(\omega_0)\frac{4\pi}{V}\frac{P_\beta(\omega_0)}{\varepsilon(\omega_0)-1} \tag{2.43}$$

Substituting in the value of $P_\beta(\omega_0)$ from equation (2.42) in equation (2.43), we get

$$\begin{aligned} E_{out,\beta}(\omega_0) &= \frac{4\pi}{V}\frac{\varepsilon(\omega_0)}{\varepsilon(\omega_0)-1}V\alpha_{eff,\beta\beta}(\omega_0)E_{0,\beta}(\omega_0) \\ &= \frac{4\pi}{V}\frac{\varepsilon(\omega_0)}{\varepsilon(\omega_0)-1}\frac{V\alpha_{e,\beta\beta}(\omega_0)}{1 - i\frac{1}{3}(2k_0{}^3)V\alpha_{e,\beta\beta}(\omega_0)}E_{0,\beta}(\omega_0) \end{aligned} \tag{2.44}$$

Using definition of $\alpha_{e,\beta\beta}$ from equation (2.32) in (2.44), we get

$$\begin{aligned} E_{out,\beta}(\omega_0) &= \frac{\varepsilon(\omega_0)}{1+[\varepsilon(\omega_0)-1]\left[A_\beta - i(\frac{Vk_0{}^3}{6\pi})\right]}E_{0,\beta}(\omega_0) \\ &= f(\omega_0)E_{0,\beta}(\omega_0) \end{aligned} \tag{2.45}$$

Comparing with (2.28), we see that the depolarization factor A_β has been replaced by an effective $A_{eff,\beta}$ that accounts for radiation damping. Radiation damping is proportional to particle volume and inversely proportional to λ^3; i.e., radiation damping is more sever for shorter wavelengths. For high eccentricity particle, the large increase in enhancement is partly offset by the smaller fractional area near the tips. Thus enhancement averaging over surface is required and EF can be corrected by multiplying with a reduction factor φ that can be significantly smaller than unity. The radiation damping limits the maximum achievable SERS enhancement due to dipolar radiation loss. The effect of radiation damping is more severe for large particles. **Figure 2-5** shows the effect of radiation damping on SERS enhancement for different aspect ratio of gold nanorods modeled as prolate spheroids. The enhancement factors are calculated at the resonant wavelengths corresponding to the aspect ratio. The enhancement is negligible for simple sphere and increases as the aspect ratio of the particle increases due to concentration of the electric field at the tip. For a particular aspect ratio, the enhancement starts to decrease as the volume of the particle increases due to radiation damping. It can be seen that the radiation damping begins to effect enhancement for $\frac{V}{\lambda^3} \geq 10^{-4}$.

Enhancement factor $|E(\omega_{res})|^2$

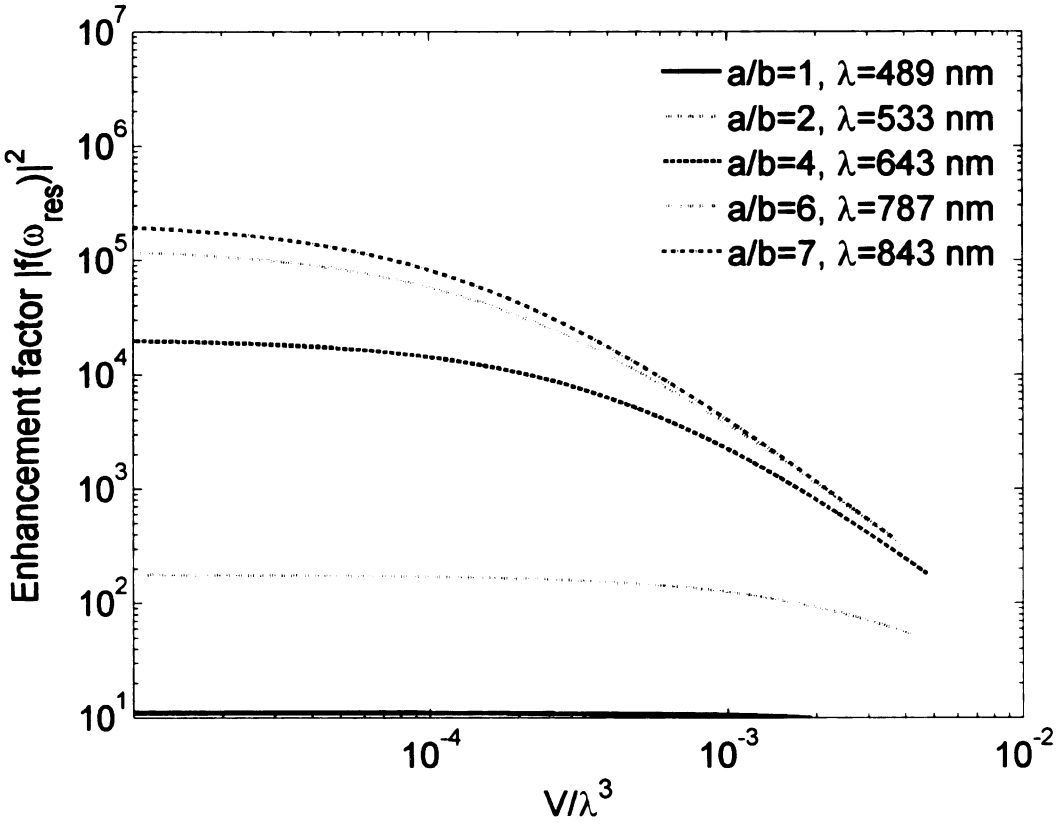

Figure 2-5. Effect of radiation damping for different aspect ratio of gold nanorods. Also shown is the resonant wavelength for each aspect ratio.

2.3.1.4 Interacting particles

Appreciable SERS enhancement from an isolated or single particle is hardly noticeable. The real substrate often consists of interacting colloidals or rough surfaces. The electromagnetic field between two closely spaced particles is not a simple coherent sum of the fields from individual particles. The particles exhibit capacitive coupling that causes significant changes in the polarization of each particle. Heuristically, the dipole near field of one particle induces quadruple and higher order moments in its neighbors. As a result of these mutual inductions, the near fields from all these moments coherently add to produce maximum external field in the junction and the Raman enhancement

factor can approach 10^{10} to 10^{12} for separation of 1 nm[39]. **Figure 2-6** shows two closely spaced metal nanospheres illuminated by plane polarized light and the resulting induced charges on each sphere. The conjugate nature of charges on each sphere gives rise to enhanced electric field and correspondingly enhanced Raman scattering for a molecule localized in the junction between two particles. It is worth reiterating that the dipole induced in each particle arises not only from the incident field but also for the intense field of its partner. The effect of light polarization relative to the axis of the dimmer is also illustrated. This simple example can be extended to large aggregates of particles where each particle will have its own characteristic field strength and the accumulative effect could yield giant enhancement making the cluster a "hot" site.

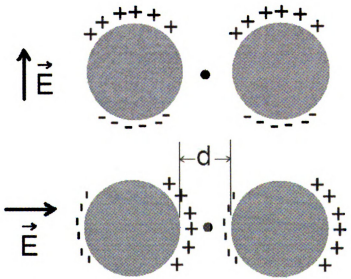

Figure 2-6. Light interaction with metal nanospheres dimmers[73]. Analyte molecule is shown by small green filled circle in between two particles.

Another important feature of aggregates of particles or other interacting nanostructures is the short range of the enhanced field. This not only requires the metallic particles to be closely located but the analyte molecule must also be present within the enhanced field range to get good SERS enhancement. **Figure 2-7** shows the calculated Raman enhancement factors at the midpoint of 60 nm diameter dimmer (material: Ag, Al, Si, SiO_2) for 497 nm excitation[39]. The Raman enhancement decreases rapidly with increasing inter-particle distance and ideal spacing is of the order of few nanometers. This is due to the fact that the field of the dipole scales $\propto \frac{1}{r^3}$ and the fourth power dependence of enhancement in equation (2.18) results in very sharp gain decay ($\propto \frac{1}{r^{12}}$).

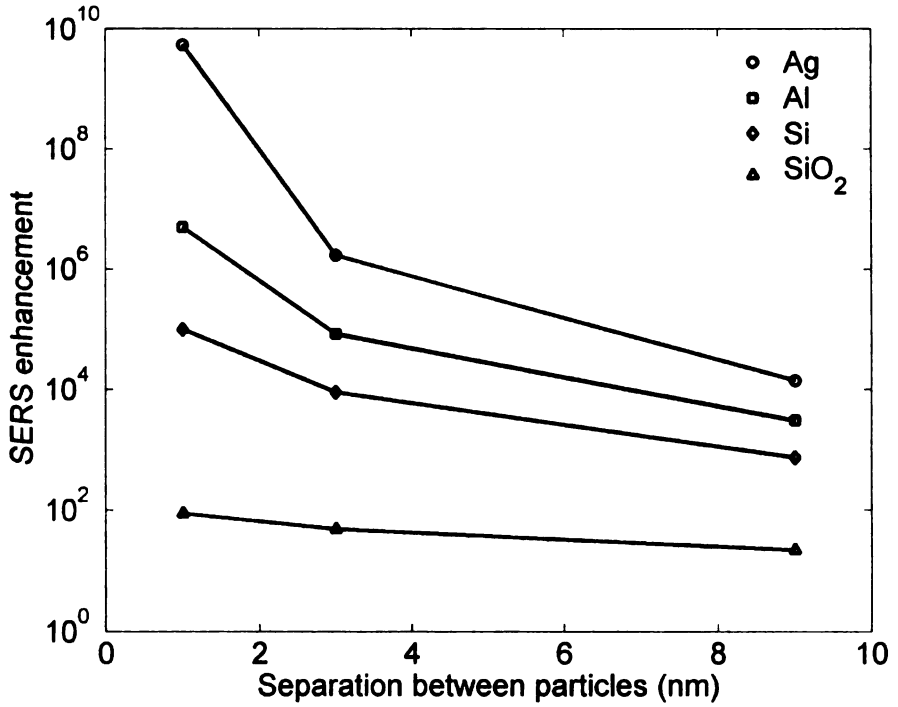

Figure 2-7. Calculated Raman enhancement factors at the junction of 60 nm diameter dimmers for 497 nm excitation[39].

The electromagnetic model provides for most of the SERS observations including need for nanostructured material for SERS activity, better SERS response for noble metals, greater enhancement for interacting nanoparticles compared to isolated particle, and the few hot sites (appropriately structured clusters) among an ensemble of particles[79]. However, the EM model does not account for all observations, such as molecular resonance, charge-transfer transitions etc.[39, 80]. For example, EM enhancement is expected to be an isotropic amplifier of Raman scattering of a molecule adsorbed on a rough surface but the SERS intensities for CO and N_2 under similar conditions differs by more than a factor of 200[51]. This observation could not be explained by the EM model alone, and introduces a chemical enhancement mechanism in the SERS picture.

2.3.2 The chemical enhancement

Many studies support a second enhancement mechanism known as chemical enhancement or charge transfer[8, 52, 53]. This mechanism is less well understood due to the problem of experimentally decoupling it from the electromagnetic mechanism as both operate simultaneously for most SERS experiments involving rough surfaces or colloids. In this mechanism, the analyte is assumed to form a bond with the metal that facilitates transfer of electrons between metal and analyte[3]. The chemical enhancement can be explained by a resonance Raman effect in which either molecular energy levels shift and broaden, or a new resonant intermediate energy level involving the metal surface is created. In the resonant intermediate state formation hypothesis, the metal absorbs the light and charge is transferred into the analyte-metal complex. Then the Raman process

occurs, excitation is transferred back into the metal and re-radiation of Raman scattering takes place from the metal surface[3]. The chemical enhancement predicts larger enhancement factor of the first adsorbate layer compared to the subsequent layers. However, it is generally agreed that the electromagnetic enhancement mechanism (of the order 10^4 to 10^6) plays a much greater role in overall SERS enhancement than the chemical enhancement (of the order 10^2)[52]. This difference in the scales of the two enhancements makes the EM mechanism a dominant factor and most research has focused on enhancing the SERS effect through the use of interacting nanostructures.

2.4 Ordinary Raman spectra and SERS spectra

Since we will be dealing with both ordinary as well as SERS Raman spectra of different species in the later part of this dissertation, it is worthwhile to mention a few important differences between the two. The ordinary Raman spectra SERS spectra usually differs from normal Raman spectra in that

a. New peaks may appear.
b. Some strong normal mode peaks may become weak or disappear.
c. Raman intensity versus analyte concentration relationship may become non-linear in SERS
d. High energy bands intensity falls more rapidly in SERS due to different gain for scattered radiation.
e. Spectra tends to be depolarized.
f. Departure from ω^4 dependence.

g. Broad background may appear[51].

For example, for pyridine the SERS spectra is very weak below monolayer coverage (because the carbon ring is parallel to surface). At monolayer coverage, a rapid rise in SERS intensity results as the carbon ring is forced normal to surface to allow more molecules. The light induced dipole in the metal can be divided into two components (parallel and normal). It is the molecular polarizability caused by perpendicular component which leads to scattering from a rough surface[3]. The appearance of new bands in SERS is due to adsorption of molecule on metal that breaks the molecule's center of symmetry. The mutual exclusion rule (IR active, Raman inactive and vice versa) is no longer valid and allows IR bands to appear in the Raman spectra. Some types of bands are more intense in SERS than normal. The problem with chemical enhancement is that the nature of the species formed between the analyte and metal is not well defined. The selection rules should refer to the surface species instead of isolated molecules. However, treating the molecules as separate entities simplifies the rules and gives reasonable results. Also in SERS the strong intensity means contaminants in trace amount have a greater impact and may alter the spectra. All these factors need be taken into consideration while attempting to compare the SERS spectra of any species against its ordinary Raman spectra.

Chapter 3: Experimental Set up

This research effort can be broadly categorized into two steps. First step involves the fabrication and characterization of SERS substrate while second part involves the evaluation of substrates using the Raman system. The substrates were prepared by either growing oxide nanowires in tube furnace system or growing metallic nanorods using an e-beam evaporation set up. The evaluation of the SERS substrates was done utilizing a near IR Raman system. Accordingly the experimental systems used in this study can be classified into three categories - a nanowires synthesis set up, nanorods synthesis set up and Raman Spectroscopy set up.

3.1 Oxide nanowire synthesis set up

The nanowires employed in this study are germanium dioxide (GeO_2) and zinc oxide (ZnO). The GeO_2 nanowires are synthesized utilizing vapor-liquid-solid (VLS) growth mechanism first proposed by Wagner and Ellis in 1964[81]. The ZnO nanowires synthesis followed a self-catalytic growth mechanism. The synthesis of nanowires is carried out using a horizontal tube furnace as shown in **Figure 3-1**. The furnace consists of coiled resistive heating element encapsulated by ceramic thermal insulation in a hollow cylindrical shape. The furnace is 12 in. long and has an outside diameter of 8 in. A 3.35 in. diameter quartz tube is inserted through central 4 in. diameter bore of the furnace to facilitate control of the temperature and environment for the growth. The quartz tube is sealed on both ends using stainless steel end caps with double 'O' ring seals. The upstream end of tube is connected to two-gas lines that can independently

supply a measured amount of gas flow through respective Mass Flow Controllers (MFC's). The downstream end is connected to a mechanical rotary pump that can achieve a vacuum of less than 100 mTorr inside the quartz tube. The pressure is measured by a convector type vacuum gauge located at the downstream end of the furnace in the vacuum line. The temperature of the furnace is monitored by a type 'K' thermocouple (not shown) placed between the quartz tube and the inside wall of furnace. The maximum temperature that can be achieved at the location of the thermocouple is ~1000 °C. The sample and the source material are placed on a flat quartz plate (2.5 in. × 6 in.) at the desired positions. **Figure 3-2** shows a typical layout for the germanium source material and silicon substrate on the quartz support plate. For ZnO nanowires, the substrates are placed at the top of boat containing zinc powder and the boat is then loaded on the support plate. After positioning source material and substrates, the support plate is inserted into the quartz tube and localized within the heating zone of the furnace. The desired vacuum level, temperature range and gas flow rate for the experiment can be controlled using furnace controller, MFC's and the isolation valve in the vacuum pump line. In a typical synthesis experiment, the quartz tube is evacuated to ~200 mTorr, backfilled with Ar to ~10 Torr and then evacuated again to improve vacuum. This is followed by a quick leak test of the system by closing the vacuum isolation valve and observing the rise in pressure for fixed period of time. After satisfactory set up of vacuum inside the quartz tube, the gas flow and pressure are established to desired value utilizing MFC and vacuum valve. Next temperature is ramped to the target value using temperature controller. At this stage, additional gas/gases can be introduced and/or flow rates can be modified using two MFCs. The growth of the nanowires is carried out for the

set amount of time and then furnace is shut down. Argon is usually allowed to flow into the tube during cooling of furnace to room temperature. The quartz tube can be opened after the pressure inside reaches atmospheric pressure. This may require bleeding additional Ar gas or room air into the tube.

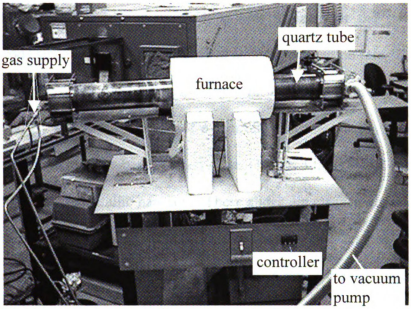

Figure 3-1. Photograph of nanowire synthesis set up.

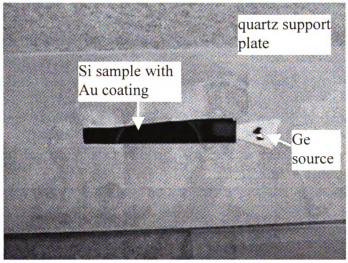

Figure 3-2. Quartz support plate with typical sample layout (A top view).

3.2 Silver nanorods synthesis set up

Silver nanorods are synthesized using Oblique Angle Deposition (OAD) of the metal onto a glass substrate[36]. The synthesis of nanorods was carried out in an AXXIS physical vapor deposition system (PVD) from K. J. Lesker as shown in **Figure 3-3**. This deposition system is equipped with one 4-pocket e-beam evaporation gun and two sputtering guns. Only the e-beam evaporation was utilized for the growth of these metallic nanorods since it allows precise control over the deposition rate. The e-beam can be used to evaporate up to four different sources in turn without breaking the vacuum. This is achieved by rotating the hearth of e-beam so that the crucible with the desired material is illuminated by the e-beam. Glass slides (1 in. × 3 in., VWAR Inc.) are used as typical substrates for the metallic nanorods. These slides are cleaned and loaded onto the substrate stage of the PVD system. The deposition chamber is evacuated to ~3×10^{-6} Torr and heated radiatively by a pair of quartz lamps located under the substrate platen. The OAD synthesis involves first depositing a thin layer (typically ~50 nm) of metal on the glass slide using e-beam evaporation. During this deposition, the substrate faces the e-beam evaporation source and is continuously rotated as schematically illustrated in **Figure 3-4**(a). Then the substrate rotation is stopped and the substrate stage is tilted such that the incident flux arrives at almost grazing angle ($\leq 15^{\circ}$) to the surface of the stationary substrate as shown in **Figure 3-4**(b). The oblique angle deposition of metal is done to the desired thickness at a rate of ~0.4 Å/s as measured by a Quartz Crystal Monitor (QCM) operating at 6 MHz. The temperature of the substrate is maintained at $85\pm3\,^{\circ}C$ throughout the deposition. The nanorods start to grown during oblique deposition due to shadowing effects of nanoscale islands. The substrate can be inspected

visually from the 6 in. glass view port of the chamber during growth. Typically substrate surfaces have a mirror finish after normal deposition that changes to more dull appearance after deposition of ~200 nm metal at oblique angle. This is an indirect evidence of the start of formation of nanorods on the substrate.

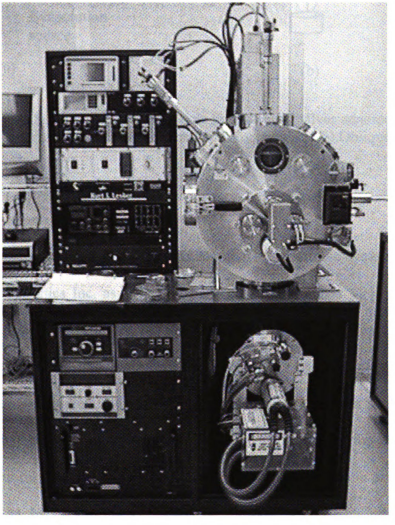

Figure 3-3. Physical vapor deposition systems for metallic nanorods synthesis.

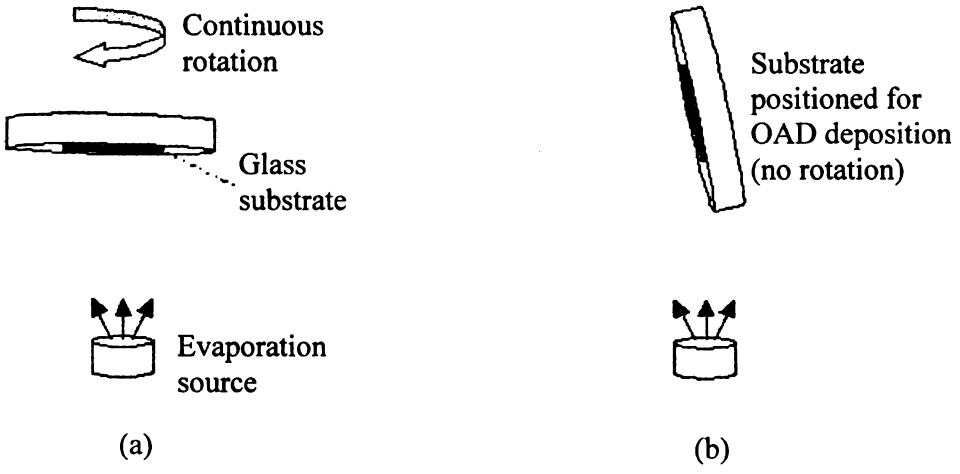

Figure 3-4. Schematic of oblique angle deposition of silver nanorods using e-beam evaporation. (a) Normal angle deposition. (b) Oblique angle deposition.

3.3 Raman spectroscopy set up

The Raman system utilized for this research is a portable system (EzRaman-L) from Enwave Optronics Inc. as shown in **Figure 3-5**. It employs a Near IR frequency stabilized diode laser operating at 785 nm with maximum power output of ~400 mW. The NIR excitation frequency was chosen to minimize fluorescence from the samples. The laser power is delivered to the sample through 100 μm excitation fiber and scattered light is collected by 200 μm collection fiber. The fiber optic probe head contains a replaceable lens tube, which focuses the laser light onto the sample and also collects scattered light in backscattering geometry. In addition, a Rayleigh rejection filter of optical density (OD) > 8 in the collection path provides rejection of the laser line from the spectra. The high OD is a unitless measure of the transmittance of an optical element at a given wavelength and is defined as

$$OD = -\log(\frac{I}{I_0}) \quad (3.1)$$

where I and I_0 are the intensity of the transmitted and incident laser respectively.

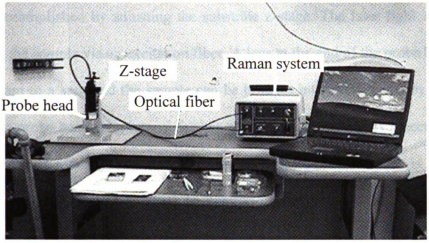

Figure 3-5. Raman system set up.

The spectrograph has an f/4 aperture, symmetrical crossed Czerny-turner with a resolution of better than 6 cm^{-1}. The spectral range covered is from 200-2400 cm^{-1}. The system is equipped with a charge-coupled device (CCD) array detector having a pixel size of 14 μm x 200 μm and 16-bit digitization. Computer interface with software for collection and analysis is provided through a USB cable. The system is supplied with an optical fiber probe and a vial holder to analyze liquid samples. The fiber head has a replaceable lens tube and that can carry different numerical aperture (NA) lenses. The as supplied system has been optimized for the study of liquid samples with laser always focused inside the sample vial when using sample holder. The analysis of samples using SERS mostly involves solid substrates and this warrants precise focusing of laser on the substrate surface. Moreover, the ability to scan the substrate surface for homogeneity is

also needed for uniformity studies. Due to these considerations, a three axes linear sample stage was installed to allow precise motion of substrate as shown in **Figure 3-6**. The laser head of the optical fiber is mounted on a separate linear z-stage that allows quick and coarse focus of laser beam on substrate. The precise focusing of laser on the sample is accomplished by adjusting the substrate z-stage. The laser light at 785 nm is delivered to the sample via an excitation fiber. A lens at the end of the probe head focuses the laser beam to a spot and the sample can be brought into sharp focus by adjusting z-height of the probe head. In a typical focusing exercise, the sample is placed at a course focus depending upon the focal length of the lens and then fine focus is achieved by adjusting the height of the substrate while monitoring the strength of the Raman signal.

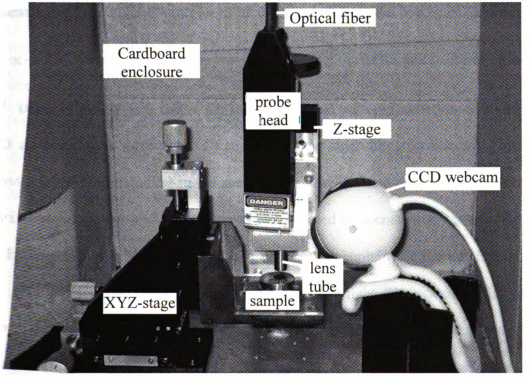

Figure 3-6. Raman system optical fiber head and sample stage.

The scattered light is collected in the backscattering geometry (Raman scattering is isotropic and incoherent) by the same lens and carried to the spectrograph via the collection fiber. The fiber head also incorporates a Raleigh rejection filter to remove the elastically scattered signal from the sample signal. The spectrograph separates different wavelengths from the Raman scattered light which is then focused onto a linear CCD array detector. The output of the CCD is the Raman spectrum of the sample. The Raman system can be interfaced to a PC or laptop with a USB cable and the collected spectra is displayed on the computer running proprietary software. The Raman scan always starts with collection of the CCD dark current with the laser off to account for CCD noise. Then the laser illuminates the sample and Raman scattered signal is integrated by the CCD for the duration of excitation. The Raman spectrum (only Stokes scattering) is then presented on the computer monitor as an energy shift from the energy of the laser beam. The x-axis of Raman spectra is the wavenumber ($\varpi = \frac{1}{\lambda}$) of Raman scattered radiation in cm^{-1} units[3]. The y-axis shows the intensity of the scattered radiation detected by the CCD at a particular wavevector. Often a smoothing algorithm (like boxcar) is applied to remove sharp discontinuities in the spectra. The near IR laser used in the Raman system is invisible to the eye and caution has to be exercised in operation of system. The whole laser head and sample stage is enclosed in a box to contain the laser radiation and to avoid false detection due to interference from ambient light. The system is also supplied with protective eyewear to minimize risk of eye injury in case of accidental exposure to the laser beam. The coarse position of the laser beam on the sample can be monitored using a common CCD camera like a USB computer webcam.

3.3.1 Laser spot size determination

The laser is focused to a fine spot on the substrate by focusing lens at the end of optical fiber. The size of the laser spot on the substrate is needed to determine the amount of analyte excited by the laser for Raman enhancement factor calculations. There are many ways to measure the diameter of laser beam. These include ray tracing, fluorescence correlation spectroscopy, and multiphoton ionization yield. Though these methods provide accurate results, they also require sophisticated experimental set up and analysis. The knife-edge method is a simple and practical method that can be easily implemented in most situations. In this method, a knife-edge mounted on a translation stage is used to eclipse the laser beam more and more by slowly translating it across the focal plane of the laser. The power of the laser beam reaching a detector is recorded as a function of translated positions of knife-edge. The diameter of the beam can be defined in terms of a threshold power that is contained in that diameter. A commonly employed threshold of D_{86} was used. The knife-edge measurement was realized using a razor blade attached to a micrometer stage as depicted in **Figure 3-7**. The measured diameter of the laser beam using knife-edge method was found to be ~94 μm. This value agrees well with the manufacturer specified diameter of less ~ 100 μm.

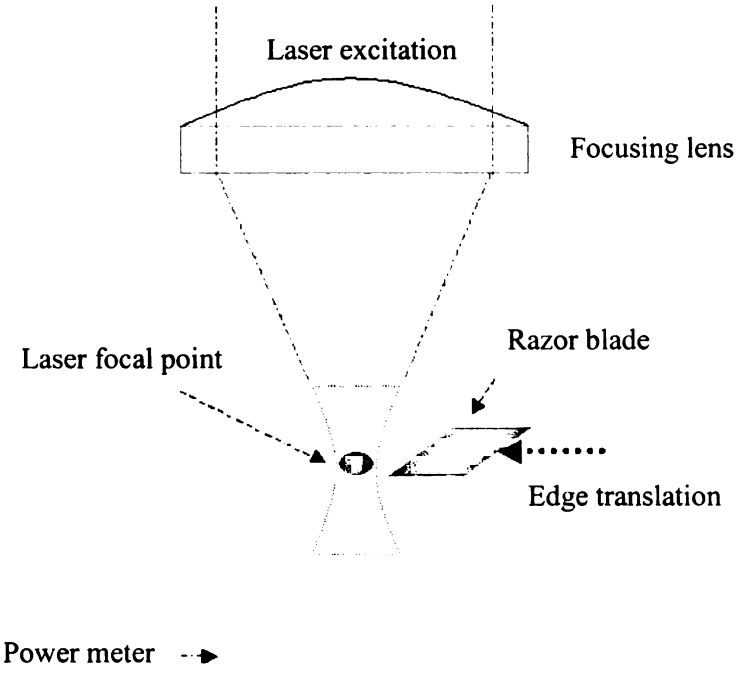

Figure 3-7. Knife edge method for determining laser beam diameter.

3.3.2 Raman system calibration

An important factor in getting accurate spectra is the x-axis calibration of the spectrum to ensure correct assignment of wavenumbers. This is done calibrating the CCD pixel positions against the Raman peaks of a reference sample. Isopropanol (also known as isopropyl alcohol) was used as reference sample for calibration and its Raman spectra is shown in **Figure 3-8**. For calibration, the instrument is set to pixel mode and the pixel numbers corresponding to the eight Raman peaks of isopropanol spectra are noted. Finally these pixels are entered into the x-axis calibration dialog box of the Raman software which generates the calibration coefficients for accurate pixel to wavenumber mapping.

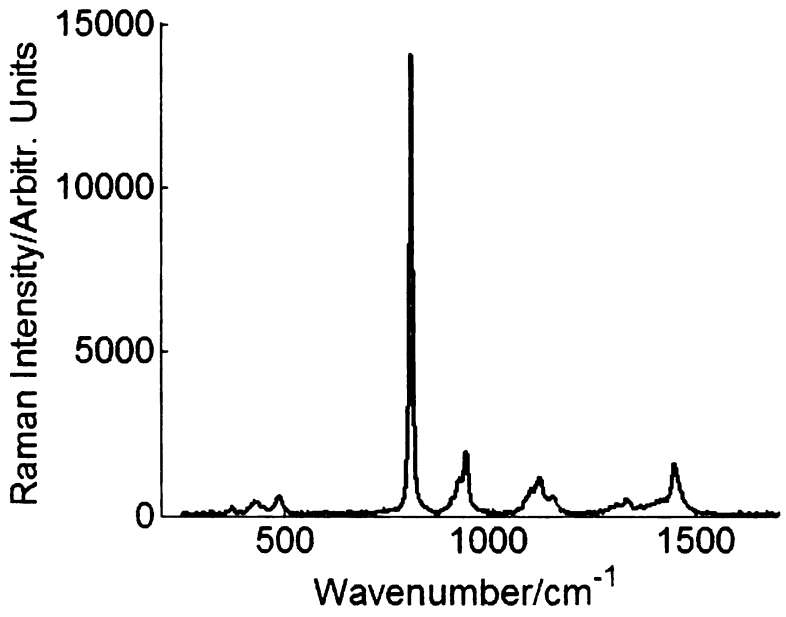

Figure 3-8. Reference Raman spectra of Isopropanol, t_{acc}= 20 s.

Table 3-1 shows the pixel and the wavenumbers corresponding to different Raman peaks of isopropanol that are used to generate x-axis calibrations data.

Table 3-1. Isopropyl alcohol Raman peaks and wavenumbers.

Peaks	Pixels	Wavenumber (cm^{-1})
1	139	374.2
2	179	433.4
3	222	491.2
4	460	817.6
5	564	945.6
6	708	1129
7	892	1339.8
8	988	1453

Although y-axis calibration can be done, it is much more complicated due to non-availability of a suitable standard. Other factors such as laser power, frequency, and environment also affects the scattering intensity and makes it more difficult to achieve y-calibration. Fortunately for the qualitative work like detection of material, y-calibration is not essential

Chapter 4: Germanium Oxide Nanowires based SERS Substrates

This chapter presents details of synthesis, growth kinetics and SERS results for germanium dioxide (GeO_2) nanowires (NWs). Germanium dioxide nanomaterials exhibit blue photoluminescence (PL) material with peak energies around 3.1 eV and 2.2 eV[82]. Germanium oxide nanowires can emit stable and high brightness blue light at 485 nm (2.56 eV) under excitation at 221 nm (5.61 eV)[83]. Germanium oxide-based glass is thought to be more refractive than the corresponding silicate glass so that the GeO_2 NWs may be used for nano-connections in future opto-electronic communications. It has also attracted considerable attention as a potential material for optical fibers with less transmission loss than SiO_2[84]. The NWs were synthesized on silicon (Si) substrates using the Vapor Liquid Solid (VLS) growth mechanism and were investigated for their potential use as SERS substrates. Characterization of the NWs was done using a Scanning Electron Microscope (JEOL 6400V), a Field Emission Scanning Electron Microscope (JEOL 6300F), and a Transmission Electron Microscope (JEOL 2200FS). The as synthesized substrates were coated with gold/silver to provide a plasmon active surface. The SERS performance of these substrates was evaluated using commonly employed probe molecule analytes including Rhodamine 6G, Nile Blue, 4-methylbenzenthiol, 1,2-benzenedithiol and trans-1,2-bis(4-pyridyl)ethylene.

4.1 Nanowire synthesis

There have been a number of reports of GeO_2 NWs synthesis in past decade using a variety of techniques. Some of the past efforts and present synthesis technique are discussed in this section. A growth model to explain the synthesis is also presented.

4.1.1 Reviews of past efforts

Germanium dioxide NWs were first synthesized by Bai *et al.*[85] using physical evaporation of a mixture of Ge and Fe (8%) powder at 820 °C under continuous flow of 130 sccm of Ar at 200 Torr. The product was collected on inside walls of the quartz tube in front of a copper cold finger. Since then there have been a number of reports of GeO_2 NW synthesis using a variety of techniques. Zhang *et al.*[86] used carbon nanotube-confined reaction in which pure Ge powder, carbon nanotubes and mixture of Si/SiO_2 powders were kept at 850 °C under flowing Ar (150-200 sccm) for 3-4 hrs. Germanium dioxide nanorods of 50-200 nm diameter and several μm lengths were formed at location of carbon nanotubes. Wu *et al.*[83] reported carbothermal reduction based synthesis of NWs by mixing equal amounts of Ge and carbon powder and heating to 840 °C under 20 sccm flow of N_2 for 3.5 hr. The GeO_2 NWs having 50-120 nm diameter and hundreds of μm length were formed on the inside walls of alumina boat containing source powder. Dang *et al.*[87] used thermal oxidation by heating Ge powder to 1000 °C under 120 sccm gas flow (80% Ar, 20% O_2) for 30 min to get NWs of 80 nm diameter and several tens of microns long at the location of source material. Hu *et al.*[88] heated a mixture of 2 g Ge powder with 4 g $Fe(NO_3)_3$ on an alumina wafer to 800 °C for 30 min. Then the temperature was raised to 1300 °C and synthesis was carried out for 6 hr under Ar flow

(containing 5% H_2) of 50 sccm at a pressure of 400 Torr. Nanowires having diameter of 150 nm with lengths of several tens of microns were collected on inside walls of alumina tube in the 700 °C temperature region. Su *et al.*[89] thermally evaporated Ge powder at 1050 °C in an oxidizing environment (90% Ar, 10% O_2) for 40 min at 300 Torr. The self catalytic synthesized nanowires (100 nm diameter and 800 nm length) were collected on Si substrate kept at 950 °C. The tips of NWs were found to have Ge particles of 500 nm diameter (tip showed 3% O_2 in addition to Ge) and NW PL spectra showed two blue emission peaks at 448 nm and 471 nm and a violet emission peak at 411 nm. Higalgo *et al.*[90] annealed compacted GeO_2 powder discs under flowing Ar for 24-48 hrs and got NWs and needles having diameters of 100-500 nm. Tang *et al.*[91] utilized laser ablation of Ge powder compacted as a disc at 820 °C and 700 Torr under Ar flow of 50 sccm. Nano whiskers having diameter of ~ 2μm and lengths of up to 2 mm were collected on quartz substrate located near target. Wu *et al.*[92] employed thermal annealing of Ge under oxidizing environment (room air at 200 sccm and 350 Torr) at 850 °C to synthesize NWs with diameters of 40-500 nm.

4.1.2 Our synthesis technique

The GeO_2 nanowires used in this work were synthesized utilizing the VLS growth mechanism[81] in a simple horizontal tube furnace set up as shown in **Figure 4-1**. In the VLS mechanism, the catalyst forms a eutectic with the nanowire material and acts as a preferential growth site for the nanowires. The location and diameter of the nanowire is mainly controlled by the position and size of the catalyst particle[93]. The synthesis technique is similar to thermal annealing growth technique[92] previously reported but

employs stoichiometric flow of dry gases instead of room air to allow greater control over reaction variables. Silicon substrates were cleaned by sonication for 15 min each in acetone, methanol, and DI water and finally dried by blowing compressed nitrogen. The substrates were then coated with 3 nm to 28 nm thick gold film using an e-beam evaporator or by sputtering. In the case of e-beam evaporation, the film thickness was monitored using Inficon Quartz Crystal Monitor. The Au coated silicon substrate was placed on a quartz support plate, several centimeters downstream of the solid germanium source material. The support plate was then positioned in the center of a quartz tube placed in a cylindrical tube furnace. The tube was evacuated to less than 200 mTorr by a mechanical vacuum pump and subsequently backfilled with argon at a flow rate of 50-80 sccm. Temperature of the furnace was raised to 855 °C over 30 min and allowed to stabilize for 10 min. The temperature was measured using 'K' type thermocouple sandwiched between quartz tube and tube furnace as shown. After reaching growth temperature, the downstream isolation valve was closed and pressure was allowed to increase to about 5-10 Torr. The increased background pressure allows confining the source vapors over the substrates. Then oxygen mixed with Ar (40% O_2 and balance Ar) was introduced into the reaction chamber at a flow rate of ~30-50 sccm. The nanowire growth was carried out for nearly 5-30 min and then the gas flow was switched from oxygen/argon (40/60) to pure argon. The furnace was allowed to cool to room temperature before opening the tube to atmosphere.

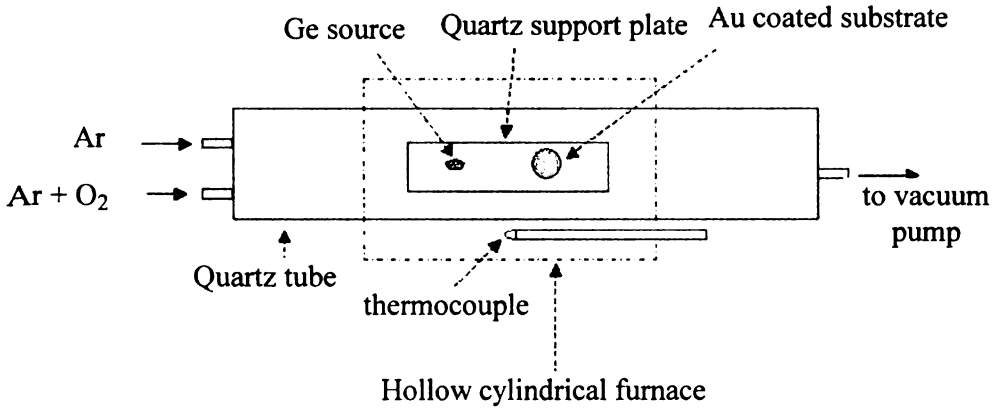

Figure 4-1. Schematic of germanium dioxide nanowire synthesis.

4.1.3 Characterization of nanowires

The substrate surface was covered with white powder-like material after synthesis that could be seen with the naked eye. The product was characterized using JEOL 6400 scanning electron microscope (SEM). **Figure 4-2** shows the SEM image (15 keV with ~15 mm working distance) of the substrate fully covered with dense nanowires. The x-ray Energy Dispersive Spectroscopy (EDS) analysis shown in **Figure 4-3** confirmed the NWs were composed of germanium and oxygen. The atomic ratio of germanium to oxygen was found to be 25:54 which is quite close to the actual ratio of 1:2 suggesting the product to be GeO_2. The nanowires were also characterized by JEOL 2200FS 200 kV field emission transmission electron microscope (TEM). The TEM samples were prepared by ultrasonicating the nanowire substrate in ethanol and then dispersing a drop of solution on a holey carbon-coated TEM grid. **Figure 4-4** shows the TEM image of a single GeO_2 nanowire with a diameter of ~31 nm. The TEM image shows a dark spherical tip at the end of the nanowire. The EDS of the tip shows some gold while that from the stem of the nanowire does not show gold in the EDS spectrum. This confirms

that growth is taking place by the VLS mechanism. The selected area electron diffraction (SAED) pattern from the nanowire is also shown in **Figure 4-4** and confirms that the nanowires are single crystalline.

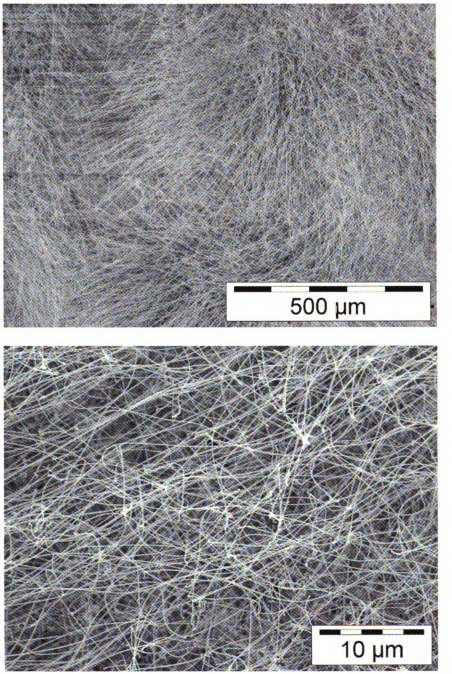

Figure 4-2. SEM image of GeO_2 nanowires on different samples of Si.

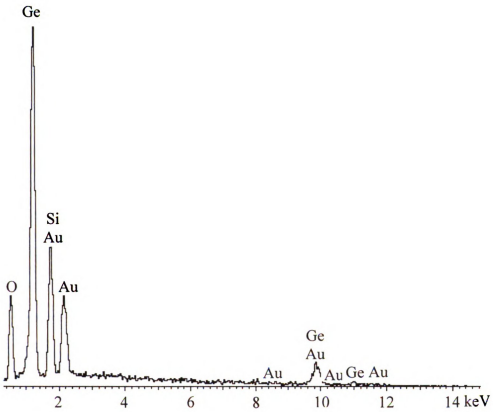

Element	App Conc.	Intensity Corrn.	Weight%	Weight% Sigma	Atomic%
O K	0.55	0.9780	21.61	0.87	53.97
Si K	0.25	0.7934	11.97	0.46	17.03
Ge L	0.88	0.7524	44.66	0.94	24.59
Au M	0.37	0.6500	21.76	1.07	4.41
Totals			100.00		

Figure 4-3. EDS spectrum and quantification results for GeO_2 nanowires.

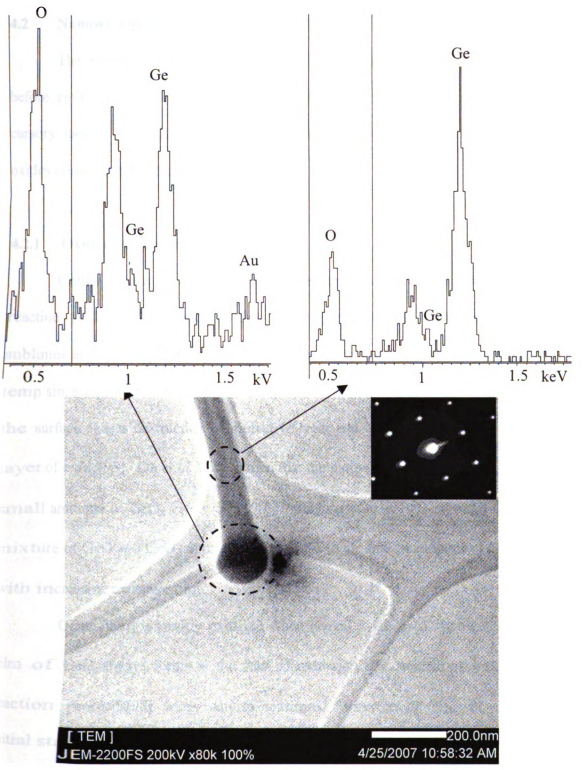

Figure 4-4. TEM image showing gold at tip and EDS spectra for two regions of nanowire and the diffraction pattern.

4.2 Nanowire growth kinetics

The synthesis of nanowires involves both oxidation as well as annealing, so before embarking on explaining oxide nanowire growth kinetic, it is useful to take a cursory look at the oxidization process of metallic germanium and the behavior of its oxides under high temperature annealing.

4.2.1 Oxidation of germanium

Unlike silicon the formation of germanium oxide is complicated by the interim reaction product of a monoxide that is thermodynamically unstable as a solid and sublimes at high temperature[94]. Germanium is stable to atmospheric oxygen at room temp since a protective thin oxide film covers its surface. Adsorption of water vapors on the surface causes destruction of protective layer and results in the formation of a thick layer of oxide[95]. Oh *et al.* have shown that the native oxide on Ge is mostly GeO_2 with small amounts of GeO_x $(1 < x < 2)$ [96]. Prabhakaran *et al.*[97] reported formation of a mixture of GeO and GeO_2 upon exposure of Ge to air and the amount of GeO_2 increases with increasing exposure time.

Germanium is readily oxidized when heated in air or in a stream of oxygen. A film of GeO always forms at the start of oxidation that transforms into GeO_2 as the reaction proceeds[98]. Many studies confirmed formation of GeO_x $(1 < x < 2)$ during initial stages of thermal oxidation of Ge[99-101]. Prabhakaran *et al.*[97] found that *in situ* oxidation of germanium by leaking oxygen into UHV chamber only produces GeO. In their study, GeO_2 was obtained only by exposing Ge to air and they attributed formation of GeO_2 to moisture effects. Molle *et al.*[101] reported formation of significant amount

of sub-oxides at room temperature during germanium oxidation using atomic oxygen. Increasing temperature to 300 °C, strongly enhanced formation of GeO_2. However, GeO_2 started transforming to GeO at 400 °C and completely desorption of oxide occurred at 450 –475 °C.

The main reactions during thermal oxidation of germanium in an oxidizing environment are[98]

$$Ge(s) + 1/2\,O_2(g) \rightarrow GeO(s) \tag{4.1}$$

$$GeO(s) \rightarrow GeO(g) \tag{4.2}$$

$$GeO(s) + 1/2\,O_2(g) \rightarrow GeO_2(s) \tag{4.3}$$

A study of oxidation rate of Ge at 450-700 °C showed that above 550 °C, the oxidation rate of Ge increases with decreasing oxygen pressure[98]. The relative contribution of these reactions is a strong function of oxygen partial pressure. For example, the rate of Ge vaporization (i.e., loss due to oxidation) is ~5.4 mg/min in stream of air at 4 mm Hg. The vaporization of Ge, however is nearly zero if stream is at a pressure of 34 mm Hg[98]. Indeed as the oxygen pressure decreases, all of the GeO formed on the surface manages to sublimate i.e., reactions (4.1) and (4.2) take place, the rate of reaction (4.3) being very slow. When oxygen partial pressure increases, the oxidation proceeds according to reactions (4.1) and (4.3), the reaction (4.3) begins to prevail over reaction (4.2). After a continuous film of GeO_2 has formed on the surface of the sample, the reaction is determined by the rate of diffusion of oxygen and GeO through this film, and the reaction slows down considerably. Similarly if Ge is heated

under conditions where the amount of oxygen is insufficient to convert it to GeO_2 (for example in stream of N_2 or Ar containing oxygen admixture), formation of volatile GeO results[95].

4.2.2 Stability of germanium oxides

The oxidation/annealing step at high temperature has significant impact upon oxidation process due to formation of volatile GeO that can diffuse away or decompose during oxidation/annealing process. Annealing of germanium sample having a thin oxide film at 500 °C under N_2 environment confirmed thermal decomposition of GeO_2 into GeO which desorbs from the surface[98]. A similar observation was reported by Prabhakaran *et al.* during their study of thermal decomposition of oxides for Si and Ge[102]. They found that on annealing, both the oxides (GeO_2 and SiO_2) undergo thermal decomposition and the desorbing species is the corresponding monoxide. However, their decomposition pathways were entirely different. On annealing the Ge oxide layer, the GeO_2 species transforms to GeO on the surface and finally desorbs from the surface at ~425°C. In contrast, annealing results in the transformation of SiO to SiO_2 up to a temperature, lower than the desorption temperature (~760 °C). Hansen *et al.* only detected GeO(g) as desorption product during exposure of Ge (100) to molecular oxygen[103]. It has been reported that the GeO desorbs from germanium surface on annealing at 400 °C in vacuum without undergoing any further transformation[97]. In contrast to GeO, the GeO_2 is very stable and does not melt unless temperatures greater than 1116 ± 4 °C are reached[104]. On heating bulk GeO_2 to 1000-1100 °C, vaporization

is hardly noticeable and there is no dissociation to Ge and O_2 or GeO and $1/2O_2$[95]. The situation changes when GeO_2 is in contact with Ge (e.g., thin GeO_2 film on Ge) and a volatile GeO may be formed at the interface. In summary, it is widely agreed that GeO is the only desorption product of oxidation of Ge and the GeO desorption occurs in the temperature range 400 – 500 °C.

4.2.3 Growth model

The main ingredients in the synthesis of GeO_2 nanowires are the solid phase reactant of Ge metal and gas phase species of Ar, H_2 and oxygen. Obviously the most important of these are Ge and oxygen as these are to form the final product. The Ar is used mainly as the carrier gas to transport the source material to the substrate(s). The beginning source material of Ge is expected to have thin layer of native GeO_2 since it has been exposed to atmosphere during storage. As the source temperature is ramped under low vacuum (300-400 mTorr) with protective flow of Ar and H_2, the native oxide is expected to be reduced to Ge or will escape by transforming into GeO above 400 °C. During ramping and even at the reaction temperature, the source evaporation is negligible since Ge has a negligible vapor pressure at the growth temperature (the melting point of Ge is 937.2 ± 0.5 °C[105, 106] whereas the actual temperature at Ge source inside the furnace is ~ 800 °C). Hence, any direct evaporation of Ge is not a significant contributor to nanowire growth. This was further confirmed from a control experiment in which neither any discernable loss of Ge source nor NWs growth was observed when an experiment was carried out without flowing oxygen into the chamber.

The introduction of oxygen in the gas stream Ar initiates the oxidation of germanium source. It is hypothesized that the insufficient supply of oxygen results in the formation of GeO on the surface on source material. Even if small amount of GeO_2 is formed, it will react with the underlying layer of Ge and transform into GeO. Any thicker layer of GeO_2 is ruled out since thermal stability of GeO_2 (Melting point 1116 ± 4 °C) will bring the further oxidation of Ge to a stand still. This is contrary to the experimental observation that the source material completely disappears in less than 10 minutes of reaction. Therefore, the first reaction occurring during the growth of NWs is

$$Ge(s) + O_2(g) \rightarrow 2GeO(s) \qquad (4.4)$$

It may be emphasized that for every temperature, there is an optimum oxygen concentration at which the oxidation rate of germanium does not surpass the sublimation rate of the monoxide being formed. Otherwise, a thick layer of dioxide will form on the surface of the germanium and the oxidation process will virtually come to a halt. The GeO(s) formed during reaction (4.4) is very volatile and has high vapor pressure as shown in **Figure 4-5**.

The GeO sublimates at 710 °C[107] and at the reaction temperature, it immediately transforms to gas phase according to

$$GeO(s) \rightarrow GeO(g) \qquad (4.5)$$

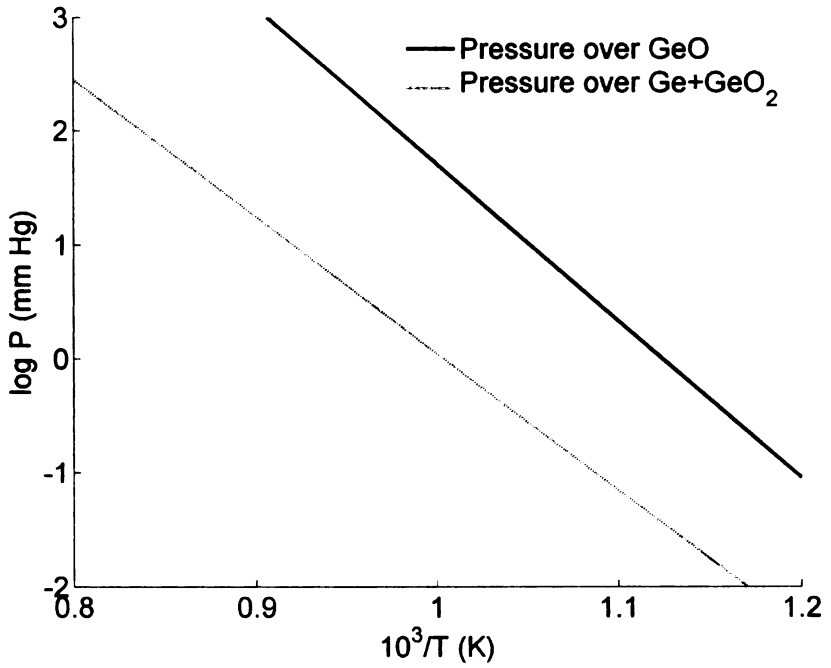

Figure 4-5. Vapor pressure of GeO at different temperatures.

However, oxidation of GeO in air begins at 550 °C and the presence of oxygen in the growth chamber can lead to oxidation of GeO vapors as these diffuse away from the source under the flow of carrier gas according to reaction[107]

$$GeO(g) + 1/2\,O_2(g) \rightarrow GeO_2(s) \qquad (4.6)$$

Oxidation of GeO is not expected to be significant due to the low concentration of oxygen in the environment otherwise thermally stable layer of GeO_2 will deposit on the substrate(s) and the walls of reaction chamber. The walls of the quartz tube in the high temperature region do not get any discernable coating and the substrates tend to turn black (color of GeO) instead of white (color of GeO_2) at the beginning of synthesis.

Nevertheless, the actual vapor phase is expected to be a mixture of mostly GeO along with some GeO_2. The GeO_2 is likely in the form of fine particles due to its thermal stability at reaction temperature. The visual observation of a whitish cloud formation that rises from the source material after starting the oxygen flow supports the presence of some GeO_2 in the vapor phase as is evident in **Figure 4-6**. In fact, some experiments did yield some spherical or faceted particles along with nanowires on the substrate as shown in **Figure 4-7** and **Figure 4-8**. However, precise quantitative analysis of vapor phase species requires more elaborate experimental set up (like X-ray photoelectron spectroscopy) than the one available.

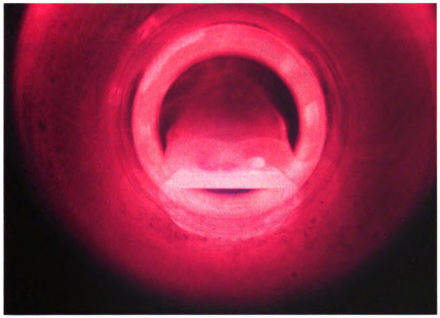

Figure 4-6. Formation of cloudy reactants after introducing oxygen into the quartz tube.

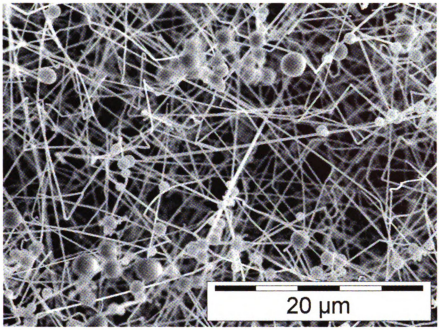

Figure 4-7. Spherical particles and GeO_2 NWs.

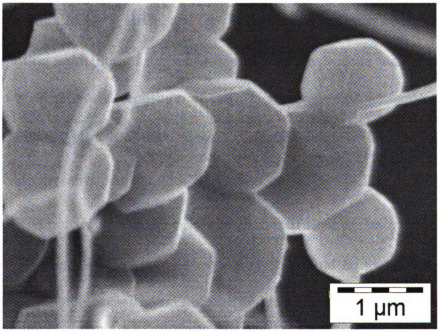

Figure 4-8. Faceted germanium oxide particles with NWs.

In the vapor phase, there is also a thermal decomposition pathway for GeO(g) coming off the Ge source. It is known that solid GeO disassociates into GeO_2 and Ge at high temperatures. The dissociation reaction of GeO is highly temperature dependent. It may take several hours for decomposition at 600 °C but at 700 °C it takes a few minutes[98]. The thermal dissociation of GeO proceeds according to reaction

$$2GeO(g) \Leftrightarrow Ge + GeO_2$$

The reaction temperature controls the probability of forward or reverse reaction[98]. In case of deposition on a condenser (or cold finger), GeO will deposit without decomposition. On the other hand, it will decompose into Ge and GeO_2 without a condenser at fairly high temperatures. Since the substrates are also located in the high temperature zone, we expect the higher rate of decomposition based deposition i.e., substrate gets a mix of GeO, GeO_2, and Ge. The situation is further complicated by the presence of a thin gold film on the substrate that forms a eutectic with the underlying silicon. Kim *et al.* proposed deposition of GeO on substrates that subsequently oxidizes to form GeO_2 during growth of nano-cones by thermal heating of Ge powder at 950 °C under an oxidizing environment with a N_2 background[108]. The exact manner of adsorption of GeO or GeO_2 into Au cannot be predicted since no information about the ternary phase diagram for Ge, Au, and oxygen system could be found. However, it is postulated that the presence of liquid eutectic droplets facilitate incorporation of GeO, Ge, and GeO_2 into the droplet yielding an initial sub-oxide composition GeO_x $(1 < x < 2)$ of NW[109]. The composition of the nanowire then transforms to more stable GeO_2 by incorporation of oxygen from environment as well as through loss of

GeO by vaporization. The excess GeO diffuses away from the reaction zone and condenses in the colder part of the tube. The ends of tube get a yellowish to brownish back coating that is characteristic color of GeO. Some fine powder like coating is obtained further downstream part of tube.

Thus the most plausible mechanism for the formation of GeO_2 NWs can be summarized as:

(a) Oxidation of Ge to form GeO(s).

(b) Transformation of GeO(s) to GeO(g).

(c) The transport of GeO(g) (and possibly some small percentage of GeO_2 formed in gas phase) to substrate.

(d) Preferential adsorption of GeO on the substrate (black appearance of substrate) at the sites of gold catalyst and possibly some associated decomposition into Ge and GeO_2.

(e) The growth of $GeO_x\,(1 < x < 2)$ NWs via the VLS mechanism by absorbing more source material from the vapor phase.

(f) The evolution of stable GeO_2 NWs by incorporation of oxygen and loss of GeO.

It may be noted that a different mechanism was proposed in past in which the reaction results in adsorption of GeO_2 vapors on the Au eutectic on the substrate[110]. However, the thermal stability of GeO_2 does not support the feasibility of having any

significant quantity of GeO_2 in vapor phase at temperature below 1100-1200 °C. The smooth surface of the NWs also suggest a viscous state of the nanosize $GeO_x (1 < x < 2)$ exists at the tip of the NW during growth[100]. The existence of very fine GeO_2 particles in the gas phase cannot be ruled out but any large concentration of GeO_2 is not expected. If that was the case, one would expect much coarser NW surface (the GeO_2 particle are likely to be incorporated as such into NWs due to high thermal stability). This is contrary to the actual observation (TEM and SEM studies) of smooth NW surface with the exception of some instances where ~ micron size particles were observed along with NWs. Additional evidence relates to the physical appearance of substrates during synthesis. One will expect visual whitening of the substrate upon adsorption of GeO_2 instead of first blackening followed by appearance of random white dots on the substrate. The density of these white dots then gradually increases as reaction proceeds and tends to cover the whole substrate. In one control experiment, some of the fine GeO_2 powder collected from the walls of the quartz tube was placed on Au coated Si substrate to see if the GeO_2 on Au film can form a eutectic and promote NWs growth. However, GeO_2 particles remained as such on the substrate and no NW growth was observed as shown in **Figure 4-9**. Only the Au film broke into small particles as expected. The EDS of the substrate next to GeO_2 particles did not show any Ge or GeO_2 indicating stability of GeO_2 for the given the reaction conditions.

The explanation so far has ignored the presence of H_2 in the chamber. It is known to be an oxide reducing agent depending upon the partial pressures of hydrogen and that of water in the system for a given temperature. As a practical manner, the partial pressure

of water is equal to the base pressure of the system[111]. In our case, the base pressure is ~ 200 mTorr and partial pressure of H_2 is ~ 250 mTorr (for a total pressure of 5 Torr).

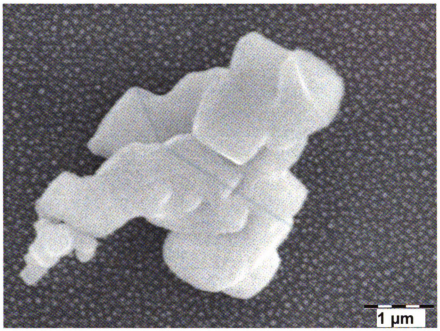

Figure 4-9. GeO_2 particles on Au coated Si substrate after typical synthesis run.

Figure 4-10 is a plot of thermodynamic stability of GeO_2 as a function of ratio of hydrogen pressure to water pressure for different reaction temperatures[112]. For a $\frac{P(H_2)}{P(H_2O)} \approx 1.25$, the GeO_2 is unstable for all temperatures above 500 K and is expected to decompose to constituent elements. Since the NWs synthesis is carried out above this temperature, we do not expect any GeO_2 on the source material at the start of oxygen flow. The situation changes after introduction of oxygen into the system and the oxidation of Ge/GeO become dominant compared to the reduction of GeO/GeO_2 by H_2.

The effect of H_2 will be discussed again later in this chapter during study of background gases on NWs synthesis.

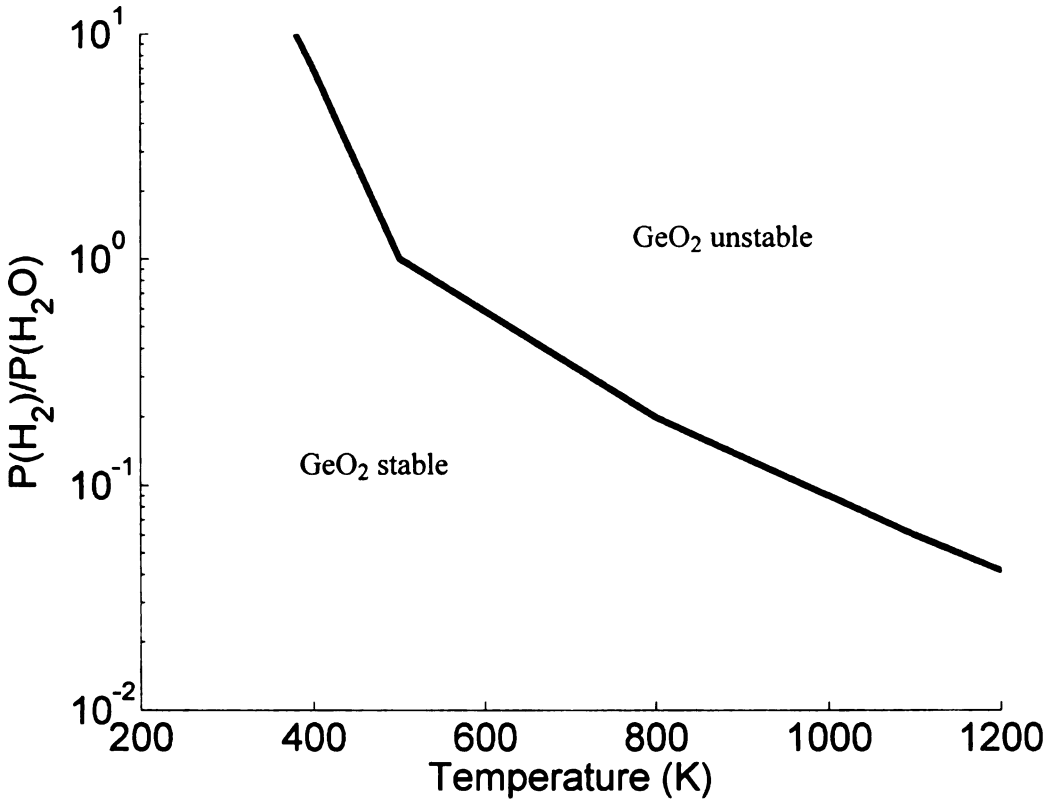

Figure 4-10. Plot showing GeO_2 stability as function of temperature and the hydrogen to water vapors pressure ratio[112].

4.2.4 Synthesis temperature profile

The furnace temperature was measured and controlled by using a 'K' type thermocouple placed between quartz tube and furnace. The actual growth temperature inside the quartz tube at the site of source and substrates is expected to be somewhat different from that measured by the outside thermocouple due to physical separation and environment. To get a more accurate value of temperature inside the furnace, a second

'K' type thermocouple was placed inside the quartz tube. **Figure 4-11** shows a typical temperature profile during NWs synthesis run measured by the two thermocouples. As expected the actual temperature inside the quartz tube is lower than the outside temperature by about 65–75 °C under steady state for an outside temperature of 850 °C.

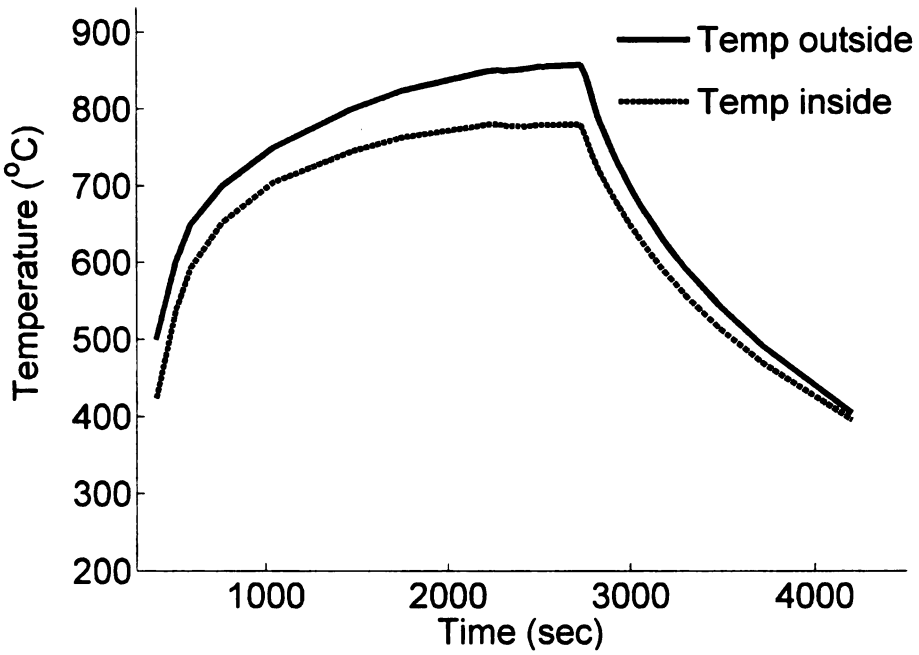

Figure 4-11. Tube furnace typical temperature profile during nanowire synthesis.

4.2.5 Synthesis pressure profile

Pressure dependent studies during NWs synthesis revealed a typical variation pattern as shown in **Figure 4-12**. It is important to mention that the pressure is measured at the downstream end of the tube and may have minor deviation from the actual value at the location of source. However, calculation of conductance of vacuum line from tube center to gauge location for a viscous flow yields a value of 21.32 L/s at 5 Torr and this is much larger than the total gas throughput of ~1.267 Torr-L/s (corresponding to 100 sccm

flow rate). The calculated difference between measured and true values of pressure at the location of the reaction is only 0.06 torr for a total flow rate of 100 sccm at 5 Torr and room temperature. The synthesis is initiated at ~5 Torr by introducing Ar + O_2 (Ar 60%, balance O_2) mix in the system at a flow rate of 50 sccm. The variation of the pressure at the synthesis temperature of ~850 °C can be analyzed to get some insight into the different reactions taking place during synthesis. Three distinct pressure regimes can be identified in **Figure 4-12**:

1. Region I : This region is marked by the rapid rise to a peak value. The rise in pressure can be attributed to the formation of volatile GeO that is in vapor phase at the synthesis temperature. Also one can notice a brief hold of pressure near 10 Torr, which is probably an artifact of the pressure gauge.
2. Region II : This region indicates a gradual drop in pressure value from the peak attained in Region I. This is probably due to the conversion of GeO(g) to GeO_2(s) that reduces the contribution of gas phase to pressure. Also some of the GeO(g) is expected to escape the high temperature region and condense in the colder part of the chamber. The lowest value of pressure is reached once nearly all of the GeO vapors are transformed into solid phase. The source material is found to completely disappear before reaching the pressure minimum in this region.
3. Region III : Pressure starts to slowly rise in this region which is attributed to the continuous flow of background and reaction gases into the chamber.

It is important to re-iterate that a convector P-type gauge is used to measure the pressure. The readings of convector type of gauge at higher pressure (>1 Torr) are highly dependent upon the type of gas. This is due to different thermal conductivity of different gases. Typically the gauge is calibrated for a certain type of gas (mostly nitrogen or air) and a correction factor needs be applied to convert indicated pressure to true pressure when using a gas different from calibration gas. For example, a gas calibrated with nitrogen will practically give accurate reading for nearly every gas below a pressure of 1 Torr. However, same gauge will indicate a pressure of only 8.83 Torr for a true pressure of 100 Torr when used with Ar gas. Hence the analysis presented above shows an accurate trend of pressure variations but the absolute values of pressure are expected to have significant variations from indicated values. This will discussed again later in this chapter while studying effect of different background gases on NW synthesis.

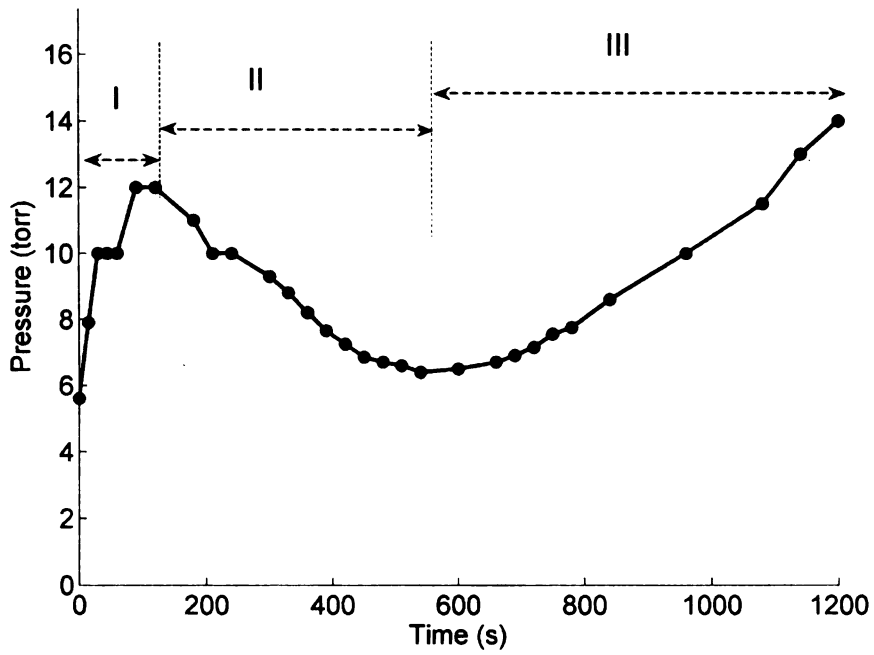

Figure 4-12. Typical pressure profile during NW synthesis.

4.3 Factors affecting growth of nanowires

The NWs synthesis is affected by a number of factors including thickness of catalyst film, temperature, pressure, and background gas type, flow rate, oxygen flow rate etc. The effect of these parameters on the resulting NWs will be discussed in turn in this section.

4.3.1 Role of gold catalyst

The catalyst plays an important role as the nucleation site for initiation and continued growth of the nanowires in VLS mechanism. In typical semiconductor nanowire growth by VLS mechanism, the metal catalyst forms a eutectic with semiconductor and this eutectic has a lower melting point than either of its constituents. For example, a eutectic containing 19.5 atomic % Si and 80.5 atomic % Au is in liquid phase for temperature $\geq$ 360 °C. This liquid phase serves as the preferential site for adsorption of gas phase species into the liquid phase catalyst or its eutectic form at the growth temperature. This results in nanowire growth that is highly localized to the catalyst coated area. **Figure 4-13** shows dense and patterned NWs growth on Si(100) substrate that was partially coated with 7 nm Au film. As can be seen, the NWs growth (white areas) is strongly limited to the Au coated area with no growth on uncoated area (bottom left corner of image). The catalyst specific growth is one of the strong characteristics of VLS mechanism and gives evidence of VLS mechanism taking place.

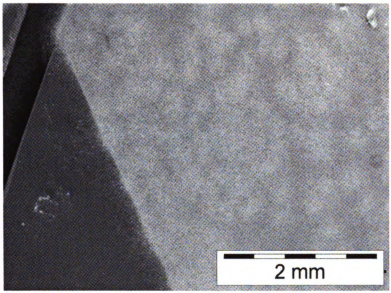

Figure 4-13. GeO_2 NWs on Si(100) partially coated with 7 nm Au film.

Another characteristic of VLS is that the NWs generally terminate in catalyst particle that has a spherical shape. However, not all of our NWs were found terminated in catalyst particle. This could be due to breaking off of the catalyst particle during growth or cooling, or the catalyst might be incorporated into the nanowire during cooling. Another factor could be co-existence of other synthesis mechanisms like oxide-assisted growth (OAG)[88] or vapor-solid (VS)[91]. However, the argument against OAG or VS is the complete absence of NWs in uncoated area whereas none of these other mechanisms need a catalyst to yield NWs. It is postulated that the VLS is the dominant mechanism but other mechanism may exist. The catalyst coating significantly enhances the adsorption of vapor phase species to initiate growth and subsequently different growth mechanism including VLS, VS and OAG may contribute to NW growth to varying degrees. Some of the NWs do show a spherical particle at the tip confirming

existence of VLS growth. **Figure 4-14** shows the SEM image of such a single NW with a particle at the tip.

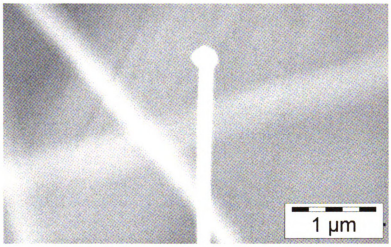

Figure 4-14. GeO_2 NW showing particle at tip.

4.3.1.1 Gold film annealing

The initial catalyst film thickness is the main controllable parameter in VLS mechanism as it has a direct bearing on the diameter of the nanowires. A systematic study of the evolution of catalyst film into particulates was carried out to get an estimate of initial size distributing of catalyst particles. Different thickness of gold films were deposited on Si(100) wafer and the samples were subjected to typical synthesis conditions without germanium source material or oxygen flow. **Figure 4-15** through **Figure 4-19** show the SEM images and corresponding particle size distributions after annealing different thickness films. It may be mentioned that the particle size measurement for very thin films (3 nm) is not very accurate (an error of ~20%) due to poor image quality at very high magnification of the SEM. Nevertheless such coarse

measurement is sufficient to give an idea of the size distribution expected for very thin films.

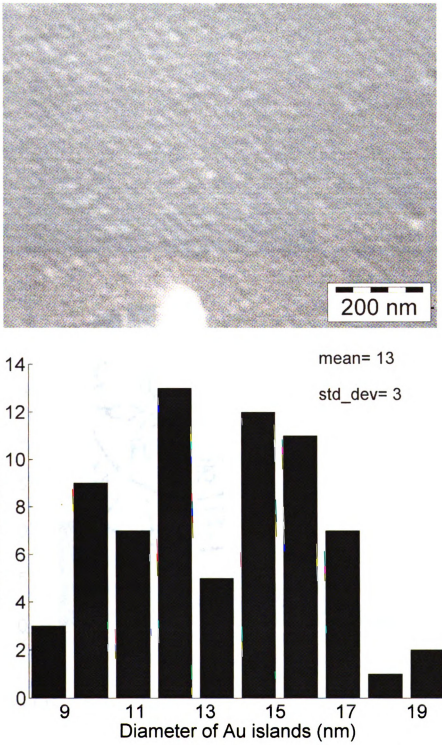

Figure 4-15. SEM image and particle size distribution for 3 nm Au film.

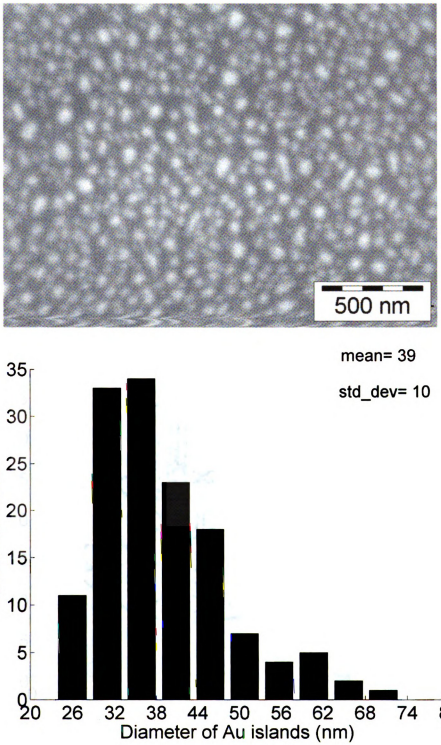

Figure 4-16. SEM image and particle size distribution for 7 nm Au film.

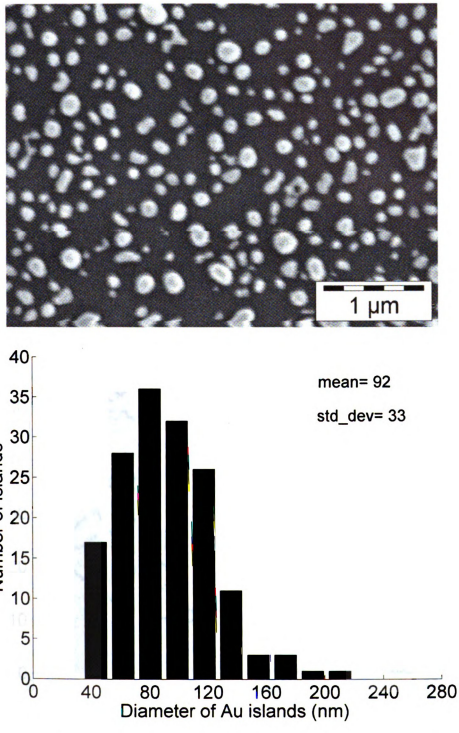

Figure 4-17. SEM image and particle size distribution for 15 nm Au film.

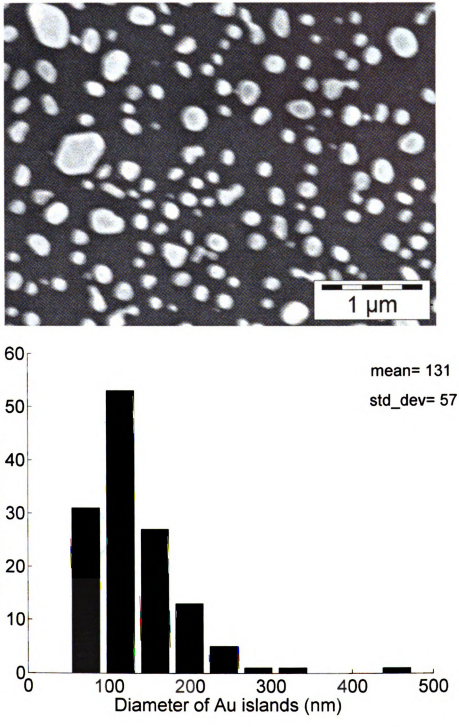

Figure 4-18. SEM image and particle size distribution for 21 nm Au film.

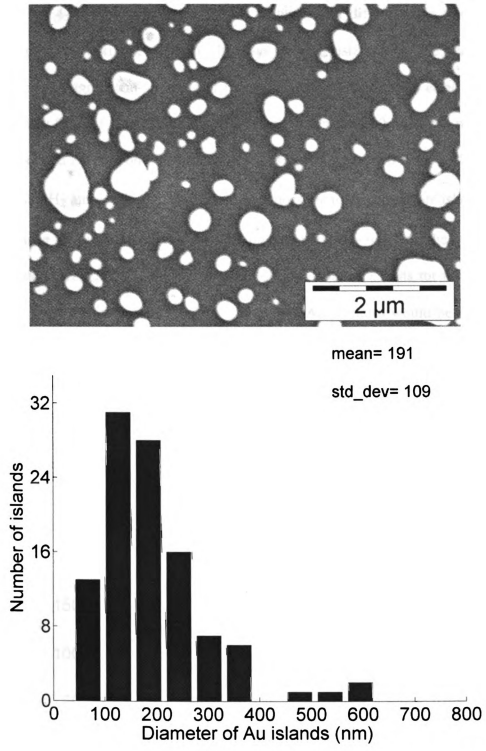

Figure 4-19. SEM image and particle size distribution for 28 nm Au film.

Figure 4-20 shows the mean particle diameters for different film thickness and relationship is approximately linear. It may be emphasized that the particle size distribution is in agreement with earlier reports. For example, Sharma *et al.* found that approximately 85% of the eutectic droplets were smaller than 50 nm for 5 nm thick e-beam evaporated Au film on Si substrates that were annealed at 940 K for 5-10 min at 95 Torr in 1 slm H_2 ambient[113]. Though it is not possible to directly relate island sizes in our case since we differ in ambient, anneal time, and temperature. Still the mean values of metal island sizes are comparable (we get ~40 nm diameter islands for film thickness of 7 nm). It may also be noted that the size of the Au particles would be expected to change from these dimensions when at the actual conditions (flow of reaction gases and formation of reactants) since the surface energies are dependent upon the ambient phase.

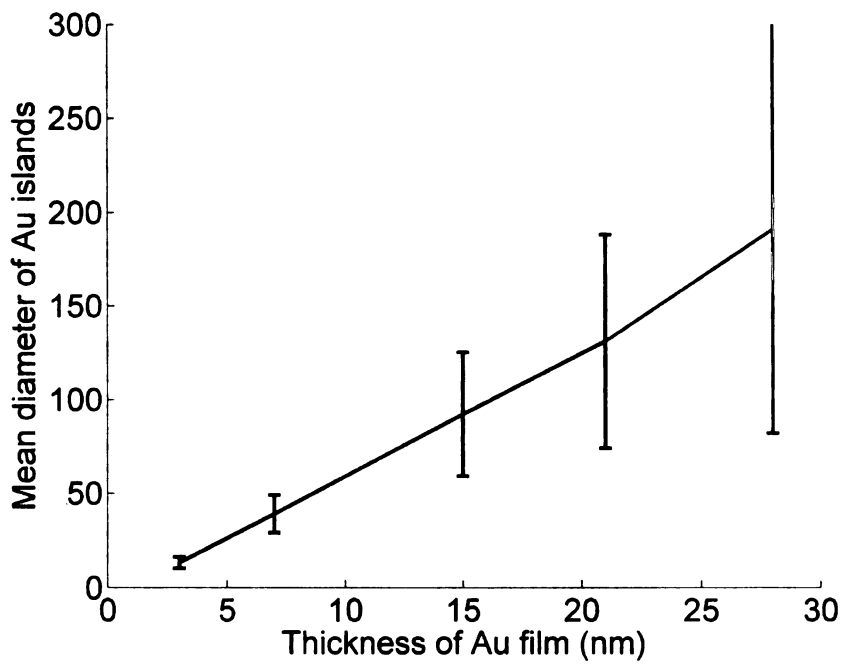

Figure 4-20. Mean particle size distributions after annealing different thickness Au films. Error bars indicate standard deviation from mean.

4.3.1.2 Gold film thickness affect on GeO_2 NWs diameter

Next we move on to study diameter of the nanowires that result from different thickness gold films. NWs were synthesized on Si substrates that had different initial Au film thickness in a single experiment to seclude any variations from one experiment to another. The diameters of the NWs were determined from SEM studies by selecting at least three different areas on each substrate. For each substrate, more than 100 NWs were characterized using SEM. **Figure 4-21** through **Figure 4-23** show the diameter distribution for NWs synthesized on Si substrate from 3 - 15 nm thick Au films. It may be mentioned that the sizes of the particles were measured from high-resolution SEM images using measurement tool box of SEM software and then Matlab histogram function was used to plot the size distributions.

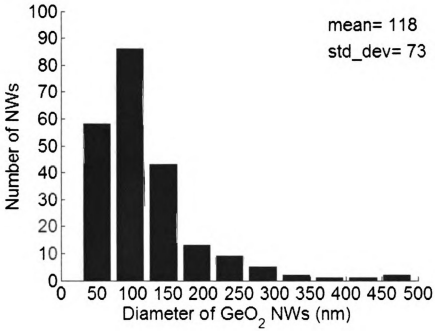

Figure 4-21. GeO_2 NW diameter distribution for 3 nm Au film.

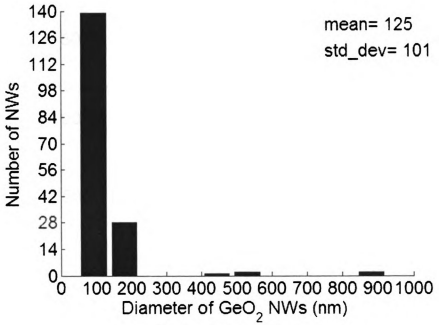

Figure 4-22. GeO_2 NW diameter distribution for 7 nm Au film.

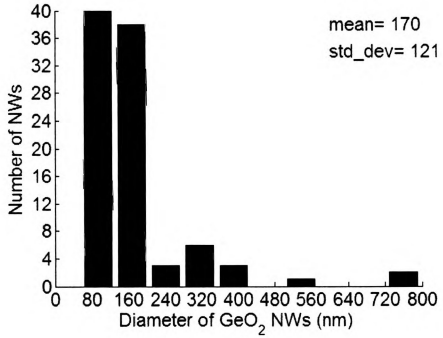

Figure 4-23. GeO_2 NW diameter distribution for 15 nm Au film.

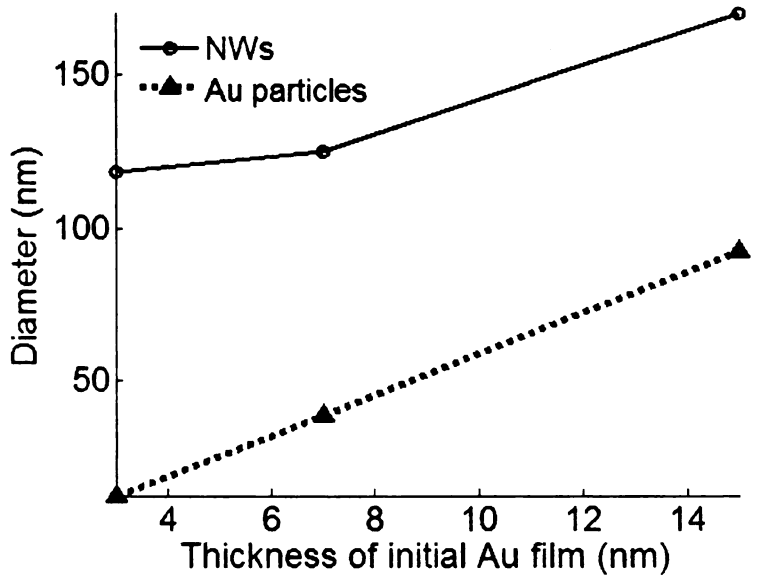

Figure 4-24. Mean diameters of GeO_2 NWs and annealed Au film particles.

Figure 4-24 shows the mean diameter for the gold particles and resulting NWs for different catalyst film thickness. It is immediately evident that the diameters of the synthesized NWs do not have a one-to-one correspondence with the measured particle diameters for that film thickness. It is also important to point out that the size of the final eutectic particle at the tip of the NW is typically larger than the diameter of the nanowire as can be seen in **Figure 4-4** and **Figure 4-14**. Hence we start with a small Au particle that yields a relatively large diameter NW ending in a tip particle of even larger diameter. An obvious explanation for the increase in the diameter of the NW compared to the starting Au particle is the increase in the size of eutectic particle following adsorption of vapor phase species that increases diameter of NWs. This is supported by the EDS analysis of tip particles with TEM that shows presence of germanium as well as oxygen in the eutectic particle. The oxidation of sub-oxides following nucleation can also

increase NW diameter. The dynamic conditions at the reaction temperature and ambient may dictate different morphological evolution of NW. For example, the Au alloy may be more distributed at the tip of the nanowire during growth and then the Au gets pushed out during cooling leading to the formation of larger spherical particle at tip. Also the mechanisms other than the VLS can be occurring simultaneously that contribute to larger NWs than expected from VLS alone. For example, VS mechanism can result in micron size whisker[91]. We did observe some faceted whiskers during synthesis as shown in **Figure 4-25**. The surface of the whisker appears rough in the image but is probably due to gold coating to facilitating SEM imaging. Some lateral growth on the NW can also result in NWs thicker than the catalyst particle. The difference between annealed Au eutectic particle size and the resulting NWs diameter is large for thinner film. This can be explained from the Gibbs-Thomson effect that predicts higher vapor pressure for smaller diameter wires. As a result, very small diameter NW (in case of thin Au film) may not be feasible under the synthesis conditions employed in this work.

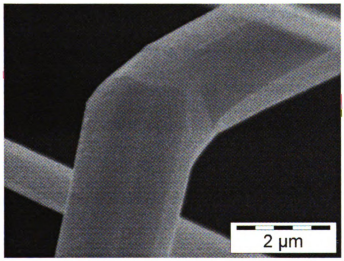

Figure 4-25. A faceted GeO_2 whisker.

4.3.2 Effect of growth time on length of nanowires

In a typical VLS growth, the length of NWs is proportional to growth time. However, this is valid only if precise control over the amount of reactant supply is exercisable as is the case of chemical vapor deposition (CVD) reaction. However, such control in not feasible in the experimental set up used in this work. The main reason is the high volatility of reactants at growth temperature and the associated thermal inertia of the system. It was observed that nearly all the source material manages to oxidize even if the furnace is turned off after reaching growth temperature. The thermal inertia of the system and fast oxidation of source makes it difficult to exercise control over length using growth time as variable. Although it is difficult to precisely determine the amount of reactants (like GeO in this case) but it is speculated that the supply of reactant is high at the beginning of reaction and then decreases gradually as the source material is consumed. The rate of growth of NWs is also expected to follow a similar trend. The typical length of NWs was found to be several tens of microns. The random and intertwined/entangled orientation of NWs on the substrate makes the precise length measurement difficult during SEM studies. A better insight can be obtained by studying cross-section of the substrate and looking at the height of the NW cluster layer. **Figure 4-26** shows cross-section of the substrate and confirms randomly oriented NWs extending up to 100 μm above the substrate. It is therefore concluded that the overall length of NW is of the order of tens of microns.

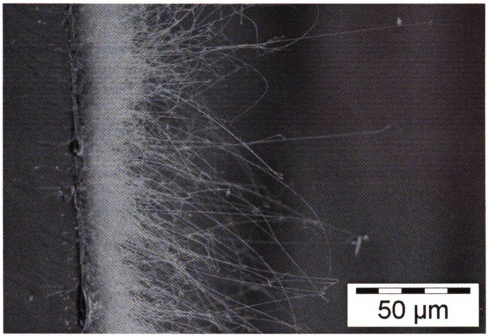

Figure 4-26. Cross-section of substrate showing long NWs extending from substrate.

4.3.3 Effect of oxygen flow rate

The NWs synthesis was found to be very sensitive to oxygen concentration as expected. **Figure 4-27** shows NWs synthesized on Si substrate with 7 nm initial catalyst coating using different oxygen flow rates. As can be seen, the best coverage (white area) is obtained for an oxygen flow rate of ~ 50 sccm. This agrees with earlier discussion of Ge oxidation where it was found that the oxidation of Ge to produce GeO or GeO_2 is a strong function of concentration. The observed low yield of NWs for high flow rate of oxygen can be explained by increased conversion of GeO into GeO_2 that limits the spatial coverage of NWs on substrate closer to source. On the other hand, low concentration allows more of GeO to escape from reaction zone, thus reducing yield of NWs. The total flow rate was also found to be a significant parameter impacting the NW growth.

Reducing the total flow rate generates high GeO pressure area over the source and incoming flow of oxygen cannot penetrate this high-pressure area. Instead GeO vapors from source diffuse toward the upstream end and meet with O_2 in the incoming gas flow to form GeO_2 at upstream. This was evidenced by white coating on upstream end of quartz tube for low total flow rate. High flow rate on the other hand pushes the GeO vapor quickly out of the reaction zone resulting in increased coating at the downstream end. A total flow rate of ~ 100 sccm was found to yield optimum yield of NWs on the substrates.

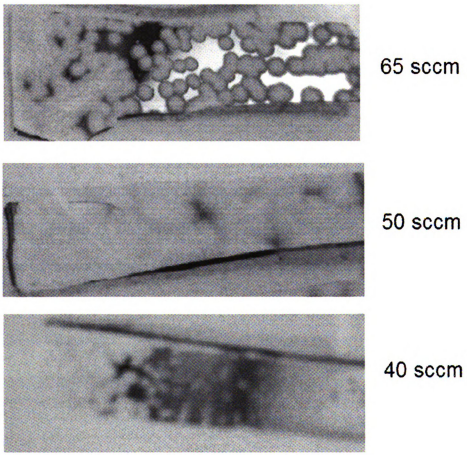

Figure 4-27. Effect of oxygen concentration on NW synthesis. In all cases, the total flow rate (background + oxidation mix) was 100 sccm.

4.3.4 Effect of synthesis temperature

Synthesis temperature showed a pronounced impact on NWs yield. **Figure 4-28** shows optical images of Si substrates covered with NWs synthesized in the temperature range 865 – 765 °C. The yield of the NWs was found to be optimum in the range 830-840 °C. The density of substrate coverage is less at high temperature as can be seen in **Figure 4-28**(a). This can be explained in terms of high energy of volatile GeO formed at high temperature that tends to quickly move out of the reaction zone. Also the corresponding high temperature of the substrates results in less sticking on substrate and greater desorption. This implies that most of the source material manages to escape out of the reaction zone at high temperatures (≥ 850 °C) without yielding nanowires at the substrates. As the temperature is lowered, better yield of NWs is obtained for temperatures of 850-800 °C. This may be considered optimal temperature range for creation of GeO reactants and subsequent conversion into GeO_2 nanowires at the substrate. Lowering the temperature further results in reduced yield as seen in **Figure 4-28**(e). The low temperature effect can be attributed to low evaporation rate of source decreases. The growth is also found to be localized closer to source indicating GeO vapors do not have enough supersaturation to yield uniform growth far from source.

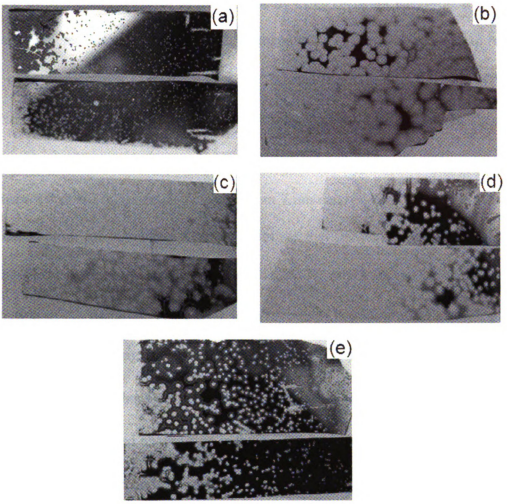

Figure 4-28. GeO_2 NWs synthesized at different temperatures (a) 865 °C (b) 840 °C (d) 830 °C (d) 800 °C (e) 765 °C.

4.3.5 Effect of background gas

Although most of the nanowires were synthesized using a mixture of Ar (95%) and hydrogen (5%), some experiments were carried out using pure Ar or N_2 as a background gas. The morphology of the NWs synthesized using N_2 and Ar gases is similar as shown in **Figure 4-29** and **Figure 4-30** respectively. However, some variations in the diameters were noticed. **Figure 4-31** shows the mean diameter of GeO_2 NWs

obtained for different initial Au film thickness by using different background gases. The smallest diameter is obtained for Ar and hydrogen mix. This is probably due to reducing affect of H_2, which in a way etches away, or reduces lateral growth of oxide NWs. The diameter versus gold film thickness dependence is similar for the case of Ar and Ar mixed with H_2. However, the case of N_2 background has relatively smaller increase in NW diameter as Au thickness is increased from 7 nm catalyst film to 15 nm. There is no clear explanation for this affect. One possibility is that the annealing studies of the Au film was done in Ar environment and annealing in N_2 might somewhat change the size distribution of Au particles. There have been reports of breaking up of catalyst particles due to electrical charging in N_2 background flow. This might explain why the NWs synthesized using N_2 background show less diameter dependence on catalyst film thickness. Another related observation is the different pressure profile for N_2 background compared to Ar background. In case of N_2 background, the pressure initially rises to ~180 Torr (~12 Torr for Ar) and then drops down to 110 Torr (~7 Torr for Ar). The ratio of the pressure change in the two cases (N_2:180/110 = 1.64 and Ar:12/7 = 1.71) is compatible. The convector pressure transducer has different calibration curves for different gases at higher pressure (>1 Torr) due to their different thermal conductivities. Hence it is mainly the different response of the sensor to the two gases that is responsible for observed disparity of pressure in case of different background gases. The values of pressure for nitrogen background are considered more authentic since that is the typical calibration gas for the sensor. The reading of atmospheric pressure as 760 Torr also supports the gauge is reading nitrogen pressure more accurately.

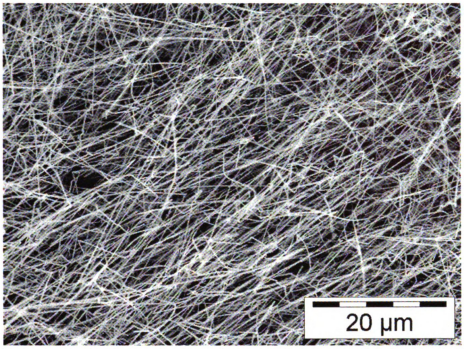

Figure 4-29. SEM image of GeO_2 NWs synthesized using N_2 as background gas.

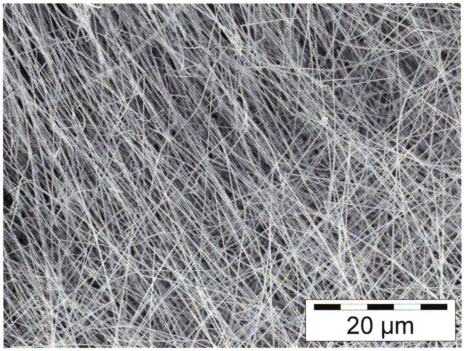

Figure 4-30. SEM image of GeO_2 NWs synthesized using Ar as background gas.

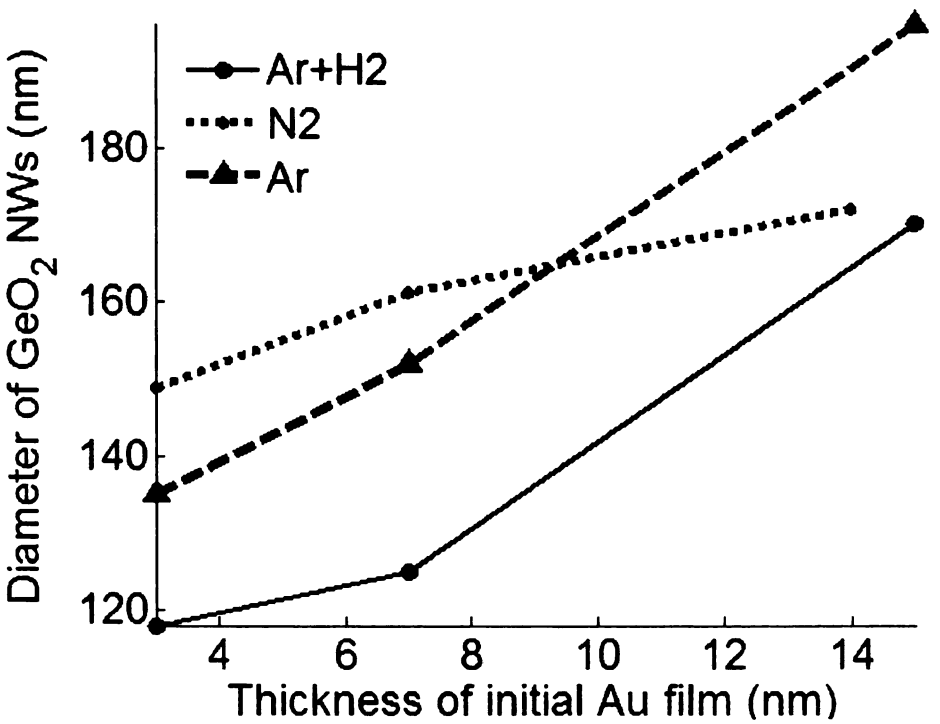

Figure 4-31. GeO_2 NWs diameters for different background gases.

4.3.6 Effect of background gas pressure

The background gas pressure at the start of the synthesis affects the yield of the NWs by changing the degree of supersaturation in the gas phase. The main role of the background gas pressure is to confine the gas phase reactant near the source and substrate. **Figure 4-32** shows two substrates next to location of Ge source with NWs synthesized at two different background gas pressures. The low gas pressure allows the reactants to reach relatively far from the source material. On the other hand, high background gas pressure keeps the reactants localized and some of the GeO_2 is found even at the location of the source. This can be seen for the synthesis at 72 Torr where the dome shaped white GeO_2 is formed at the location of Ge source, i.e, high pressure kept the GeO vapors so localized that these transformed to dioxide at the source instead of

reaching to the substrate. Another indirect evidence of background pressure at work can be from the observation of coatings at the ends of quartz tube. **Figure 4-33** shows optical images of quartz tube downstream end before and after reaction. The amount of white coating of GeO_2 can be an indirect measure of the confining capacity of the background gas. In case of too much coating at the downstream end of the tube, one can conclude insufficient gas pressure for confinement of reactants in the hot zone. Negligible or no coating means too much pressure exists in chamber to let the reactants reach out to the substrates.

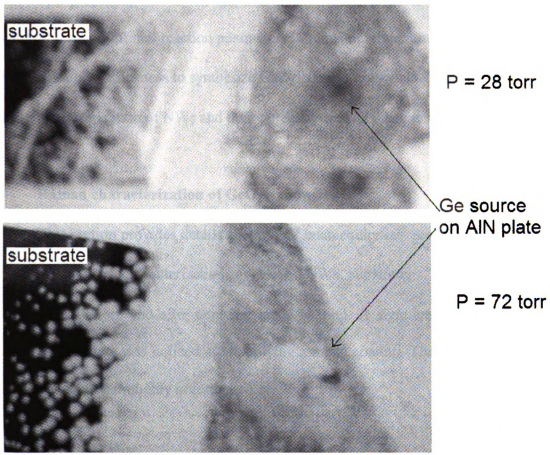

Figure 4-32. Effect of background gas pressure on NW synthesis.

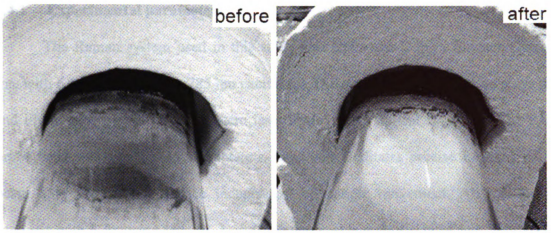

Figure 4-33. White GeO_2 coating at the end of quartz tube.

The preceding discussion has elaborated various aspects of NWs growth and identified a set of optimal reaction parameters in terms of temperature, pressure, gas flow rates, and catalyst thickness to synthesize GeO_2 NWs in high yield. This sets the stage for Raman characterization of NWs and their potential used as substrates for SERS.

4.4 Raman characterization of GeO_2 nanowires

This section provides details about the Raman equipment parameters used and the results of Raman characterization of GeO_2 NWs substrates. The substrates were characterized before and after applying metal coating. A significant change in Raman spectra of substrate was noticed after applying a metal coating. The potential sources of this change were thoroughly investigated.

4.4.1 Experimental parameters

The Raman system used in this study was EzRaman-L from Enwave Optronics Inc. with 6 cm^{-1} resolution at 785 nm excitation. The sample was mounted on a xyz-stage and illuminated by the Raman system laser beam via an optical fiber link. The Raman probe head was attached to a separate z-stage that facilitates precise focusing of laser beam onto the sample surface independent of sample movement. All spectra were acquired with a focusing lens (N.A. = 0.22) that yields a spot size of less than 100 μm diameter on the substrate. The laser power on the substrate was nearly 30 mW as measured with Newport optical meter (model 815 in conjunction with 818-SL detector and 883-SL attenuator). The same laser power was used in all studies except where noted.

4.4.2 Raman spectra of GeO_2 nanowires

The bare substrate containing GeO_2 nanowires was first scanned by the Raman system to get the reference signal and to ensure no impurities are present that can cause interference with the Raman signal. **Figure 4-34** shows the Raman spectra of GeO_2 nanowires (NWs) synthesized on Si(100). The Raman lines obtained from the nanowires are similar to the ones reported by Macoulaut *et al.* for trigonal phase of GeO_2[114]. This Raman spectrum agrees very well with the trigonal phase spectra of GeO_2 and complements the EDS and diffraction results to prove that the synthesized nanowires are made up of crystalline trigonal GeO_2. The water solubility of the synthesized nanowires is also an indirect-indication of their trigonal growth phase and this has been further confirmed by the Raman spectrum.

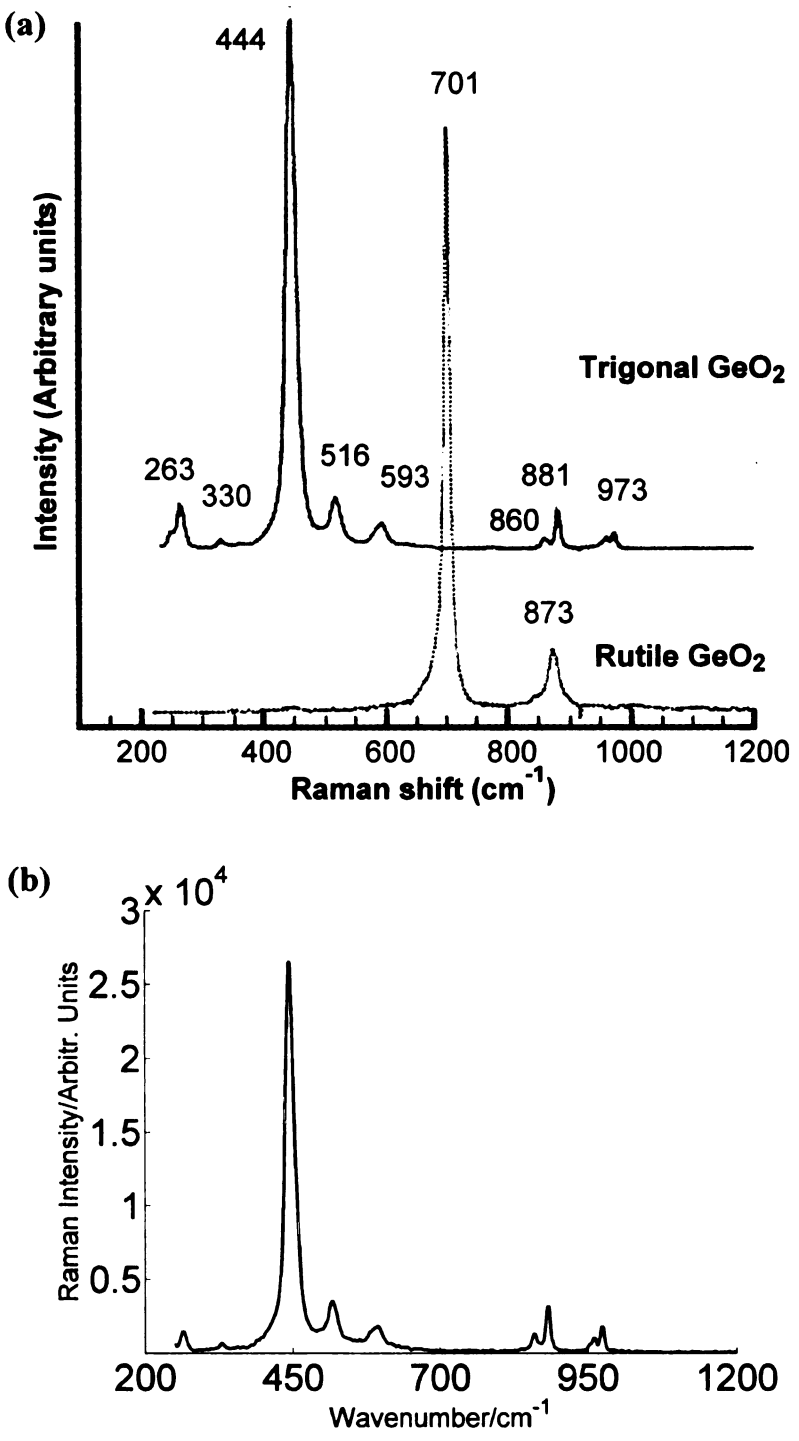

Figure 4-34. (a) Raman spectra for two phases of GeO_2. Reproduced with permission from ref [114]. (b) Raman spectra of GeO_2 nanowires on Silicon substrate, t_{acc}=15 s.

4.4.3 Gold coating of GeO_2 nanowires

The nanowire substrates were sputter coated with ~ 21nm of gold to allow excitation of surface plasmons. The choice of gold is based upon its compatibility with biological systems, chemical inactivity and good SERS enhancement for NIR excitation[115]. The coated substrates were characterized by the Raman system before application of an analyte to establish background signal. **Figure 4-35** shows the observed Raman spectra of gold-coated nanowires with 15 s integration time. This spectrum shows a broad continuum over all wavenumbers that peaks at about 800 cm^{-1} and almost completely obscures the original GeO_2 spectra. Also shown is the Raman spectrum from an uncoated part of same substrate under identical conditions. From this comparison it is clear that the gold coating is causing the broad background. Although the intensity of the NWs spectra is expected to diminish with Au coating, the source of broad background is not exactly known.

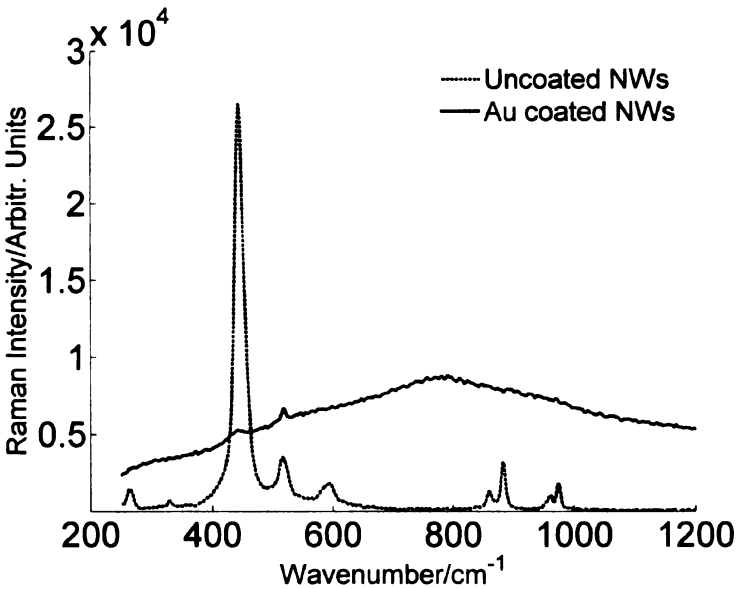

Figure 4-35. Raman spectra of 21 nm Au coated GeO_2 NWs, t_{acc}=15 s. Also shown are spectra for uncoated NWs.

Very similar broad continuum was observed from other locations of the coated area and for different substrates. For example, **Figure 4-36** shows the Raman spectra from a GeO_2 NW substrate before and after coating it with a 15 nm thick Au film and the same broad background appears after coating. The introduction of this continuum in the Raman spectrum was very puzzling since it usually arises due to fluorescence, but it is known that fluorescence is quenched in the vicinity of metal. However, what is observed is something similar to florescence introduced by the metal or the deposition process. Some potential sources of the broad background were hypothesized as impurities in the deposition process, impurity in metal source material, and moisture on the substrates. A systematic study was done to confirm or eliminate each of these potential sources.

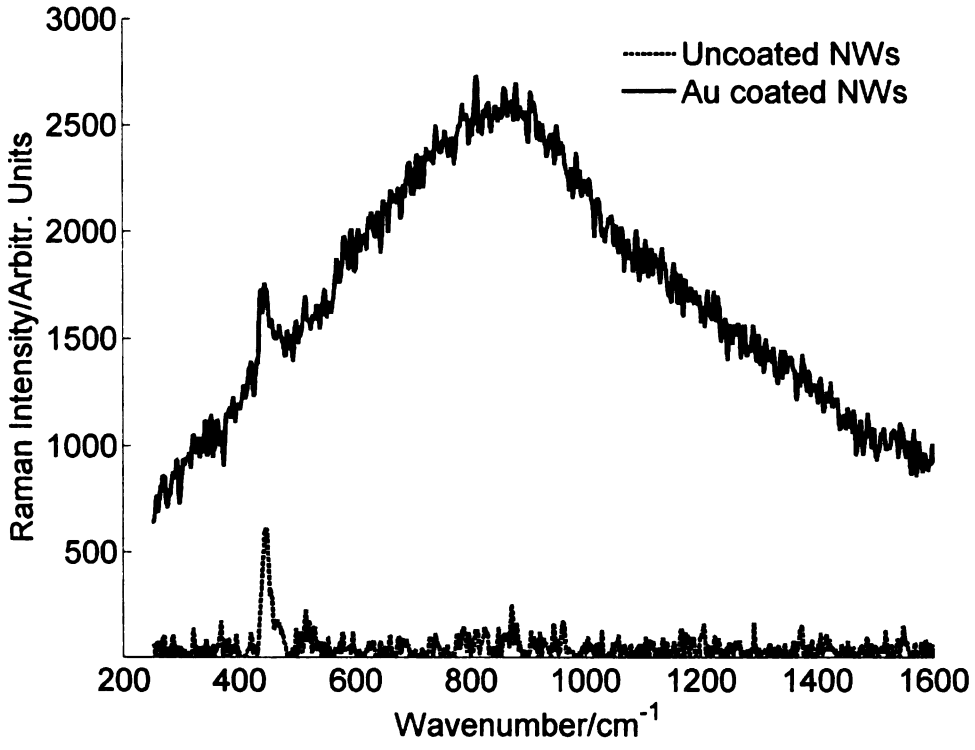

Figure 4-36. Raman spectra of 15 nm Au coated GeO_2 NWs, t_{acc}=5 s. Also shown is the spectra for uncoated NWs.

The first step towards isolating the source of the broad background is an understanding of how the gold film affects the Raman spectra of a reference material like silicon. For this purpose, a bare silicon wafer was sputter coated with ~21 nm thickness of gold by the same sputter coating process. **Figure 4-37** shows the effect of gold coating on the Raman spectra of a bare Si(100) wafer acquired at 785 nm laser excitation with 5 s integration time. The bare wafer spectra shows a strong Si peak at 520 cm^{-1} and a characteristic broad fluorescence background towards higher wavenumbers (beyond 1200 cm^{-1}). The intensity of the characteristic peak at 520 cm^{-1} is reduced by more than 75% with gold coating. An even more striking effect of gold coating is the almost complete elimination of the Si fluorescent tail. This is expected, as the metal tends to quench fluorescence and shows that the sputter gold coating process is not a likely source for the introduction of broad continuum seen in the Raman spectra of gold-coated nanowires.

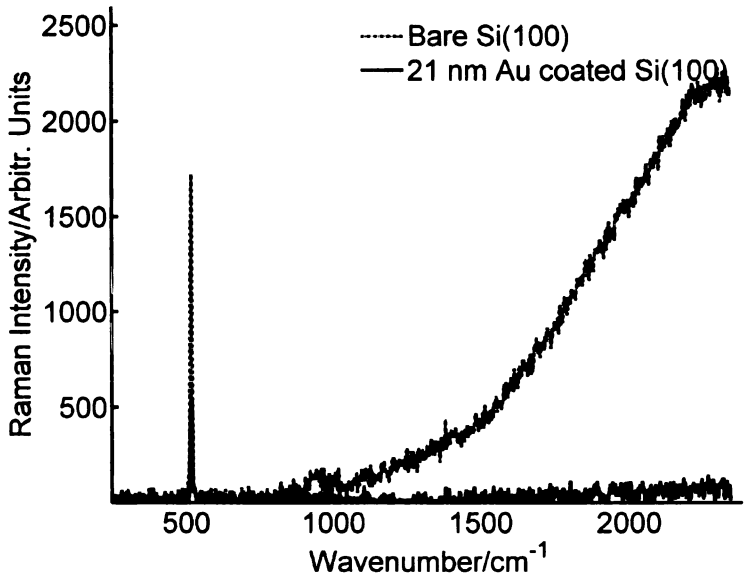

Figure 4-37. Raman spectra for bare silicon wafer and after coating with ~21nm gold.

A further insight into the impact of gold-coating on substrate can be achieved by studying the effect of Au thickness on the Raman spectra of Si. Four Si(100) wafers were coated with gold films having thickness from 5 – 20 nm. Raman spectra from these gold coated wafers was acquired under the same experimental conditions and the intensity of the main Raman peak was used to compare the effect of gold thickness. **Figure 4-38** shows the variation of the 520 cm^{-1} Raman peak of Si as the Au film thickness increases from 5 nm to 20 nm. As expected the Raman intensity decreases with increasing Au thickness due to the attenuation affect. This further confirms that a smooth metal coating attenuates the Raman signal from underlying substrate.

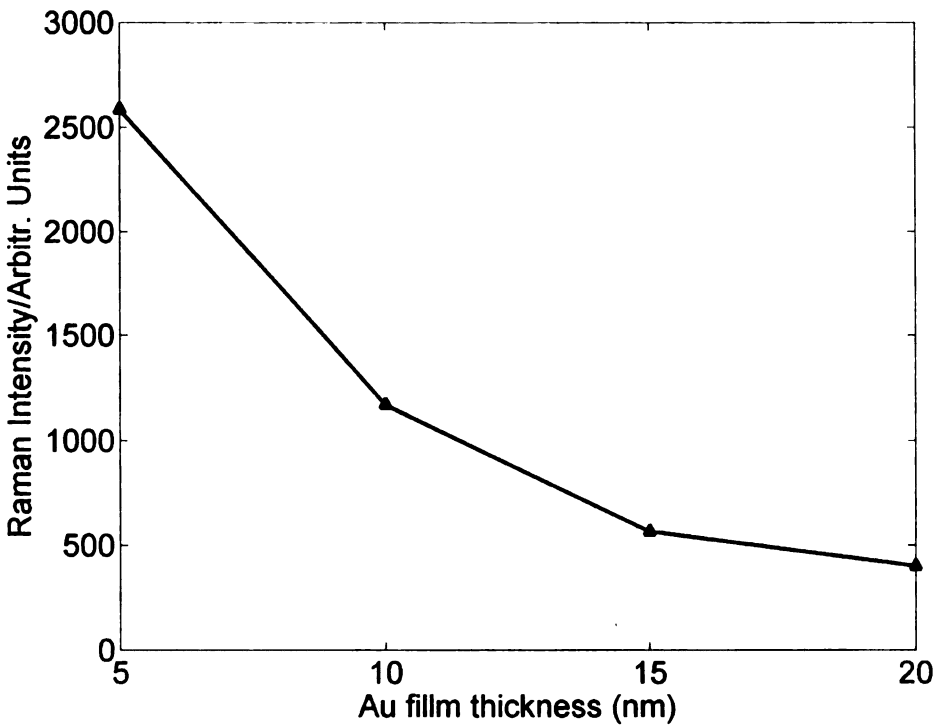

Figure 4-38. Variation of 520 cm^{-1} Raman peak intensity with Au film thickness.

A supplemental study was done to verify deposition process purity by using a much cleaner e-beam evaporation with new gold source material. The nanowire substrates were loaded in the deposition chamber that was evacuated to $5x10^{-6}$ Torr. The substrate was set to continuous rotation and 10 nm gold was deposited using e-beam evaporator as measured by a quartz crystal monitor (QCM). The Raman spectra from the e-beam deposited Au coated substrate is shown in **Figure 4-39** and once again the impact of the gold coating is evident as a strong continuous background that peaks in the 800-1000 cm^{-1} region of spectrum. This experiment confirms that the source of background does not relate to the impurities in the coating process or source of the metal.

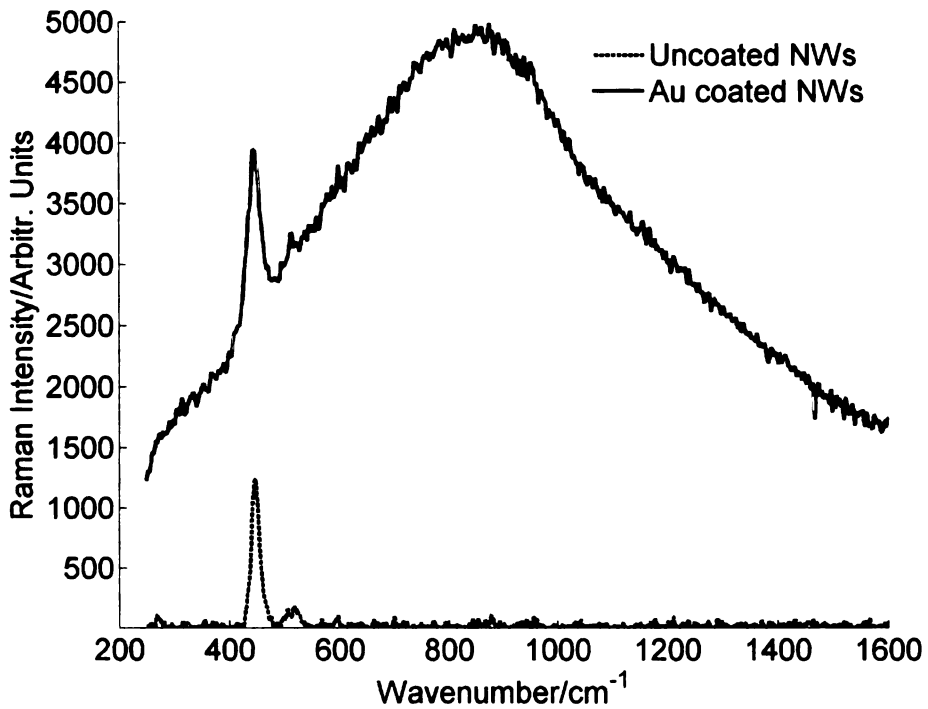

Figure 4-39. Raman spectra of 10nm e-beam high purity gold coated GeO_2 nanowires, t_{acc}=5 s. Also shown is the spectra from an uncoated part of the sample.

The GeO_2 is known to absorb moisture from environment and the gold coating might trap it under the metal. Although water is a weak Raman scatterer, the presence of gold can enhance its signature and contribute to the broad background observed after gold coating. To eliminate the influence of adsorbed moisture, the samples coated with 21 nm gold were stored in desiccator for 36 hrs and then analyzed with the Raman system. **Figure 4-40** shows 10 spectra obtained from the same spot on the sample with 5 s signal integration and 10 s delay between two acquisitions. No significant change in shape or intensity of the broad continuum is found after drying of the samples and suggests that moisture is not causing it.

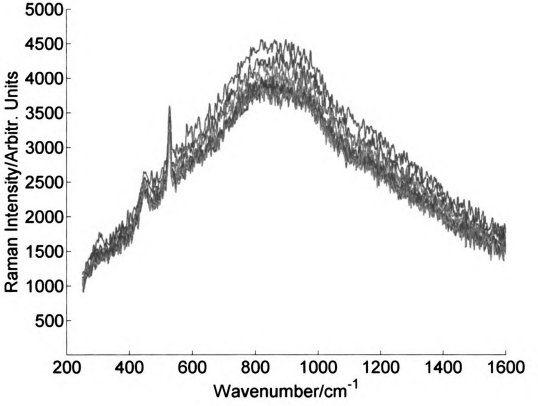

Figure 4-40. Successive Raman spectra from same point on sample for 21 nm Au coated GeO_2 NW sample dried in a desiccator for 36 hr.

As a last step in the investigation of background continuum, the sample was heated *in situ* to burn off or drive out any contaminant that might be causing observed fluorescence and then observe any change in its Raman spectrum. This was done by placing sample on top of a resistive button heater and monitoring the temperature by a K-type thermocouple. **Figure 4-41** shows the Raman spectra of ~21 nm gold coated GeO_2 nanowires heated to 146 °C. For comparison, the room temperature spectra is also shown as a dotted line in **Figure 4-41**. No significant change due to heating of sample is observed. It is therefore, concluded that the broad background introduced is caused only by the presence of gold coating rather than any contaminant or moisture effect. The exact cause of this broad continuum is not fully understood yet. It is a common observation that the molecular SERS spectrum is accompanied by a broad background covering most of the normal 0-3000 cm^{-1} range[73]. Some researchers attribute it to electronic Raman scattering from metal[116, 117] while others consider it luminescence[118]. In our case, the broad background appears following the metal coating of nanowire substrate. Since the background continuum is present even before the application of analyte molecule, the most probable cause of the continuum is the electron scattering off defects from rough gold film covering the nanowires that allows for electronic Raman scattering over a broad energy range[39]. Further understanding of the broad continuum is of interest, however for the purpose of detection measurements it can be removed through a baseline correction.

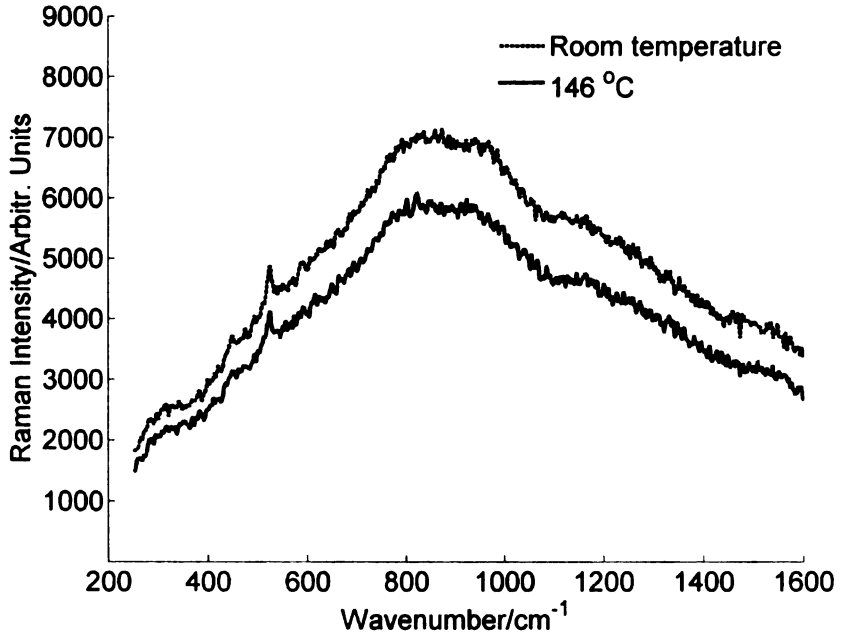

Figure 4-41. Effect of ~21nm gold coated GeO_2 nanowires at 146 °C, t_{acc}=5 s. Insert shows room temperature Raman spectra.

TEM studies of gold-coated NWs were also carried out to investigate the morphology of the Au coating. The e-beam deposition of Au on the NW covered substrate was done at room temperature without any subsequent annealing. **Figure 4-42** shows the TEM image of GeO_2 NWs broken off from Au coated Si substrate and clearly confirms that the Au does not wet the NW but forms 3D islands. It is known that mid-to-late transition and noble metals do not generally wet oxide surfaces, but make particles that only cover a fraction of the surface[119]. Similar 3D islands of thermally evaporated Au on TiO_2 at room temperature have been previously observed[120]. Also only the side of NW facing the incident Au source vapor is being coated. Most of the NWs showed similar wetting pattern with some variation in density and size distribution (typically 2-10 nm) of Au islands. This type of metal island formation during low temperature deposition

has been explained using an island growth model in which kinetic effects dominate and a large density of smaller Au islands are nucleated[120, 121]. The shadowing effects can also supplement anisotropic growth of 3D islands since the nanowires are oriented at random angle with respect to the incident vapor[36].

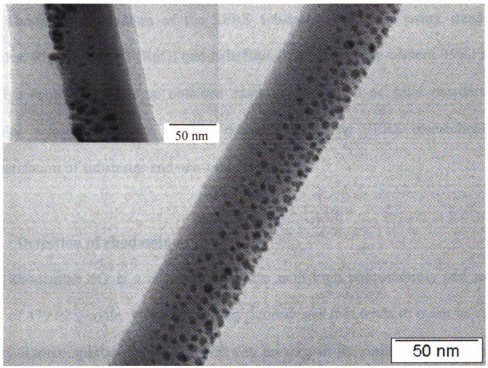

Figure 4-42. TEM image of 21 nm Au coated GeO_2 NW. Insert shows another NW with larger Au particles.

4.5 Evaluation of SERS substrate

SERS evaluation of GeO_2 NWs was done using different analytes including Rhodamine 6G, Nile Blue, 4-methylbenzenthiol, 1,2-benzenedithiol and trans-1,2-bis(4-pyridyl)ethylene. These analytes are the one commonly employed for evaluating SERS substrates and can be broadly categorized into two groups – (a) Dye molecules like R6G

and nile blue, and (b) Thiol molecules like MBT and BDT that form self assembled monolayers on noble metals. SERS results for GeO_2 NWs substrates using these two analyte groups are presented in the following section.

4.5.1 SERS of rhodamine and nile blue

The initial evaluation of the SERS substrates was done using standard dye molecules. Rhodamine 6G (R6G) and Nile Blue (NB). R6G (dye content 95%) and Nile blue (dye content 80%) were obtained from Sigam-Adrich as solid powders. These molecules were chosen due to their common usage by SERS researchers in the characterization of substrates and non-toxic nature.

4.5.1.1 Detection of rhodamine

Rhodamine 6G is a common laser dye with high photostability and molecular weight of 479.02 g/mole. It exhibits strong fluorescence that tends to mask its spectra in ordinary Raman spectroscopy[122]. This can be seen in the ordinary Raman spectra of R6G as shown in **Figure 4-43**. Here one can see the Raman peaks of R6G background at 1178 cm^{-1} (C—H in-plane bending), 1304 cm^{-1} (C—O— C stretching), and 1360 cm^{-1} and 1513 cm^{-1} (C—C stretching of aromatic ring) on the top of strong florescence background[123]. The fluorescence is expected to be quenched in SERS spectra due to presence of metal in the vicinity of analyte that provides a fast path for transfer of energy between substrate and molecule[122].

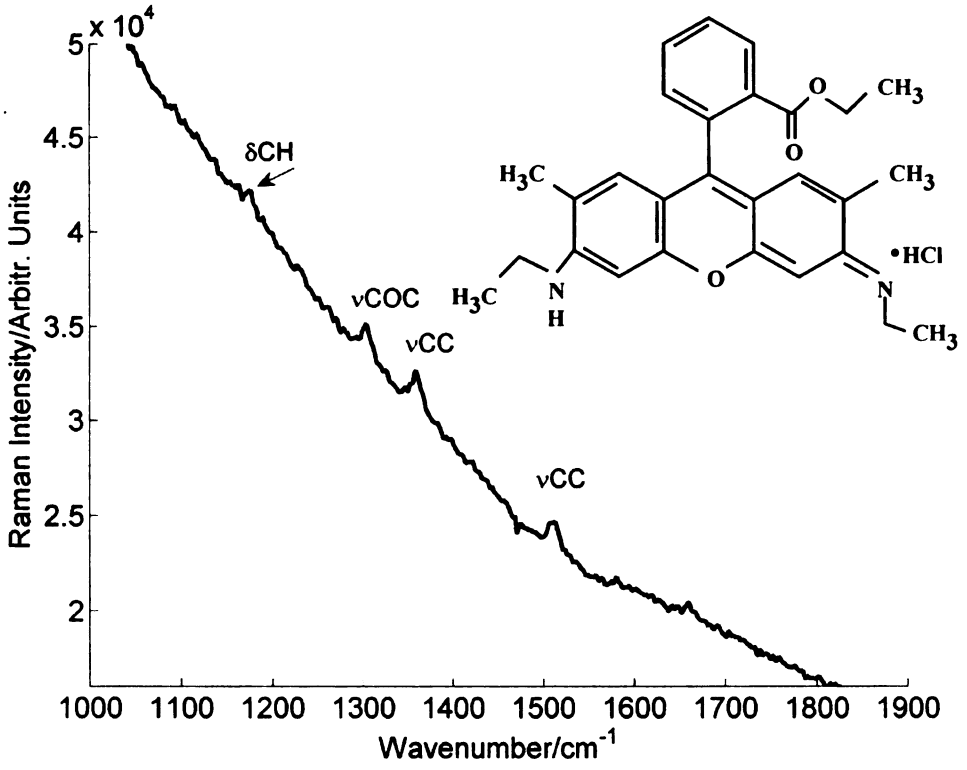

Figure 4-43. Chemical structure and ordinary Raman spectra of R6G with 785 nm excitation.

For SERS studies, R6G was dissolved in DI water and the stock solution was diluted to a concentration of 3 micromoles (μM). Care had to be taken to store the prepared solution in plastic bottles as R6G has tendency to stick to glass. About 200 μL diluted solution was applied to the substrate using plastic pipette but it was found to form a drop on the substrate rather than wetting it. So the substrate was soaked in solution for 10-15 min and then allowed to dry at room temperature. Raman spectra were collected from different parts of the substrate and very few sites yielded discernable spectra of R6G. **Figure 4-44** shows Raman spectra of a 2 μM R6G in DI water from one of the active sites. It can be seen that the R6G spectra rides on a slowly varying broad

background that was observed after gold coating of nanowires. The dotted gray line shows the Raman spectrum of a bulk 2 μM R6G solution, not placed on the SERS substrate, and obtained under same conditions. The bulk solution spectrum does not yield any discernable peaks and this confirms the enhancement is due to gold-coated nanowires. However, the enhancement is from isolated locations only.

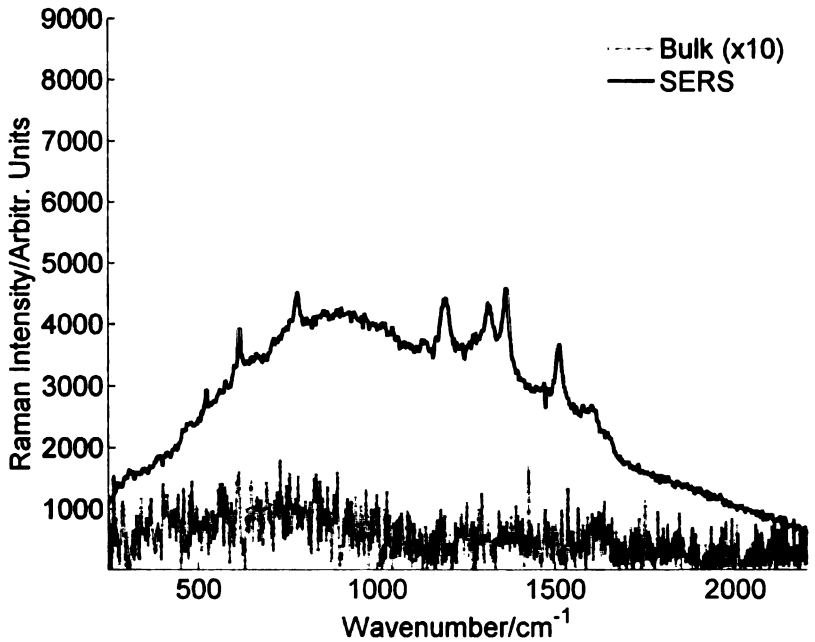

Figure 4-44. Raman spectra of 2μM R6G in DI water for 14nm gold coated GeO_2 nanowires. Bulk solution spectrum of same concentration is also shown, t_{acc}=15 s. Bulk spectrum is ×10 times the value to show features.

To avoid the problem of substrate wetting, ethanol was used as solvent instead of DI in the rest of this study. The use of ethanol as a solvent also helps in preventing the dissolution of GeO_2 nanowires which would occur if water is used as the solvent. The

R6G was dissolved in ethanol (95%) and diluted successively to obtain a concentration of 3 μM. The Raman spectra of the prepared concentration in liquid form did not yield any discernable spectrum. A small drop of the liquid (~250 μL) was applied to the substrate using plastic pipette and allowed to dry under ambient conditions. Again the Raman signal was observed from few isolated spots and **Figure 4-45** shows spectra from one such spot. The bulk solution (insert of **Figure 4-45**) yields only ethanol spectra but the R6G peaks are clearly visible in the enhanced spectra from gold-coated GeO_2 nanowire substrate.

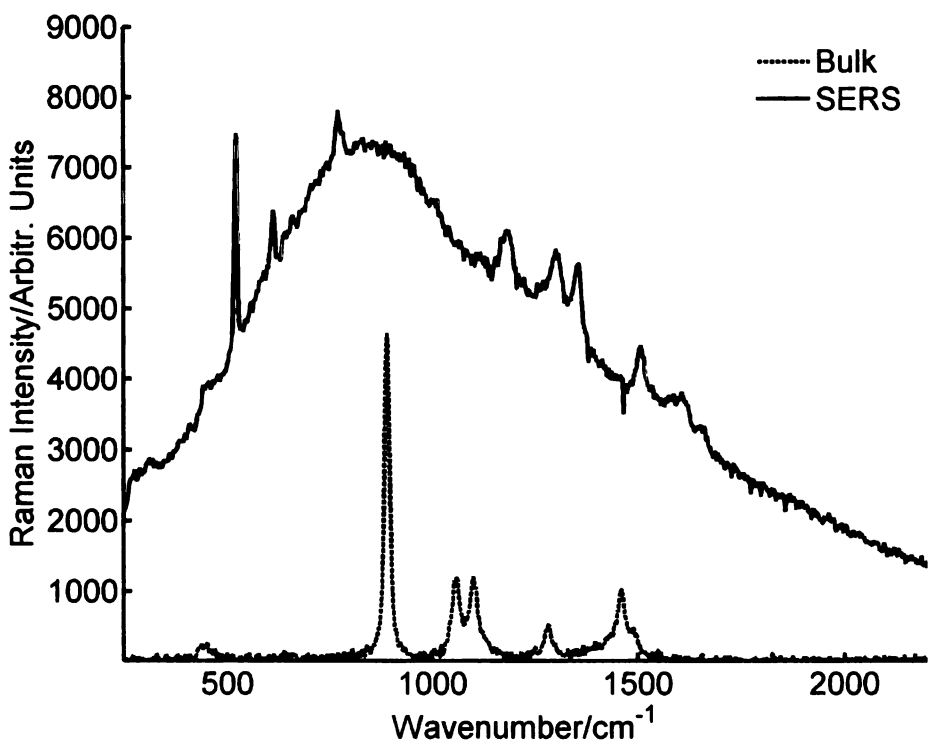

Figure 4-45. Raman spectra of 3 μM R6G in ethanol for 21 nm gold coated GeO_2 nanowires. Also shown is the ordinary Raman spectra of 3 μM ethanolic R6G bulk solution, t_{acc}=15 s.

4.5.1.2 Detection of R6G using Au nanoparticles decorated nanowires

To study and compare the effect of gold colloid versus gold film on nanowires substrates, theGeO_2 nanowires were decorated with gold colloidal. A drop of ~300 μL of 60 nm gold colloidal suspension (from Alfa Aesar) in water was added to the substrate and allowed to dry. The 3 μM ethanolic solution of R6G was also drop coated to the substrate. The enhanced Raman signal can be detected at isolated spots from the substrate as shown in **Figure 4-46** with a characteristic broad background. However, most areas of the substrate just showed the spectra of GeO_2.

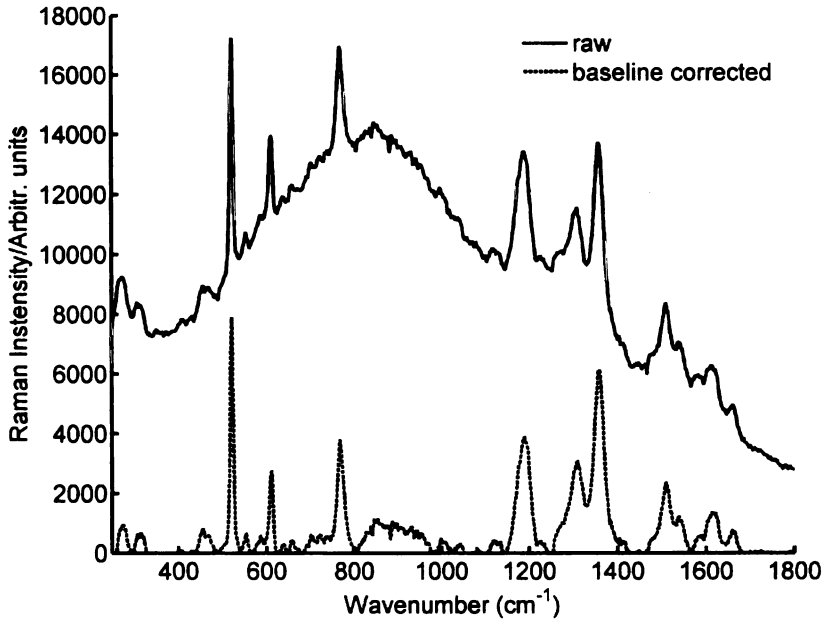

Figure 4-46. Raman spectra of 3 μM R6G in ethanol from GeO_2 nanowire substrate decorated with 60 nm gold colloidal. Also shown is the baseline corrected spectra, t_{acc}= 15 s.

The broad background was subtracted from the spectra using baseline correction feature of the Raman system software as shown in **Figure 4-46**. This feature of the

software takes up to 20 user defined points on x-axis that should have zero Raman intensity and then fits a curve through these points to determine background signal. This background signal is then subtracted from the Raman spectra to yield background free signal. The technique does require few iterations and fine-tuning of parameters before yielding an acceptable background free spectra.

4.5.1.3 Detection of nile blue

Nile blue A is a common stain used in biology and fluorescence studies. It has molecular weight of 732.85 g/mole. **Figure 4-47** shows the reference Raman spectra of nile blue (NB) recorded with 531 nm laser excitation after removal of fluorescence background[124]. The NB molecule has 126 normal modes but most of the Raman intensity is contained in seven modes at 590, 1141m 1351, 1429, 1492, 1544, and 1640 cm^{-1}[124]. The main peaks in the spectrum are the 590 and 1640 cm^{-1} modes corresponding to ring breathing and ethylenic-stretching motions respectively. For SERS studies, a 2.73 μM solution was prepared by dissolving measured amount of NB in 95% ethanol and successively diluting the solution until desired concentration was achieved. About 250 μL of this ethanolic NB solution was placed on the GeO_2 nanowire substrate that had been sputter coated with 21 nm gold film and allowed to dry. The Raman spectra of the NB from the gold coated nanowire substrate is shown in **Figure 4-48** with all the major peaks of NB clearly visible. The insert gives the Raman spectra recorded for the 2.73 μM ethanolic NB from bulk solution under similar experimental conditions and all that can be observed are the ethanol peaks with NB signal buried below the noise line. On the other hand, the strong SERS enhancement form gold-coated nanowires makes all

main peaks of NB clearly visible while quenching the fluorescence. **Figure 4-49** shows SERS spectra of NB from different arbitrarily selected points on the substrate and main peaks are clearly visible. However, the enhancement was found to be location dependent with some locations yielding low or no enhancement.

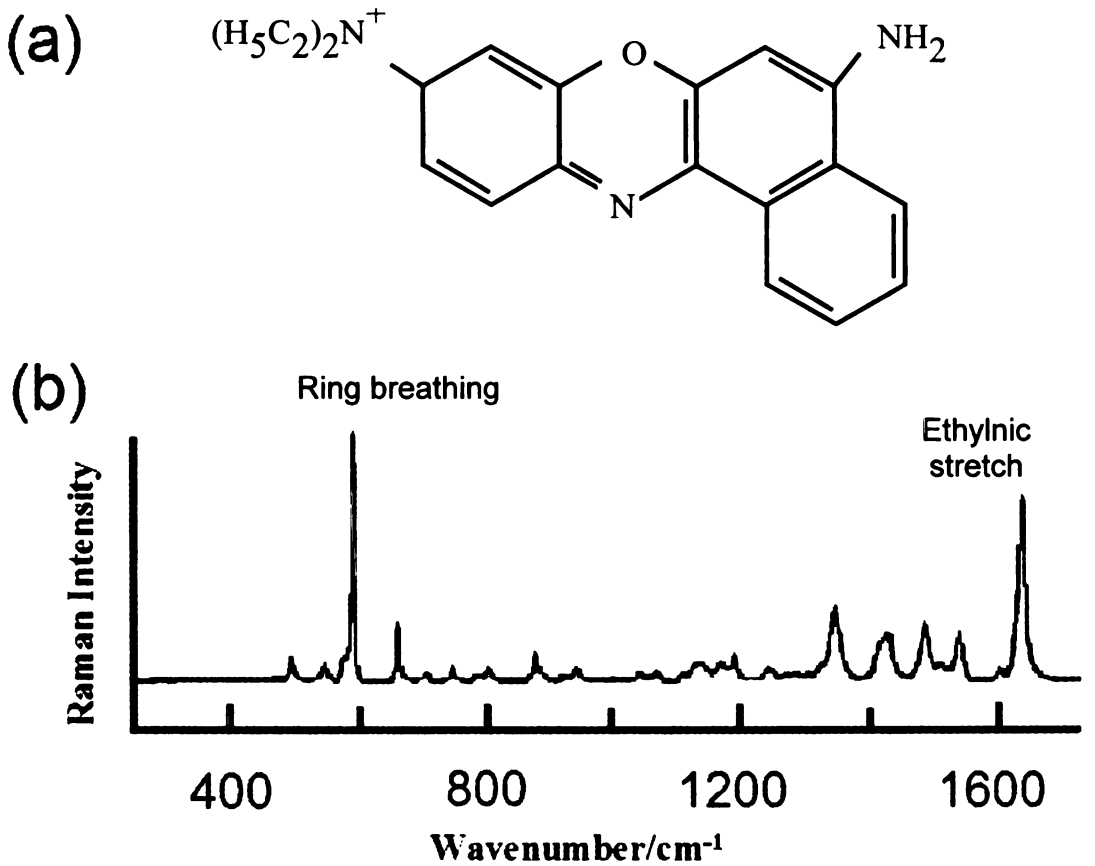

Figure 4-47. (a) Nile blue molecular structure. SERS spectra of NB with 531 nm excitation[124].

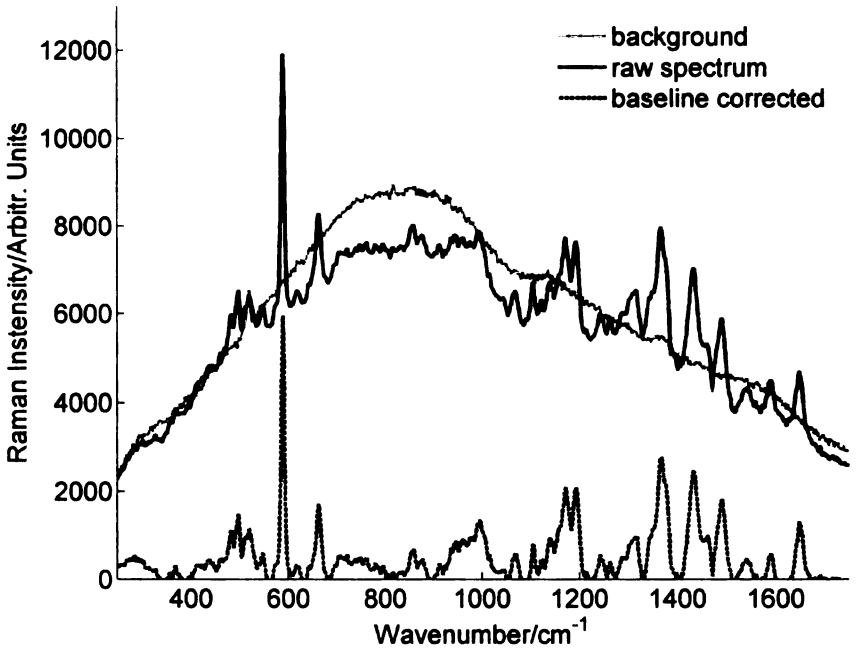

Figure 4-48. SERS spectra of 21 nm Au film coated GeO_2 NWs before and after application of 2 μL of 10 μM NB, t_{acc}= 15 s. Baseline corrected spectra of NB is also shown.

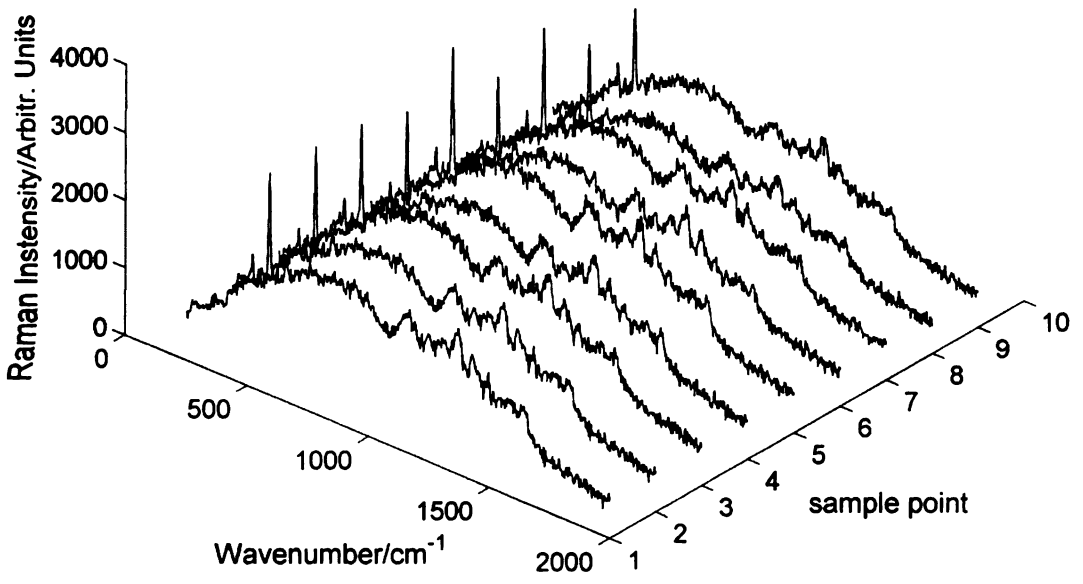

Figure 4-49. SERS spectra from 2 μL of 10 μM ethanolic NB along a line from GeO_2 NWs, t_{acc}= 5 s.

4.5.1.4 Detection of nile blue using silver coated nanowires

Silver is another coinage metal that shows strong Raman activity due to excitation of surface plasmons in the visible region of spectrum. Although gold is a better choice for SERS due to its chemical inertness, silver coating of NWs was also studied since it exhibits strong SERS due to its capability to support surface plasmons in optical spectrum. GeO_2 nanowires synthesized on Si were coated with a 15 nm silver film using e-beam evaporation and continuous substrate rotation. The coated substrates were characterized by the same Raman system as shown in **Figure 4-50**.

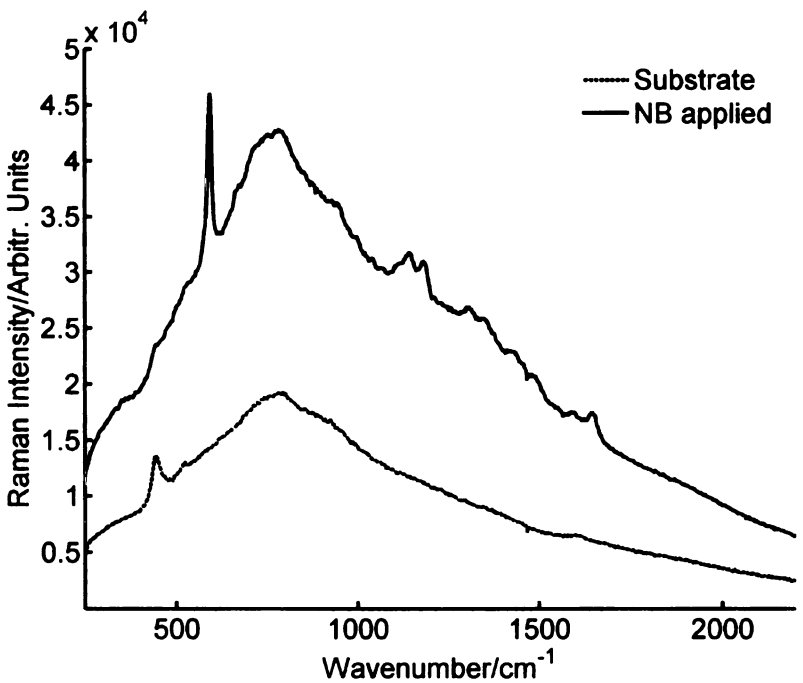

Figure 4-50. Raman spectrum of spectra of 15 nm Ag coated GeO_2 nanowire substrate before and after applying 2.73 μM Nile blue in ethanol, t_{acc}= 5 s.

Similar to the case of gold coating, the silver coating has also introduced a strong and broad background that peaks near 800 cm^{-1}. Next a drop of 2.73 μM NB in ethanol is applied to the substrate and allowed to dry at room temperature. **Figure 4-50** gives the Raman spectra of substrate after drying of NB. As can be seen, the main peak of NB at 592 cm^{-1} is clearly identifiable whereas the remaining peaks show up as weak peaks on the top of broad background.

The initial evaluation of substrates using R6G and NB as probe molecules provided evidence of strong enhancement, sufficient to easily detect μM concentrations of the two species. On the other hand, no discernable Raman spectra could be obtained from bulk solutions at these concentrations. This clearly confirms the SERS from nanowires; however only at a few isolated locations. Although there is a high density of the NWs on the substrate only a few "hot spots", where significant SERS could be measured, were found. It was thus speculated that the cause lies in inadequate adsorption of the analytes on the NWs substrates. It is known that the SERS effect diminishes within a few nm away from the active metal surface[39]. To test this hypothesis, the thiol based probe molecules were investigated which are known to form self-assembled monolayers on gold.

4.5.2 SERS of thiols

Thiols are chemical compound that contain a functional group composed of a sulfur atom and a hydrogen atom. The aromatic thiols are special class of thiols that contain an aromatic hydrocarbon (benzene ring) and are commonly employed in SERS studies due to their ability to form self-assembled monolayers on noble metals. This

allows for relatively simple evaluation of the SERS performance of substrates based on knowledge of the number of molecules contributing to the SERS signal. Two aromatic thiols 4-methylbenzenthiol (purity 98%) and 1,2-benzenedithiol (purity 96%) and one non-thiol analyte trans-1,2-bis(4-pyridyl)ethylene (purity 98%) were purchased from Sigma-Aldrich and used without further purification. **Figure 4-51** shows the molecular structure of analyte molecules used in this study. The diluted solutions with various concentrations were prepared in methanol (99.8% HPLC grade).

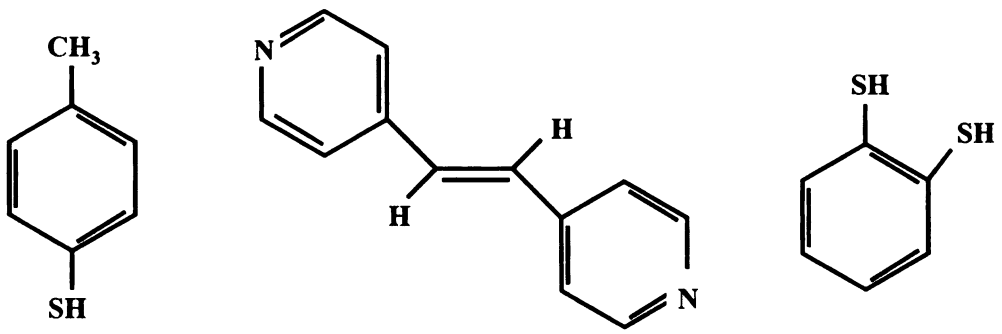

4-methylbenzenethiol **1,2-bis(4-pyridyl)ethylene** **1,2-benzenedithiol**

Figure 4-51. Chemical structures Raman ethylene analytes.

4.5.2.1 SERS dependence on Au thickness

The NWs were coated with a SERS active metal such as gold to provide a surface plasmon active surface. The thickness of the metal layer is expected to affect the SERS performance of the substrate. The effect of metal thickness was studied by coating different parts of the same NWs substrate with different gold thickness. The 4-MBT was used as target molecule to study the effect of gold thickness since these aromatic thiols are known to form self-assembled monolayers (SAMs) on gold, silver, and copper[125].

The SAM was prepared on the substrate by soaking it in 1 mM methanolic 4-MBT solution for 14 hrs. The substrate was then rinse in methanol and dried by blowing air. **Figure 4-52** shows SERS spectra from substrate for 4 different thickness of Au film. It is evident that strong enhancement with moderate background continuum is achieved for ~10-20 nm thick Au coatings.

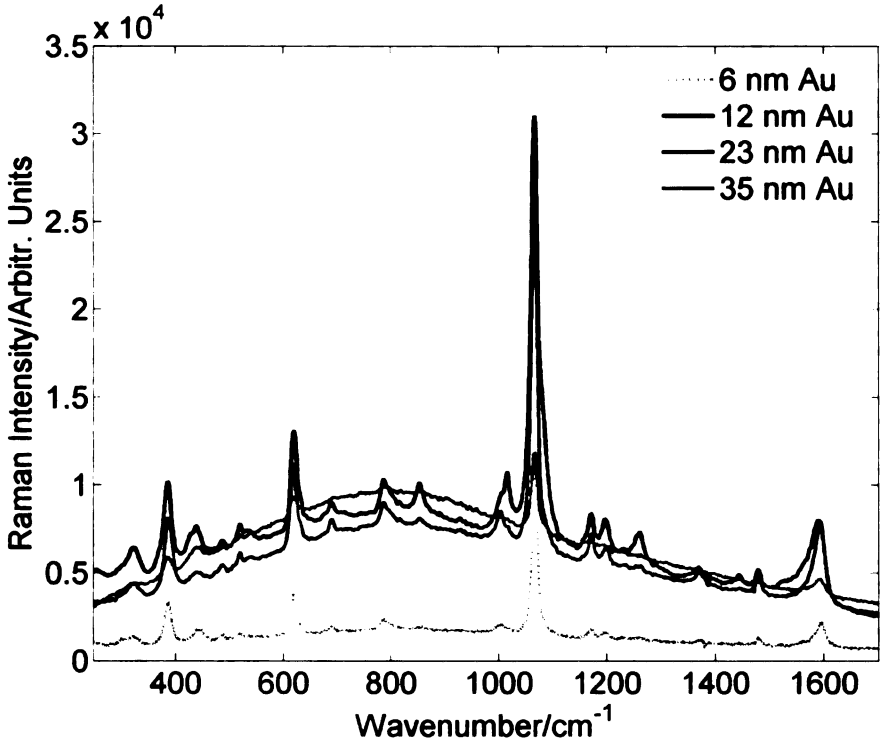

Figure 4-52. Effect of Au thickness on SERS spectra.

To assist in a generalized conclusion of the effect of Au coating thickness on SERS enhancement, a different analyte was also investigated. In this case, the substrate was soaked in 1 mM methanolic 1,2-BDT solution for 20 min to form a SAM. The substrate had been coated with 3 different Au film thickness in three different areas of the same nanowire coated substrate. This ensured that all experimental variables were the

same for the synthesis of NWs. The substrate was rinsed with methanol and dried before acquiring the spectra. **Figure 4-53** shows the SERS spectra of a SAM of 1,2-BDT from three different Au coated NWs. Again good enhancement above a broad background continuum can be found for Au films having thickness of 10-20 nm.

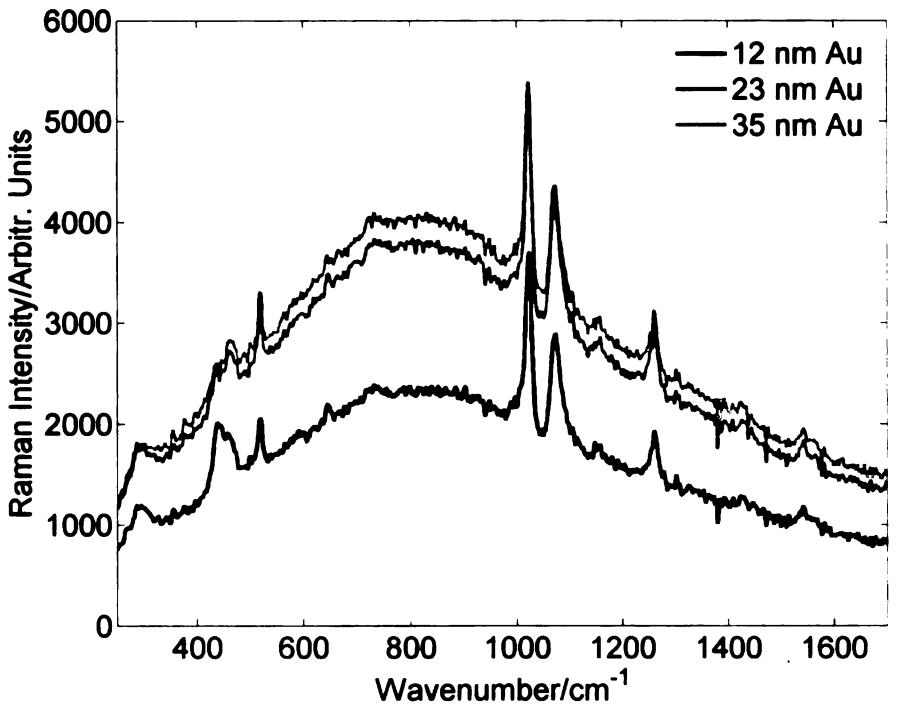

Figure 4-53. SERS from 1mM BDT for 20 min soak.

It is also important to study the affect of the age of the Au coating on SERS performance of the substrate to assess deterioration over time. Storage of samples in open environment can degrade their SERS activity due to contaminations on the Au coating. The nanowire substrate was coated with gold and stored for 10 days in a petri dish at ambient conditions. Subsequently the SAM of 4-MBT was synthesized as discussed earlier. **Figure 4-54** shows the effect of Au coating aging on SERS spectra for a

monolayer of 4-MBT. It can be seen that the 10 days old Au coating exhibit a lower signal strength as compared to corresponding fresh coating. This can be attributed to contamination, which reduces the monolayer coverage of analyte. It had been reported that the aged gold films do not produce as strong enhancement as fresh films due to contamination of films during storage.

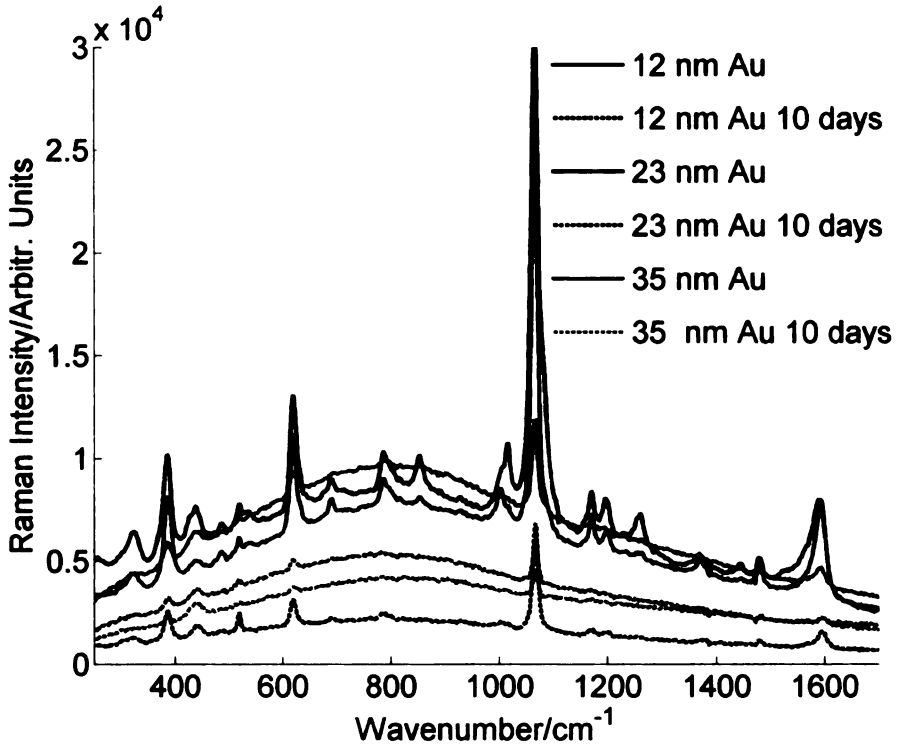

Figure 4-54. Effect of gold coating age on SERS from 1mM MBT.

Another important aspect in the SERS study of any substrate is the affect of application of the analyte to the SERS substrate. A commonly employed technique is the application of a solution containing the analyte to the substrate. The drying of the solvent creates strong surface tension forces on the nanostructures such as NWs. The resulting stresses can change the morphology of the substrate as shown in **Figure 4-55**. Here the

substrate has been soaked in 1 mM methanolic MBT for 12 hr, then rinsed in methanol and blown dry. The clustering of NWs due to solvent evaporation is clearly noticeable.

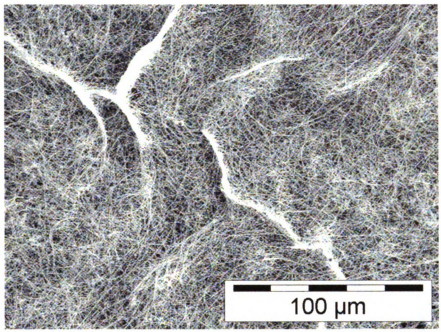

Figure 4-55. SEM image of GeO_2 NW substrate after 12 hr soak in 1mM MBT.

The qualitative SERS study of gold coated GeO_2 nanowire substrate presented in this section shows that the thiols can be used to carry out detailed quantitative assessment of these substrates. This includes the study of reproducibility of the SERS and calculation of SERS enhancement factor as discussed in the following section.

4.5.2.2 Detection of 4-methlybenzenethiol

The 4-MBT belongs to para-distributed benzene class of chemicals with D_{2h} symmetry. **Figure 4-56** shows the chemical structure and ordinary Raman (OR) spectrum

of 4-MBT. It can form SAM on gold by forming S-Au bond after loss of hydrogen. The Raman vibrational band ~910 cm^{-1} is assigned to the S-H bond of the molecule and is clearly seen in the OR spectra. However, the same band does not show up in SERS spectra because sulfur atom bonds to the metal surface by giving up the hydrogen atom[126]. Thus the study of the Raman peak corresponding to SH vibrations can be used to determine the type of adsorption of 4-MBT on metal surface.

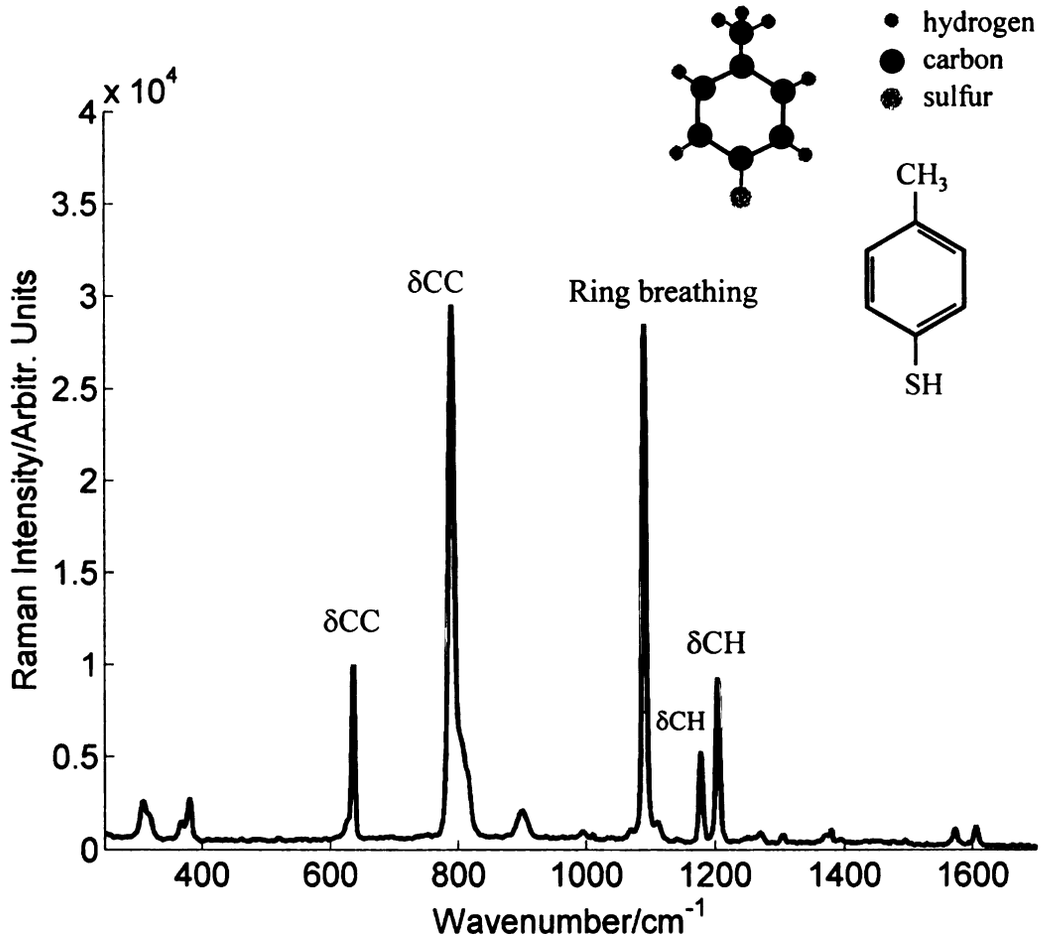

Figure 4-56. Chemical structure and ordinary Raman spectrum of 4-MBT.

The gold-coated GeO_2 nanowire substrate was soaked in 100 μM methanolic 4-MBT solution for 10 hrs. It has been reported that 1mM methanolic 4-MBT forms SAM on gold film after 12 hr of incubation[127]. The concentration used in this study is an order of magnitude smaller than the one used for SAM and is expected to yield sub-monolayer coverage. For conservative estimates of the Raman enhancement factor, a monolayer coverage assumption is used in our calculations. After the 4-MBT soak, the substrate was thoroughly rinsed with methanol to remove multilayers and/or crystals that might have formed[127]. The substrate was dried in the stream of nitrogen before acquiring the SERS spectra shown in **Figure 4-57**(a). SERS spectra does not show the S-H vibrational Raman band at ~916 cm^{-1} confirming the formation of S-Metal bond[128]). An interesting effect is the suppression of continuous background of raw substrate following the formation of the 4-MBT monolayer. **Figure 4-57** (b) shows Raman spectra from five consecutive 250 μm spaced points on the substrate and the characteristic peaks of 4-MBT are easily identifiable. It may be mentioned that no Raman signal was detected from a Si(100) substrate with 21 nm smooth Au film that was soaked in 4-MBT alongside nanowires substrate, confirming the enhancement is indeed from the nanowires. Similarly the bulk solution of 100 μM methanolic 4-MBT only yielded spectra for the methanol solvent.

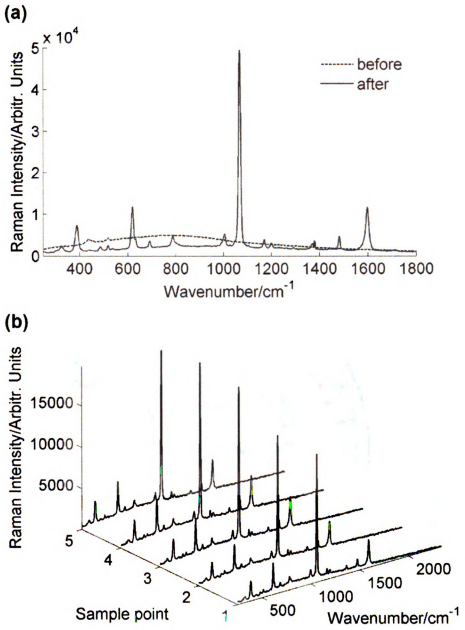

Figure 4-57. (a) SERS spectra of a SAM of 4-MBT. Also shown is the Raman spectra of substrate before formation of SAM, t_{acc}=15 s for both spectra. (b) SERS spectra of a SAM of 4-MBT from 5 adjacent points 250 μm apart, t_{acc}= 5 s.

The homogeneity of the substrate has been a challenging issue for the scientific community in SERS research. To verify the repeatability of SERS measurement from

substrate, SERS spectra were acquired from 100 points covering an area of 1.2 mm × 1.4 mm. The 1068 cm^{-1} Raman band of these spectra is then plotted in **Figure 4-58** to give a spatial map of enhancement from the substrate. It can be seen that the substrate provides unambiguous and uniform SERS spectra for a monolayer of analyte over the tested area with a standard deviation of approximately 20% from the mean.

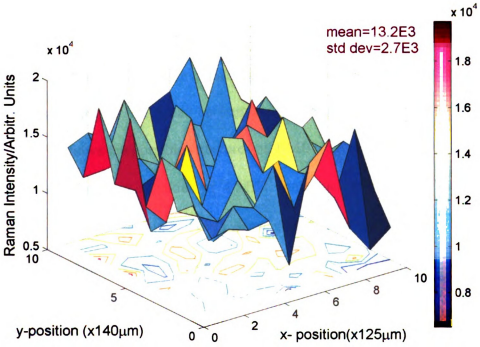

Figure 4-58. 4-MBT 1068 cm^{-1} Raman peak intensity distribution for randomly chosen area on substrate, t_{acc}= 5 s.

The experimental Raman enhancement factor (*EF*) for our substrate was calculated using the standard equation[129]

$$EF = \frac{I_{SERS}}{I_{REF}} \frac{N_{REF}}{N_{SERS}} \qquad (4.7)$$

where I_{SERS} is the Raman intensity of some specific band from the analyte adsorbed on SERS active substrate and I_{ref} is the Raman intensity of the same band from the bulk analyte. N_{SERS} and N_{ref} are the number of molecules that yield I_{SERS} and I_{ref} respectively. Thus equation (4.7) gives the Raman enhancement per molecule for a specific vibrational band of analyte. The specific band is usually the one that gives the strongest Raman scattering and its intensity is directly read from SERS spectra. An obvious choice therefore in our case is the 1068 cm^{-1} Raman band and we utilize the average intensity from 100 sample points in equation (4.7). The number of 4-MBT molecules contributing to SERS can be estimated from the surface density of SAM on Au. **Figure 4-59** shows the possible structures of 4-MBT SAM on Au(100) surface[130]. The corresponding surface densities of 4-MBT molecules are 3.5×10^{14} and 4.6×10^{14} molecules /cm^2 for $4\times\sqrt{3}$ and $2\sqrt{3}\times\sqrt{3}$ respectively. Seo *et al.* estimated surface concentration of 4-MBT as 4.5×10^{14} molecules /cm^2 on Au(111)[130].

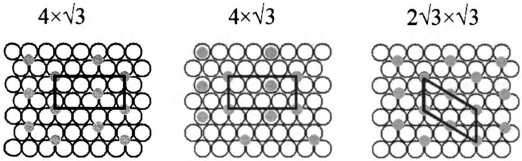

Figure 4-59. Possible structures of 4-MBT SAM on Au(111)[130]. Open circles are gold atoms and solid circles represent sulfur head group of 4-MBT.

Taking 4.5×10^{14} molecules/cm^2 for a monolayer of 4-MBT on gold, we find approximately 5.87×10^{-14} moles (3.53×10^{10} molecules) of 4-MBT are exited in the laser spot (100 μm diameter). The determination of N_{ref} is more challenging and different methodologies have been reported to estimate it. Ideally the reference I_{ref} and N_{ref} may be obtained by recording the Raman signal from a flat metal coated part of the same substrate; however it is very challenging to get ordinary Raman spectra for a monolayer of analyte. Even such an arrangement does not yield true ordinary spectra due to the presence of metal in the vicinity of analyte[54]. The commonly employed techniques to circumvent this problem are to use solid bulk form or a higher concentration solution of the analyte to get the approximate values of the reference parameters. Both these techniques need an estimate of the laser interaction volume. This can be calculated from laser depth of field considerations. We did not detect any ordinary Raman spectra from ~20 mM 4-MBT methanolic bulk solution. Therefore, we used a solid form of 4-MBT to get values of I_{ref} and N_{ref}. **Figure 4-60** shows the ordinary Raman spectrum of 4-MBT. The number of molecules excited in the solid phase was determined by assuming the excitation volume to be a cylinder of diameter equal to laser spot size and length equal to depth of field. This assumption underestimates the N_{ref} since the actual interaction volume has the shape of a two back-to-back truncated cones with waist diameter equal to the focused laser beam spot size. It is expected to yield a more conservative estimate of *EF*. **Figure 4-61**(a) shows the correction factors for the calculated *EF* if the actual interaction volume of the laser beam is taken into account. A good estimate of depth of field is important for an accurate assessment of *EF*. Many

factors influence the depth of field including laser wavelength and power, numerical aperture and focal length of lens, and type of sample (opaque, transparent or turbid with respect to laser wavelength). However, only sample type is the main variable in present case since all other parameters were kept same while measuring SERS signal from nanowires and bulk sample. The depth of field was determined by moving the laser focus point from under to over-focus on bulk crystal of 4-MBT and noting the 1/2 power points. The measurement of depth of field with 4-MBT bulk crystal ensures a more accurate estimate of number of molecules contributing to Raman signal from bulk sample. **Figure 4-61**(b) shows the intensity variation for two Raman peaks of a 4-MBT crystal as the laser focus was moved from under focus to over focus on the sample. The depth field of view (DFOV) was estimated to be 902 μm for 790 cm^{-1} band and 842 μm for 1090 cm^{-1} peak. A more conservative estimate of 800 μm for DFOV was used in *EF* calculations. Taking the monolayer thickness of 4-MBT as 0.5 nm[127], we get a quick estimate of N_{ref} /N_{SERS} ratio. The estimated enhancement factor was found to be 2.64×10^6. We also calculated I_{ref} and N_{ref} by using polystyrene as a reference whose Raman cross-section can be assumed to be equal to that of 4-MBT[127]. Ordinary Raman spectrum of polystyrene is shown in **Figure 4-60**. Following a similar line of calculations, the *EF* was estimated to be 1.43×10^6. This *EF* is in good agreement with that calculated using bulk solid form of 4-MBT and shows that polystyrene can also be used as reference for 4-MBT enhancement factor calculations. It may be noted that we have used a flat area approximation while determining N_{SERS} in our *EF* calculations. The actual or effective area of the nanowires is somewhat increased (~ 57% for half coated NW) due to their cylindrical nature. However, the effect is not expected to be significant

due to the line of sight deposition of Au that only coats the part of the nanowires facing the evaporation source.

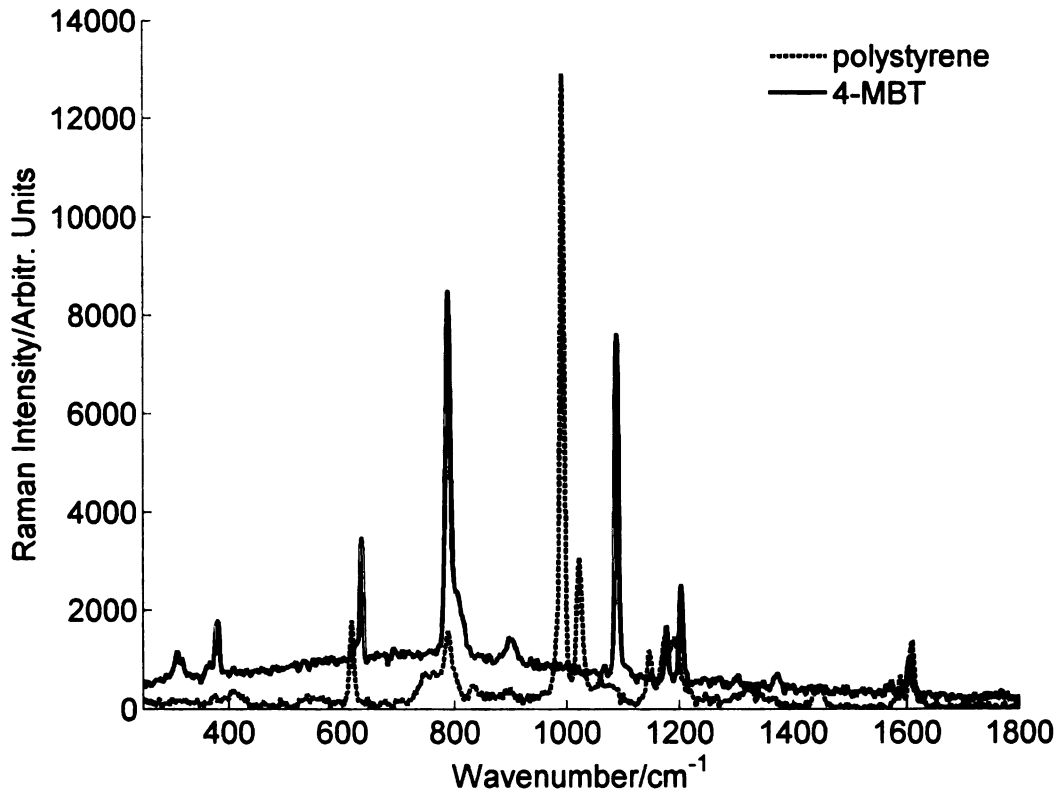

Figure 4-60. Ordinary Raman spectra of 4-MBT and polystyrene, t_{acc}= 5 s.

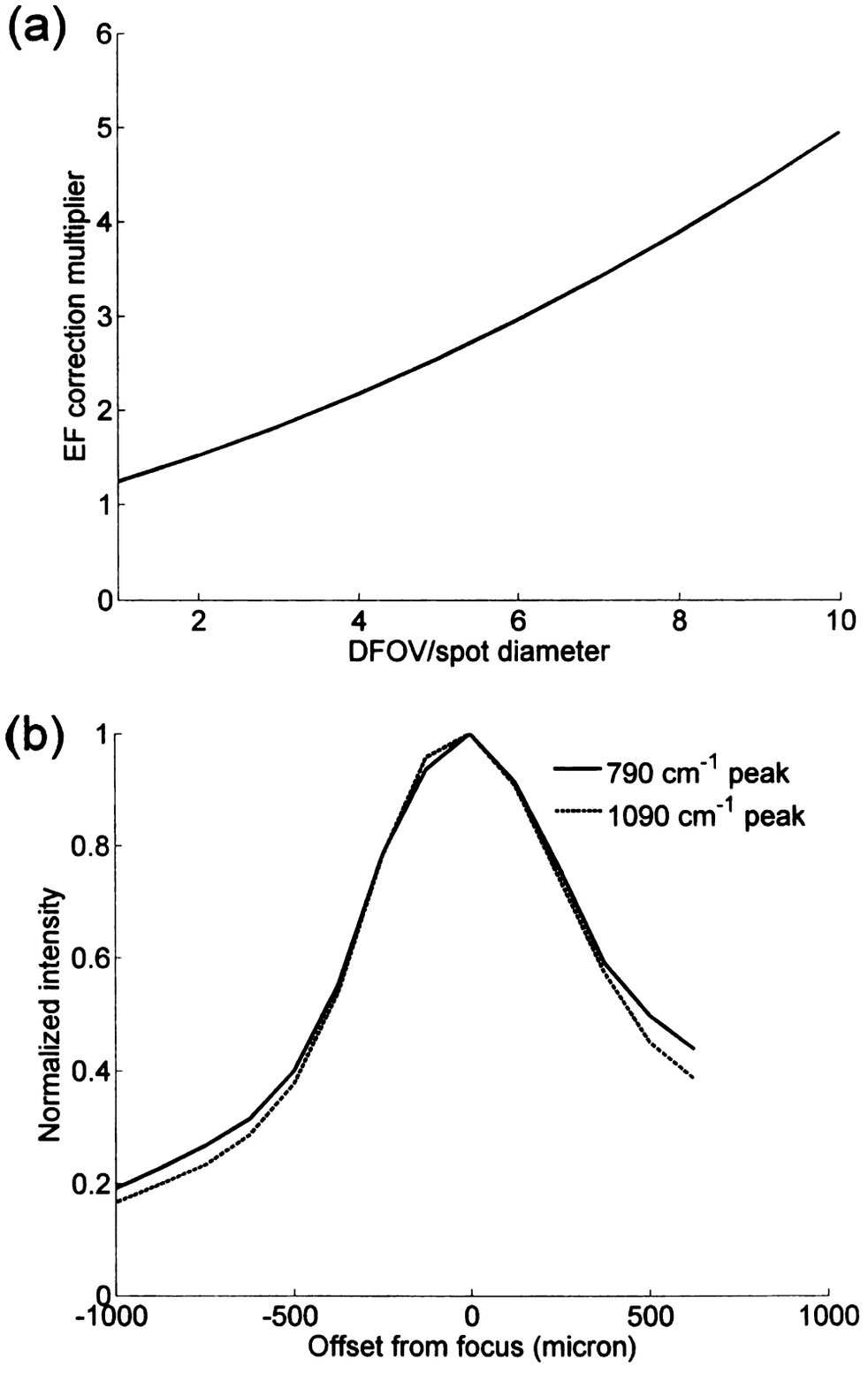

Figure 4-61. (a) EF correction for cylindrical excitation volume assumption. (b) DFOV estimation using two Raman bands of solid 4-MBT crystals.

It is pertinent to compare the *EF* from the nanowire substrate to that of other commonly employed SERS substrates. **Table 4-1** lists *EF* reported in literature for some commonly employed SERS substrates. It can be seen that the SERS EF for nanowires is reasonably placed in the range reported by different researchers. Considering the average enhancement is of the order of 1×10^6, the *EF* for nanowires can be categorized above average.

Table 4-1. SERS EF for common substrates.

Substrate	*EF*	Ref.	Remarks
Au island film	6×10^3	[131]	1064 nm excitation
Au film over Al_2O_3 nanoparticles	2×10^4	[131]	1064 nm excitation
Roughened Au film (peak)	4.3×10^6	[127]	785 nm excitation
Ag film over nanospheres	1×10^7		752.3 nm excitation
Ag nanorods (max)	1×10^8	[36]	785 nm excitation
Klarite chip from 3D Technologies Ltd.	1×10^6 1×10^4	Manufacturer data	Binding molecules. Most other molecules.
Vials from Real Time Analyzer Inc.	1×10^6	Manufacturer data	

Next we analyze the SERS performance of a commercial SERS chip – Klarite from 3D Technologies Ltd. This chip contains lithographically etched pattern of regular

pits (inverted pyramids) in silicon wafer and the pattering is optimized for 785 nm excitation. The chip is coated with nearly 300 nm gold film to provide plasmon active surface. The Klarite chip was soaked in 1 mM methanolic MBT for 14 hr to assemble SAM of analyte. It was rinsed in methanol and dried before acquiring the spectra. **Figure 4-62** shows spectra for SAM of 4-MBT on Klarite chip for randomly chosen points on substrate.

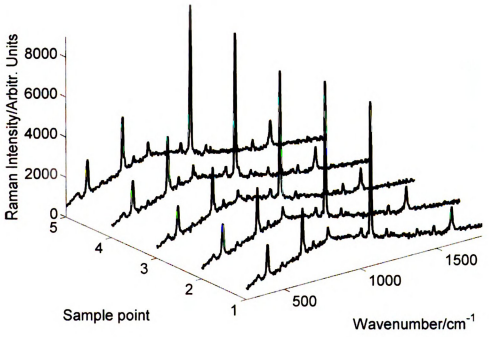

Figure 4-62. SERS spectra of a SAM of 4-MBT on Klarite chip from 5 different points, t_{acc}= 5 s.

The spatial variation of 1068 cm^{-1} peak of 4-MBT over 6.25 mm^2 area is shown in **Figure 4-63** and shows good reproducibility of the signal with a standard deviation of ~ 6 %. The average *EF* for Klarite chip was estimated as ~1.5×10^6 and agrees well with the value suggested by manufacturer. The analysis of Klarite chip serves a twofold

purpose; (1) it validates the mechanism of *EF* estimation, and (2) it shows that the nanowires yield a better *EF* than the commercially available product.

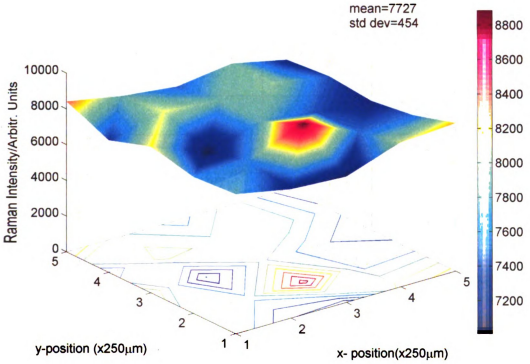

Figure 4-63. 4-MBT 1068 cm^{-1} Raman peak intensity distribution for randomly chosen area on Klarite chip, t_{acc}= 5 s.

Table 4-2 shows the Raman peak assignment for 4-MBT (wavenumbers in cm^{-1}). The Raman peak assignment is based on the knowledge of Raman bands for p-distributed benzene derivatives. The assignment is further refined by using the spectral correlation with the ordinary Raman (OR) spectra of 1-chloro-4-methylbenzene. This was based on the well-known similarity in the ordinary Raman spectra of mecaptans and the corresponding chlorides (1-chloro-4-methanebenzene in this case)[128, 132]. It is evident from **Table 4-2** that the SERS Raman peaks of 4-MBT measured here are in good agreement with those reported earlier.

Table 4-2. Raman band assignment for 4-MBT.

OR p-distributed benzene Ref [132], [133]	OR 4-MBT (this work)	OR p-chlorotoluene Ref[134]/Ref[135]	SERS 4-MBT[136] (514 nm)	SERS 4-MBT (this work)	Assignment
240-340	*309 m*	*-/303*		*322.8±2 w*	γCH; *(10b)*
240-400	*368 vw*	*360/377*			*νCS; A1 (7a)*
380-420	381 m	386/405	386	387.5±0.5 m	τCC; A2 (16a)
481-680	**636 s**	**547/636**	**623**	**619±0.6 s**	**δCC; A1 (12)**
720-840	*790 vs*	*765/797*	*794*	*786.6±1.4 w*	*δCC; A1 (6a)*
1004-1022	1011 w		999 /1016	1004.4±1 m	δCH; τCC 18a
1050-1100	**1069 w**		**1078**	**1067.7±0.48 s**	**Ring; 1**
1050-1100	*1091 vs*	*1056/1090*			*Ring; A1(1)*
1100-1128 *1085-1129*	*1112 w*				*δCH;18b*
1156-1190 *1142-1190*	*1178 s*	*1072/1176*	*1181*	*1170.5±1.07 w*	*δCH;A1 (9a)*
1100-1300	*1204 s*	*1194/1208*	*1209*	*1199.5±0.7 w*	*δCH;A1 (13)*
1260-1310	1305 w	-/1300	1378	1369.8±1 m	δCH; B2 (3)
1460-1530	1495 vw		1483	1480.8±0.7 m	νCC; 19a
1552-1605	*1572 m*	*-/1574*	*1579*	*1579.7±1 sh*	*νCC; B2 (8b)*
1570-1628	**1606 m**	**1595/1596**	**1593**	**1597±0.6 s**	**νCC; A1 (8a)**

vw:very weak; w: weak; m: medium; s: strong; vs: very strong; sh: shoulder.

ν: in-plane stretching; δ: in-plane bending; γ: out-of-plane bending.

4.5.2.3 Detection of bis(4-pyridyl)ethylene

The second analyte used was trans-1,2-bis(4-pyridyl)ethylene (BPE). BPE belongs to N-heterocyclic compounds that are of biological, pharmaceutical and industrial importance[137]. BPE is centrosymmetric and photostable with well resolved spectral lines in SERS spectra. BPE has 66 vibrational mode but only 23 modes of A_g symmetry (in C_{2h} symmetry) and 10 of B_g symmetry are Raman allowed[138]. The A_g modes are in-plane while the B_g modes are out-of-plane. Many of these modes are very weak (like 5 A_g modes of CH stretch near 3000 cm^{-1}) or below 250 cm^{-1} and are difficult to measure accurately.

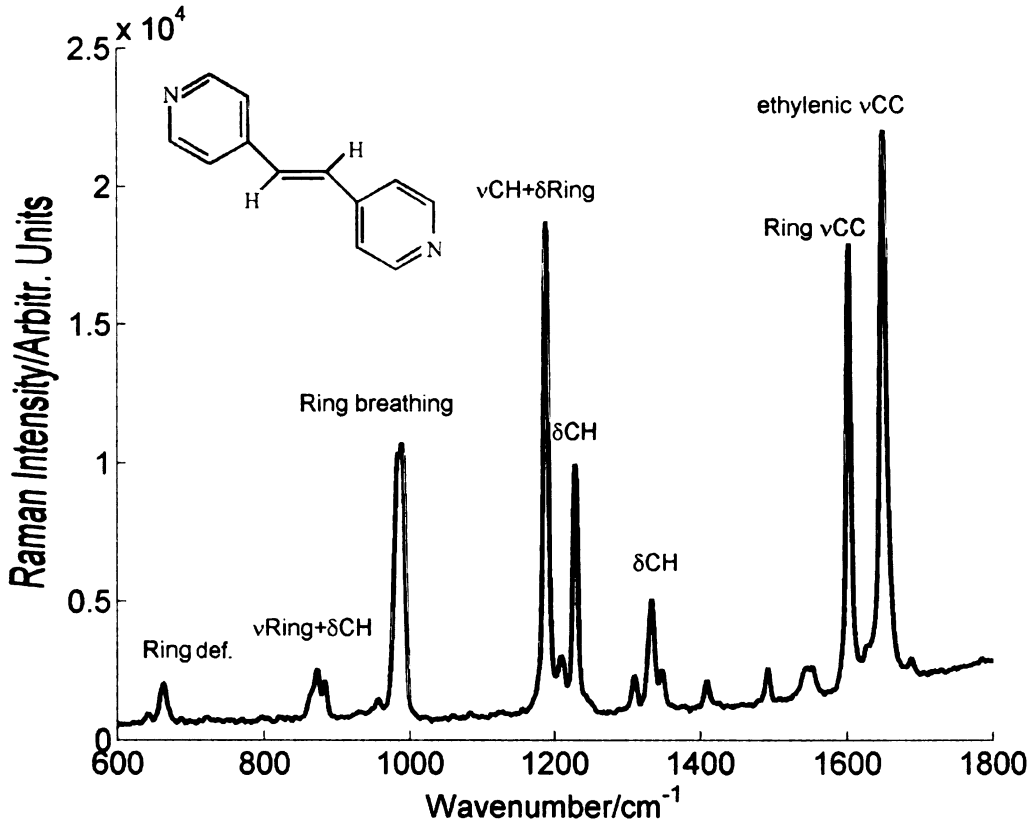

Figure 4-64. Chemical structure and ordinary Raman spectrum of BPE.

For SERS studies, a 0.83 μM solution of BPE was prepared in methanol and 2 μL solution was applied to the nanowire substrate. The solution immediately spread on the substrate to a spot of nearly 5 mm diameter, and was allowed to dry before acquiring the Raman spectra shown in **Figure 4-65**. The BPE peaks can be clearly identified on the top of broad background that was found after Au coating of the substrate. The BPE spectra can be easily identified from different points on substrate with just few seconds of signal accumulation.

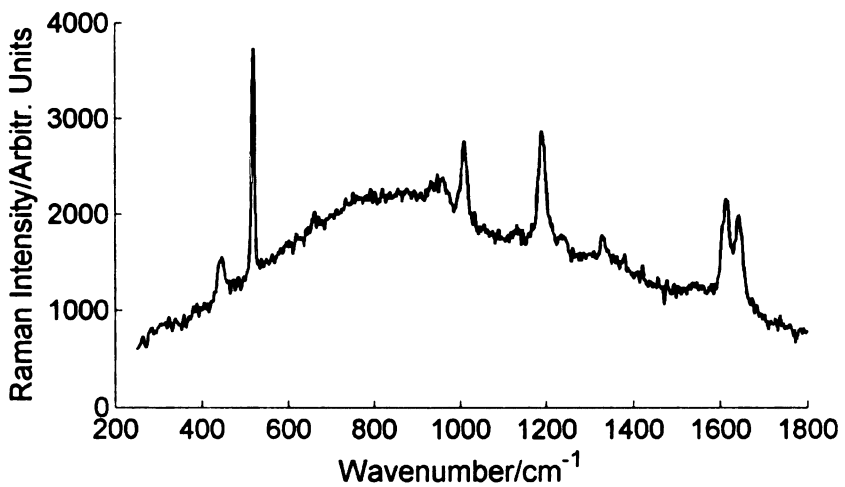

Figure 4-65. SERS spectra of 0.83 μM BPE from Au coated GeO_2 NWs, t_{acc}= 15 s.

Figure 4-66 shows SERS spectra of BPE from five different points (~125 μm spacing between points) on the substrate and the main peaks of molecule can be clearly seen in all the spectra. The SERS uniformity of our substrate was verified by plotting 1190 cm^{-1} Raman of BPE for 100 sample points recorded over a random substrate area as shown in **Figure 4-67**. The plot confirms that the substrate provides a relatively uniform enhancement with a standard deviation of less than 23% from the mean.

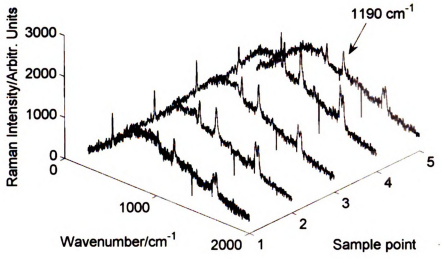

Figure 4-66. SERS spectra of 0.83 μM BPE from different points on substrate, t_{acc}= 5 s.

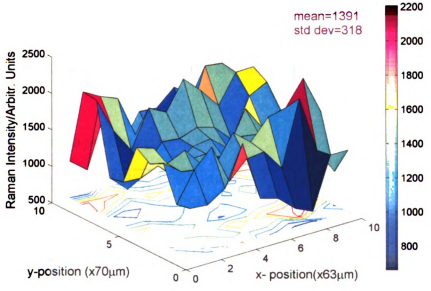

Figure 4-67. BPE 1190 cm^{-1} Raman peak intensity distribution for randomly chosen area on substrate, t_{acc}= 5 s.

We also calculated the experimental enhancement factor for BPE using the 1190 cm^{-1} Raman band. This band is the strongest in the SERS spectra and also has the added benefit of being relatively insensitive to molecular orientation on a metal surface[36]. The molar concentration and applied volume of BPE means that nearly 10^{12}

molecules are added to the substrate. Assuming uniform spatial adsorption of these molecules on the substrate, it is estimated that nearly 6.65×10^{-16} moles of BPE are contributing to SERS signal for the laser spot size of 100 μm diameter. The 0.83 μM solution of BPE could not be used as reference since it did not yield a detectable Raman signal. We therefore prepared ~0.75 M solution of BPE in methanol for reference measurements. The intensity of 1190 cm^{-1} Raman line from this reference solution was used as I_{ref} in equation (4.7) to calculate Raman *EF*. The number of molecules excited in the bulk solution (N_{ref}) were estimated to be 1.78×10^{15} from depth of field considerations. This translates into an average enhancement factor of ~ 1.70×10^{6}. The Raman peak assignments for ordinary Raman (OR) and SER spectra of BPE molecules are given in **Table 4-3** (wavenumbers in cm^{-1}) and agree well with the reported literature.

Table 4-3. Raman peak assignment for BPE.

OR[138]	OR (this work)	SERS [138] (532 nm)	SERS (this work	Assignment [137, 138]
640	662	652	649±2.8 w	A_g 17; ring deformation
995	**989**	**1008**	**1012±1.8 s**	**A_g 13; Ring breathing of pyridine**
1194	**1189**	**1200**	**1188±2.7 s**	**A_g 9; ethylenic C=C stretch**
1230	1229	1244		A_g 8; CH bending on pyridine ring
1348	1348	1338	1336±2.6 w	A_g 6; CH wag
1418	1409	1421		A_g 5; ring str. + CH bend
1491	1492	1493		A_g 4: ring stretch
1550	1552	1544		A_g 3; ring stretch
1600	1603	1604	1615±3 m	A_g 2: pyridine ring C=C stretch
1641	1650	1640	1640±3.1 m	A_g 1: ethylenic stretch

4.5.2.4 Detection of benzenedithiol

To confirm the enhancement for other molecules, we also investigated 1,2-BDT as a probe analyte. The 1,2-BDT belongs to C_{2v} symmetry point group if the hydrogen atoms are ignored and has 36 Raman active with the A1 modes polarized in the Raman[139]. **Figure 4-68** shows the ordinary Raman spectra of 1,2-BDT in liquid state with significant vibrational modes annotated.

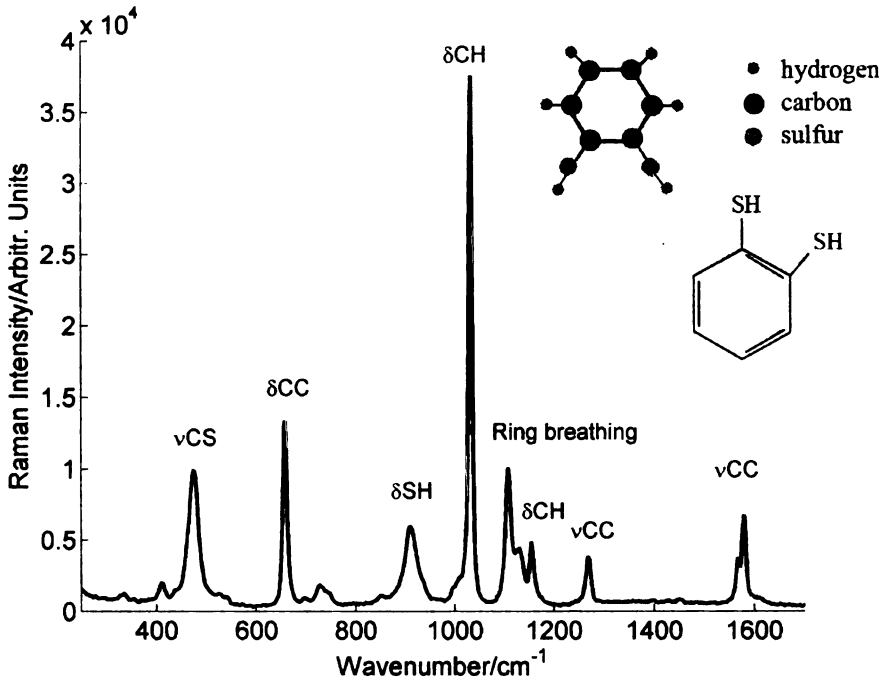

Figure 4-68. Ordinary Raman spectra of 1,2-BDT in liquid state. Also show is the chemical structure of molecule.

The 1,2-BDT molecule is known to form self assembled monolayer (SAM) on 200 nm thick Au film for concentration $\geq 1 \times 10^{-3}$ M after more than 20 min of soaking[126]. We immersed our SERS-active nanowires substrates in 20 μM solution of 1,2-BDT in methanol for 20 min. This concentration is less than the one reported for

monolayer coverage and is expected to yield a more conservative estimate of the enhancement factor. The sample was then rinsed with methanol and dried under dry nitrogen stream to ensure removal of excess analyte. **Figure 4-69** shows the SERS spectra from Au coated GeO_2 NWs, which clearly shows the 1,2-BDT peaks. The broad continuum is also somewhat suppressed following the formation of the BDT SAM on the Au coated nanowires. The SERS spectra of 1,2-BDT helps to identify the mechanism of adsorption molecule on metal surface. Comparing to the ordinary Raman spectra, the Raman band at ~910 cm^{-1} corresponding to SH bending is absent in SERS spectra and confirms the molecule absorbs on the surface by forming sulfur to metal bond after losing hydrogen[128].

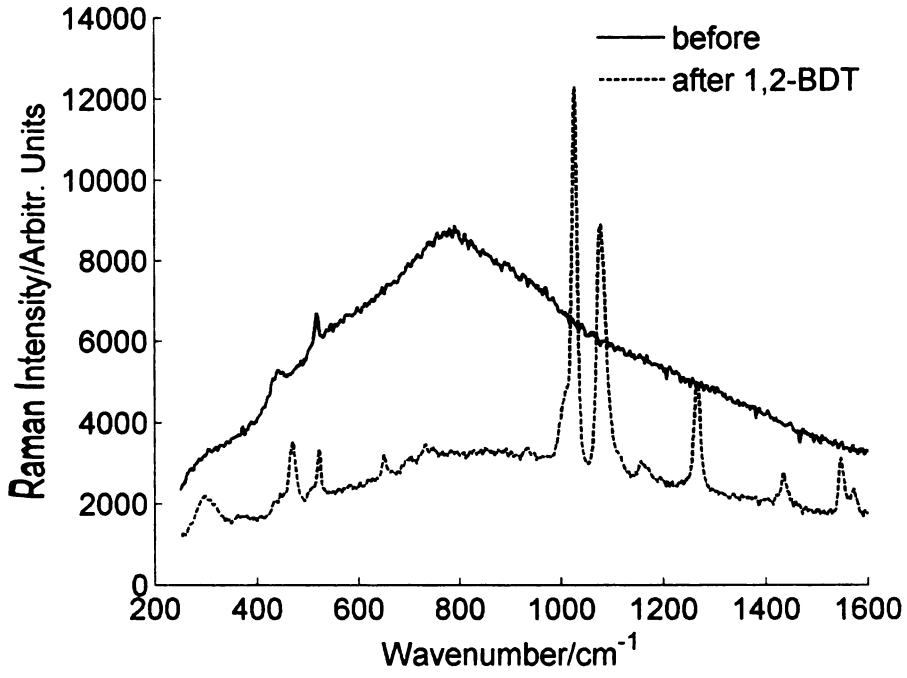

Figure 4-69. SERS spectra of self-assembled monolayer of 1,2-BDT from Au coated GeO_2 nanowires, t_{acc}= 15 s.

Table 4-4 shows the Raman band assignment (wavenumbers in cm^{-1}) for different vibrational modes of 1,2-BDT. The Raman peak positions in SERS spectra are somewhat shifted compared to ordinary Raman spectra of 1,2-BDT. This is not unexpected given that a shift of 10-20 cm^{-1} has been reported earlier[139].

Table 4-4. Raman band assignment for 1,2-BDT.

Ordinary Raman[128]	Ordinary Raman[139]	SERS [128] (514.5 nm)	SERS [139] (1064 nm)	SERS (this work) (785 nm)	Assignment[139]
471 s	**474(5) p**	**466 s**	**468 (3)**	**472±1.16**	**νCS; A1 (7a)**
658 s	658(5),p	647 m		655±1.81 m	δCC; A1 (6a)
698 vw	*700 w*	*696 w*		*703±2.64 vw*	*τCC; A2 (4)*
733 w	*734w p*	*725 w*		*728±2.54 vw*	*δCC; B2 (6b)*
	1010 sh		*1010 sh*	*1008 sh*	*δCC; B2 (12)*
1039 vs	**1038 p**	**1034 vs**	**1035**	**1028±0.6 s**	**δCH; A1 (18b)**
1113 s	**1114 p**	**1087 vs**	**1089**	**1078±1.67 s**	**Ring; A1 (1)**
1159 m	1160 dp	1161 m	1162 w	1155±2.48 m	δCH; B2 (18a)
1271 m	**1273 p**	**1263 s**	**1264**	**1266±1.89 s**	**νCC; A1 (14)** **δCH; B2 (3)**
1451 w	1452 w p	1433 m	1435	1436±1.69 m	νCC; A1 (19b)
1560 w	*1560 p*	*1543 w*	*1544*	*1547±1.34 m*	*νCC; A1 (8a)*
1570 m	1572 dp	1563 m	1565	1573±0.75 m	νCC; B2 (8b)

vw: very weak; w: weak; m: medium; s: strong; vs: very strong; sh: shoulder.

ν: in-plane stretching; δ: in-plane bending; γ: out-of-plane bending.

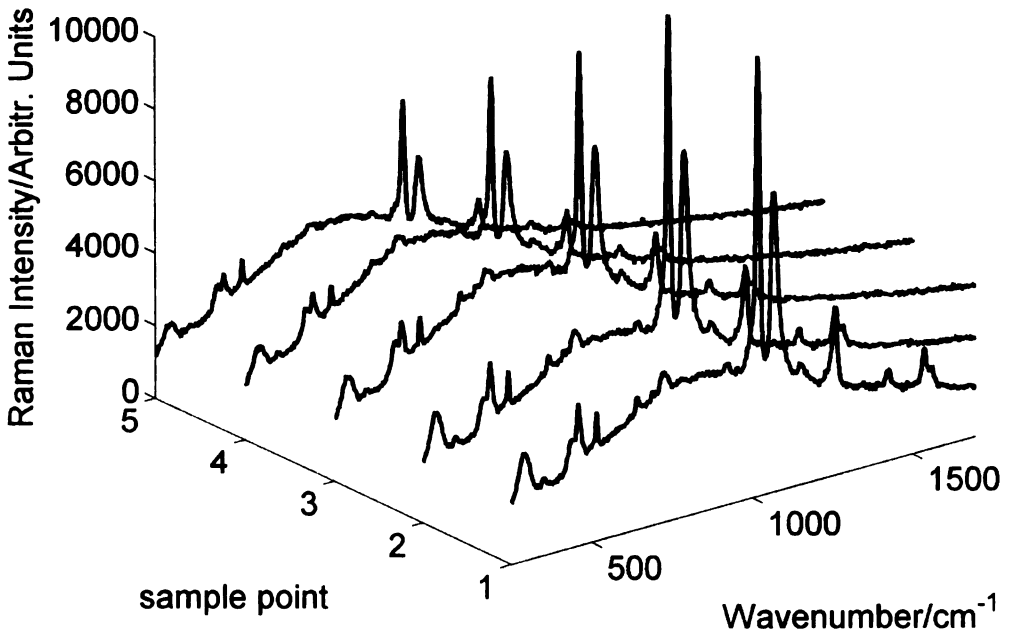

Figure 4-70. SERS spectra from 1mM BDT along line on substrate.

Figure 4-70 shows successive spectra from the substrate collected from points spaced 250 μm apart and show good reproducibility of measurement. **Figure 4-71** shows the plot of the 1028 cm^1 peak of 1,2-BDT for 100 points scanned in a rectangular area of 1.25 mm × 1.4 mm. The data show the substrate provides very uniform SERS enhancement with a standard deviation of approximately 18%.

The SERS *EF* for 1,2-BDT was again calculated using equation (4.7) and this time the 1028 cm^{-1} Raman band of 1,2-BDT was utilized. The calculation of I_{SERS} in equation (4.7) requires a knowledge of molecule adsorption of substrate. The 1,2-BDT is known to self assemble on Au(111) by forming two sulfur-gold bonds as shown in Figure 4-72. Assuming monolayer coverage of substrate with 1,2-BDT and each molecule binding to 2 Au atoms on the surface, we get 6.4×10^{14} molecules/cm^2 on the substrate.

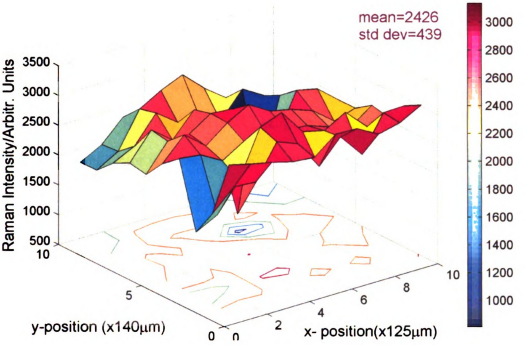

Figure 4-71. Area map of 1028 cm^{-1} Raman peak of 1,2-BDT, t_{acc}=5 s.

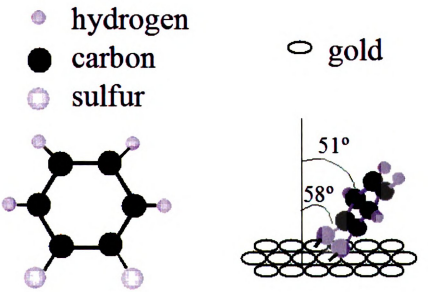

Figure 4-72. Molecular structure of 1,2-BDT and formation of SAM on Au(111) face[126].

Considering the laser spot size of 100 μm diameter, nearly 8.35×10^{-14} moles (5.03×10^{10} molecules) of 1,2-BDT contribute to the SERS signal. The ordinary Raman spectra of the source 1,2-BDT was used as reference to calculate Raman *EF*. The laser excitation volume was estimated to be ~6.28 nL from depth of field considerations. The average enhancement factor was found to be ~ 1.27×10^5. The low enhancement factor relative to other analytes is probably due to sub-monolayer coverage of 1,2-BDT on the substrate. Assuming 1,2-BDT surface coverage depends linearly on bulk solution concentration, we get 0.02 monolayer of 1,2-BDT from 20 μM solution. The enhancement factor using this sub-monolayer coverage will be almost 50 times the one calculated for the complete monolayer assumption.

It is useful to conjecture on the mechanism involving the interaction between laser and analyte in the present system of Au coating oxide NWs. It is hypothesized that the high dielectric nature of oxide NWs helps to confine and guide the light to a much larger area on the substrate than that directly illuminated by the laser beam. This is supported by the observation that the laser spot is hardly noticeable in CCD camera when focused on Si wafer. However, the illuminated size is much larger (few mm diameter) when NWs substrate is targeted suggesting light waveguiding and coupling among NWs. This is depicted in **Figure 4-73** where CCD image of laser spot on bare Si wafer and GeO_2 NWs substrate is shown. The NWs contain large number of gold particles on top surface, which are also expected to immobilize analyte molecules. The light coupling between NWs excites surface plasmons in Au particles that in turn excite Raman modes of analyte. The analyte Raman radiation is again amplified by the Au nanoparticles, coupled back to the NWs and finally travels to the receiver in the reverse direction. This plausibly

explains the observed laser spot broadening and good reproducibility of SERS from GeO_2 NWs substrate.

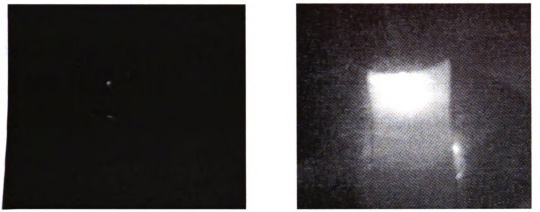

Figure 4-73. Optical image of laser illumination of Si wafer (left) and GeO_2 NWs substrate (right).

4.6 Conclusion

This chapter mainly presented the details of synthesis and results of Raman enhancement from gold-coated GeO_2 nanowires. The EDS, TEM and Raman studies of nanowires confirmed the trigonal phase of crystalline GeO_2 nanowires. The gold coating introduced a broad background in the Raman spectrum of nanowires. By changing gold deposition process and studying the impact of sample heating and drying in desiccator, the impurity and water vapor were eliminated as possible sources for broad background in the spectra. The silver coated nanowires also exhibit a background continuum similar to the one observed for gold-coated nanowires. The exact source of the background continuum is not known but is probably due to electronic scattering from metallic nanostructures. The SERS substrates were evaluated using R6G and NB as probe molecules. Strong enhancement was found at isolated locations, which was sufficient to

easily detect μMolar concentrations of these two probe molecules. On the other hand, no discernable Raman spectra could be obtained from bulk solutions at these concentrations. This clearly confirms the SERS from nanowires but at few isolated locations. The isolated enhancement was attributed to the nature of analytes that do not chemically bind to the substrate. The substrates were also studied for SERS by using 4-MBT, BPE and 1,2-BDT as probe molecules. The aromatic thiol based analytes are known to chemically bind with the metal coating on the substrate and yield better estimate of SERS enhancement. The substrates yielded an average enhancement factor of the order of 10^6 with good repeatability and small standard deviation of approximately 20% over the tested areas. The amount of analyte that yields these strong SERS spectra is on the order of $\sim 10^{-14}$ moles and confirms the high sensitivity of these novel substrates. The SERS performance of the nanowire substrates was also compared with that of commercial SERS chip, Klarite from 3-D Technologies Ltd. This result demonstrates that the gold coated nanowires can be a promising candidate for SERS.

Chapter 5: Low Temperature Synthesized GeO_2 Nanowires based Substrates for SERS

In the last chapter, experimental details and growth kinetics for GeO_2 NW synthesized at a temperature (~ 830 - 850 °C) above sublimation temperature of GeO (710 °C) were presented. The SERS evaluation of gold coated NWs showed strong enhancement for analyte that bond well to the substrate. However, the synthesis investigation revealed little control over the parameters of the nanowires like length, diameter, density etc. Raman enhancement from the substrate is expected to be significantly dependent on these parameters. In an effort to achieve greater control over these parameter, an alternate synthesis approach was developed that limits the maximum temperate of the source to ~ 650 °C i.e., below the sublimation temperature for GeO. Thus this new synthesis is termed low temperature growth. This chapter presents the synthesis details and Raman studies. Characterization of the substrate was done with Scanning Electron Microscope (JEOL 6400V), Field Emission Scanning Electron Microscope (JEOL 6300F) and Transmission Electron Microscope (JEOL 2200FS). The as synthesized substrates were evaluated for their SERS performance using NIR Raman system. 4-MBT and 1,2-BDT were utilized as probe molecules for SERS analysis. In this chapter, first the growth environment for nanowires is discussed and this is followed by results of Raman analysis.

5.1 Limitation of high temperature nanowire synthesis

As noted in the last chapter, there have been a number of reports of GeO_2 NWs synthesis using thermal evaporation[85], carbon nanotube confined reaction of Ge[86] , laser ablation[91], thermal oxidation[87-89, 92], carbothermal reduction[83] etc. All these techniques have utilized high source temperatures in the range 820-1300 °C to generate sufficient vapor pressure of Ge or GeO in an oxidizing or inert environment and relied on residual or leakage oxygen to form the GeO_2 NWs or whiskers. Mostly the NWs were collected on the source, or close to it, at almost the same temperature. The only exception is the synthesis by Bai *et al.*[85] where the NWs were collected in the low temperature zone (exact temperature in the growth zone was not reported by the authors) in front of a copper cold finger on the inside walls of quartz tube. Another relatively low temperature synthesis was carried out by Hu *et al.*[88] that had the source material at 1300 °C, but substrate was at 700 °C. The main rationale of using the high temperature is to generate sufficient vapor pressure of reactants to facilitate growth at a reasonable rate. There are mainly two parameters governing the oxidation of Ge – temperature and the oxygen concentration. While the temperature is expected to have a monotonic effect, the oxygen concentration can have a non-trivial dependence on its partial pressure. For most metals, the oxidation rate above 1 Torr are either independent of pressure or increase with increasing pressure. However, Ge shows a strong inverse dependence of oxidation rate on oxygen pressure at and above 550 °C[140]. Since GeO is the main oxidation product of Ge oxidation, we expect a very high GeO vapor pressure above its sublimation point at 710 °C. Germanium monoxide vapor pressure of 28.48 Torr at 705 °C has been reported[98]. The high vapor pressure of GeO and its diffusion is responsible for the

observation that most of the source material is gone within 5-6 minutes of the start of oxygen flow. The rapid oxidation of Ge source rapidly infuses a lot of GeO onto the substrate making it difficult to exercise good control over growth. This is evident by cracking of the top layer of the substrate as shown in **Figure 5-1**. The corresponding SEM shows Ge:O atomic ratio of nearly 30:63 without any signature of the underlying Si substrate. The thick peeled layers are therefore mainly comprised of GeO_2 and thickness can be in excess of 10 μm. Thinner GeO_2 layers are expected to decrease the electron beam penetration and allow detection of Si in the EDS. This suggests that the substrate is getting significantly thick coating of probably GeO during the initial deposition that later transforms to GeO_2. The NWs start to grow out of this thick coating as the process continues and generally become dense enough to shield the underlying thick layer. The film cracking is probably the result of thermal mismatch between top coating and underlying substrate. The formation of an alloy at the interface cannot be ruled out as we didn't see a clean break between the substrate and film as shown in **Figure 5-2**. Here one can see the underlying Si substrate from region where top film patch has been removed. The corrugated nature of the substrate suggests formation of an alloy at the interface and strong adhesion between the film and substrate. The elemental mapping of the substrate (imaged in **Figure 5-2**) clearly shows the cavity is mainly composed of Si whereas the surround area is made of germanium and oxygen as illustrated in **Figure 5-3**.

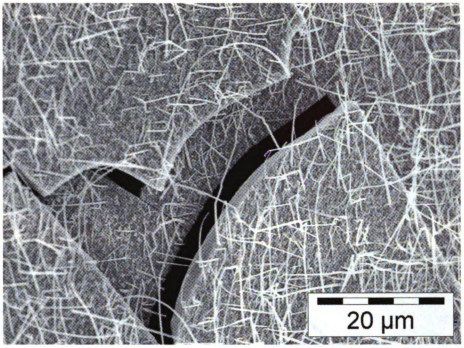

Figure 5-1. SEM image of GeO_2 NW substrate.

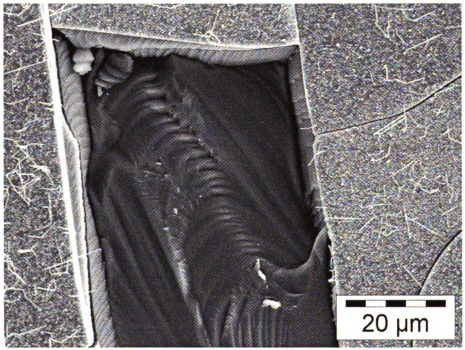

Figure 5-2. SEM image of cracked GeO_2 film on Si substrate during nanowire synthesis.

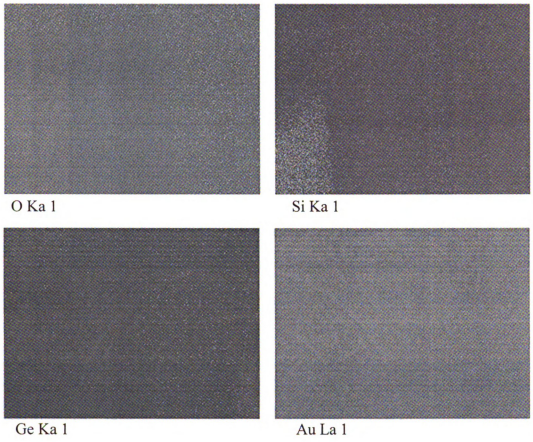

Figure 5-3. EDS elemental map for top right corner of cavity in **Figure 5-2**.

Another issue relates to the uniformity of NWs growth across the surface of the substrate as shown in **Figure 5-4**. In many cases agglomerations of particles, especially closer to the source, are observed alongside the NWs as shown in **Figure 5-5**. Here one can see nearly stoichiometric GeO_2 (Ge:O ratio 33:63) particles without any signature from underlying Si substrate.

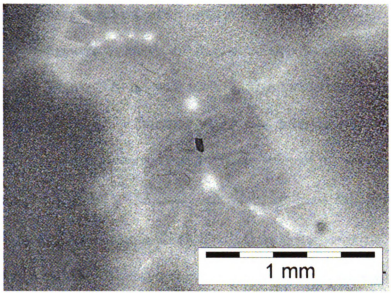

Figure 5-4. SEM image showing non-uniformity of the film on the substrate.

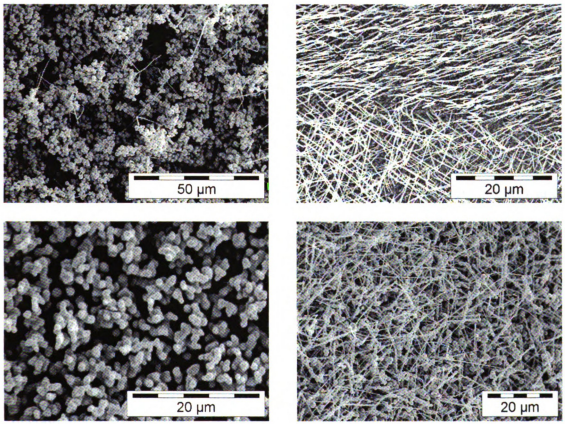

Figure 5-5. SEM image of substrate showing different morphologies of GeO_2 particles and NWs.

5.2 Low temperature Synthesis of nanowires

The low temperature synthesis of nanowires also uses the same quartz tube experimental set up (**Figure 5-6**) that was used for high temperature synthesis, however the experimental conditional of temperature, flow rate, pressure and synthesis duration are varied. This has led to a technique that addresses some of the issues associated with the high temperature synthesis. The GeO_2 nanowires synthesis still follows the vapor-liquid-solid (VLS) growth mechanism[81]. The source material of Ge is placed on a quartz support plate and silicon substrates coated with 3 - 28 nm thick gold catalyst film are placed few inches from the Ge source material. The support plate is inserted in the quartz tube such that the source is located in the high temperature zone near the center of the furnace whereas the substrates are in the low temperature zone towards downstream end of the furnace. The temperature was measured using 'K' type thermocouple placed inside the quartz tube that can be moved along the length of the tube using magnetic coupling without braking vacuum. The tube was evacuated to less than 200 mTorr by a mechanical vacuum pump and subsequently backfilled with argon at a flow rate of 50 sccm. Temperature at the source was raised to 640-650 °C over 20 minutes and the vacuum valve at the downstream end was adjusted to obtain a pressure of ~ 2 Torr for the constant flow of background gas. The temperature at the substrates was measured at ~ 400 –500 °C. The growth of the NWs was initiated by introducing Ar mixed with oxygen (40% O_2 and balance Ar) at the rate of 10 sccm. The growth was done for 1 hr and the pressure increased to ~ 3 Torr over this time. The furnace was switched off and allowed to cool to room temperature before opening the tube to atmosphere. The substrates

surface turned white to pink after the experiment. The substrate was characterized using JEOL 6400 scanning electron microscope (SEM) and TEM.

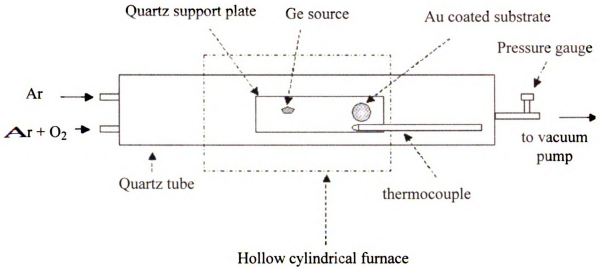

Figure 5-6. Schematic of low temperature synthesis of germanium dioxide nanowire.

Figure 5-7 shows the SEM image (15 keV with ~15 mm working distance) of the substrate fully covered with dense nanowires.

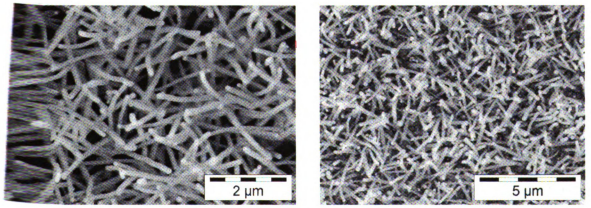

Figure 5-7. SEM image of GeO_2 nanowires on Si at 400-500 °C.

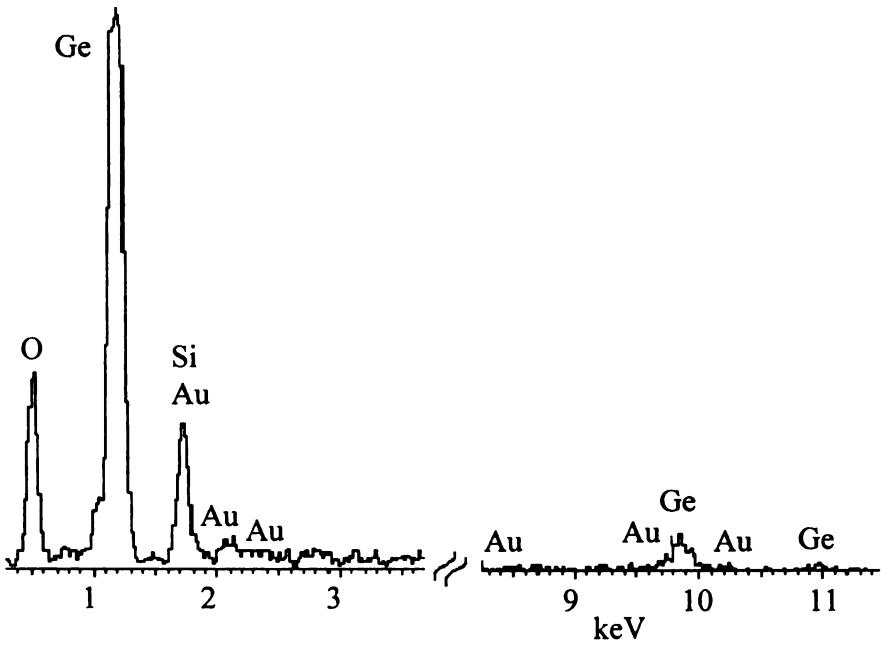

Element	App Conc.	Intensity Corrn.	Weight%	Weight% Sigma	Atomic%
O K	0.19	1.1035	29.39	1.81	60.99
Si K	0.04	0.6767	10.11	0.90	11.95
Ge L	0.27	0.7751	58.36	2.00	26.70
Au M	0.01	0.5909	2.14	1.78	0.36
Totals			100.00		

Figure 5-8. EDS spectrum and quantification results for GeO_2 nanowires.

Figure 5-8 shows the x-ray Energy Dispersive Spectroscopy (EDS) spectra and quantization results for the NWs substrate. Though it is difficult to measure the Ge/O ratio of the wires quantitatively due to the intensity uncertainty of the EDS detection for lighter elements, it is estimated that the chemical composition of the GeO_2 NW is close to

GeO_2. The atomic ratio of germanium to oxygen from the quantization results is found to be 27:61 that is quite close to the actual ratio of 1:2. It may be mentioned that a clear signature of gold and the underlying Si substrate was observed in EDS, which confirms thin top layer of NWs. The nanowires were also characterized by JEOL 100 CXII field emission transmission electron microscope (TEM). The TEM samples were prepared by sliding holey carbon-coated TEM grid across the sample face. **Figure 5-9** shows the TEM image of a two GeO_2 nanowire with a diameter of ~52 nm - 87 nm. The TEM image shows a dark spherical tip at the end of the thin nanowire that is probably the catalyst particle. The other NW doesn't show catalyst particle at the tip and may have been broken during sample preparation. The right side image of **Figure 5-9** shows some nanowires with and without catalyst tip. Interestingly it also contains an isolated dark spherical particle (denoted by red circle) and supports the hypothesis of catalyst particle being broken during sample handling or preparation.

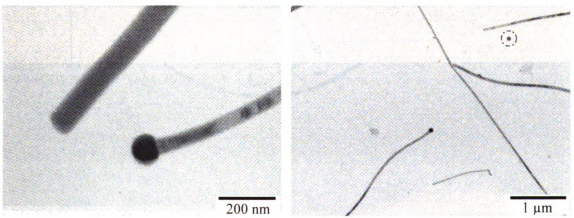

Figure 5-9. TEM image showing dark catalyst particle at tip. Right image shows a dark spherical particle probably broken during sample preparation.

The NWs synthesized at low temperature show good uniformity over large areas of the substrates but do show some circular clusters of different morphology as shown in **Figure 5-10**. Here, one can see isolate circular islands superimposed on more uniform NWs. The morphology of NWs in the islands is different from the other NWs in that these are much longer, curved and narrower. The cross-section of the substrate also shows the normal length of NWs is few microns but in these circular regions, nanowires reach tens of microns in length.

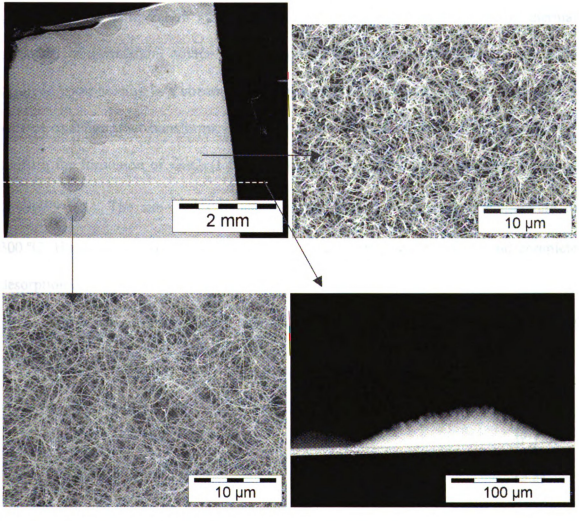

Figure 5-10. Different morphology of low temperature GeO_2 NWs.

5.3 Nanowire growth kinetics

The synthesis of GeO_2 NWs involves oxidation of germanium source to generate germanium oxide vapors. These vapors then diffuse away from the source and condense on the gold coated substrate to synthesize NWs. This section presents the details of oxidation of the germanium source at low temperatures and the subsequent growth of NWs from the vapor phase germanium oxide.

5.3.1 Oxidation of germanium

The low temperature synthesis of nanowires is also characterized by thermal oxidation of germanium source in an oxidizing environment. Germanium is readily oxidized upon heating in a stream of oxygen/air and a film of GeO always forms at the start of oxidation that transforms into GeO_2 as the reaction proceeds[98]. Many studies confirm the formation of $GeOx(1 < x < 2)$ during the initial stages of thermal oxidation of Ge[99-101]. The sub-oxides transformed to GeO_2 with increasing temperature to 300 °C. However, further heating caused the formation of volatile GeO and complete desorption of oxide occurred at 450 –475 °C.

The main reactions during thermal oxidation of germanium in an oxidizing environment are: [98]

$$Ge(s) + 1/2\,O_2(g) \rightarrow GeO(s) \tag{5.1}$$

$$GeO(s) \rightarrow GeO(g) \tag{5.2}$$

$$GeO(s) + 1/2\,O_2(g) \rightarrow GeO_2(s) \tag{5.3}$$

press

oxida

Indee

mana

being

accor

reacti

produ

oxyg

sema

decer

GeO_2

reach

as di

pathw

The r

transfo

produc

Page

The relative contribution of these reactions is a strong function of oxygen partial pressure. The oxidation rate of Ge increases with decreasing oxygen pressure and the oxidation rate is independent of crystal orientation of Ge source above 550°C[140]. Indeed as the oxygen pressure decreases, nearly all of the GeO formed on the surface manages to sublimate. i.e., reactions (4.1) and (4.2) take place, the rate of reaction (4.3) being very slow. When oxygen partial pressure increases, the oxidation proceeds according to reactions (4.1) and (4.3) i.e., the reaction (4.3) begins to prevail over reaction (4.2) and the oxidation rate slows down considerably. Similarly the oxidation product is mainly GeO if oxidation is carried out under conditions where the amount of oxygen is insufficient to converts it to GeO_2 (for example in a stream of N_2 or Ar containing oxygen admixture)[95]. The volatile GeO can diffuse away from source or decompose during oxidation/annealing process at high temperatures. In contrast to GeO, GeO_2 is very stable and doesn't melt unless temperatures above 1116 ± 4 °C[104] are reached. On heating GeO_2 to 1000-1100 °C, the vaporization rate is very low and there is no dissociation to Ge and O_2 or GeO and $1/2O_2$[95]. The only possible decomposition pathway for GeO_2 is through reaction with Ge to form GeO at or above ~425°C[102]. The resulting GeO then desorbs from the surface without undergoing any further transformation[97]. In summary, it is widely agreed that GeO is the only desorption product of oxidation/annealing of Ge and its desorption takes place in the temperature range 400 – 500 °C.

5.3.2 Growth kinetics

The synthesis of GeO_2 nanowires involves a solid phase Ge source and gas phase species of Ar, H_2 and oxygen. The Ar is used mainly as the carrier gas to transport the source material to the substrates and H_2 is included to avoid source and substrate oxidation during the heating phase. The beginning source material of Ge is likely covered with a thin layer of native GeO_2 since it has been exposed to atmosphere during storage. During heating of the source under low vacuum (2 Torr) with a protective flow of Ar and H_2, the native oxide is expected to be reduced to Ge or will escape by transforming into GeO above 400 °C. The integrity of the source (weight loss due to vaporization) is maintained during ramping and even at the reaction temperature of 650 °C, since the Ge (melting point ~ 937.2 ± 0.5 °C[105, 106]) has negligible vapor pressure at these temperatures. Hence, direct evaporation of Ge is not considered to be a contributor to nanowire growth.

The oxidation of germanium begins with the introduction of oxygen in the gas stream. It is hypothesized that the insufficient supply of oxygen results in the formation of GeO on the surface of the source material. Even if a small amount of GeO_2 is formed, it will react with the underlying layer of Ge and transform into GeO at 650 °C. We don't expect any thicker layer of GeO_2 to form on the source for the experimental conditions. The thermal stability of GeO_2 (Melting point 1116 ± 4 °C) will prevent the further oxidation of Ge but we observe significant loss of the source as the reaction proceeds. Therefore, the first reaction occurring during the growth of NWs is

$$Ge(s) + O_2(g) \rightarrow 2GeO(s) \qquad (5.4)$$

It may be re-emphasized that for every temperature, there is an optimum oxygen concentration at which the oxidation rate of germanium doesn't surpass the sublimation rate of the monoxide being formed in reaction (5.4). Otherwise, a thick layer of dioxide will form on the surface of the germanium and the oxidation process will virtually come to a halt. This is evident from **Figure 5-11** where Ge oxidation rate is plotted versus oxygen pressure at 550 °C. The lower oxidation rate at higher oxygen pressure is due to the formation of a top GeO_2 layer that acts as a diffusion barrier for diffusion of O_2 and GeO to/from GeO_2/Ge interface.

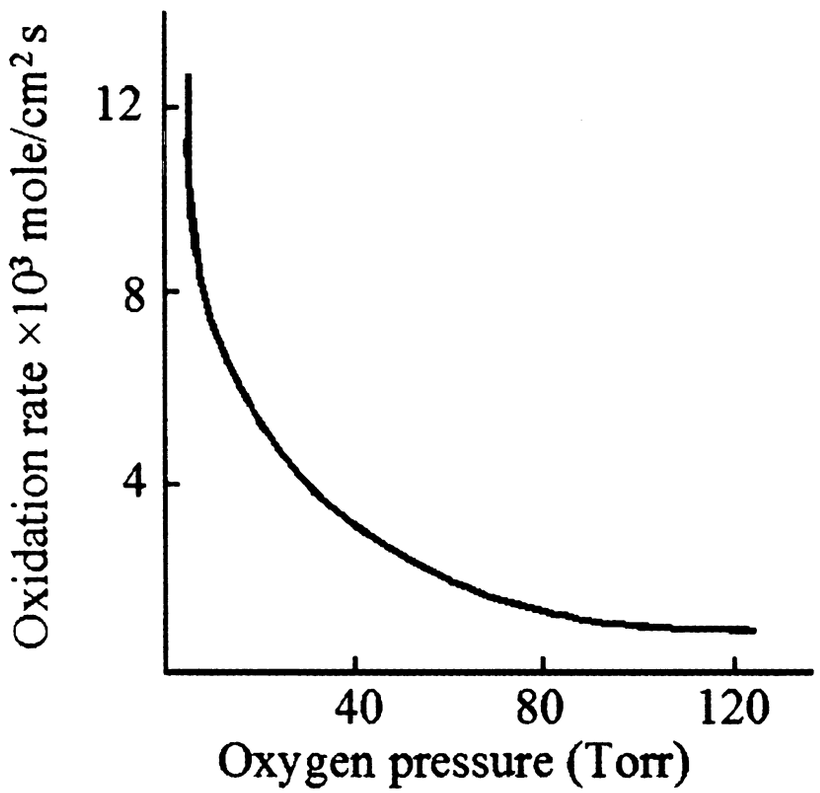

Figure 5-11. Rate of Ge oxidation versus oxygen pressure at 550 °C [98].

The GeO(s) formed during reaction (5.4) is volatile at high temperatures (vapor pressure ~ 3.29 Torr at 644 °C[98]), so some part of it goes to gas phase

$$GeO(s) \rightarrow GeO(g) \tag{5.5}$$

The GeO vapors formed in reaction (5.5) can undergo further oxidation (GeO oxidation starts 550 °C in air) in the presence of oxygen to yield GeO_2 according to the reaction[107]

$$GeO(g) + 1/2\,O_2(g) \rightarrow GeO_2(s) \tag{5.6}$$

But oxidation of GeO is not expected to be significant due to the low concentration of oxygen in the environment. If reaction (5.6) proceeds at a significant rate, a thermally stable layer of GeO_2 will deposit on substrates and the walls of reaction chamber. Nevertheless, the actual vapor phase is expected to be a mixture of mostly GeO along with some GeO_2. The precise analysis of vapor phase species requires more elaborate experimental set up (like X-ray photoelectron spectroscopy) than the one available.

In the vapor phase, there is also a possible thermal decomposition pathway for GeO. It is known that solid GeO disassociates into GeO_2 and Ge at high temperature according to reaction

$$2GeO(g) \Leftrightarrow Ge + GeO_2$$

The reaction temperature controls the relative probability of forward or reverse reactions[98]. It may take several hours for decomposition at 600 °C but at 700 °C it takes few minutes[98]. In the case of deposition on a condenser, GeO will deposit without decomposition. On the other hand, it will decompose into Ge and GeO_2 without a condenser at fairly high temperature. Since the substrates are also located in a relatively low temperature zone (400-500 °C), we don't expect a higher rate of decomposition-based deposition i.e., substrate gets mostly GeO, and some decomposed GeO_2 and Ge. Nevertheless the existence of Ge nanocrystals (NCs) in the deposited GeO film cannot be ruled out. In fact, Gorokhov *et al.* synthesized Ge NCs in GeO_2 films by depositing from supersaturated GeO vapors[141]. The situation is further complicated by the presence of a thin gold film on the substrate that forms a eutectic with the underlying silicon. The exact manner of adsorption of GeO or GeO_2 into Au cannot be predicted since no information about phase ternary phase diagram for Ge, Au and oxygen system could be found. However, it is postulated that the presence of liquid eutectic droplets will facilitate incorporation of GeO into the droplet yielding an initial sub-oxide composition GeO or possibly some $GeO_x\,(1 < x < 2)$ of NW[109]. The composition of nanowire then might transform to more stable GeO_2 by incorporation of oxygen from the background gas as well as through loss of GeO by vaporization. Under such a scenario, the excess GeO diffuses away from the reaction zone and condenses in the colder parts of the growth chamber. A yellowish to brownish-black coating (characteristic color of GeO) found at the ends of the quartz tube supports this hypothesis.

Thus the most plausible mechanism for the formation of GeO_2 NWs can be summarized as:

(a) Oxidation of Ge to form GeO(s).

(b) Transformation of some part of GeO(s) to GeO(g).

(c) The transport of GeO(g) (and possibly some small percentage of GeO_2) to the substrate under a reduced pressure.

(d) Preferential adsorption of GeO on the substrate at the sites of the gold catalyst and possibly some associated decomposition into Ge and GeO_2.

(e) The growth of $GeOx(1 < x < 2)$ NWs via the VLS mechanism by absorbing more source material from the vapor phase at the tip of the nanowires.

(f) The evolution towards more stable GeO_2 NWs by incorporation of oxygen and loss of GeO.

It may be noted that the low temperature synthesis follows similar kinetics as that of high temperature growth. The important difference lies in the temperature regime, which slows down the oxidation rate of Ge and GeO considerably to yield better control over the amount of gas phase species generated and transported to the substrate. This slows the rate of material deposition onto the substrate leading to better control over length and diameter of the NWs. The low substrate temperature also helps to reduce

desorption of the incident material yielding better surface converge, i.e, no dots appear but uniform surface color changes are observed over whole surface of the substrate.

The discussion so far has ignored the presence of hydrogen in the gas stream. It is known to be an oxide reducing agent depending upon the partial pressures of hydrogen and that of water in the system for a given temperature. As a practical manner, the partial pressure of water is equal to the base pressure of the system[111]. In our case, the base pressure is ~ 200 mTorr and partial pressure of H_2 is ~ 100 mTorr (for a total pressure of 2 Torr of a gas mixture containing 5% H_2). **Figure 5-12** is a plot of thermodynamic stability of GeO_2 as a function of ratio of hydrogen pressure to water pressure for different reaction temperatures[112]. For a $\frac{P(H_2)}{P(H_2O)} \approx 0.5$, the GeO_2 is unstable for all temperatures above 600 K and is expected to decompose to constituent elements. Since the NW synthesis is carried out above this temperature, we don't expect any GeO_2 on the source material at the start of oxygen flow. The situation changes after introduction of oxygen into the system and the oxidation of Ge becomes appreciable compared to the reduction of GeO/GeO_2 by H_2.

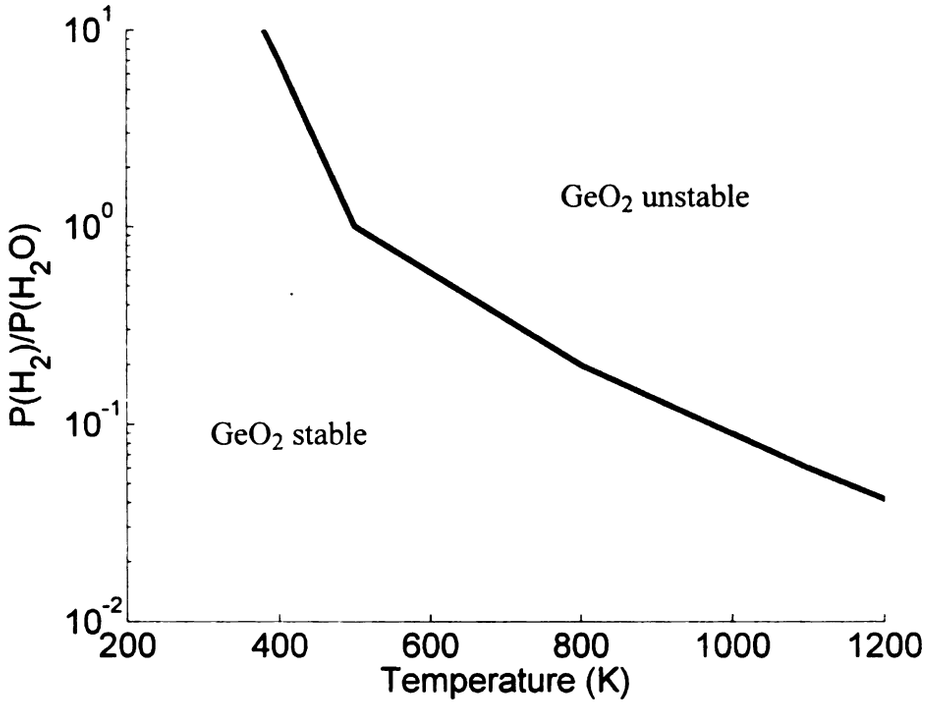

Figure 5-12. Plot showing GeO_2 stability as function of temperature and the hydrogen to water vapors pressure ratio[112].

5.3.3 Synthesis temperature profile

The actual temperature inside the furnace was measured with a 'K' type thermocouple placed inside the quartz tube. The thermocouple can be moved along the length of the furnace by using a magnetic coupling without breaking the vacuum. This arrangement allowed mapping the temperature profile of the furnace at different spatial locations. **Figure 5-13** shows a typical temperature profile along the length of the furnace during NWs synthesis run. To get a more accurate profile, the thermocouple was moved from its initial downstream position towards center of the furnace and then brought back to the initial position. The temperature profiles for the inward and outward movement of the thermocouple showed good agreement. The furnace has good temperature uniformity for the center zone (center ±2 inch) and then the temperature drops rapidly (~ 50 °C /in.)

toward open end of the furnace. This temperature gradient allowed the source and substrate to have different temperatures from the optimal growth of NWs.

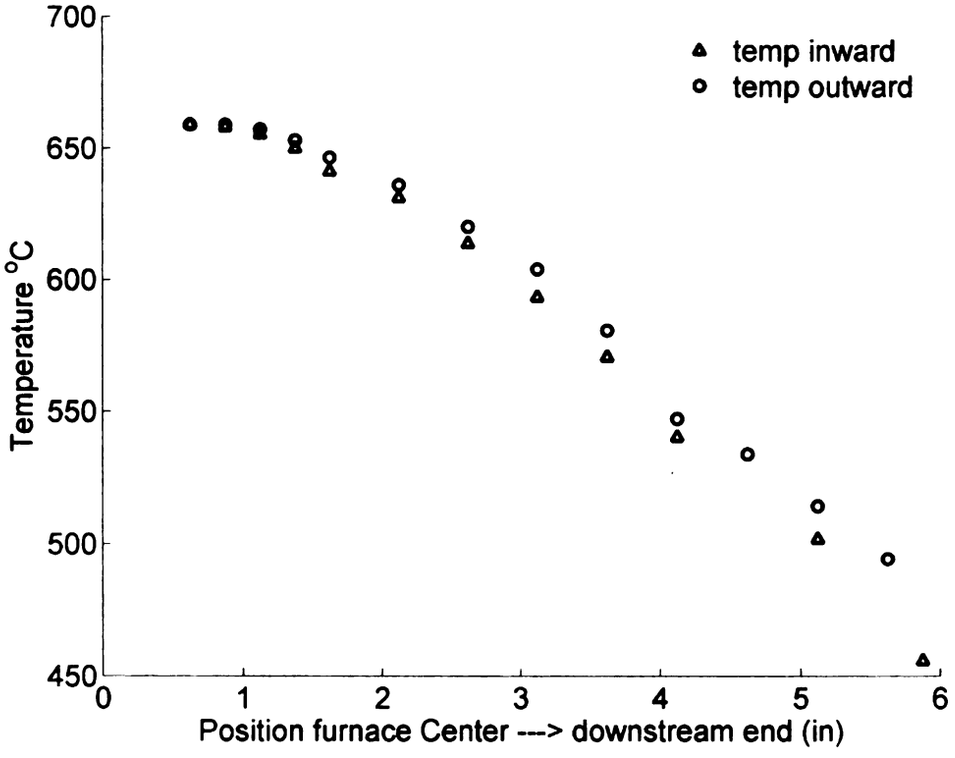

Figure 5-13. Tube furnace typical spatial temperature profile during nanowire synthesis.

5.3.4 Pressure profile

Observation of pressure during NWs synthesis revealed a typical variation pattern as shown in **Figure 5-14**. It is important to mention that the pressure is measured at the downstream end of the tube and may have some deviation from the actual value at the location of the source. The synthesis is initiated at ~2 Torr by introducing a mixture of Ar and oxygen (Ar 60%, O_2 40%) at a flow rate of 10 sccm. The initial rapid rise of pressure can be attributed to the increased gas flow as well as the contributions from GeO vapors

that are formed as a result of oxidation of Ge source. Then there is a more gradual rise of pressure to a final constant value of ~2.9 Torr, which can be related to the temperature rise during a long growth period. The temperature varied by almost 5-6 °C during 1 hr of growth.

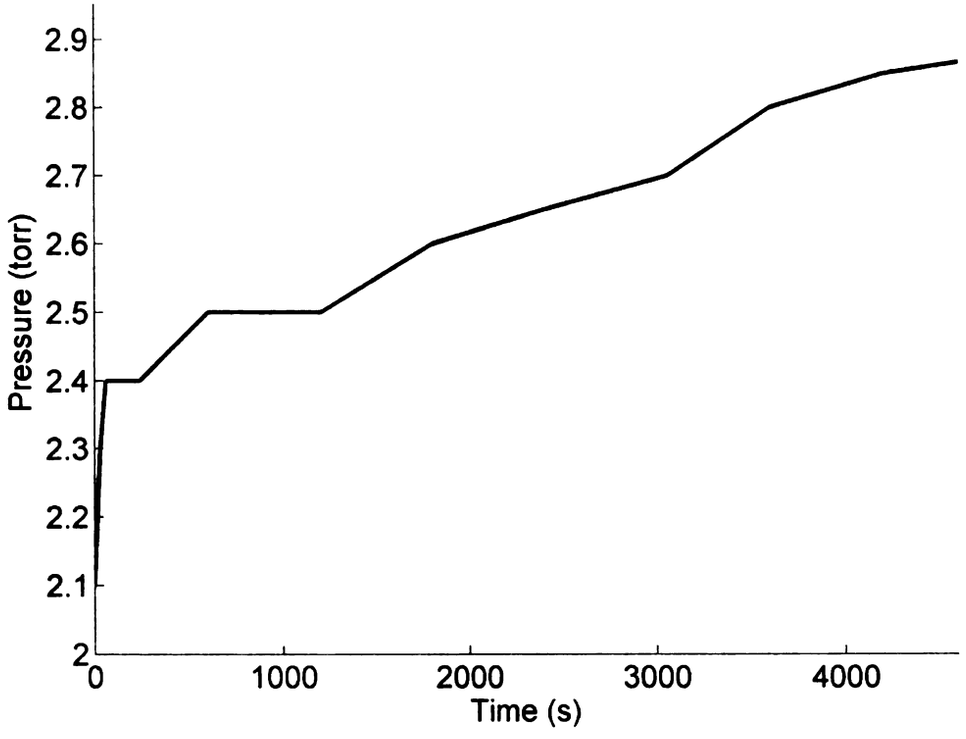

Figure 5-14. Typical pressure profile during NW synthesis.

5.4 Factors affecting NWs synthesis

The low temperature synthesis of GeO_2 NWs is dependent upon a number of experimental parameters that control the yield and characteristics of nanowires. These include thickness of the catalyst film, growth time, gas flow rates, background pressure, temperature, etc. The detailed study of the affect of these parameters on nanowires is presented in this section.

5.4.1

nano-st

throug

during

for NW

initial f

5.4.1.1

of the

adsorp

at the g

gold-co

spectra

seen, th

switch

Subsec

Using

place

5.4.1 Effect of gold film thickness

The control over the diameter of NWs is an important factor in engineering the nano-structured substrates for possible applications. This control is mainly exercised through the initial gold film thickness. The thin gold film breaks down in small islands during heating phase and subsequently these islands become nucleation and growth sites for NWs. Both the annealing of gold films and the diameter dependence of NWs on initial film thickness is studied in this section.

5.4.1.1 Gold film annealing

The catalyst plays an important role as the nucleation site and subsequent growth of the nanowires in the VLS mechanism. The main emphasis is the preferential adsorption of gas phase species into the catalyst or its eutectic form that is in liquid phase at the growth temperature. This results in nanowire growth that is highly localized to the gold-coated area. **Figure 5-15** shows dense and patterned NWs growth on Si(100) substrate that had Au removed in "X" pattern from the 21 nm thick Au film. As can be seen, the NWs growth (white areas) is strongly limited to the Au coated area with no growth on uncoated area (X pattern). The high degree of uniformity of the NWs is also evident from the low magnification image. The catalyst specific growth is one of the strong characteristics of VLS mechanism and gives evidence of VLS mechanism taking place.

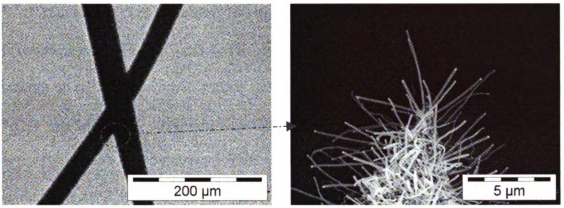

Figure 5-15. GeO_2 NWs on Si(100) that has patterned Au film (No gold was coated in the dark "X" pattern). Right image shows close up of the red circled area of left image.

Another characteristic of VLS growth is that the NWs generally terminate in a catalyst particle that has a spherical shape. **Figure 5-16** shows the SEM and TEM image of NWs. The SEM image shows NWs growth around two horizontal slits patterned into the Au film on a silicon substrate. The bright particles at the tips of NW can be easily seen for most NWs that grew to cover the uncoated (dark) area. The TEM image clearly shows a dark eutectic particle at the tip.

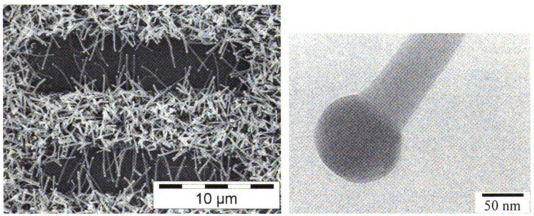

Figure 5-16. GeO_2 NW showing particle at tip.

the nar

breakin

catalys

site for

the dia

particu

were d

conditi

Figure

Au par

images

differen

softwar

narrowi

Matlab

The catalyst film thickness plays an important role in determining the diameter of the nanowires in VLS mechanism. The thermal annealing of the catalyst film results in breaking up of film into small islands due to the differences in surface energies of the catalyst and underlying substrate. These islands or particles then become the nucleation site for the growth of the nanowire. The size of the metal islands has a direct bearing on the diameter of the nanowires. A systematic study of evolution of catalyst film into particulates was carried out at the reaction temperature. Different thickness of gold films were deposited on Si(100) wafer and the samples were subjected to typical synthesis conditions without a germanium source material or oxygen flow. **Figure 5-17** through **Figure 5-21** shows the SEM images and corresponding particle size distributions for the Au particles. The diameters of the particles were determined from high magnification images of the sample. For each sample, at least diameters of nanowires from at three different locations were measured using distance measurement tool of SEM imaging software. This ensures that the measured diameters are better representatives of general nanowire sizes. The distribution plots were then generated using histogram function of Matlab.

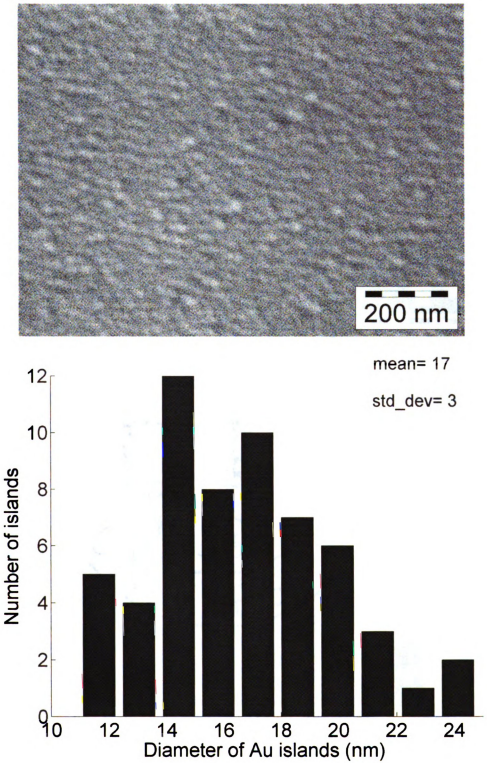

Figure 5-17. SEM image and particle size distribution for 3 nm Au film.

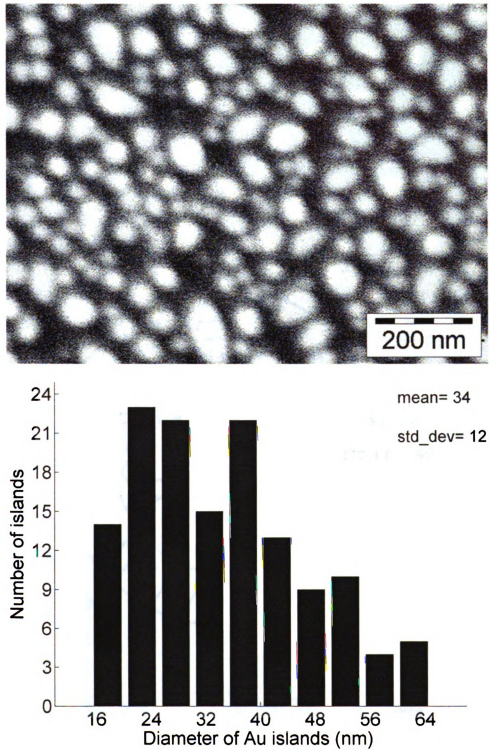

Figure 5-18. SEM image and particle size distribution for 7 nm Au film.

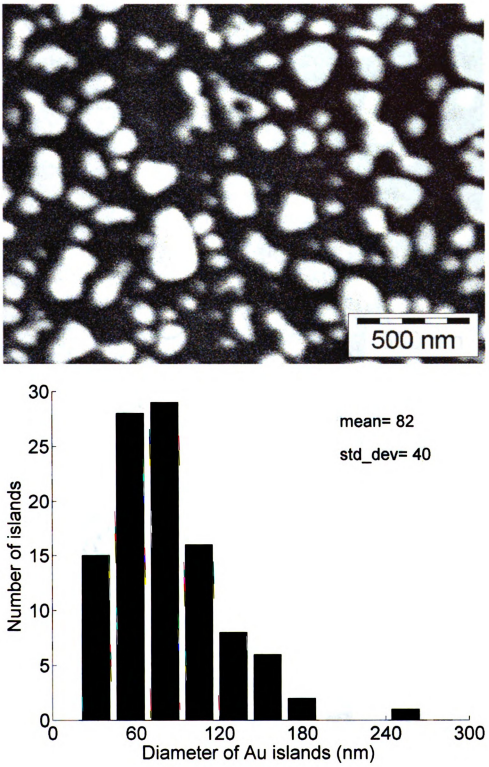

Figure 5-19. SEM image and particle size distribution for 15 nm Au film.

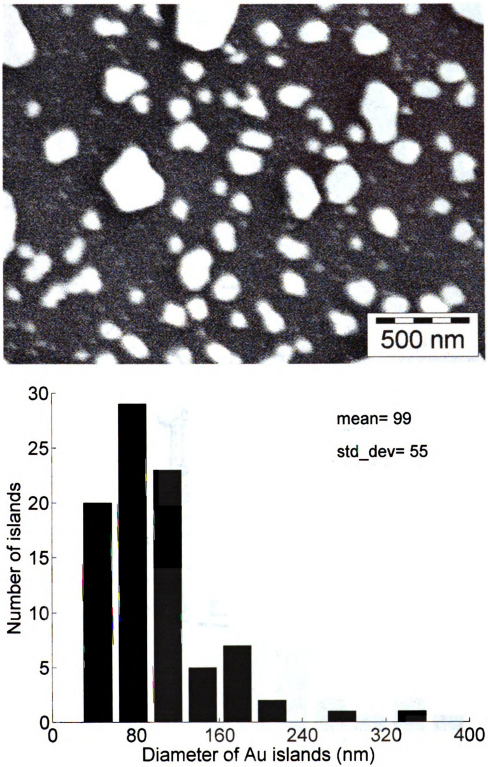

Figure 5-20. SEM image and particle size distribution for 21 nm Au film.

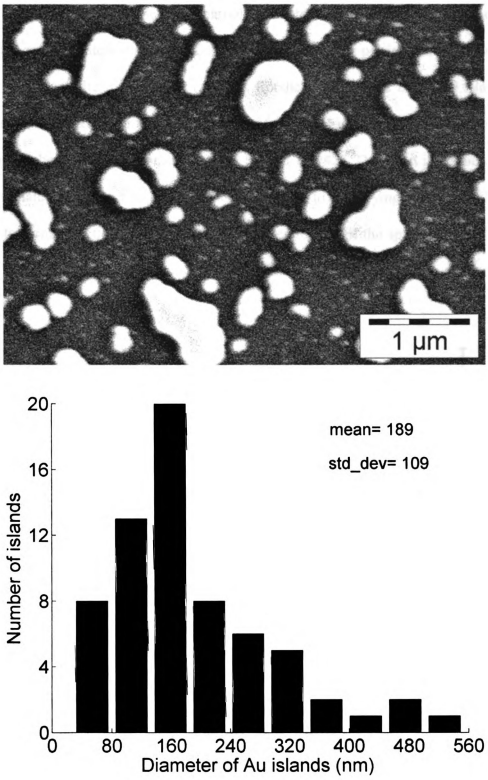

Figure 5-21. SEM image and particle size distribution for 28 nm Au film.

Figure 5-22 shows the mean particle diameters for different film thickness and relation is approximately linear. It may be emphasized that the particle size distribution is in line with the earlier reports. For example, Borshch *et al.* found the metal island size distribution has spread from 10 - 250 nm for 15-25 nm thick vacuum sputter coated Au film on polished glass after annealed at 740 K for 1 hr[142]. Though it is not possible to directly relate island sizes in our case since we differ in underlying substrate (silicon is known to form eutectic with Au), time and temperature. Still the spread of metal island sizes is comparable (we get 25 – 360 nm for thickness 15-21 nm).

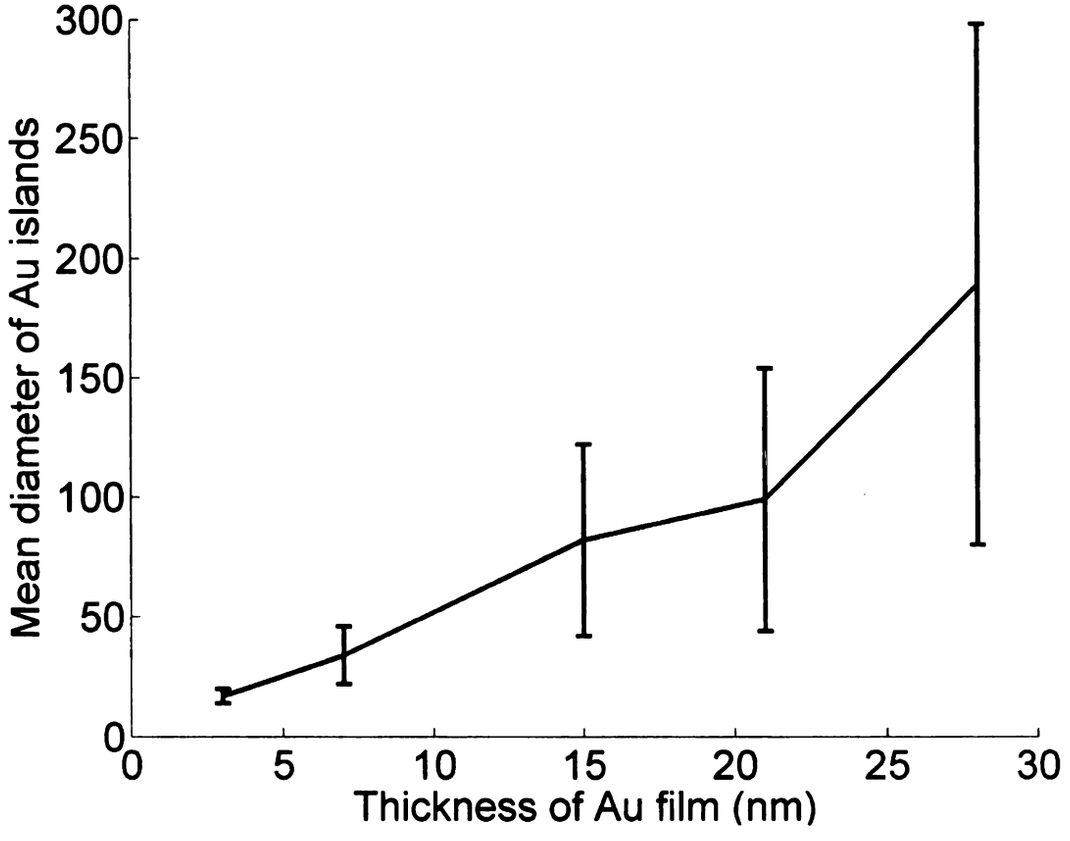

Figure 5-22. Mean particle size distribution for different initial Au film thickness at 500 °C. Error bars indicate standard deviation from mean.

5.4.

wit

subs

usin

char

show

5.4.1.2 Effect of gold film thickness on diameter of nanowires

The diameter dependence of NWs was investigated by coating silicon substrates with different initial thickness of gold films. The GeO_2 NWs were synthesized from these substrates under similar experimental conditions. The diameter measurements were done using SEM images. For each substrate, NWs from at least three different areas were characterized to ensure a greater generality of results. **Figure 5-23** through **Figure 5-25** show the diameter distribution for NWs synthesized from 7 - 21 nm thick Au films.

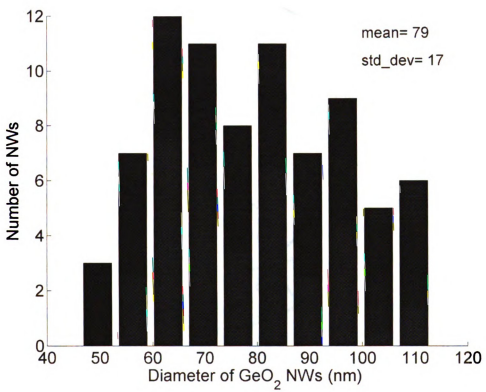

Figure 5-23. GeO_2 NW diameter distribution for 7 nm Au film.

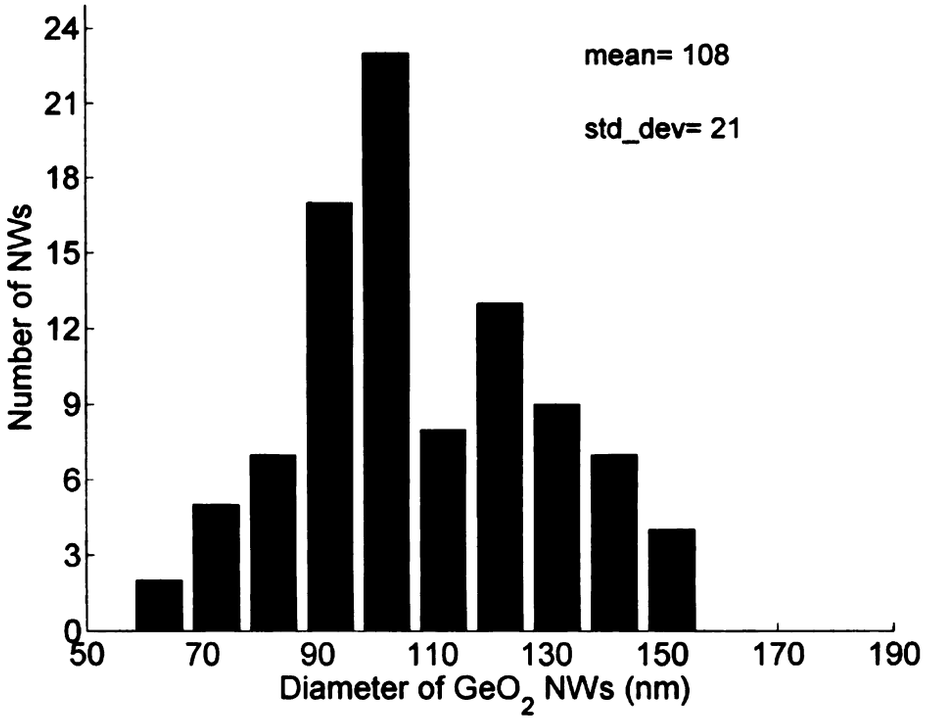

Figure 5-24. GeO_2 NW diameter distribution for 14 nm Au film.

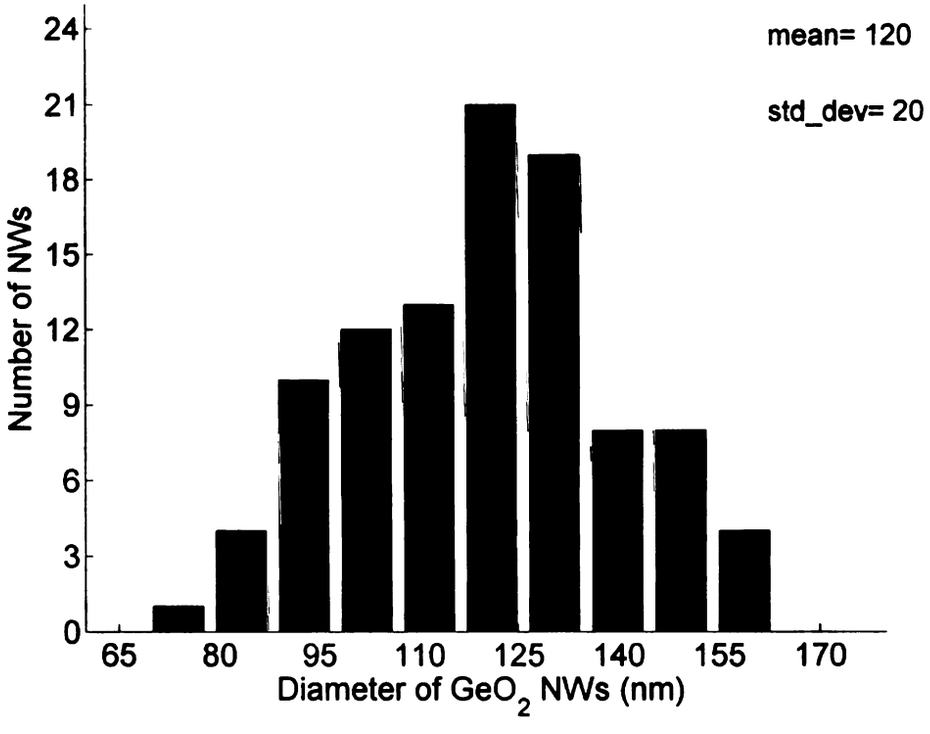

Figure 5-25. GeO_2 NW diameter distribution for 21 nm Au film.

The diameters of annealed Au islands and NWs for different gold film thickness are plotted in **Figure 5-26**. Although the diameter of the NWs is not the same as the corresponding measured Au island size, the diameters of the synthesized NWs do have a one-to-one correspondence with the measured particle diameters for that film thickness. An obvious explanation for the increase in the size of NWs compared to corresponding eutectic particle is that the liquid alloy catalyst can not move up another atomic layer until the entire layer under that droplet is formed. For a larger diameter liquid alloy droplet, a larger capture cross-section exists for gathering GeO molecules from the gas phase, however a larger volume also exists which must be supersaturated before the next atomic layer is added to the end of the nanowire. The increased volume of the liquid alloy is reflected in the larger diameter of the corresponding NWs. Another observation that relates to the large size difference between the initial gold particles and the NWs for very thin gold films. This can be attributed to the Gibbs-Thomson effect that prevents growth of very small diameter NWs for a given degree of supersaturation. This happens due to higher vapor pressure for sharp curvatures (small diameter) and the growth of very thin NWs becomes thermodynamically unfavorable.

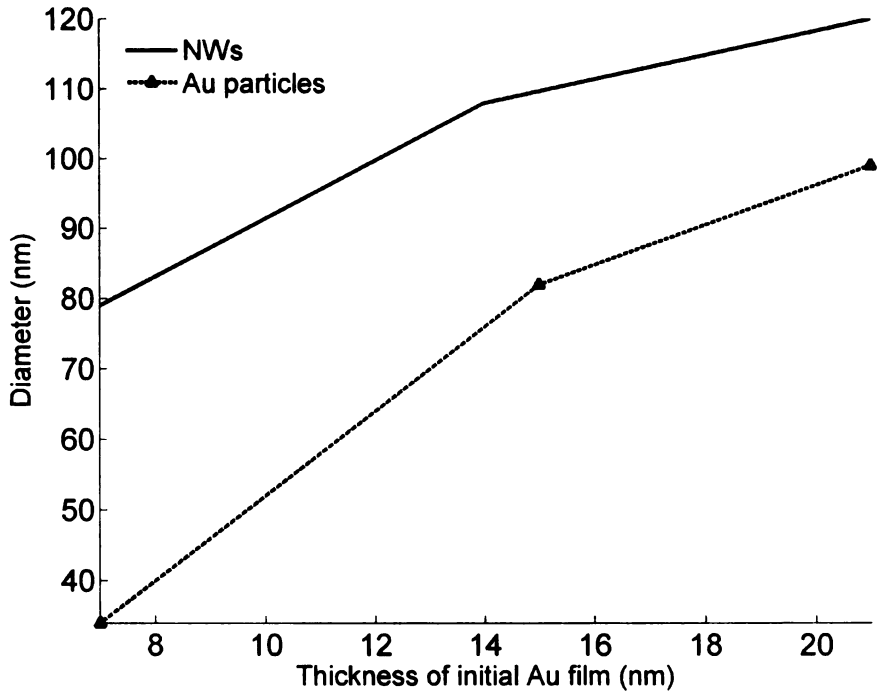

Figure 5-26. Mean diameters of GeO_2 NWs and annealed Au film particles.

5.4.2 Effect of growth time on length of nanowires

In the VLS growth mechanism, the length of the NWs is controlled by growth time. The NWs were synthesized for different length of time while keeping the rest of the experimental conditions the same. The lengths of synthesized NWs were measured using SEM images. The length of nanowires, however cannot be precisely measured from top view images of substrates since NWs are located at random orientation on the substrate and the SEM image just gives the top projection. To avoid this difficultly, cross-sectional images were taken as shown in **Figure 5-27** for different lengths of growth time. It is obvious that the length of NWs is directly related to the growth time. The same relationship can be more clearly evident in **Figure 5-28**. Here one can see that the length

is almost linear with the growth time. For thinner metal catalyst films, the length of the NWs is somewhat longer than thicker metal catalyst films for same growth time. This is not unexpected, as thinner will tend to grow faster for same degree of supersaturation of vapor phase species.

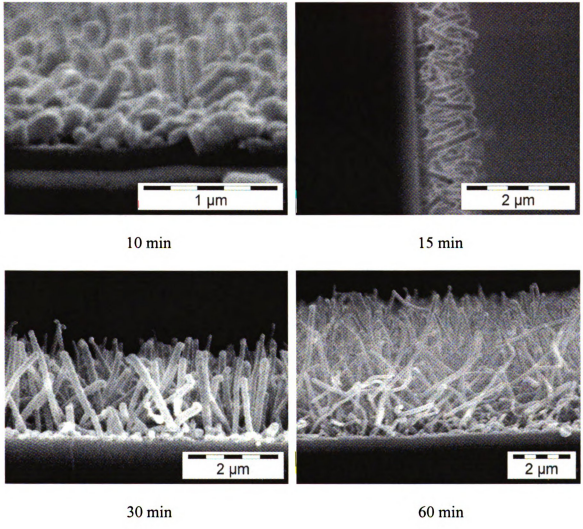

Figure 5-27. Effects of growth time on the length of the NWs.

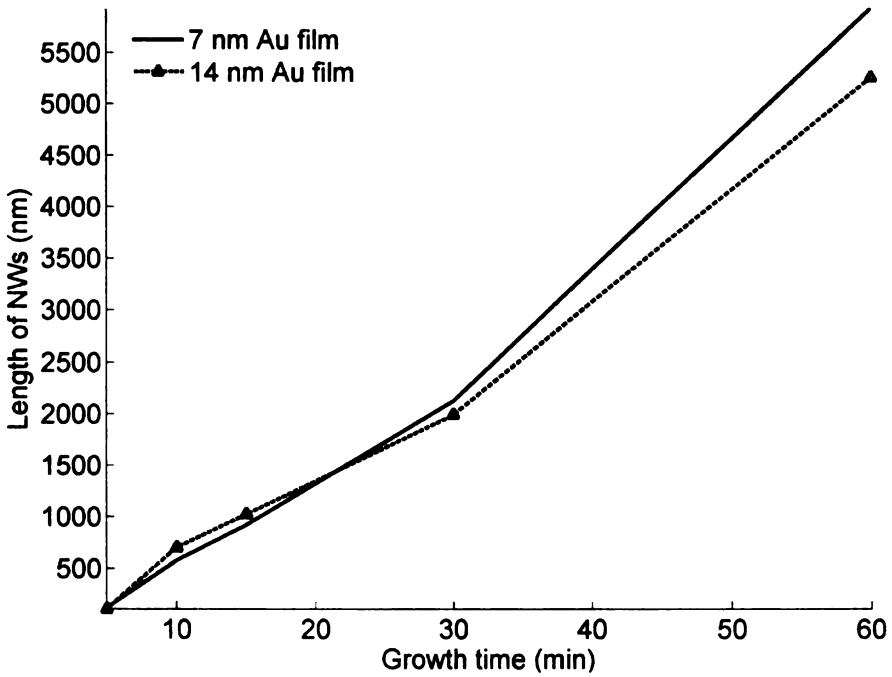

Figure 5-28. Length of NWs versus growth time.

5.4.3 Effect of oxygen flow rate

The synthesis was found to be very sensitive to oxygen concentration as discussed in the section on kinetics of reaction. **Figure 5-29** shows NWs synthesized on a silicon substrate coated with 7 nm Au catalyst film for different concentrations of oxygen. The oxygen concentration is controlled by varying the flow rate of the oxygen in the chamber while keeping the total flow rate constant. As can be seen, the best growth is obtained for an oxygen flow rate of 5-15 sccm (corresponding background gas flow of 55–45 sccm). Low oxygen flow results in an oxygen deficient synthesis. This decreases the probability of forming GeO_2 on the source surface that can inhibit further oxidation of the source. On the other hand, the low oxygen concentration results in a decreased growth rate. Increasing the oxygen concentration leads to longer NWs due to increased transformation

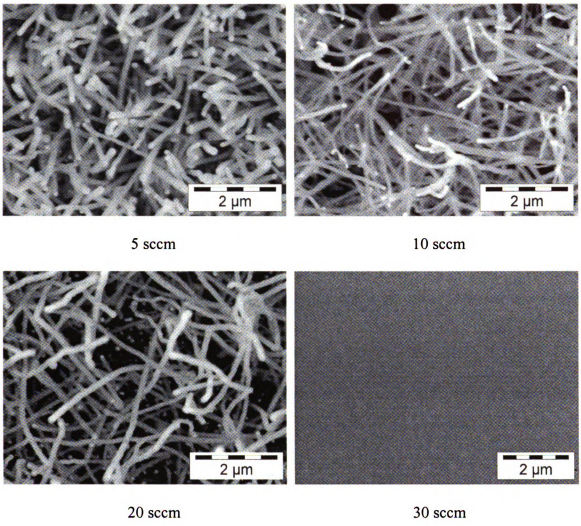

Figure 5-29. Effect of oxygen concentration on NW synthesis.

of sub-oxide into more stable GeO_2. The growth was found to completely vanish for flow rates of 30 sccm or more. It is interesting to note the substrate did get a GeO_2 coating for the 30 sccm gas flow rate (Ar with 40% oxygen) but no NWs were formed. The EDS studies showed Ge:O ratio of 27:66 whereas the case of a 20 sccm flow rate with NW showed a ratio of 23:61. This implies that the substrate is almost getting the same amount of reactants for the oxygen flow rates of 20 and 30 sccm with very different

NWs results. It is suspected that the higher oxygen is resulting in an increased formation of GeO_2 in the vapor phase. This GeO_2 then condenses on the substrate but the absence of GeO prevents growth of NWs. Perhaps GeO is depositing on the wet Au droplet, then forming GeO_2 either while still in the Au, or on the surface of the Au ball, or it is forming a short section of the nanowire as a GeO nanowire that then converts to GeO_2 as suggested in the growth model. The incorporation of some GeO_2 during growth explains the roughness seen on the nanowires. The concentration of oxygen affects the balance of GeO and GeO_2 on the substrate and inhibits the nanowire growth beyond an optimal value.

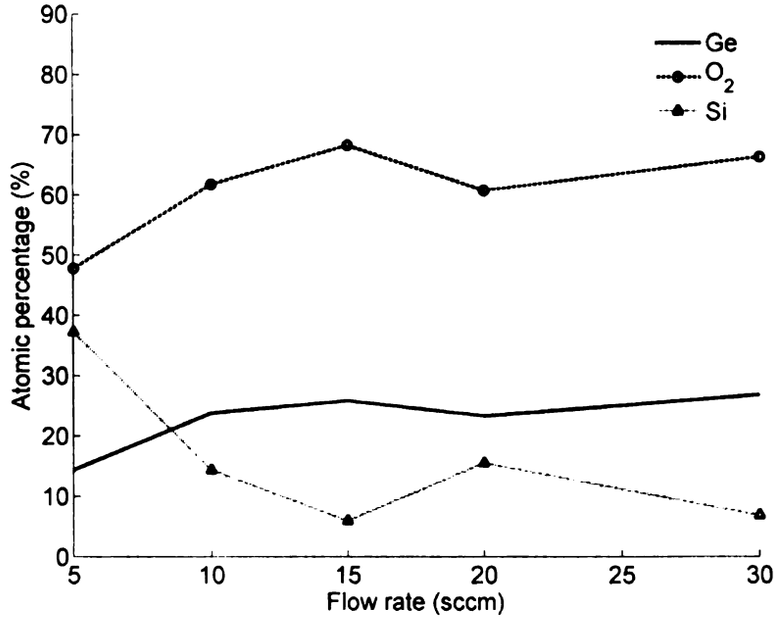

Figure 5-30. Elemental composition of the sample surfaces after growth for different oxygen concentrations.

Figure 5-30 shows the results of EDS study of substrates for different flow rates of oxygen. It is interesting to see how the silicon composition varies for different flow rates. Silicon being the underlying substrates, its composition gives an indirect estimate of the density and length of the NWs. As discussed earlier, the low flow rate yields shorter NWs so we get higher silicon signal for low flow rates. It decreases as the density and length of NWs increases for increasing flow rate. However, it tends to increase for higher flow rate (around 20 sccm) where the density tends to diminish. Silicon concentration shows a decreasing trend at higher flow rate (~30 sccm) that can be attributed to formation of relatively uniform GeO_2 coating instead of NWs.

5.4.4 Effect of background gas flow rate

The effect of background flow rate was studied by varying the flow rate while keeping all other parameters like catalyst thickness, growth time, and temperature the same. **Figure 5-31** shows NWs synthesized on silicon substrate coated with 7 nm Au catalyst film for different background gas flow rates. It is evident that the best growth occurs for a background flow rate of ~ 60 sccm. The lower and higher rates yield sparse growth of NWs. Low flow rate, implying lower oxygen concentration, decreases the formation of the vapor phase reactants and the degree of supersaturation. This decreases the yield of NWs as is the case for 33 sccm gas flow rate. On the other hand, high flow rate means fast transport of source material through the reaction zone (to maintain constant pressure) and this decreases the probability of incorporation into the NWs. Another effect could be the cooling and/or rapid source vapor drift associated with the high flow rate that reduces local temperature at the substrate to decrease NWs yield.

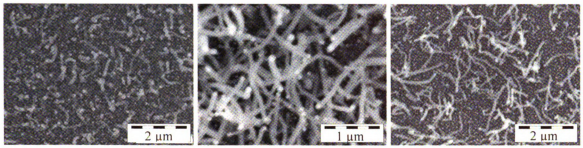

33 sccm 60 sccm 120 sccm

Figure 5-31. Effect of background gas flow rate on NWs synthesis.

5.4.5 Effect of temperature

Temperature has pronounced impact on NWs yield. **Figure 5-32** shows the SEM images of NWs observed at different substrate temperatures from 600 – 400 °C. The yield of the NWs was found to be optimum in the range 400-500 °C. All experiments were carried out with Ar (mixed with 5% hydrogen) as background gas at a flow rate of 50 sccm and 10 sccm of Ar (with 40% oxygen) was used to synthesize NWs. The substrates only show randomly distributed and interconnected clusters containing small particles (bright spots) at high temperature (601-591 °C). These clusters tend to diminish in size leading to more isolate islands as the temperature decreases (577-561 °C). The isolated growth from 2D to 3D can be seen at ~533 °C where few nanostructures appear to grow. The substrate at ~523 °C shows a number of isolated and long nanowires. The yield of nanowires can be seen to increase for the lower temperature regions. The low yield at higher temperature is probably due to less sticking of the high energy volatile GeO on the substrate.

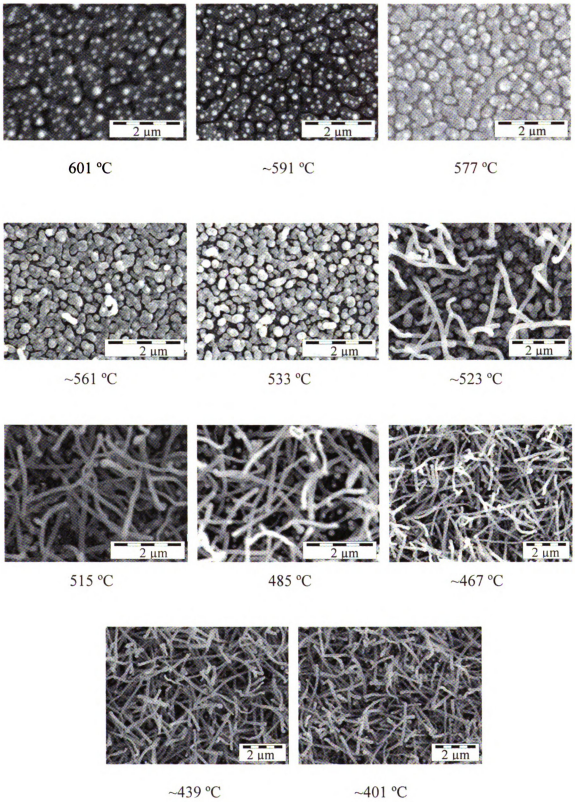

Figure 5-32. GeO_2 NW growth at different temperatures.

5.4.6 Background gas type

Although most of the nanowires were synthesized using a mixture of Ar (95%) and hydrogen (5%), some experiments were carried out using pure Ar or N_2 as a background gas. The morphology of the NWs synthesized using different gases turned out to be different. **Figure 5-33** shows the some of GeO_2 NWs obtained for using Ar as background gas. There have been large variations in the morphology of yield from NWs to nano-particles. Similar types of morphologies were noted for NWs synthesized with N_2 background as shown in. **Figure 5-34**.

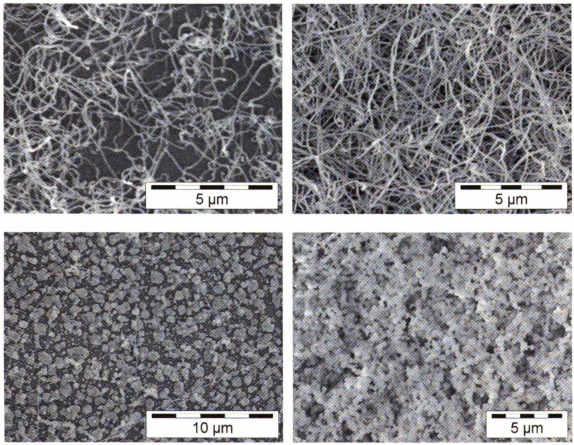

Figure 5-33. SEM images of GeO_2 NWs synthesized using Ar as background gas.

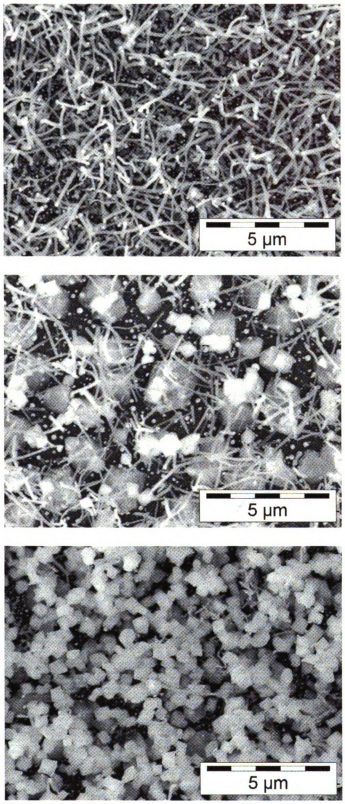

Figure 5-34. SEM image of GeO_2 NWs synthesized using N_2 as background gas.

Th

investigat

hydrogen

or stops

depender

smaller c

substrate

condensa

different

Torr) du

The diameter of NWs obtained using different background gases was also investigated and is shown in **Figure 5-35**. The smallest diameter is obtained for Ar and hydrogen mix. This is probably due to reducing affect of H_2, which in a way etches away, or stops lateral development of oxide NWs. The diameter versus gold film thickness dependence is similar for the case of Ar and N_2. The Ar background, however results in smaller diameter wires than when N_2 is used. One possible reason could be greater substrate cooling with N_2 that has a greater thermal conductivity resulting in higher condensation of vapors leading to larger diameter wires. Another reason could be a different actual pressure inside the tube than the one measured (synthesis done at ~ 2 Torr) due to different response of pressure sensor to different gases.

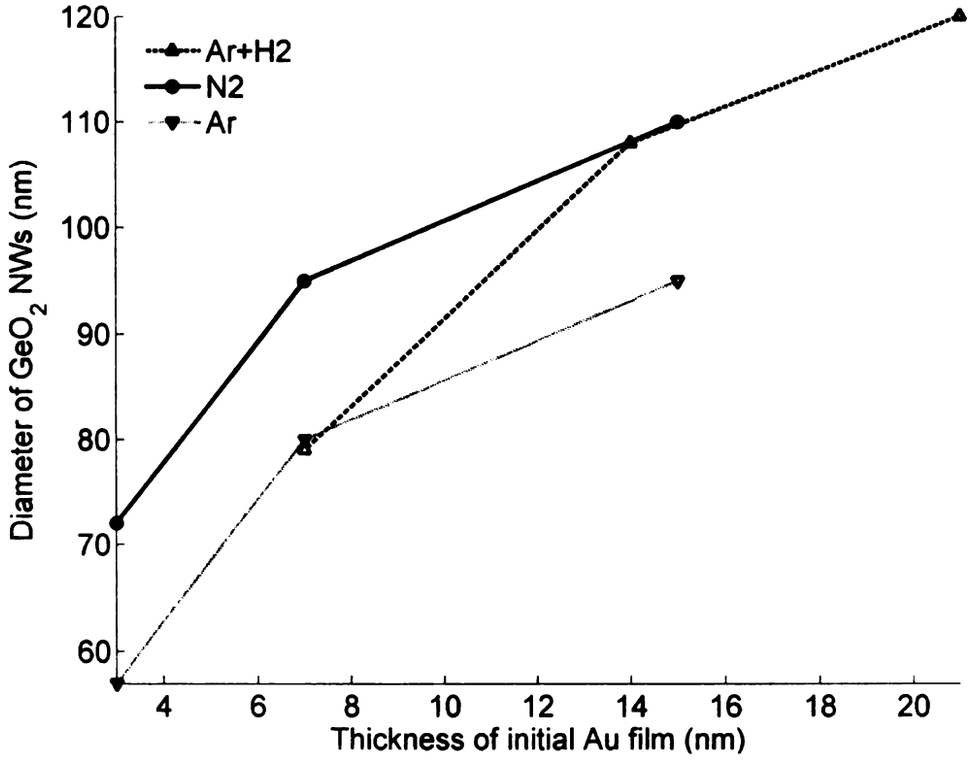

Figure 5-35. GeO_2 NWs diameters for different background gases.

Another effect of background gas type is noticeable from the appearance of the substrate. The substrate was found to have white dots distributed randomly as was the case when Ar with H_2 was used as background gas. However, the density of such island like formations of NWs was found to be much greater for N_2 and Ar background as shown in **Figure 5-36** and **Figure 5-37** respectively. The islands are actually formed of dense, long and curved nanowires. The density and thickness of the NWs in island area can be gauged from the EDS signature that doesn't show any Si signature.

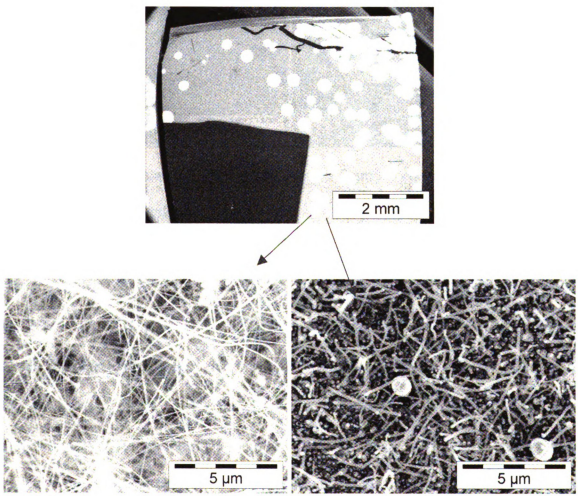

Figure 5-36. Island like growth of NWs for 7 nm Au coated Si substrate with N_2 as background gas.

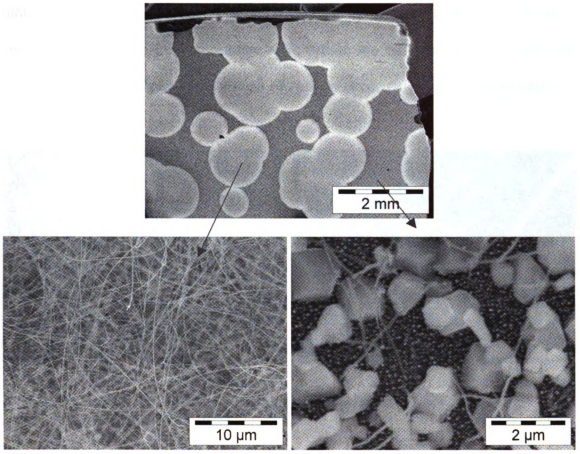

Figure 5-37. Island like growth of NWs for 7 nm Au coated Si substrate with Ar as the background gas.

Another interesting effect of the background gas lies in the temperature at which the NWs can be obtained. In case of Ar and H_2 environment, the best growth was obtained in the temperature region 400-500 °C. Although NW growth was observed in this temperature region for N_2 and Ar background, the morphology of the structures varied from NWs to particles. On the other hand, significant NWs growth was found at higher temperatures in case of Ar background gas. **Figure 5-38** and **Figure 5-39** show the GeO_2 NWs found at the high temperature (~600 °C) region of the furnace for catalyst

film thickness of 7 nm and 15 nm respectively. It is evident that the NWs are much longer than the typical low temperature NWs seen in low temperature regions. Another difference is the morphology where these NWs show strong curvature and sharp turns.

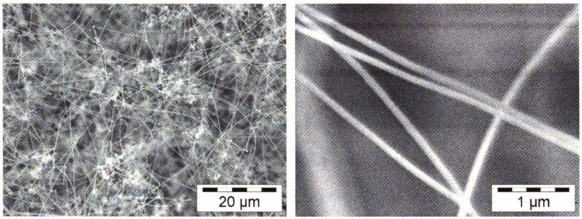

Figure 5-38. GeO_2 NWs found at higher temperature region of furnace on 7 nm Au coated Si substrate.

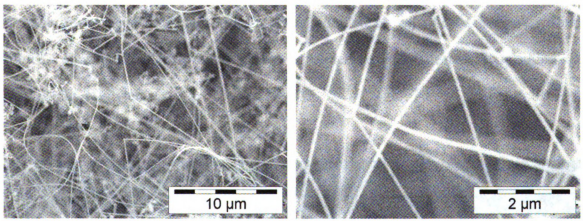

Figure 5-39. GeO_2 NWs found at higher temperature region of furnace on 15 nm Au coated Si substrate.

5.4.7 Effect of background gas pressure

The background gas pressure at the start of the reaction affects the yield of the NWs by changing the degree of supersaturation in the gas phase. Background gas pressure mainly helps to confine the gas phase reactant near the source and substrate. **Figure 5-40** shows NWs synthesized on Si substrate having different Au film thickness at background gas pressure of 1.1 Torr. All three substrates show sparse growth indicating background pressure is insufficient to yield enough supersaturation of vapors for efficient NWs growth. **Figure 5-41** shows the NWs synthesized on Si substrates with 7 nm Au coating at a background pressure of 6 Torr. Here, we see a strong location dependent growth of NWs depending upon the proximity of the substrate to the source material. There is some NW growth at the upstream end (closer to source) of the substrate but diminishes sharply within few mm away from it. This can be explained by the effect of high background gas pressure that keeps the reactants localized and only those parts of the substrate close to source get enough vapors to initiate growth. As we move away from source, concentration of vapor phase or supersaturation decreases resulting in diminishing NW yield.

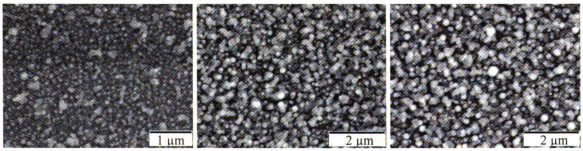

7 nm Au 14 nm Au 21 nm Au

Figure 5-40. NW synthesis at a background gas pressure of 1.1 Torr.

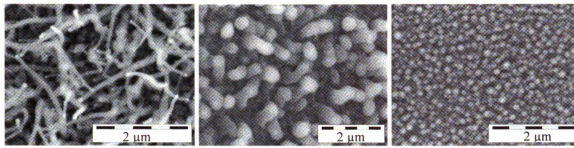

Upstream end 5 mm 10 mm

Figure 5-41. NW synthesis at a background gas pressure of 6 Torr shows location dependent growth.

5.5 Raman characterization of GeO_2 nanowires

The Raman system used in this study was EzRaman-L from Enwave Optronics Inc. with 6 cm^{-1} resolution at 785 nm excitation. The sample was mounted on a xyz-stage and illuminated by the Raman system laser beam via optical fiber link. The Raman probe head was attached to a z-stage that facilitates precise focusing of laser beam onto the sample surface. All spectra were acquired with a focusing lens (N.A. = 0.22) that yields a spot size of less than 100 μm diameter on the substrate. The laser power on the substrate was nearly 30 mW as measured with Newport optical meter (model 815 in conjunction with 818-SL detector and 883-SL attenuator).

5.5.1 Raman spectra of substrate

The bare substrate containing GeO_2 nanowires were first scanned by Raman system to get the reference signal and to ensure no impurities are present that might cause interference with the Raman signal. **Figure 5-42** shows the Raman spectra of GeO_2 nanowires of two different diameters synthesized on Si(100) by using different initial

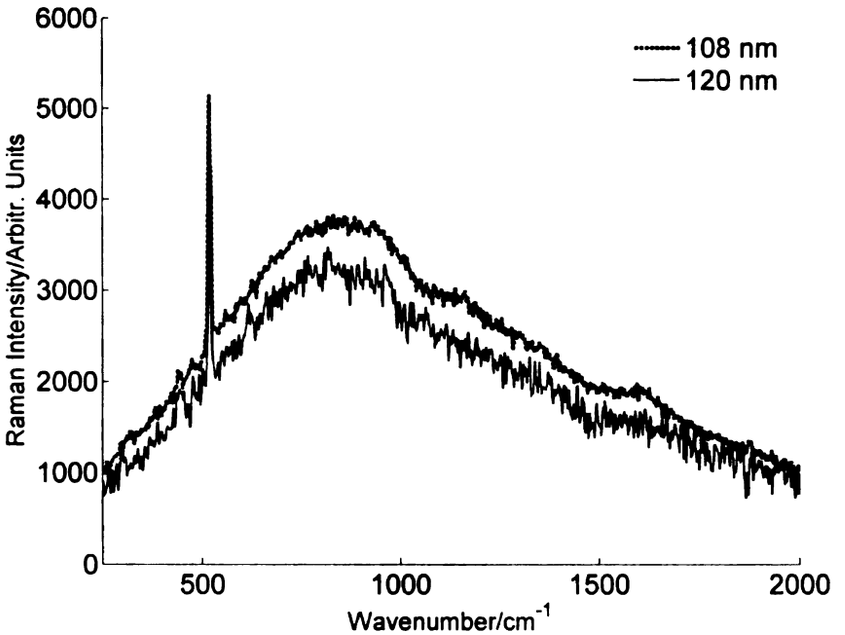

Figure 5-42. Raman spectra of GeO_2 NWs of different diameters, t_{acc}=15 s.

catalyst film thickness. Unlike the case of high temperature growth, here only the main peak at ~444 cm^{-1} is noticeable. Also the strong substrate peaks at ~ 520 cm^{-1} alongwith a broad background is clearly visible. This broad background is similar to the one we observed after coating high temperature synthesized NWs with Au. We speculate that the source of this background comes from the Au catalyst for NW growth. The Au coating breaks down into isolated islands to act as nucleation sites for NW growth in the VLS mechanism. A portion of these gold particles ends up at the tip of the NWs while some are broken off during the process. Yet another part may stay on the substrate and it is the combination of these isolated Au particles that are giving rise to a broad background. The main difference from the high temperature growth lies in the amount of GeO_2 deposited on the substrate. The high temperature growth has a large quantity of GeO_2 deposited at a

high rate and the Au is buried under it. This gives strong GeO_2 spectra but weak scattering from the Au and thus a relatively small broad background signal is measured. Conversely, low temperature growth has little GeO_2 to give a strong Raman peak but relatively large Au content and a correspondingly larger broad background signal is measured. As mentioned before, the low temperature short NWs growth is accompanied by isolated island of long NW as was shown in **Figure 5-10**. The Raman spectra from the uniform short NWs and those in the white island region are shown in **Figure 5-43**. Here, we clearly see the main Raman peak of GeO_2 is more prominent but background is substantially reduced for high density of NWs in the white island region. This directly supports that the greater amount of NWs is responsible for the stronger spectra and the

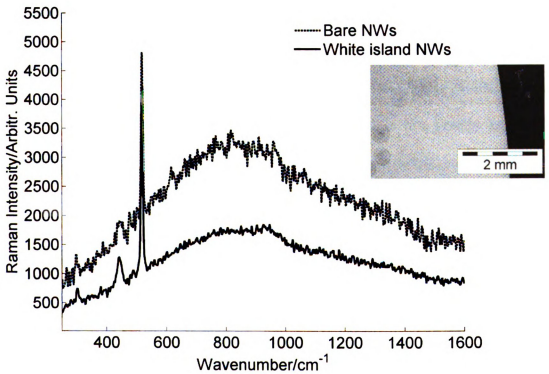

Figure 5-43. Raman spectra for two different morphologies of NWs.
Insert shows SEM image showing circular islands on uniform background.

relatively less Au compared to GeO_2 results in a smaller broad background signal. Nevertheless the Raman spectrum main peak at 444 cm^{-1} is evidence of trigonal GeO_2.

5.5.2 Gold coating of GeO_2 nanowires

The as prepared nanowire substrates are not suitable for SERS since only noble metals are known to yield strong enhancement. The substrates were made SERS active by coating with thin film of gold that allows excitation of surface plasmons. The coated substrates were characterized by Raman system before application of analyte to establish background signals. **Figure 5-44** shows the observed Raman spectra of 12 nm gold-coated nanowires with 15 s of integration time. The Raman spectrum after Au coating shows an increase in the intensity of the broad continuum over all wavenumbers peaking at about 800 cm^{-1}. It is clear from **Figure 5-44** that the gold coating is causing an increase in the intensity of the broad background. Such a broad continuum is commonly observed in SERS studies but the source of broad background is not exactly known. Some researchers attribute it to electronic Raman scattering from metal[116, 117] while others consider it luminescence[118]. It is a common observation that the molecular SERS spectrum is accompanied by a broad background covering most of the normal 0-3000 cm^{-1} range[73]. In our case, the broad background appears following the metal coating of nanowire substrate. Since the background continuum is present even before the application of analyte molecule, the most probable cause of the continuum is the electron scattering off defects from the rough gold film covering the nanowires. This allows for electronic Raman scattering over a broad energy range[39]. Further understanding of the

broad continuum is of interest, however for the purpose of detection measurements it can be removed through a baseline correction algorithm.

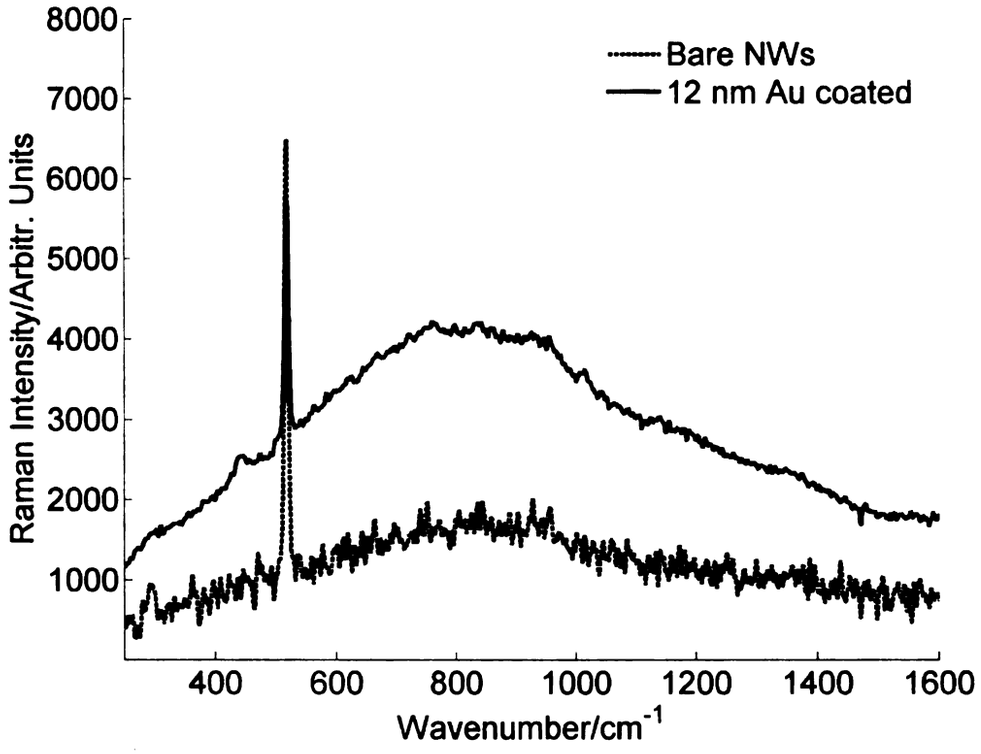

Figure 5-44. Raman spectra of bare and 12 nm Au coated GeO_2 NWs, t_{acc}=15 s.

Similar broad continuum was observed for different thickness of Au film with more or less identical shape of spectrum. For example, **Figure 5-45** shows the Raman spectra from GeO_2 NWs having an average diameter of 108 nm after coating of 12 nm, 23 nm, and 35 nm thick Au film and similar broad background appears after coating. The introduction of continuum in the Raman spectrum is not fully understood yet and needs further investigation. It usually arises due to fluorescence but it is known that fluorescence is quenched in the vicinity of metal. The observed continuum is similar to

florescence and is introduced by the metal or the deposition process. The investigation of Raman spectra of flat silicon wafer with Au film thickness has revealed a decreasing trend of Raman intensity with increasing film thickness as expected from theory. However, it is postulated that the broad background appearing in SERS active substrates is characteristic of the rough metal film, which is inherently composed of discontinuous islands as revealed by TEM study of Au coated NWs. This can be used to explain the intensity trend seen in **Figure 5-45**. As the film thickness increases, we see an initial increase in the background intensity but then it starts to decrease for thicker films. This can be attributed to the Oswald ripening of the individual isolated island towards a more continuous film. Similar trend can be seen in case of a different substrate that was synthesized with 120 nm average diameter NWs as shown in **Figure 5-46**.

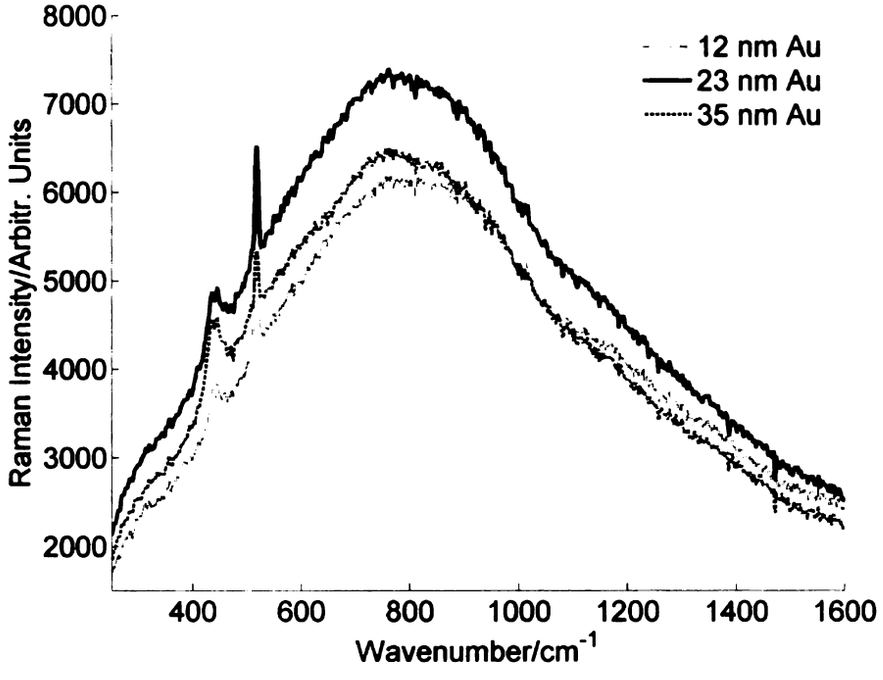

Figure 5-45. Raman spectra of Au coated GeO_2 NWs of average diameter 108 nm, t_{acc}=15 s.

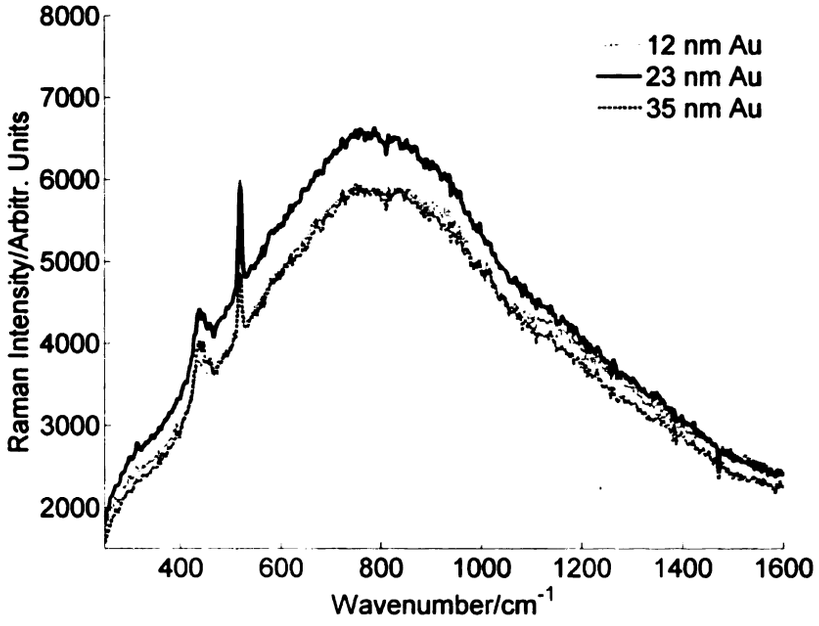

Figure 5-46. Raman spectra of Au coated GeO_2 NWs of average diameter 120 nm, t_{acc}=15 s.

It is also useful to look at the effect of application of analyte on the substrate. This is especially critical with nanostructures since the drying of the analyte containing solvent exerts strong capillary forces that can deform the nanowire structures. **Figure 5-47** shows the SEM image of the substrate before and after application of analyte. The substrate was soaked in 1mM methanolic 4-MBT solution for 12 hr and allowed to dry before imaging. It is clearly seen that the nanowires tend to bundle together after application of analyte. This is due to the capillary forces generated as the liquid dries and has been observed in the past as well. For example, Chen *et al.* reported clustering of InP nanowires in the form of shrubs after application and drying of analyte solution[143].

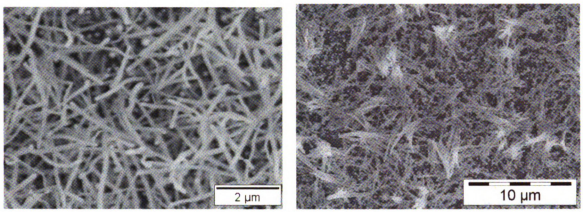

Figure 5-47. SEM images of substrate before (left) and after (right) 12 hr soak in 1 mM methanolic MBT.

5.6 SERS evaluation of substrates

SERS performance of the synthesized NWs was evaluated using commonly employed thiols analytes. SERS analyte molecules 4-methylbenzenthiol (purity 98%) and 1,2-benzenedithiol (purity 96%) were purchased from Sigma-Aldrich and used without further purification. **Figure 5-48** shows the molecular structure of analyte molecules used in this study. The diluted solutions with various concentrations were prepared in methanol (99.8% HPLC grade) and stored in glass vials.

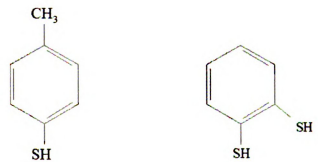

Figure 5-48. Chemical structures of 4-MBT and 1,2-BDT used as Raman analytes.

5.6.1 Detection of 4-MBT

The first analyte for SERS evaluation of low temperature synthesized GeO_2 nanowires was 4-MBT. The aromatic thiols are known to form self-assembled monolayers (SAMs) on gold, silver, and copper[125]. It has been reported that MBT forms a self assembled monolayer on gold after 12 hr soak in 1 mM or higher concentration[127]. The 23 nm gold coated GeO_2 nanowire substrate was soaked in 1 mM methanolic 4-MBT solution for 12 hrs. After the 4-MBT soak, the substrate was thoroughly rinsed with methanol to remove multilayer and/or crystals that might have formed[127]. The substrate was dried in the stream of nitrogen before acquiring the SERS spectra shown in **Figure 5-49**. An interesting effect is the suppression of the continuous background signal following the formation of the 4-MBT monolayer. **Figure 5-50** shows Raman spectra from five consecutive 250 μm spaced points on the substrate and the characteristic peaks of 4-MBT are easily identifiable. No discernible Raman signal was found from a Si(100) substrate with 21 nm smooth Au film that was soaked in 4-MBT alongside nanowires substrate, confirming the enhancement is indeed from nanowire substrate.

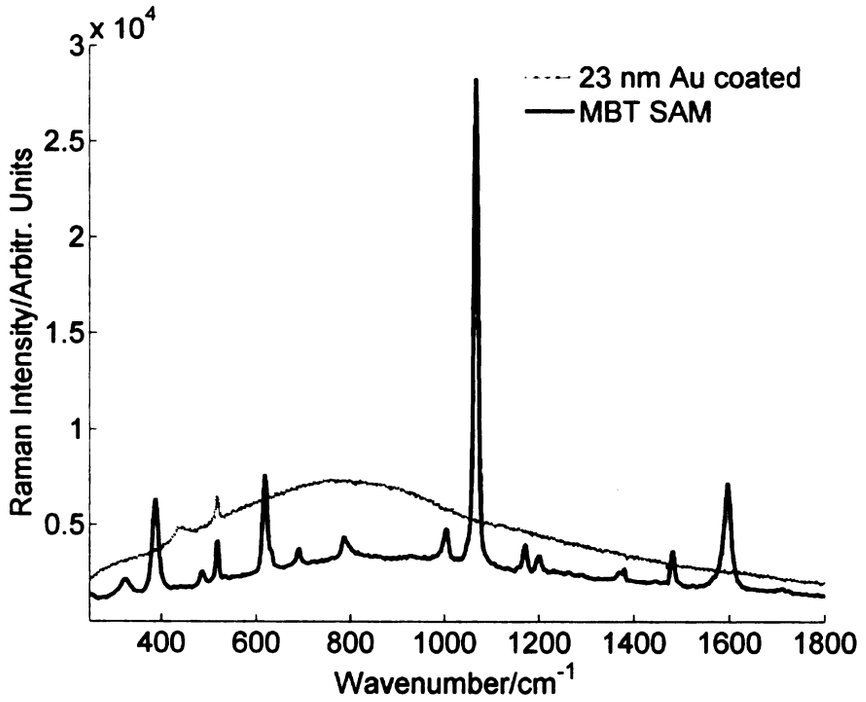

Figure 5-49. SERS spectra of SAM of 4-MBT on 108 nm dia NWs, t_{acc}=15 s.

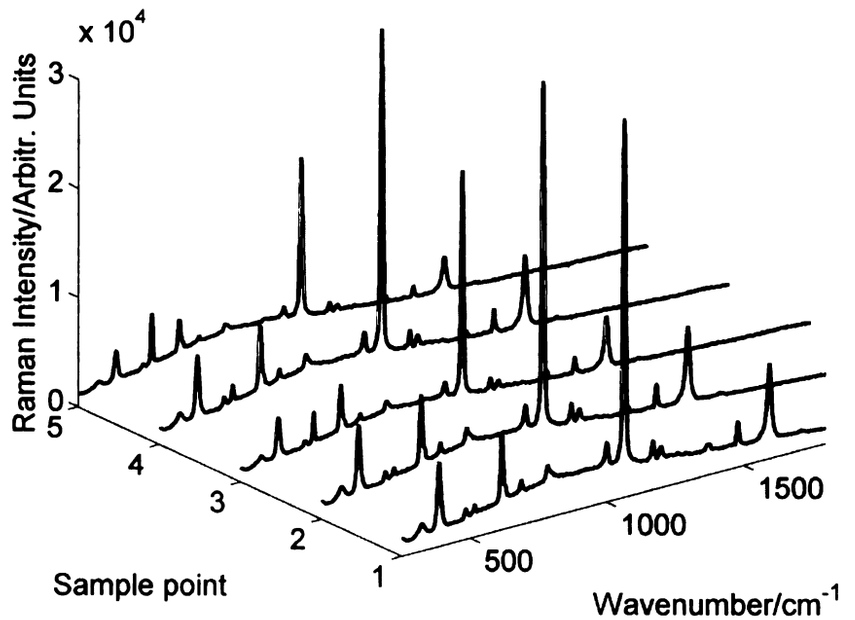

Figure 5-50. Successive spectra from substrate points spaced 250 μm along a line, t_{acc}=15 s..

Having shown good SERS activity of GeO_2 NWs, the next step is to determine the optimal thickness of the Au coating for SERS. Since gold film provides the surface plasmon active surface, its thickness is expected to have a significant impact on SERS from the substrate. To investigate the effect of gold thickness, a systematic study of the Raman enhancement of 4-MBT analyte as a function of Au film thickness was carried out. The substrates having NWs with mean diameter of 108 nm were coated with different thickness of Au film in the range 12 - 55 nm. These substrates were then soaked in 1 mM methanolic 4-MBT solution for 12 hrs, rinsed in methanol and blown dry to form SAM. **Figure 5-51** and **Figure 5-52** shows the SERS spectra for different thickness of Au. The variation of the 1068 cm^{-1} Raman peak of 4-MBT with varying gold film thickness for 108 nm diameter NWs is shown in **Figure 5-53**. As can be seen, the best enhancement is found for coating thickness of 30 – 45 nm. The representative SERS spectra for different film thickness are plotted in **Figure 5-54** and clearly show the dependence of SERS on film thickness. Similar dependence is observed for different diameters of NWs as shown in **Figure 5-55**. Here, the Au film thickness dependence of 1068 cm^{-1} Raman band of 4-MBT is plotted for different diameters of GeO_2 NWs.

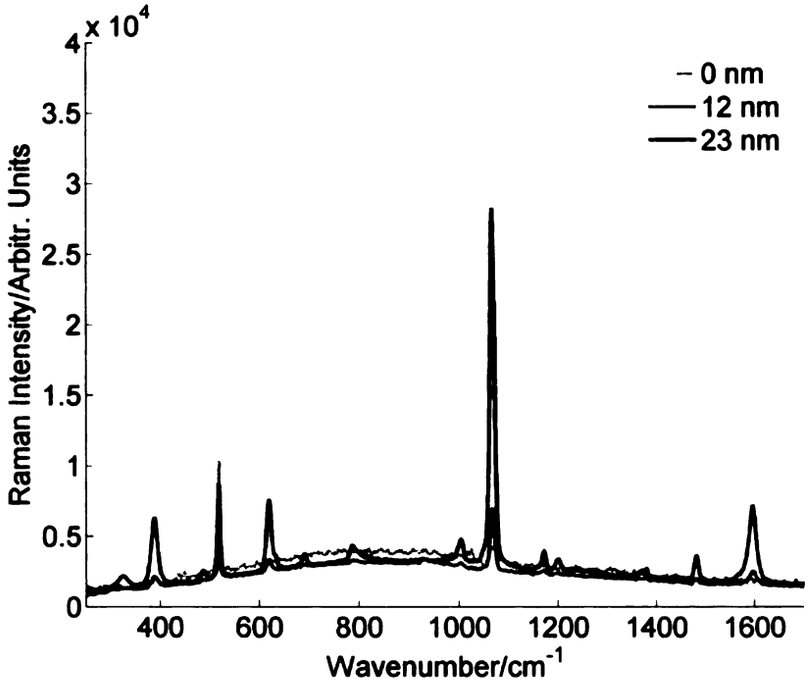

Figure 5-51. Effect of Au coating thickness on SERS activity of substrate having 108 nm mean diameter NWs.

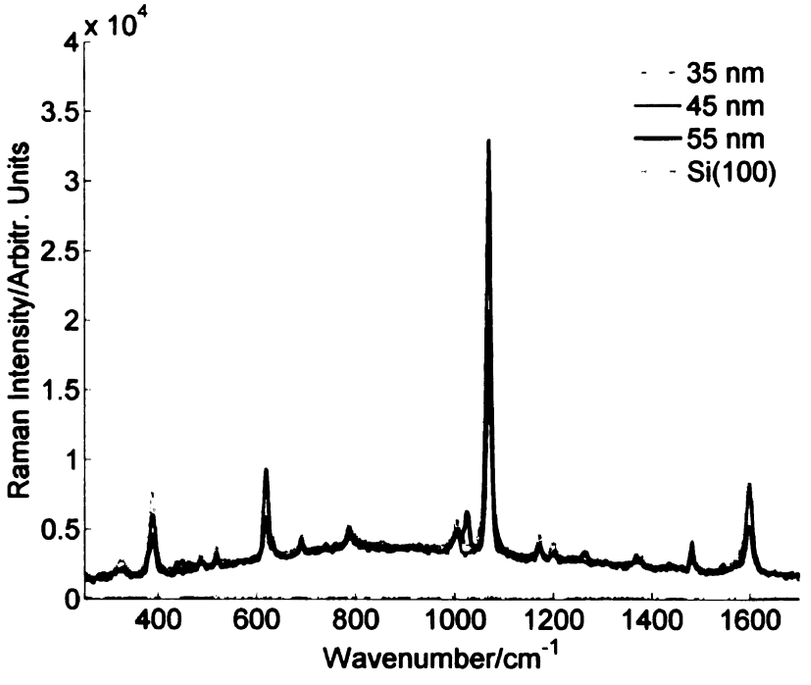

Figure 5-52. Effect of Au coating thickness on SERS activity of substrate having 108 nm mean diameter NWs. Also shown is spectra (along the *x*-axis) from a flat Si(100) with 55 nm Au coating that was soaked in 1mM MBT along with the NWs.

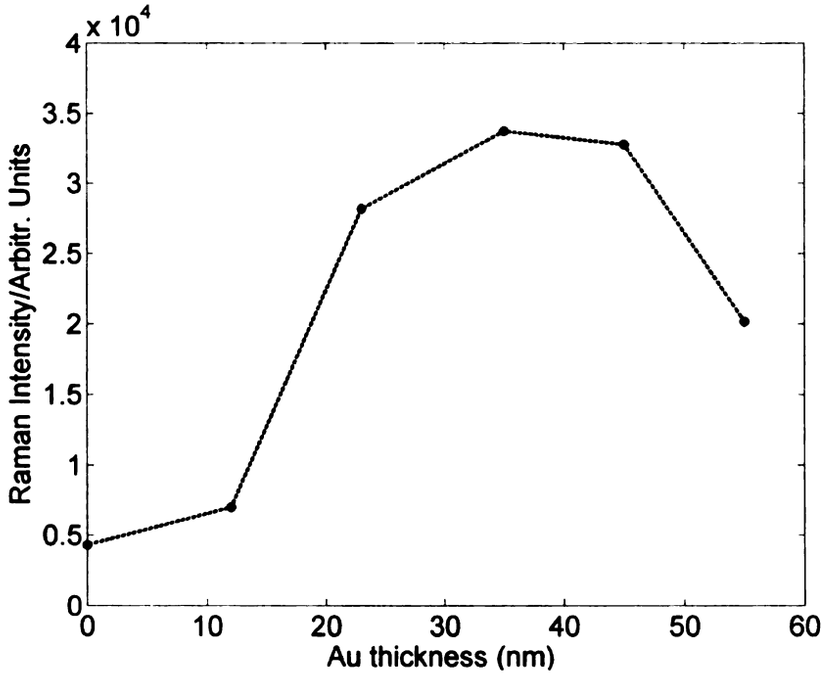

Figure 5-53. Variation of 1068 cm^{-1} Raman peak intensity of 4-MBT with Au film thickness.

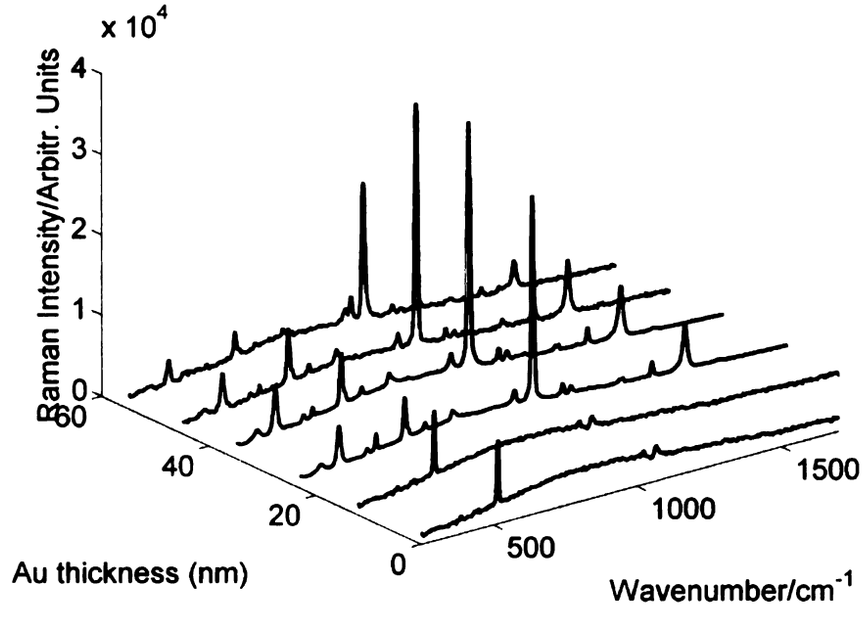

Figure 5-54. SERS spectra of SAM of 4-MBT for different Au film thickness on GeO_2 NWs with 108 nm mean diameter.

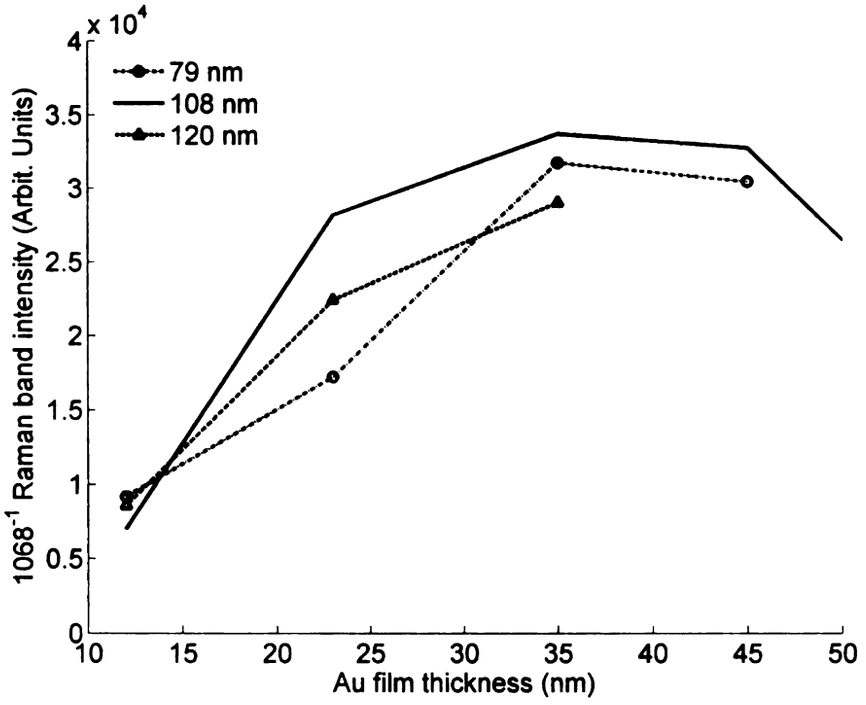

Figure 5-55. Variation of Raman intensity with Au film thickness for different diameters of NWs.

The length of nanowires is another tunable parameter in low temperature synthesis technique. The length dependence of SERS was studied by synthesizing GeO_2 NWs using 14 nm catalyst film for different lengths of time. The mean diameter of the nanowires was found to be ~108 nm whereas average lengths varied from few hundred nm to 10 microns depending upon growth duration. The nanowires substrates were coated with ~40 nm thick Au film and SAM of 4-MBT was formed by soaking in 1 mM methanolic solution for 12 hr. The relative Raman enhancement from different lengths of nanowires was estimated by comparing the Raman intensity of 1068 cm^{-1} peak. **Figure 5-56** shows the variation of the Raman enhancement for different length of GeO_2 nanowires. The maximum enhancement was obtained for nanowires that had average lengths of 700-1000 nm corresponding to 10-15 min of growth time. For longer and

shorter nanowires, the enhancement sharply decreases. It may be noted that the peak enhancement lengths are comparable to the wavelength of exciting laser. An accurate analysis of the enhancement is not feasible due to extremely high complexity of the nanowire substrates resulting from composite nature (Au and GeO_2), non-conformal gold coating and large number of interacting nanowires.

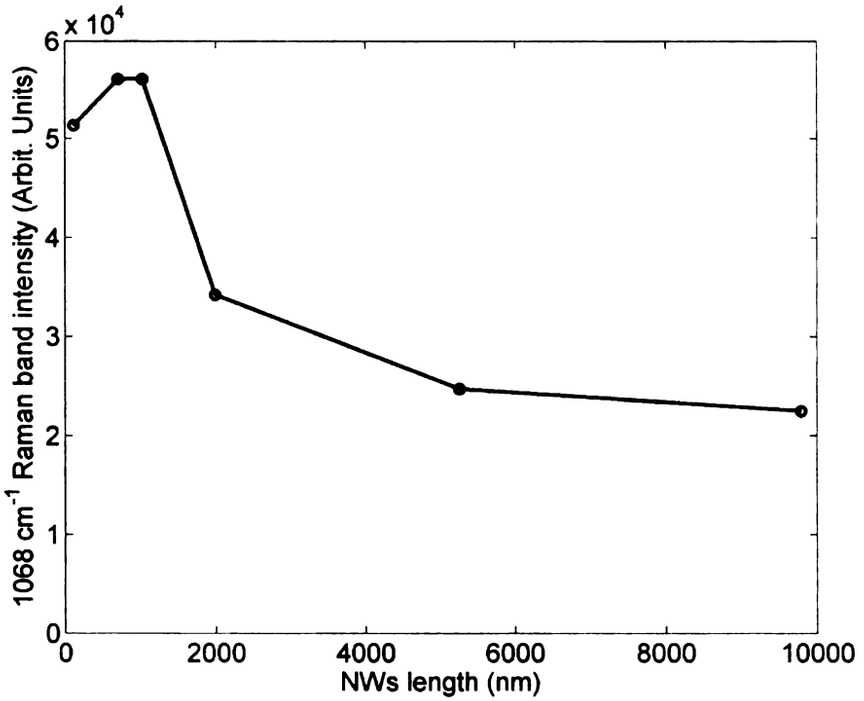

Figure 5-56. Variation of Raman EF with length of GeO_2 NWs coated with 40 nm thick Au film.

The homogeneity of the substrate has been a major issue in SERS research. The reproducibility of SERS measurements from different locations on the substrate was evaluated by acquiring Raman spectra from 100 points covering an area of 2.5 mm × 2.5 mm. Each sample spot was illuminated for 5 s and spectra were collected. The substrate was then moved in x or y-direction by 250 μm and process was repeated to

cover the target square area. The 1068 cm^{-1} Raman band of these 100 spectra is shown in **Figure 5-57** to give a spatial map of enhancement from the substrate. It can be seen that the substrate provides unambiguous and uniform SERS spectra for a monolayer of analyte over the tested area with a standard deviation of approximately 3 % from the mean.

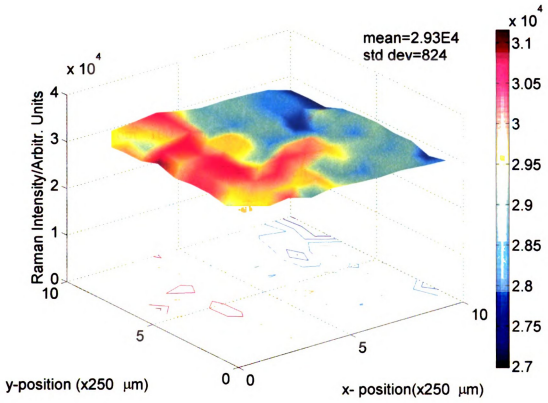

Figure 5-57. Spatial map of SERS intensity for 1068 cm^{-1} peak of 4-MBT.

The experimental Raman enhancement factor (*EF*) for our substrate was calculated using the relationship

$$EF = \frac{I_{SERS}}{I_{ref}} \frac{N_{ref}}{N_{SERS}} \tag{5.7}$$

where I_{SERS} is the Raman intensity of some specific band from the analyte adsorbed on SERS active substrate and I_{ref} is the Raman intensity of the same band from the bulk analyte. N_{SERS} and N_{ref} are the number of molecules that yield I_{SERS} and I_{ref} respectively. Thus equation (5.7) gives the Raman enhancement per molecule for a specific vibrational band of the analyte. The specific band is usually the one that gives the strongest Raman scattering and its intensity is directly read from SERS spectra. An obvious choice therefore in our case is the 1068 cm^{-1} Raman band and we utilize the average intensity from 100 sample points in equation (5.7). Taking 4.5×10^{14} molecules/cm^2 for a monolayer of 4-MBT on gold[130], we find approximately 5.87×10^{-14} moles (3.53×10^{10} molecules) of 4-MBT are exited in the laser spot (100 μm diameter). The determination of N_{ref} is more challenging and different methodologies have been reported to estimate it. Ideally the reference I_{ref} and N_{ref} may be obtained by recording Raman signal from a flat metal coated part of the same substrate but it is hardly possible to get ordinary Raman spectra for a monolayer of analyte. Even such an arrangement does not yield true ordinary spectra due to presence of metal in the vicinity of analyte[54]. The commonly employed techniques to circumvent this problem are to use solid bulk form or higher concentration solution of analyte to get the approximate values of reference parameters. Both these techniques need an estimate of laser interaction volume and that can be calculated from depth of field considerations. We did not detect any ordinary Raman spectra from ~20 mM 4-MBT methanolic bulk solution. Therefore, we use solid form of 4-MBT to get values of I_{ref} and N_{ref}. **Figure 5-58**

shows the ordinary Raman spectrum of 4-MBT. The number of molecules excited in the solid phase was determined by assuming the excitation volume to be a cylinder of diameter equal to laser spot size and the length of interaction equal to depth of field. This assumption underestimates the N_{ref} since the actual interaction volume has the shape of a two back-to-back truncated cones with waist diameter equal to the focused laser beam spot size. It is expected to yield a more conservative estimate of *EF*. The depth of field was determined by moving the laser focus point from under to over-focus and noting the 1/2 power points. Taking the monolayer thickness of 4-MBT as 0.5 nm [127], we get a quick estimate of N_{ref} / N_{SERS} ratio. The estimated enhancement factor was found to be 5.86×10^6. It may be noted that we have used a flat area approximation while determining N_{SERS} in *EF* calculations. The actual or effective area of the nanowires is somewhat increased (~ 57% for half coated NW) due to their cylindrical nature. However, the effect is not expected to be significant due to line of sight deposition of Au that only coats part of the nanowire facing the evaporation source.

Another approach to calculated I_{ref} and N_{ref} is based on using polystyrene as reference[127]. This method utilizes the fact that the Raman cross-section of polystyrene can be assumed to be equal to that of 4-MBT. Ordinary Raman spectrum of polystyrene is shown in **Figure 5-58**. Following a similar line of calculations, the *EF* was estimated to be 3.2×10^6. This *EF* is in good agreement with that calculated using bulk solid form of 4-MBT and shows that polystyrene can also be used as reference for 4-MBT enhancement factor calculations.

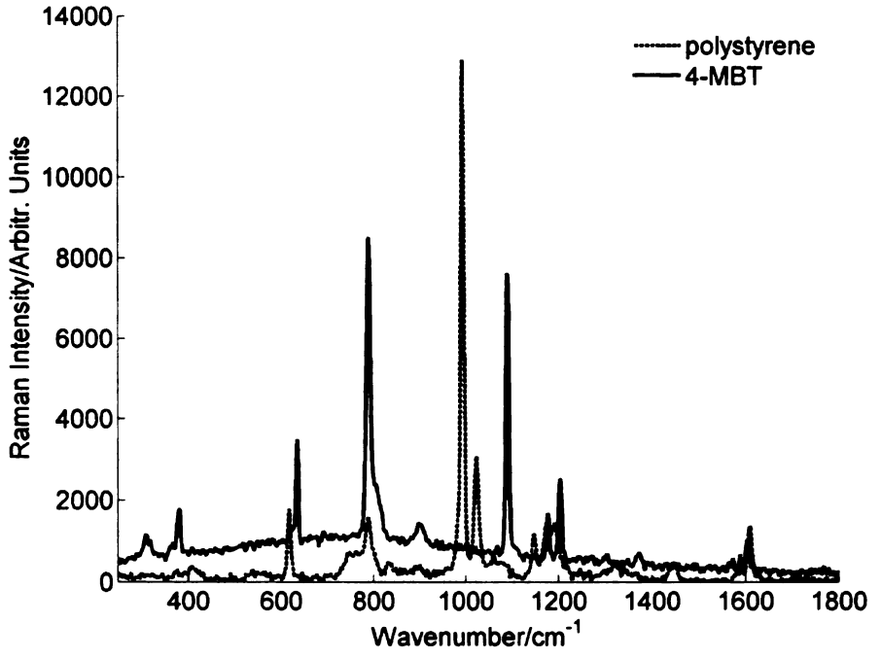

Figure 5-58. Ordinary Raman spectra of 4-MBT and polystyrene.

5.6.2 Detection of 1,2-BDT

The generality of nanowires based substrate for SERS was evaluated by probing a 1,2-BDT as a SERS analyte. This molecule is known to form self assembled monolayer (SAM) on Au for concentration $\geq 1 \times 10^{-3}$ M after more than 20 min of soaking[126]. The SERS substrate with 35 nm thick Au film was immersed in 1 mM methanolic solution of 1,2-BDT for 20 min. This concentration is the least reported for monolayer coverage and is expected to yield a more conservative estimate of enhancement. The sample was then rinsed with methanol to ensure removal of excess analyte. The substrate was allowed to dry before acquiring Raman spectra. **Figure 5-59** is a plot of SERS spectra from Au coated GeO_2 NWs, which clearly shows the 1,2-BDT peaks. The broad continuum is also somewhat suppressed following the formation of BDT SAM on the Au coated nanowires.

Stro

Figu

Strong SERS spectra from different randomly chosen points on substrate are shown in **Figure 5-60**.

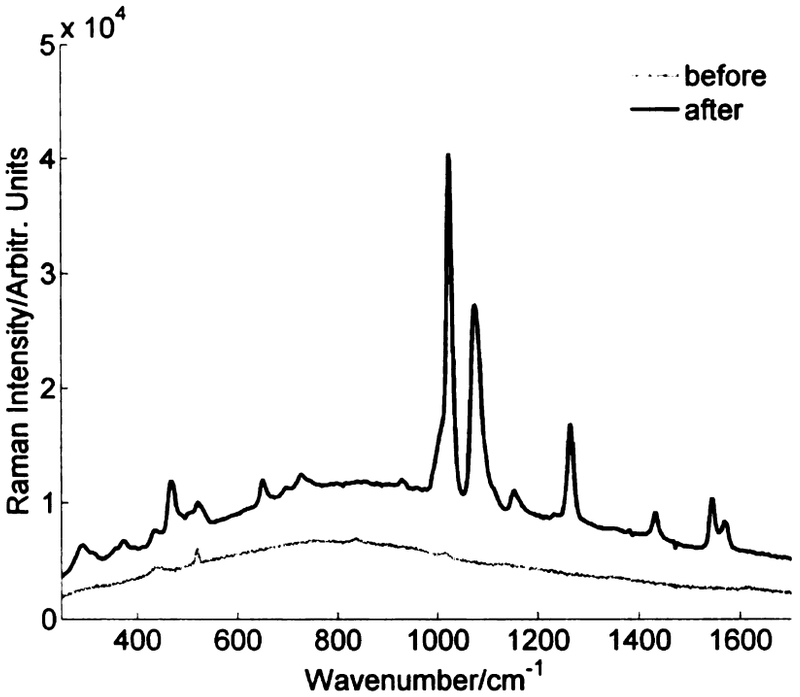

Figure 5-59. SERS spectra of SAM of 1,2-BDT on 108 nm diameter NWs, t_{acc} = 15 s.

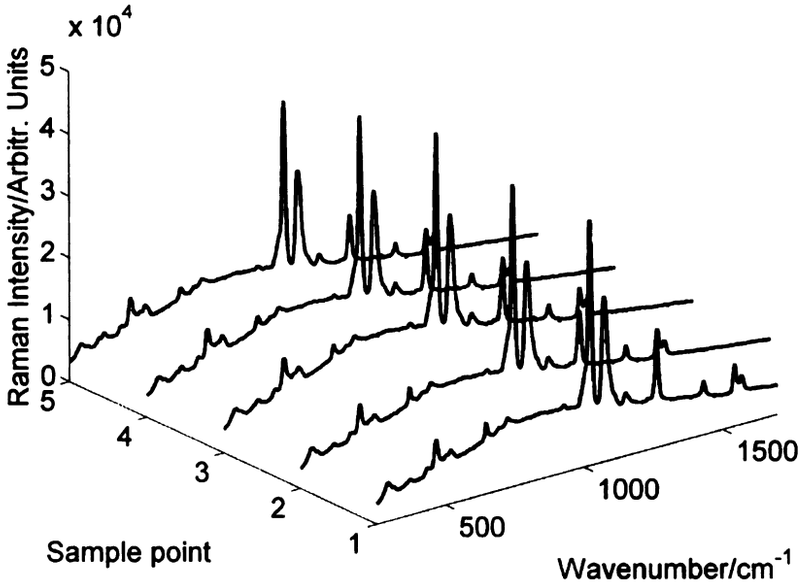

Figure 5-60. SERS spectra of SAM of 1,2-BDT from different points on substrate.

Figure 5-61 shows the plot of the 1028 cm^{-1} peak of 1,2-BDT for 100 points scanned in a rectangular area of 2.5 mm × 2.5 mm. The data show the substrate provides very reproducible SERS enhancement with small standard deviation (~ 8%).

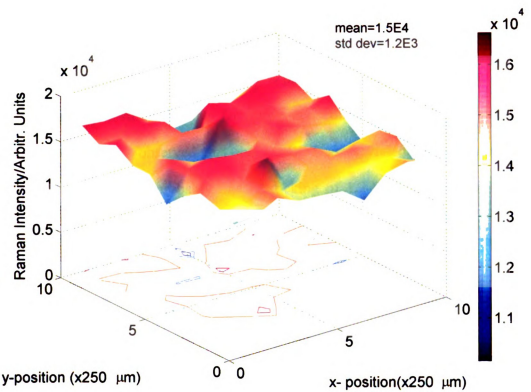

Figure 5-61. Spatial map of SERS intensity for 1028 cm^{-1} peak of 1,2-BDT, t_{acc}=5 s.

The SERS *EF* for 1,2-BDT can also be calculated using equation (5.7) and this time the 1028 cm^{-1} Raman band of 1,2-BDT is selected for estimation. Assuming monolayer coverage of substrate with 1,2-BDT and each molecule binding to 2 Au atoms on surface, the aerial density of analyte is estimated at 6.4×10^{14} molecules/cm^2 on the substrate. For a laser spot size of 100 μm diameter, nearly 8.35×10^{-14} moles (5.03×10^{10} molecules) of 1,2-BDT contribute to the SERS signal. The ordinary Raman spectra of the

source 1,2-BDT was used as reference to estimate I_{ref} and N_{ref} for use in *EF* calculations. Although I_{ref} can be directly measured from ordinary Raman spectra of bulk analyte, the estimation of N_{ref} required knowledge of laser exaction volume. This excitation volume was estimated to be ~6.3 nL from depth of field considerations. The average enhancement factor from equation (5.7) was found to be $\sim 7.4 \times 10^5$. The low enhancement factor relative to other analytes is probably due to sub-monolayer coverage of 1,2-BDT on the substrate. Another factor that is peculiar to 1,2-BDT is the storage of analyte solution. It was observed that the 1,2-BDT glass vial develops some sort of coating on the walls. It is probably due to sticking of 1,2-BDT on the glass and the coating did not dissolve back into solution even after ultrasonication. The sticking of 1,2-BDT in the form of a coating is also likely to decrease the concentration of analyte from the initially prepared 1 mM concentration. This decrease in the concentration can also cause sub-monolayer coverage and associated decrease in measured *EF*.

The above results have shown that the gold coated nanowires provides strong SERS enhancement to detect monolayer converge of thiol molecules. The SAM of the same analytes on smooth gold film over silicon wafer did not yield any discernable spectra. It is important to highlight the contributions of nanowires towards SERS. It is envisaged that the nanowires have a trifold effect towards SERS. First these provide a rough 3-D surface to host the metal coating that is a prerequisite for exciting surface plasmons. Secondly the poor wetting of gold on the oxide nanowires yields island like growth of the metal film on individual nanowires with closely spaced metal nano-particles. The closely spaced gold islands on the nanowire surface provide strong electric field enhancement in the gaps between adjacent islands. Third contribution is derived

from the optical properties of nanowires and is a major factor in improving repeatability of SERS measurement. It is hypothesize that the high dielectric nature of oxide NWs helps to confine and guide the light to a much larger area on the substrate than directly illuminated by the laser beam. This is supported by the observation that the laser spot is hardly noticeable in CCD camera when focused on silicon wafer. However, the spot size grows to a much larger areas when the NW substrate is illuminated suggesting light waveguiding and coupling among NWs. Each NW is coated with a large number of gold particles that are also expected to immobilized analyte molecules. The light coupling between NWs brings the excited surface plasmons to these metal particles, which in turn excites Raman modes of analyte. The analyte Raman radiation is again amplified by the Au nanoparticles and coupled back to the NWs where they travel to the receiver in reverse direction.

5.7 Conclusion

In this chapter, a novel low temperature synthesis of germanium oxide nanowires using thermal evaporation of metallic germanium is presented. This technique offered good control over diameter and length of nanowires. Nanowire yield was found to be highly sensitive to temperature, oxygen concentration and background gas pressure. The nanowire substrates were coated with thin film of gold to make these SERS active. The gold coating introduced a broad background in the Raman spectrum of nanowires. The performance of substrates was evaluated by using 4-MBT and 1,2-BDT as probe molecules. Optimal SERS enhancement was obtained for a gold coating thickness of 30 - 45 nm. The substrates showed an average enhancement factor of the order of 10^6

with good repeatability and small standard deviation over the tested areas. The amount of analyte that yields these strong SERS spectra is on the order of $\sim 10^{-14}$ moles and confirms the high sensitivity of these novel substrates.

Chapter 6: Zinc Oxide Nanowires based SERS Substrates

Zinc oxide (ZnO) is a versatile technological material that exhibits both semiconducting and piezoelectric properties. Its strong piezoelectric and pyroelectric properties have allowed it to be extensively used in mechanical actuators and piezoelectric sensors. It is transparent to visible light and is suitable for short wavelength optoelectronic applications owing to its wide band gap. ZnO grows in a wide variety of morphologies such as nanowires, nanocombs, nanoshells, nanocages, nanobelts, nanosprings etc[144]. The ZnO was mainly synthesized as nanowires for this research. The synthesis of ZnO nano-structures was done using a simple vapor transport and annealing mechanism. The substrates were characterization with SEM (JEOL 6400). Rhodamine 6G (R6G), Nile Blue, 4-methylbenzenthiol, and 1,2-benzenedithiol were utilized as probe molecules for SERS analysis. In this chapter, details of nanowires synthesis and the results of Raman analysis are presented.

6.1 Zinc oxide nanowires synthesis

Typical synthesis of ZnO nanowires is done using solid-vapor process in which source material is evaporated at elevated temperature and the resultant phase condenses under appropriate conditions of temperature, pressure, gas environment to form desired nanostructures. Huang *et al.* were the first to synthesize crystalline ZnO NWs by vapor transport via VLS mechanism[145, 146]. Nanowires were grown on 5 nm Au-coated Si by heating a 1:1 mixture of ZnO and graphite powder to 900-925 ^{o}C under constant flow of Ar for 5-30 min. Since then there have been a number of reports of ZnO NWs

synthesized by variety of techniques including physical vapor deposition[147-149], laser ablation[150], catalyst-free metal oxide vapor phase epitaxy (MOVPE)[151, 152], template assisted growth using electrodeposition[153], aqueous solution-based synthesis[154-156] and chemical vapor deposition (CVD)[157].

Zinc oxide nanowires were synthesized on Si(100) and quartz substrate using thermal evaporation and transport of Zn source in an oxidizing environment. The substrates were cleaned by sonication for 15 minutes each in acetone, methanol and D/I water and finally dried by blowing compressed nitrogen. Generally thin gold film (3-20 nm) was used as catalyst but some growth was also observed on uncoated part of substrate. In a typical set up, the substrates were placed on top of a quartz or ceramic boat containing zinc powder. The distance between source powder and substrates varied from 1-3 cm depending upon type of boat used. In certain instances, the zinc powder was mixed with sodium chloride to control evaporation[158]. The source boat alongwith the substrates was then placed on a quartz support plate that was inserted into the heating zone of the horizontal tube furnace as shown in **Figure 6-1**. The tube was evacuated to less than 300 mTorr and Argon mixed with 5% hydrogen at a flow rate of 50 sccm was introduced into the tube as a background gas. The reaction gas of Argon-oxygen mixture (40% oxygen balance argon) at 50sccm was introduced using a separate MFC. The introduction of gas flow increased the pressure inside the tube to about 550 mTorr. The synthesis pressure of ~2 Torr was adjusted by partially closing a vacuum valve located at the downstream end of the tube. After adjusting gas flow rates and pressure, temperature of the furnace was raised to 650 ^{o}C over 10-12 min. The control temperature was measured by a 'K' type thermocouple placed between walls of quartz tube and tube

furnace. The actual temperature inside the quartz tube at the location of source/substrate was measured by a second 'K' type thermocouple (not shown) placed inside the tube. During growth the, the pressure of the reaction chamber increased to ~2.5 Torr. The growth took about 1-2 hr and subsequently the furnace was allowed to cool to room temperature. The source powder turned white from original gray color and the substrate surface appeared light to dark gray after the experiment. The morphology of the source powder and substrates was examined by SEM and compositional analysis was done by EDS. **Figure 6-2** shows the SEM image of the ZnO NWs synthesized on Si substrate. **Figure 6-3** shows the diameter distribution of ZnO NWs. The nanowires have a mean diameter of 62 nm with small standard deviation of 14 nm. Very dense and aligned nanowires were also found at the location of source as shown in **Figure 6-4**. However, these source NWs were not further investigated since present study was mainly aimed at SERS from NWs synthesized on flat substrates. The flat substrates have the advantage of one time focusing of laser beam with predictable and stable metal coating. Nevertheless such nanowires may be useful in SERS from metallic colloidal by providing 3-D holding framework for nanoparticles[143].

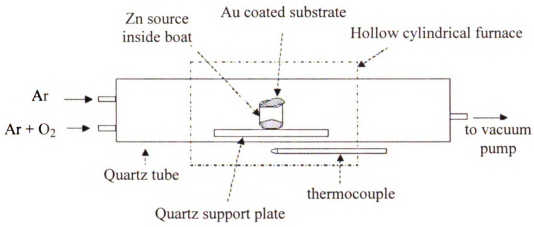

Figure 6-1. Experimental set up for ZnO nanowire synthesis.

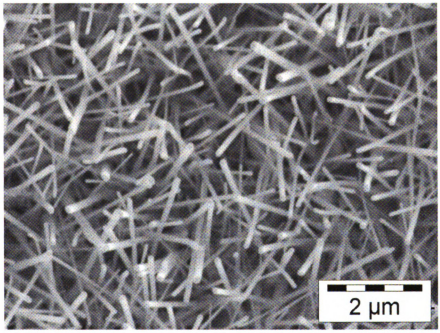

Figure 6-2. Zinc oxide nanowires on Si 100 substrate using Au as catalyst.

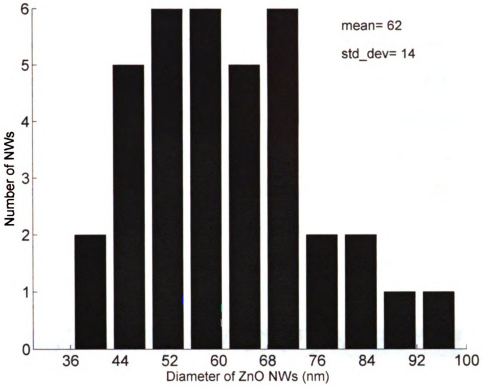

Figure 6-3. Diameter distribution of ZnO NWs.

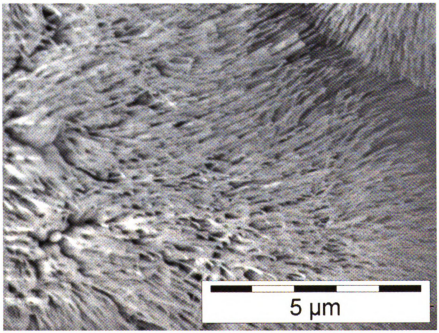

Figure 6-4. ZnO nanowires on source powder.

It may be mentioned that NWs were also found in locations where no catalyst was present as shown in **Figure 6-5**. This observation confirms the existence of growth mechanism other than the typical VLS mechanism. The composition of the nanowires was confirmed to be of zinc oxide from EDS analysis as shown in **Figure 6-6**. The EDS quantization results yield atomic ratio of Zn:O is 1:0.9 and confirm the product is stoichiometric ZnO within the accuracy of measurement. The high percentage of gold is due to sample coating that has to be done to make the sample conductive for SEM studies.

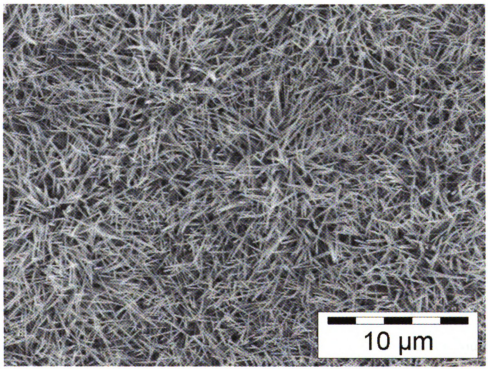

Figure 6-5. ZnO NWs found in uncoated area of Si wafer.

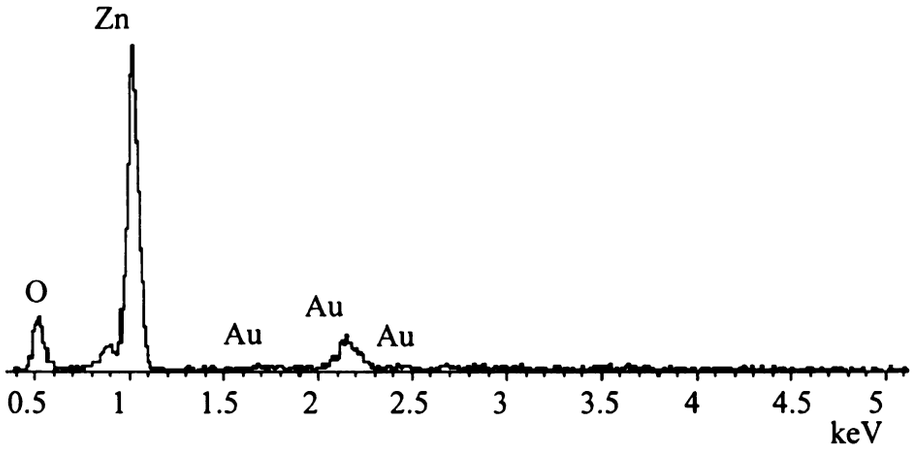

Element	App Conc.	Intensity Corrn.	Weight%	Weight% Sigma	Atomic%
O K	3.17	1.1516	115.12	1.22	45.33
Zn K	9.63	0.7622	69.32	1.83	50.88
Au M	1.86	0.6557	15.56	1.81	3.79
Totals			100.00		

Figure 6-6. EDS spectrum and quantization results for ZnO nanowires.

The NWs were not the only nanostructures obtained in the synthesis. Some nanocombs[159], nanorods[160], nanowhiskers[161], nanocages[162], nanoflowers[160] and hexagonal faceted nanorods[154] were also found as shown in **Figure 6-7**. Generally speaking, the substrate side facing the source (facedown side covering the source boat) shows greater variation of morphologies. This is probably due to high saturation of vapors and convoluted flow of source vapors inside the quartz boat. The substrate face outside the boat have more uniform growth of NWs since gas flow is unrestricted and vapors diffuse away without any restriction.

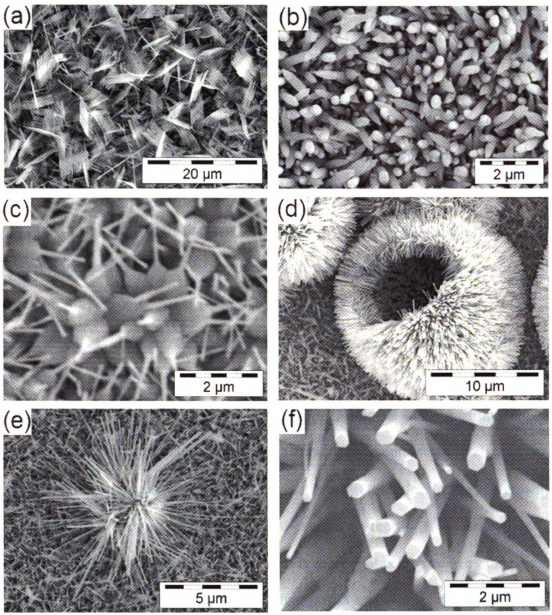

Figure 6-7. Different morphologies of ZnO nanostructures. (a) Nanocombs. (b) Nanorods. (c) Nanowhisker. (d) Nanocages. (e) Flowers. (f) Hexagonal rods.

The most common morphologies of ZnO synthesized in this research were the nanowires and hexagonal nanorods. The other morphologies were mostly found on the

top of these two structures at isolated locations. Therefore, next section will discuss the possible mechanism leading to the growth of these nanostructures.

6.2 ZnO nanowires growth model

The NWs synthesis has been reported using either catalyst assisted or catalyst free environment. However, in this case NWs are observed in both areas of substrate - with and without catalyst. The catalyst assisted growth occurs via VLS mechanism and this growth mechanism has been widely used for semiconductor nanowire growth. In this mechanism, the catalyst forms a eutectic with the NW material and the resulting liquid droplet serves as a preferential site for absorption of gas phase reactant. Once supersaturated with the reactant, the liquid droplet acts as nucleation site for crystallization and growth of nanowire. The growth continues so long as the supply of reactants is available and temperature is high enough to maintain the catalyst in liquid phase. The VLS mechanism is therefore characterized by strong localization of growth to the catalyst coated area and presence of solid catalyst on the tip of the nanowires. The oxide NW growth through the VLS mechanism is somewhat complicated by the presence of oxygen. Most oxides have very high melting points and are unlikely to be in liquid phase at growth temperatures commonly employed. Hence either pure metallic source is used in an oxidizing environment or some form of reducing agent is utilized when using oxide source material. For example, mixing of ZnO with carbon or graphite is a commonly employed technique to synthesize ZnO nanowires[146, 163, 164].

In this study, pure zinc source was used as the starting material. Zinc is highly volatile (melting point ~419.52 °C) and at high growth temperature, it can vaporize according to

$$Zn(s) \rightarrow Zn(g) \tag{6.1}$$

The zinc vapors then diffuse away from the source and condense on substrate (Au coated or uncoated) where temperature is less than boiling point (907 °C) of Zn [165]. These liquid droplets of Zn then form ideal nuclei for the self-catalytic growth of ZnO nanostructures via VLS mechanism[81]. The growth of NWs on the catalyst free area of substrate also supports the existence of a self-catalytic growth. The presence of oxygen in the reaction makes the situation more complex and is expected to result in oxidation of zinc according to reaction

$$Zn(s)+\frac{1}{2}O_2 \rightarrow ZnO(s) \tag{6.2}$$

Both of the above reactions are expected to be occurring simultaneously. The ZnO is very stable (melting point 1975 °C) at reaction temperature and is not expected to yield any significant vapor pressure at the synthesis temperature used in this work. However, the limited supply of oxygen in the reactor (the substrate is covering the top of the boat containing source material) may result in substantial amount of zinc suboxides (ZnO_x, $0 < x < 1$)[165]. It is known that the suboxides of Zn have low melting points (~419 °C) and can vaporize and condense on the substrate yielding nucleation sites[166].

These suboxide droplets can enhance the adsorption and diffusion of Zn oxides at the tips of the ZnO NWs. Further oxidation of the suboxide droplets leads to the formation of ZnO NWs. Yet another possible pathway for the growth of NW is from the direct deposition of islands ZnO on the substrate following oxidation of Zn or $ZnO_x\,(0 < x < 1)$ vapors. It has been previously reported that ZnO islands act as preferred sites for the growth of NWs[167]. Some evidence of this can be seen by probing substrate under the top layer of NWs as shown in **Figure 6-8**. Here, the top layer of NWs is scratched to reveal existence of relatively large (~ 200-300 nm) crystallite structures of ZnO. The small diameter NWs appear to be growing between these and lend credibility to hypothesis that a ZnO seed layer might be forming first. Then the small diameter NWs starts to grow as the supply of Zn is exhausted. The precise mechanism for the growth is net yet clear but all three mechanisms discussed above are expected to occur simultaneously with different degrees of contributions towards final product. It was also observed experimentally that the gold-coated substrates gave better yield of NWs compared to uncoated substrates. The catalyst-coated area typically shows high yield of the NWs under same conditions of synthesis as can be seen in **Figure 6-9**. This can be explained by better sticking of source vapors to catalyst-coated area that results in better yield.

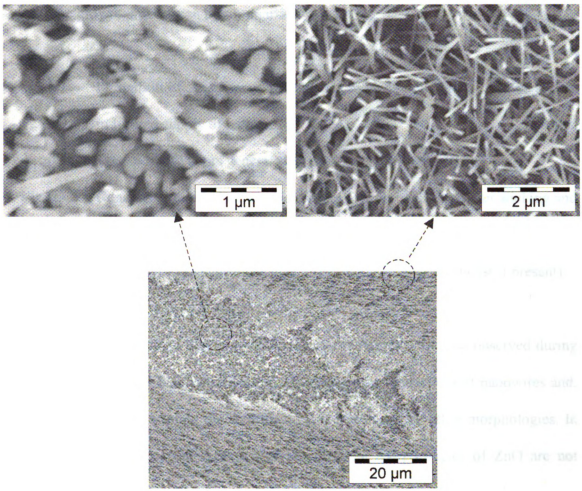

Figure 6-8. Probing structures under ZnO NWs.

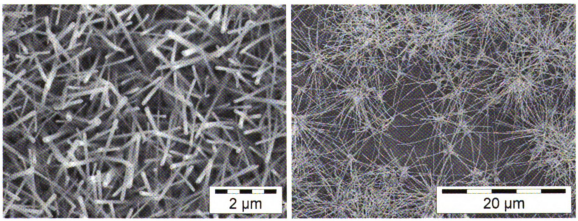

Figure 6-9. NWs on catalyst coated (left) and uncoated (right) substrates.

The growth process can be summarized as:

(a) Formation of zinc vapors and zinc suboxides upon heating of zinc source in limited supply of oxygen.

(b) Transport of vapors generated in above step to substrate.

(c) Condensation of vapor on substrate to form seed layer. Better sticking and condensation for gold coated substrate.

(d) Growth of ZnO nanowires from these seeds (and gold catalyst if present).

It may be re-iterated that some different morphologies were also observed during synthesis of nanowires. Since bulk yield in this study was of the form of nanowires and, no attempt is made to explain detailed kinetics of formation for other morphologies. In fact, detailed kinetics of the synthesis of the different morphologies of ZnO are not exactly known. These have been attributed to different synthesis conditions like oxygen concentration, temperature, pressure etc. Hu *et al.*[161] had reported formation of nanoneedle-microwhisker formation on silicon without any metal catalyst by thermal evaporation of ZnS powder at 900-950 ^{o}C in continuous flow of 100 sccm Ar containing 2 % oxygen. They attributed the initial hexagonal microwhisker due to high supersaturation of ZnO vapors during initial phase of reaction. The nanoneedle is formed due to reduction in supersaturation of ZnO as supply of ZnS is reduced favoring growth of nanoneedle. Leung *et al.*[163] reported formation of ZnO tetrapods and bone like nanorods by controlling Zn vapor release from source. Wang *et al.*[166] observed that the formation of ZnO tetrapods was extremely sensitive to oxygen concentration in the

reactor. The formation of tetrapods is also attributed to oxidation of Zn vapor during gas phase transport[168, 169]. Yao *et al.*[165] reported formation of different types of nanostructures at different temperatures confirming sensitivity to temperature. It is appropriate to conclude that these low yield isolated morphologies of ZnO are highly sensitive to experimental conditions and are synthesized only at localized spots where suitable conditions exist. A more uniform and reproducible substrate is prerequisite for SERS and only nanowires were found to satisfy this requirement.

Before proceeding to the Raman studies of ZnO substrates, it is important to highlight an observation concerning growth of NWs on gold coated substrate at low temperature. In the relatively low temperature region (less than 600 °C), the ZnO nanorods are strongly localized to location of catalyst. **Figure 6-10** shows the ZnO growth on silicon substrate located in the low temperature region of the furnace. It can be clearly seen that the growth is strongly limited to the gold-coated area of the substrate. The main difference besides low temperature is also the proximity of the substrate from the source that will reduce the supply of the reactants to this region. So it is reasonable to speculate that under low supersaturation (due to greater distance from source), there is less probability of forming a ZnO seed layer. Hence growth is more governed by the typical VLS growth mechanism of crystal growth.

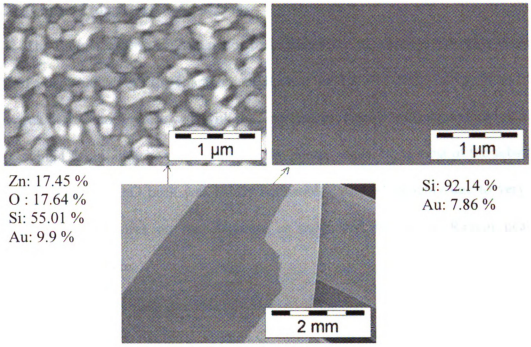

Figure 6-10. ZnO nanostructures in low temperature region on gold coated silicon.

6.3 Raman characterization of ZnO nanowires

The ZnO NWs were characterized by EzRaman-L from Enwave Optronics Inc. with 6 cm^{-1} resolution at 785 nm excitation. The sample was mounted on a xyz-stage and illuminated by the Raman system laser beam via optical fiber link. The Raman probe head was attached to a separate z-stage that facilitates precise focusing of laser beam onto the sample surface independent of sample movement. All spectra were acquired with a focusing lens (N.A. = 0.22) that yields a spot size of less than 100 μm diameter and a power of ~30 mW on the substrate.

6.3.1 Raman Characterization of NWs

The Raman spectra of ZnO nanowires synthesized on alumina substrate is shown in **Figure 6-11** and shows the characteristic Raman band at 437 cm^{-1}. The position of the main peak at 437 cm^{-1} agrees well with that reported previously with an underlying rising background[170]. It may be mentioned that the Raman signal from most of the substrates was very weak and ZnO peak was hardly noticeable. This is probably due to very thin layer of ZnO nanowires on the substrate as evidenced by strong Raman peak of underlying Si substrate.

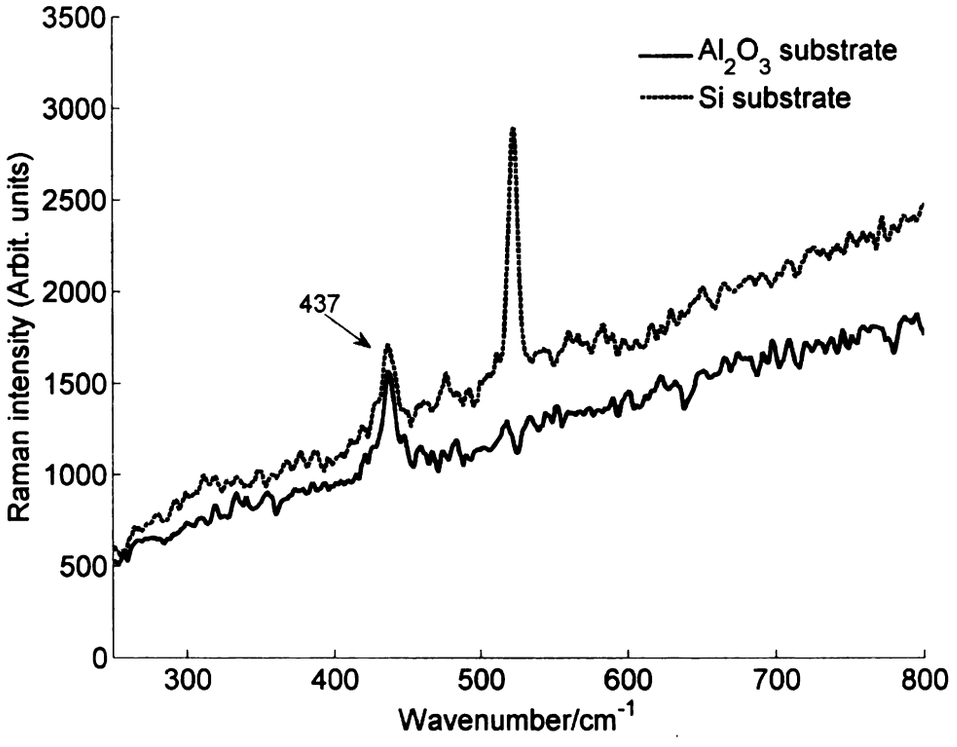

Figure 6-11. Raman spectra of Zinc oxide nanowires on alumina and silicon substrates showing characteristic peak at 437cm^{-1}, t_{acc}=20 s.

6.3.2 Gold coating of ZnO nanowires

The ZnO substrates were coated with thin film of gold to create a plasmon active surface. Similar to the observation of slowly varying background in case of gold-coated GeO_2 nanowires, a broad continuum was also observed for ZnO nanowires. For example, **Figure 6-12** shows Raman spectrum of ZnO nanowire substrate after coating with 21nm gold film. The broad continuum peaking between 800-1000 cm^{-1} is appearing after gold coating of substrate. The silicon 521 cm^{-1} peak intensity from silicon substrate is reduced as a result of metal coating. It may be noted that the substrate peak is quite strong and this is primarily due to very thin top layer of NWs as well as high transparency of ZnO for IR radiation. The fluorescence peak from substrate for high wavenumber is also somewhat quenched after gold coating. This is expected since metals are known to help reduce fluorescence[73]. **Figure 6-13** shows the Raman spectra for ZnO nanocombs and the continuous background is quite prominent. It peaks in the same general region of the wavenumber and is usually intense compared to the underlying Raman peak of substrate. It is believed that the metal is enhancing the electric field due to surface plasmon excitation and subsequently light gets trapped in the nanostructures to give rise to such broad peak at shifted wavelengths. However, this hypothesis needs further investigation and the efficacy of the ZnO nanowires in detection of R6G and NB probe molecules is discussed next.

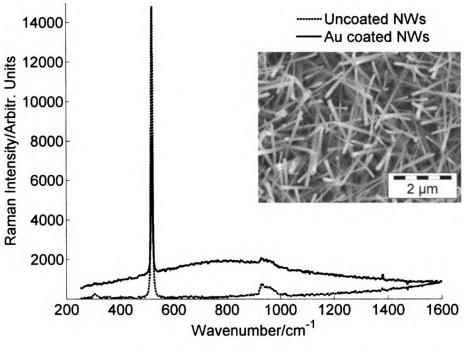

Figure 6-12. Raman spectra of 21nm gold coated ZnO nanowires on Si 100 substrate, t_{acc}=15 s. Insert shows the SEM image of substrate.

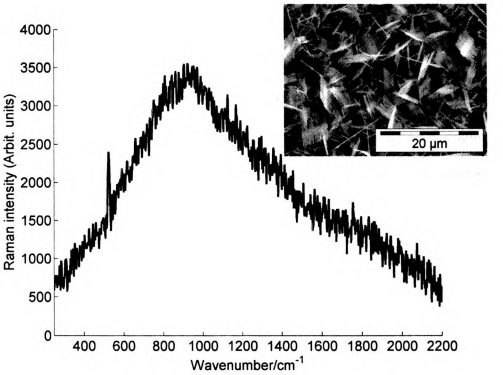

Figure 6-13. Raman spectra of ZnO combs on Si100, t_{acc}=15 s. Insert shows SEM image of the substrate.

6.4 SERS study of ZnO nanowires substrate

The initial SERS studies were done using Rhodamine 6G (R6G) and Nile Blue as probe molecules. The substrates were coated with gold or decorated with gold particles to make them SERS active. However, problem of analyte adsorption on substrate lead to the use of thiol based analytes like 4-methylbenzenthiol, and 1,2-benzenedithiol for detailed SERS analysis.

6.5 Detection of R6G probe molecule

R6G was the first probe molecule investigated using the ZnO nanowires. A 3 μM solution of R6G in 95% ethanol was prepared to act as SERS probe. This concentration of R6G is very low for ordinary Raman detection. The ordinary Raman spectra of 3 μM ethanolic solution of R6G is shown in **Figure 6-14** and only ethanol peaks are visible. Then a drop of 3 μM R6G was applied to the substrate and allowed to dry before acquiring Raman spectra. **Figure 6-15** shows the Raman spectra obtained from 21 nm gold-coated ZnO nanowires on Si(100) substrate. All the major peaks of NB are clearly identifiable on the top of a broad background that is characteristic of gold-coated nanowires substrate. However, the uniformity of the substrate to yield detectable spectra was found to be low and only few spots produces strong spectra.

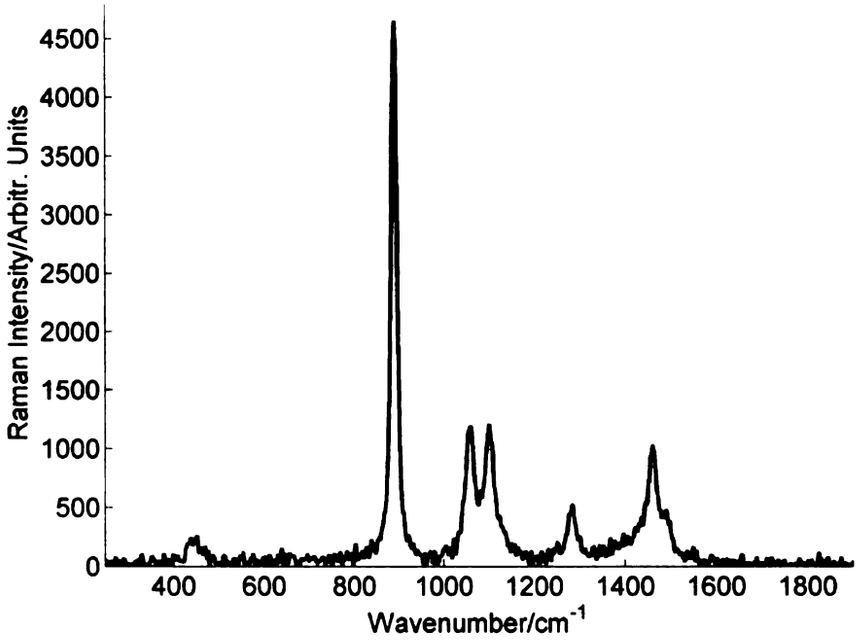

Figure 6-14. Ordinary Raman spectra of 3 μM ethanolic solution of R6G showing only the ethanol peaks.

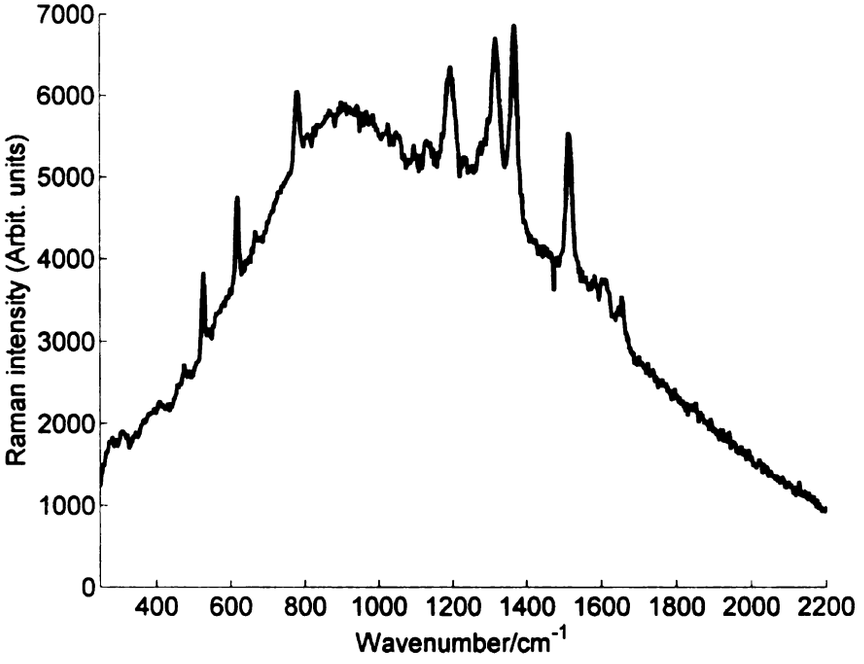

Figure 6-15. Raman spectra of 3 μM R6G from 21 nm Au coated ZnO nanowires synthesized on Si(100) substrate.

6.6 Detection of nile blue

Nile blue A is a common dye used in biology and fluorescence studies. The probe solution was prepared by dissolving nile blue in ethanol and then diluting the stock solution to get a concentration of 2.73 μM. This concentration of analyte is so small that the bulk solution on yield ethanol peaks in the ordinary Raman spectra. First the Raman spectra from the uncoated ZnO substrate was recorded as shown in **Figure 6-16** (a). Then a drop of probe ethanolic NB was added to this uncoated ZnO NW substrate and allowed to dry. The Raman spectra after application of 2.73 μM nile blue did not show any detectable NB peaks as given in **Figure 6-16** (b). This confirmed that gold coating is essential for SERS from these oxide nanowires. Subsequently a drop (about 0.25 ml) of 60 nm gold colloidal was added to the substrate and the Raman spectra were acquired again. The substrate yielded a clear Raman spectra of nile blue after application of gold colloidal as shown in **Figure 6-17**. Here, all major peaks of NB are clearly identified with very little background. This confirms that the gold metal in the form of thin film or nanoparticles is necessary for achieving strong Raman enhancement. However, it was found that certain spots of the substrate do yield a broad background and the probe molecule spectra rides on the top of such continuum. The issue of hot spots was also noticed but as a whole enhancement was found from many locations.

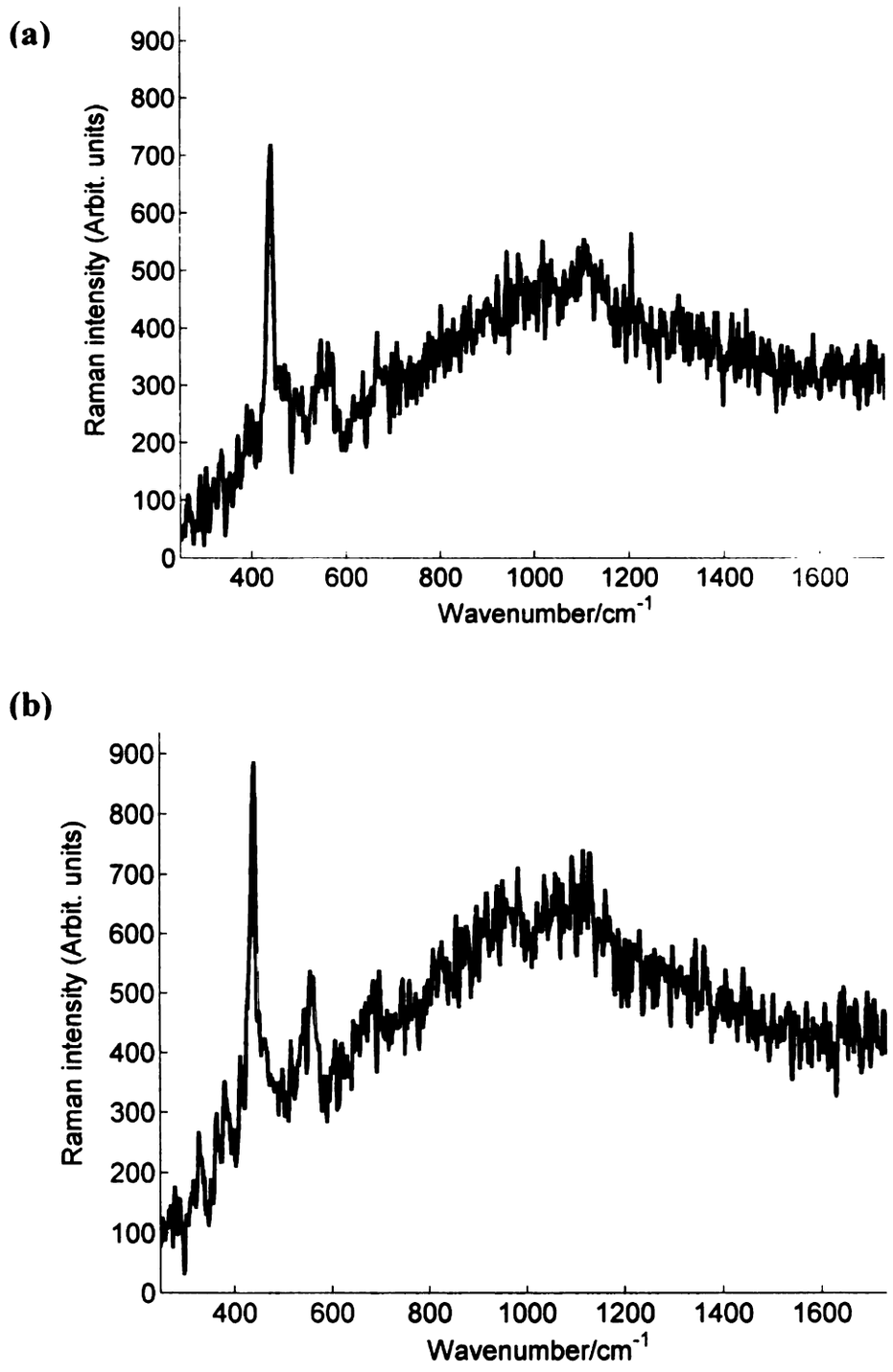

Figure 6-16. Raman spectra of ZnO nanowire. (a) Before adding NB. (b) After adding NB.

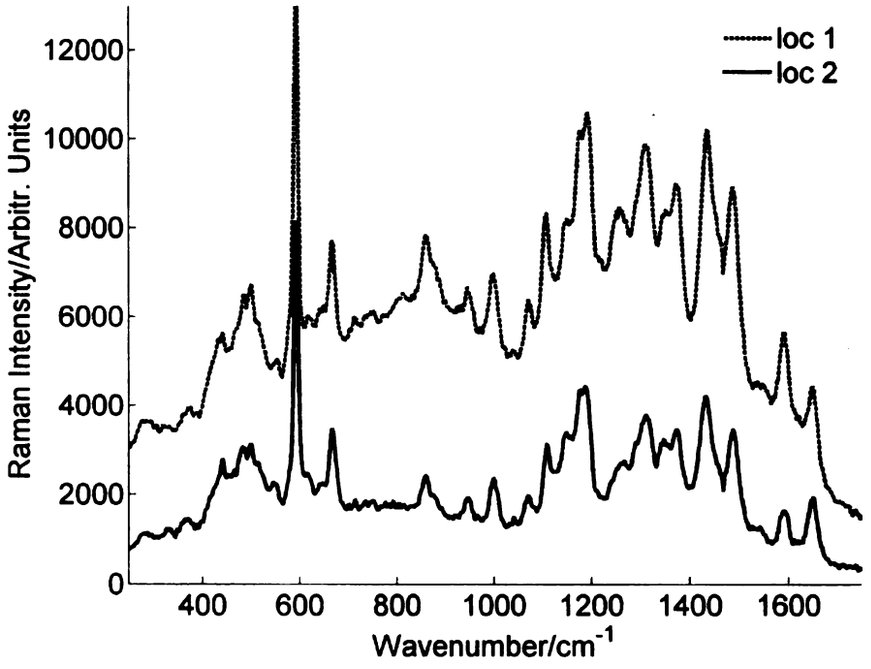

Figure 6-17. Raman spectra of 2.73 μM ethanolic NB from ZnO nanowires coated with 60 nm gold colloidal at two locations, t_{acc}=15 s.

The SERS evaluation of substrates using R6G and NB as probe molecules yielded strong enhancement to detect μMolar concentrations of analytes. However, the enhancement was localized to few isolated spots on the substrates. It was postulated that the problem of hot spots is due to selective adsorption of analyte on the substrate i.e., the analyte only adsorbs to few isolated locations on substrate that form hot spots. In order to study this hypothesis, a different class of analytes was investigated.

6.7 Detection using thiols

Thiols are commonly employed analytes in SERS studies due to their tendency to form SAM on noble metals. The two analytes investigated with ZnO NWs are the 4-methylbenzenthiol (4-MBT) and 1,2-benzenedithiol (1,2-BDT).

6.7.1 Gold coating thickness study

The substrates were coated with different thickness of metal to determine the optimal thickness for SERS. In order to minimize experimental error due to uncontrolled experimental variations, same substrate was coated with different thickness of gold film on different parts. This ensures that any substrate variations from one experiment to another do not interfere with the systematic gold coating studies. The gold coated substrates were soaked in appropriate concentration of probe molecule for set amount of time to yield a SAM of analyte. **Figure 6-18** shows the SERS spectra of 1,2-BDT for different thickness of gold film on ZnO NWs. All spectra are acquired under identical illumination conditions of laser power, exposure time, laser spot diameter etc.

The increasing of SERS with increasing thickness prompted trying even thicker coating and a second piece of same substrate was coated with thicker gold films in different parts. The probe molecule SAM was formed on this substrate following exactly the same steps as before. The SERS spectra were again acquired under identical conditions and are shown in **Figure 6-19** for film thickness of 28-56 nm. It is immediately clear that the SERS intensity increases for increasing gold film thickness upto ~40 nm and then starts to decrease for thicker films. It is envisaged that the thinner films do not yield closely spaced metal islands on oxide NWs. This results in reduced coupling between particles and a low SERS enhancement. An optimal is reached for ~40 nm thick film where best coupling exists between nanowires and metal particles. A further increase in film thickness results in continuous film and the enhancement due to inter-particle coupling is lost besides.

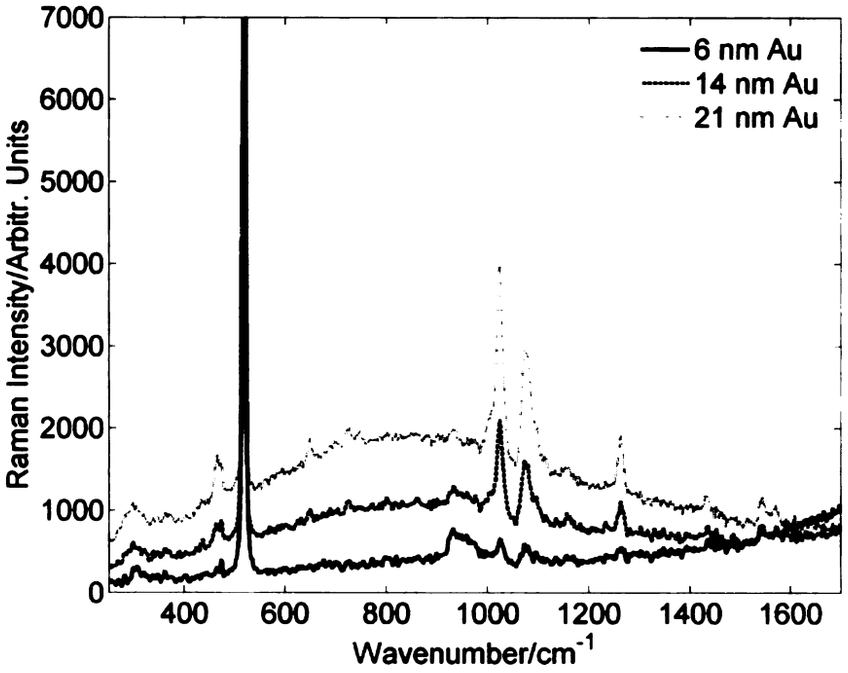

Figure 6-18. Effect of gold coating thickness of SERS from SAM of 1,2-BDT on ZnO NWs, t_{acc}=15 s.

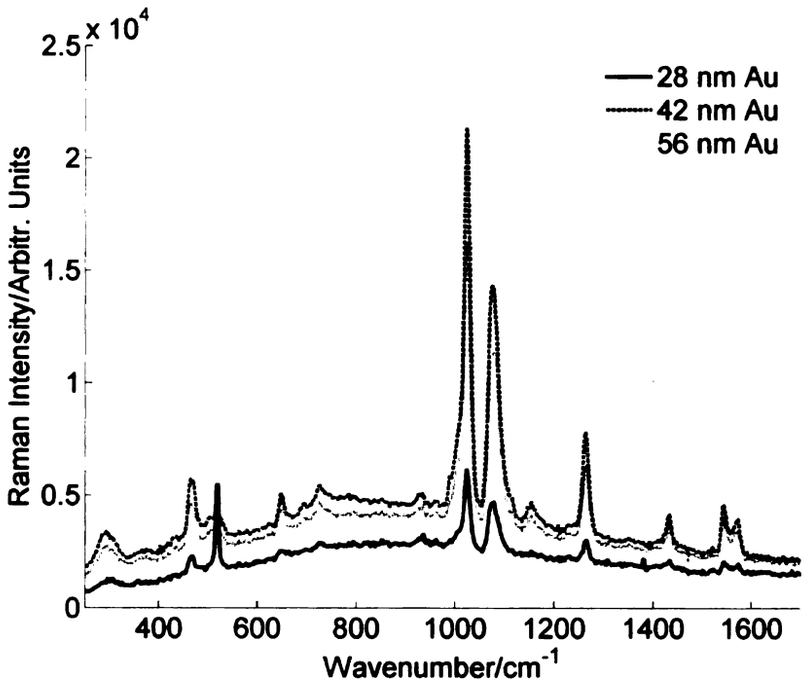

Figure 6-19. Effect of gold coating thickness of SERS from SAM of BDT on ZnO NWs, t_{acc}=15 s.

In order to ensure that the film thickness results obtained above are not limited to a single analyte, same study was repeated for a different analyte. This time 4-MBT was used as analyte and its SAM was formed following previously reported procedure[127]. The SERS spectra were acquired for similar conditions for all different gold thickness. Remarkably similar trend of SERS enhancement versus gold thick was obtained with 4-MBT probe molecule as shown in **Figure 6-20** and **Figure 6-21**. It is clearly obvious that the Raman enhancement increases monotonically with increasing gold thickness upto ~40 nm. Then the enhancement start to decrease for thicker films. The broad continuum also shows a similar trend but tends to reach saturation for films thicker than 40 nm. It is known that the thin metal films do not yield conformal coating of oxide nanostructures. Gold coating of GeO_2 nanowires and TiO_2 at room temperature has shown a 3D island growth[120, 171]. It is therefore hypothesized that the very thin film yields very small islands on nanowires and these are far apart to yield any appreciable enhancement. With thicker films, the size of islands increases and so is their mutual surface plasmon interaction leading to strong Raman enhancement[80, 172]. However, beyond a certain critical value gold coating starts to take a more continuous form on the nanowires that decreases the enhancement. Another simultaneous factor could be the dielectric metal coupling that is reduced for thicker films. The experimental results suggest a thickness of the order of ~40 nm yields the best enhancement.

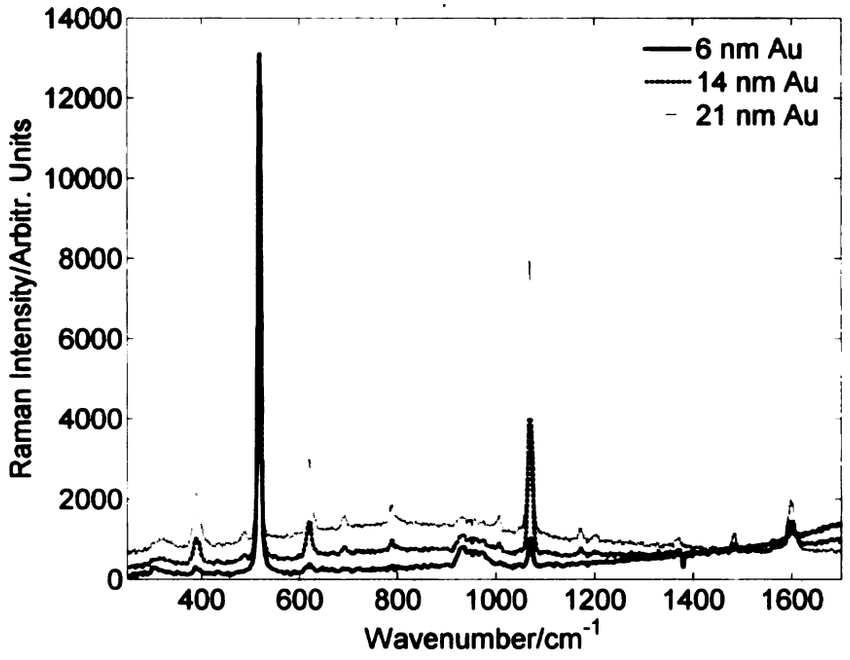

Figure 6-20. Effect of gold coating thickness of SERS from SAM of 4-MBT on ZnO NWs, t_{acc}=15 s.

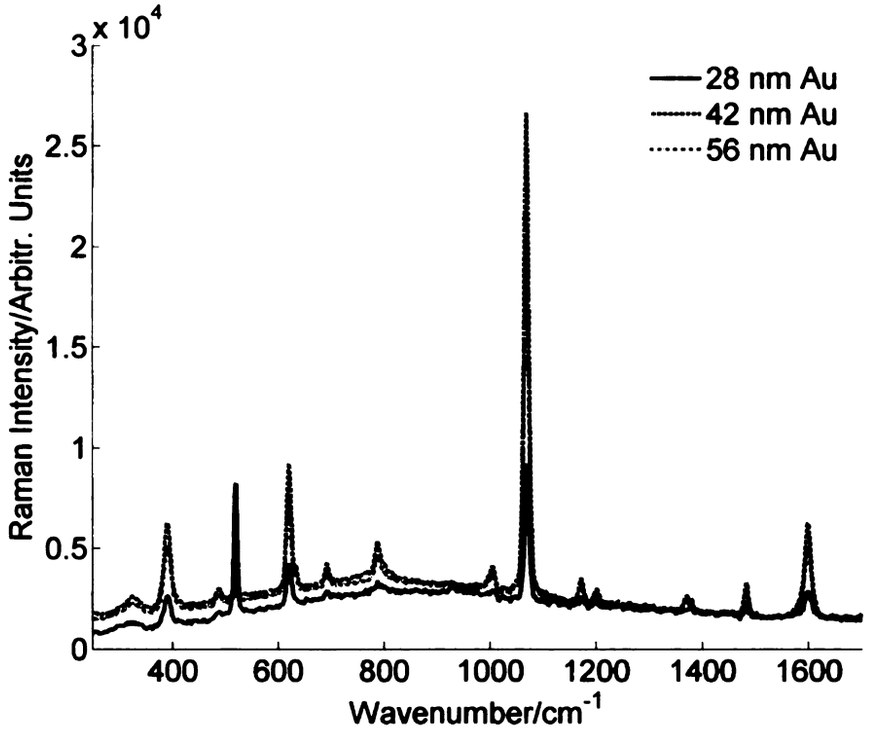

Figure 6-21. Effect of gold coating thickness of SERS from SAM of MBT on ZnO NWs, t_{acc}=15 s.

The effect of application of analyte on ZnO nanowire substrate was also studied. **Figure 6-22** shows the SEM image of substrate before and after soaking in 1 mM methanolic MBT for 12 hr. It is evident that there is no discernable change in the morphology of the substrate after application of analyte. This shows that the ZnO nanowires are robust against morphological changes unlike the GeO_2 nanowires that exhibited significant bundling and clustering.

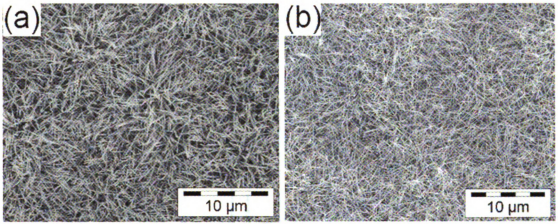

Figure 6-22. ZnO NWs substrate. (a) Before 4-MBT soak. (b) After 12 hr soak in 1 mM MBT.

6.7.2 SERS for 4-MBT

The ZnO nanowires substrate was coated with ~40 nm gold and incubated in 1 mM methanolic 4-MBT solution for 12 hrs. This concentration and soak time is known to yield a SAM of MBT on gold[127]. After the 4-MBT soak, the substrate was thoroughly rinsed with methanol to remove multilayers and/or crystals that might have formed[127]. This ensures that the SERS signal recorded is actually from a SAM of MBT and yields a more accurate estimation of enhancement factor. The substrate was allowed to dry before acquiring the SERS spectra shown in **Figure 6-23**. This figure shows the Raman spectra

from five consecutive 250 μm spaced points on the substrate and the characteristic peaks of 4-MBT are easily identifiable. An interesting effect is the suppression of continuous background of raw substrate following the formation of the 4-MBT monolayer. It may be mentioned that no discernable Raman signal was detected from a Si(100) substrate having a 40 nm smooth Au film that was soaked in 4-MBT alongside nanowires substrate, confirming the enhancement was indeed from nanowire substrate. Also the bulk solution of 1 mM methanolic 4-MBT only yielded spectra for the methanol solvent.

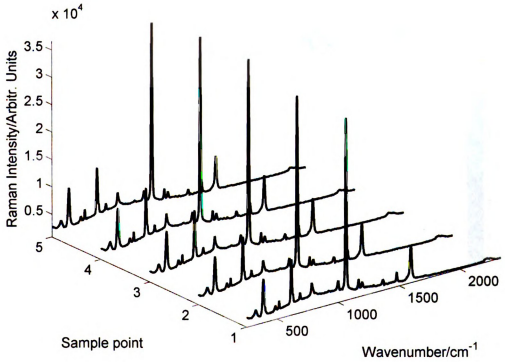

Figure 6-23. SERS spectra of a SAM of 4-MBT from 5 adjacent points 250 μm apart, t_{acc}= 15 s.

Another issue related to the SERS research is the repeatability of the enhancement over spatial area of substrate. To verify the reproducibility of SERS measurement from substrate, SERS spectra were acquired from 100 points covering an area of

2.5 mm × 2.5 mm. The 1068 cm^{-1} Raman band of these spectra is then plotted in **Figure 6-24** to give a spatial map of enhancement from the substrate. It can be seen that the substrate provides unambiguous and uniform SERS spectra for a monolayer of analyte over the tested area with a coefficient of variation ($\frac{std.\ deviation}{mean} \times 100$) of ~ 3.5%.

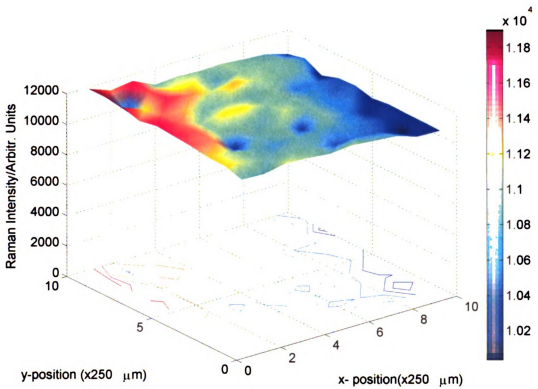

Figure 6-24. 4-MBT 1068 cm^{-1} Raman peak intensity distribution for randomly chosen area on substrate, t_{acc}= 5 s.

The experimental Raman enhancement factor (*EF*) for the ZnO substrate was calculated using the relation[129]

$$EF = \frac{I_{SERS}}{I_{REF}} \frac{N_{REF}}{N_{SERS}} \tag{6.3}$$

where I_{SERS} is the Raman intensity of some specific band from the analyte adsorbed on SERS active substrate and I_{ref} is the Raman intensity of the same band from the bulk analyte. N_{SERS} and N_{ref} are the number of molecules that yield I_{SERS} and I_{ref} respectively. Thus equation (6.3) gives the Raman enhancement per molecule for a specific vibrational band of analyte. The specific band is usually the one that gives the strongest Raman scattering and its intensity is directly read from SERS spectra. The highest Raman intensity for MBT is obtained for the 1068 cm^{-1} Raman band and the average intensity from 100 sample points of this band is used in equation (6.3). Taking 4.5×10^{14} molecules/cm^2 for a monolayer of 4-MBT on gold[130], we find approximately 5.87×10^{-14} moles (3.53×10^{10} molecules) of 4-MBT are excited in the laser spot (100 μm diameter). The determination of N_{ref} is more challenging and different methodologies have been reported to estimate it. Ideally the reference I_{ref} and N_{ref} may be obtained by recording Raman signal from a flat metal coated part of the same substrate but it is hardly possible to get ordinary Raman spectra for a monolayer of analyte. Even such an arrangement does not yield true ordinary spectra due to presence of metal in the vicinity of analyte[54]. The commonly employed techniques to circumvent this problem are to use solid bulk form or higher concentration solution of analyte to get the approximate values of reference parameters. Both these techniques need an estimate of laser interaction volume and that can be calculated from depth of field considerations. We did not detect any ordinary Raman spectra from ~20 mM 4-MBT methanolic bulk solution. Therefore, we use solid crystalline form of 4-MBT to get values of I_{ref} and

N_{ref}. **Figure 6-25** shows the ordinary Raman spectrum of 4-MBT. The number of molecules excited in the solid phase was determined by assuming the excitation volume to be a cylinder of diameter equal to laser spot size and length equal to depth of field. This assumption underestimates the N_{ref} since the actual interaction volume has the shape of a two back-to-back truncated cones with waist diameter equal to the focused laser beam spot size. It is expected to yield a more conservative estimate of *EF*. The depth of field was determined by moving the laser focus point from under to over-focus and noting the 1/2 power points. The DFOV was estimated to be ~842 μm for 1090 cm^{-1} peak but a more conservative estimate of 800 μm was used in *EF* calculations. Taking the monolayer thickness of 4-MBT as 0.5 nm[127], we get a quick estimate of N_{ref} / N_{SERS} ratio. The estimated enhancement factor was found to be 2.19×10^6. It may be noted that we have used flat area approximation while determining N_{SERS} in *EF* calculations. The actual or effective area of the nanowires is somewhat increased (~ 57% for half coated NW) due to their cylindrical nature. However, the effect is not expected to be significant due to line of sight deposition of Au that only coats part of the nanowire facing the evaporation source.

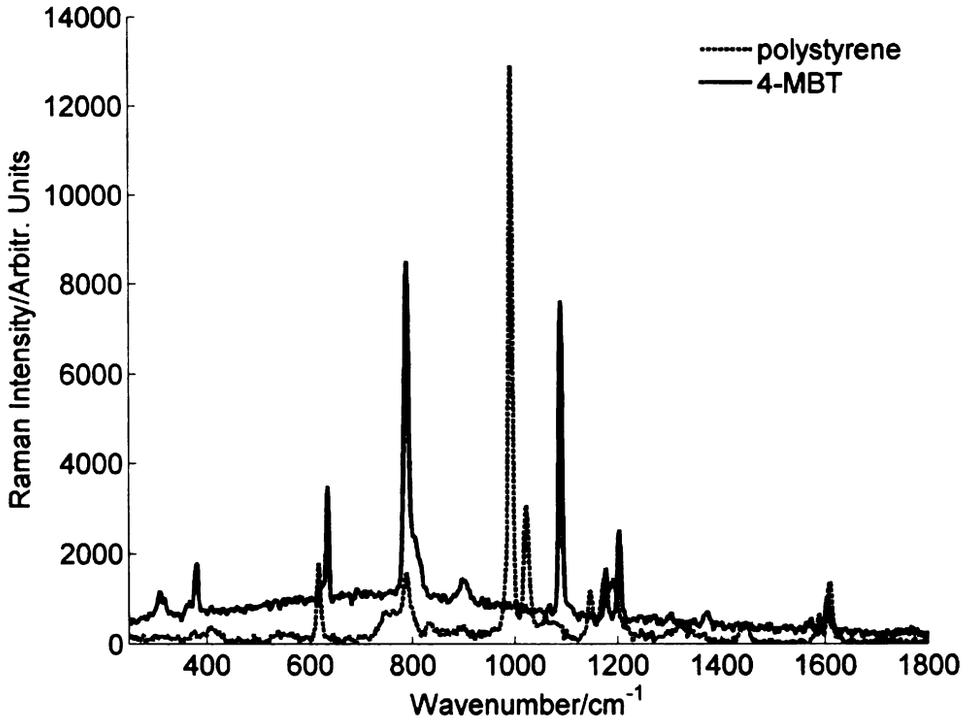

Figure 6-25. Ordinary Raman spectra of 4-MBT and polystyrene, t_{acc}= 5 s.

We also calculated I_{ref} and N_{ref} by using polystyrene as reference whose Raman cross-section can be assumed to be equal to that of 4-MBT[127]. Ordinary Raman spectrum of polystyrene is shown in. Following a similar line of calculations, the *EF* was estimated to be 1.2×10^6. This *EF* is in good agreement with that calculated using bulk solid form of 4-MBT and shows that polystyrene can also be used as reference for 4-MBT enhancement factor calculations.

The SERS enhancement discussed above are for the ZnO NWs synthesized on 7 nm Au coated silicon substrate that was placed facing down on the quartz boat containing source zinc powder. As discussed previously, these nanowires are randomly oriented as shown in **Figure 6-26**(a). The nanowires obtained on the substrate area outside the quartz

boat were more aligned as shown in **Figure 6-26**(b). The exact mechanism of this alignment is not clear at this stage. It has been attributed to the natural alignment of ZnO seed nanocrystals on the substrate and subsequent growth of nanowires from these seeds[167]. In the present case, the flow pattern of source vapors and degree of supersaturation appears to be affecting the alignment of nanowires i.e, confined flow with high supersaturation yields random nanowires. The SERS signal from these partially aligned NWs was also compared and is shown in **Figure 6-27**. It is clearly evident that intensity of SERS signal for randomly oriented NWs is more than twice from partially aligned NWs.

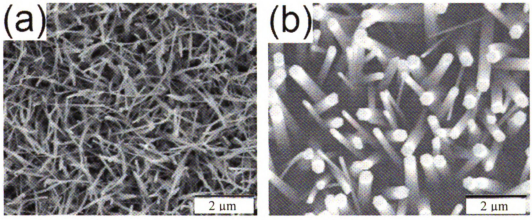

Figure 6-26. SEM image of two typical morphologies of ZnO NWs. (a) Randomly oriented. (b) Partially aligned. Scale bar is 2 µm in both images.

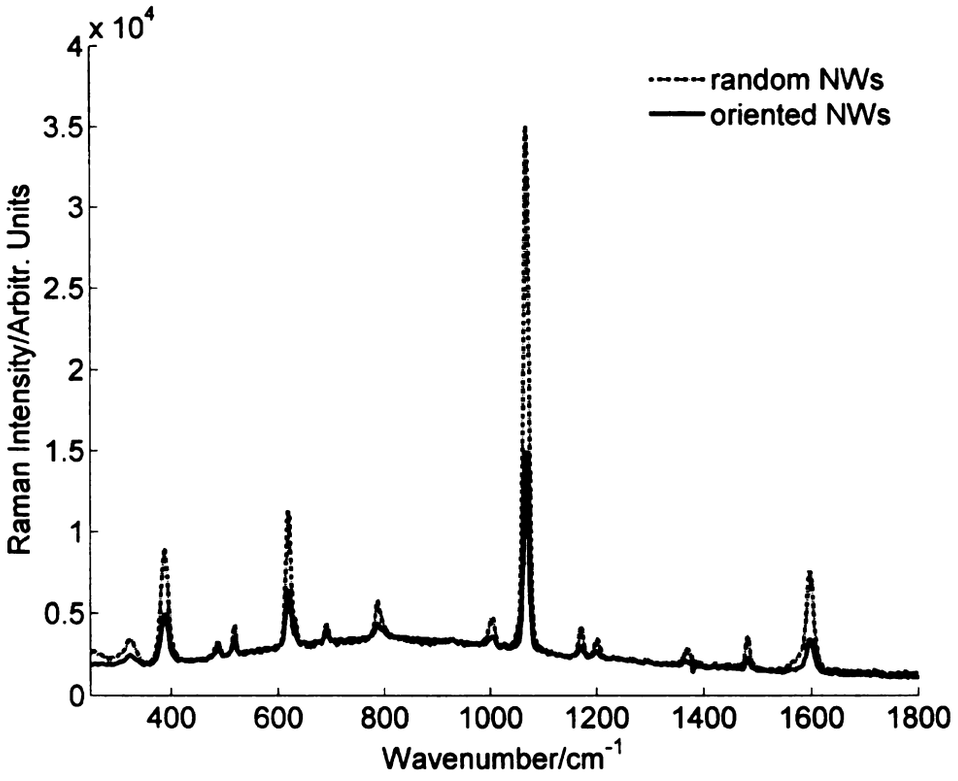

Figure 6-27. Comparison of SERS signal from random and partially aligned ZnO NWs for SAM of 4-MBT, t_{acc}=15 s.

The uniformity of SERS signal for both types of NWs was comparable as shown in **Figure 6-28** where SERS spectra from five random sample points for each type of NWs is shown. One obvious explanation for higher SERS from randomly oriented NWs is their high density as can be seen in SEM image. Also it has been reported that the NWs crossing yield stronger SERS[173] and randomly orientations has higher number of such crossings. This can be more easily seen in cross-sectional image of substrate shown in **Figure 6-29**. The randomly distributed nanowires have large number of crossings compared to partially aligned nanowires that exhibit few crossings.

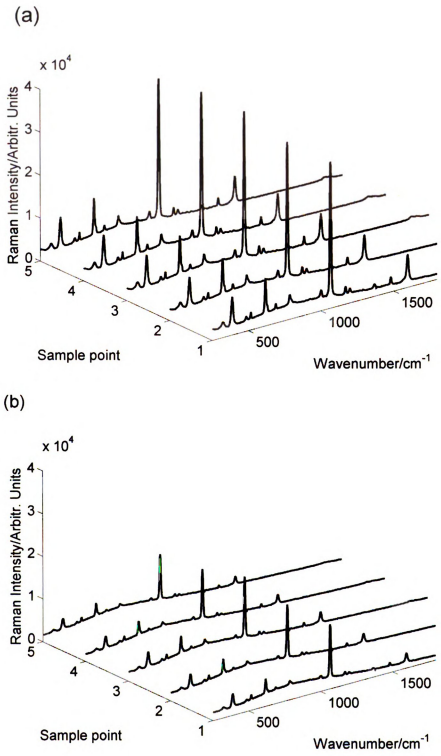

Figure 6-28. SERS from SAM of 4-MBT for (a) randomly distributed NWs, t_{acc}=15 s. (b) Partially aligned NWs, t_{acc}=15 s.

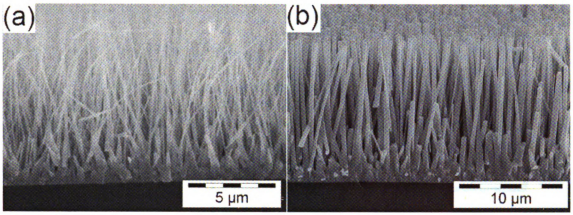

Figure 6-29. Cross-section for ZnO nanowires. (a) Randomly distributed. (b) Partially aligned.

Another morphology that yielded strong SERS was ZnO nanoparticles that were formed on gold-coated substrate in the low temperature region (~450 ^{o}C). Here the substrate gets a coating of densely packed nanometric ZnO particles as shown in **Figure 6-30**. The EDS data analysis shows nearly stoichiometric ZnO (23.37 % Zn, 21.49 % O_2) that is thin enough to pass electron beam resulting in strong signal from underlying silicon (36.14 % Si, and 19.0% Au). These densely packed ZnO nanoparticles coated with ~42 nm gold also yielded strong SERS signal for SAM of MBT as shown in **Figure 6-30**. The strong enhancement from these particles is probably due to there close proximity that allows for inter-particle couple of plasmonic field between particles[39].

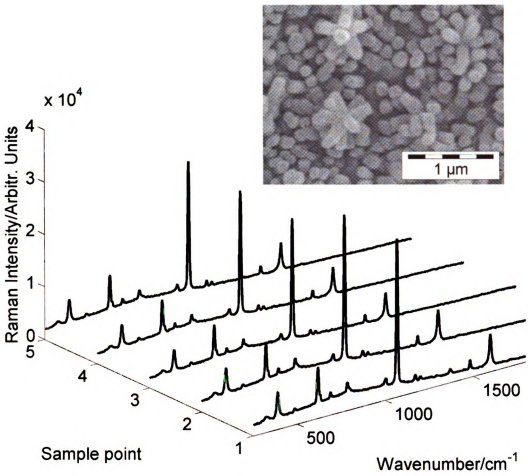

Figure 6-30. ZnO nanoparticles in low temperature region of reactor and SERS spectra of SAM of MBT after gold coating of particles, t_{acc}=5 s.

6.7.3 SERS for 1,2-BDT

To confirm the enhancement for other molecules, detection of 1,2-BDT as a probe molecule was also investigated using gold-coated ZnO NW substrate. This molecule is known to form self assembled monolayer (SAM) on Au for concentration $\geq 1 \times 10^{-3}$ M after more than 20 min of soaking[126]. We immersed our SERS-active nanowires substrates in 1 mM solution of 1,2-BDT in methanol for 20 min. This concentration is the smallest that was reported for monolayer coverage and is expected to yield a more

conservative estimate of enhancement. The sample was then rinsed with methanol to ensure removal of any excess analyte and allowed to dry before acquiring Raman spectra. **Figure 6-31** shows the SERS spectra from 42 nm Au coated ZnO NWs, which clearly shows the 1,2-BDT peaks. The broad continuum is also somewhat suppressed following the formation of BDT SAM on the Au coated nanowires. **Figure 6-32** shows successive spectra from substrate collected from points spaced 250 μm apart and shows good reproducibility of measurement.

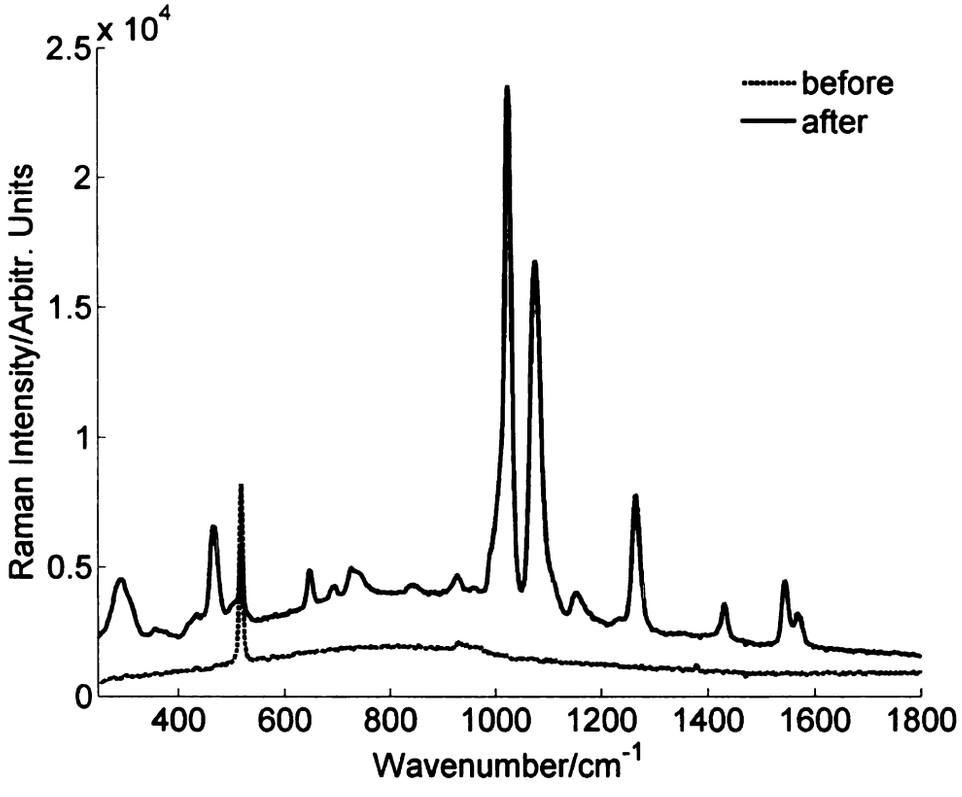

Figure 6-31. SERS spectra of self-assembled monolayer of 1,2-BDT from Au coated ZnO nanowires, t_{acc}= 15 s. Also shown is spectra before analyte application.

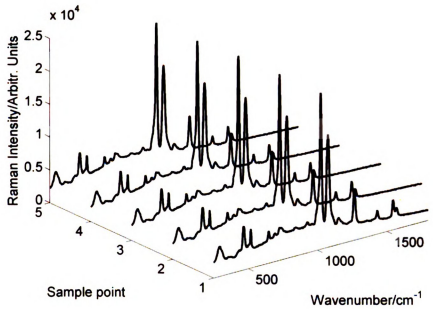

Figure 6-32. Successive SERS spectra from 1mM BDT along a line on substrate, t_{acc}=15 s .

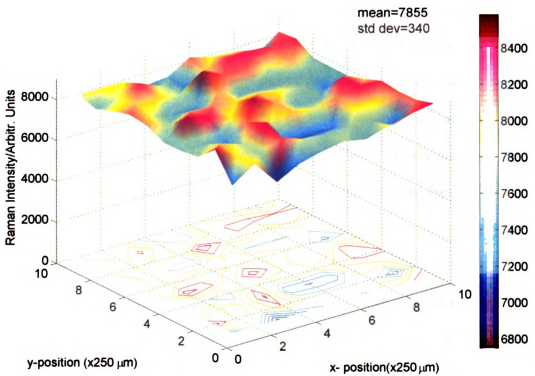

Figure 6-33. Area map of 1028 cm^{-1} Raman peak of 1,2-BDT, t_{acc}=5 s for each point.

Figure 6-33 shows the plot of the 1028 cm^1 peak of 1,2-BDT for 100 points scanned in a rectangular area of 2.5 mm × 2.5 mm. The data confirms that the substrate provides very uniform SERS enhancement with small standard deviation (~ 4.3% from mean). The SERS *EF* for 1,2-BDT is again calculated using equation (6.3) and this time the 1028 cm^{-1} Raman band of 1,2-BDT is utilized. Assuming monolayer coverage of substrate with 1,2-BDT and each molecule binding to 2 Au atoms on surface, we get 6.4×10^{14} molecules/cm^2 on the substrate. Considering the laser spot size of 100 μm diameter, nearly 8.35×10^{-14} moles (5.04×10^{10} molecules) of 1,2-BDT contribute to the SERS signal. The ordinary Raman spectra of the source 1,2-BDT was used as reference to calculate Raman *EF*. The laser excitation volume was estimated to be ~6.3 nL from depth of field considerations. The average enhancement factor from equation (6.3) was found to be ~ 4.1×10^5. The low enhancement factor relative to 4-MBT is probably due to sub-monolayer coverage of 1,2-BDT on the substrate. A thin film was found to form on the glass vial holding the analyte suggesting some sort of reaction or deposition of analyte on walls. The coating did not dissolve back into solvent even after sonication. This may cause lowering of analyte concentration from that of initially prepared yielding sub-monolayer analyte coverage and under-estimation of enhancement factor.

6.8 Conclusion

The detailed synthesis of ZnO nanowires using a simple thermal evaporation set up is presented in this chapter. The NWs synthesis is likely due to a combination of self-catalytic growth and VLS mechanism. Like the case of GeO_2 substrate presented earlier, the gold coating was found to introduce a broad background in the Raman spectrum of

nanowires. The ZnO substrates were evaluated using R6G and NB as probe molecules. Strong enhancement was found at isolated locations, which was sufficient to easily detect μMolar concentrations of the two probe molecules. On the other hand, no discernable Raman spectra could be obtained from bulk solutions at these concentrations. This clearly confirms the SERS from nanowires but at few isolated locations. The isolated enhancement was attributed to the nature of analytes that don't chemically bind to the substrate. This hypothesis was tested by using thiol based probe molecules of 4-MBT and 1,2-BDT. These aromatic thiol based analytes are known to chemically bind with the metal coating to form SAM on the substrate. The average Raman enhancement factor for 4-MBT and 1,2-BDT were estimated to the order of 10^6 and 10^5 respectively. The repeatability of SERS measurement was tested by recording spectra from 100 sample points spanning 2.5×2.5 mm^2 area of the substrate. A very uniform and repeatable SERS spectra was found for both types of analytes with small standard deviation of less than 5% over the tested areas. These results demonstrate that the gold-coated ZnO NW substrates have the potential to provide a very uniform SERS enhancement.

Chapter 7: Metallic Nanorods based SERS Substrates

Silver, gold and copper are the common metals for the plasmonic nanostructures due to their ability to support surface plasmons in the visible region of electromagnetic spectrum. Exploring the metallic nanostructures made up of these metals for SERS is a natural extension of this property. The different metallic nanostructures or more appropriately nanorods were synthesized using a grazing angle deposition technique also known as "Oblique angle deposition". The substrates were characterized using SEM and EDS. SERS studies were conducted using nile blue, 4-methylbenzenthiol, and 1,2-benzenedithiol as probe molecules.

7.1 Oblique angle deposition

Oblique Angle Deposition (OAD) is a technique to create porous films by utilizing tilt of substrate with respect to incident flux direction. The oblique incidence of the flux creates atomic shadowing from already deposited islands and this promotes inclined columnar structures under conditions of limited adatom diffusion. Such features of deposited films were first observed in 1959 while studying magnetic anisotropy of iron films and optical activity of fluorite films deposited under oblique angle of incident flux[174-176]. The technique had been known and utilized previously for enhancing contrast of weakly reflecting surfaces and to emphasize surface roughness by decoration in electron microscopy[177]. The technique is quite general and various sources including e-beam, thermal, laser, and sputter deposition can be used. The substrate can be fixed or rotated at different speeds during rotation (phased rotation) to yield desired level

of isotropy. Substrate can be flat or templated to grow ordered arrays. The technique is quite robust and practically any material or combination of materials may be synthesized. Lu *et al.* have synthesized Si springs and tungsten nanorods on flat and templated substrates[178]. Suzuki *et al.* demonstrated SERS from silver and gold coated arrays of SiO_2 nanorods prepared by a variation of OAD technique[179, 180]. More recently there have been number of reports of good SERS enhancement by using pure silver nanorods synthesized by OAD[36, 37, 181]. In this work metallic nanorods of copper, aluminum and silver were synthesized for use as SERS substrate.

7.2 Metallic nanorods synthesis

The metallic nanorods were synthesized utilizing the oblique angle deposition technique that yields a porous columnar morphology on substrate [36, 174, 175, 182, 183]. The glass slides were first cleaned using ultrasonication in acetone, followed by methanol and finally in D/I water for 15 min each. Then the slides were blown dry using compressed nitrogen. The slides were mounted on the deposition stage of PVD chamber and first a thin layer (~50 nm) of metal (aluminum, copper or silver) was deposited at normal incidence using standard e-beam evaporation. The base pressure at the start of deposition was around 3×10^{-6} Torr and substrate was continuously rotated at ~ 6 rpm during deposition. The deposited film thickness was monitored using quartz crystal monitor (Inficon XTM/2) operating at 6MHz. The substrate was heated from rear to $85\pm3\,^{\circ}C$ during deposition using two quartz lamps housed under the substrate holder. The substrate was then tilted (82 ± 3° with respect to source flux direction) so the incident flux arrived at a grazing angle and another 400-900 nm of metal was deposited

without rotating the substrate to get different length of nanorods. The actual deposited film at grazing angle is expected to be somewhat less than this thickness since quartz crystal monitor measures the normal incidence flux. In case of aluminum nanorods, first we synthesized the desired length of nanorods and then coated only the tips of nanorods with ~10 nm of silver by switching the source vapor flux from aluminum to silver. The substrate angle change was achieved by tilting the substrate assembly with respect to the fixed incident vapor flux from e-beam source. **Figure 7-1**(a) shows the schematic of the OAD set up utilized to synthesize the nanorods. It is worth mentioning that the substrates were having a mirror finish following initial normal deposition. However, the surface finished changed to a dull appearance after about 200 nm metal at grazing angle deposition as can be seen from optical images of silver and copper nanorods on glass substrates in **Figure 7-1**(b) and (c) respectively.

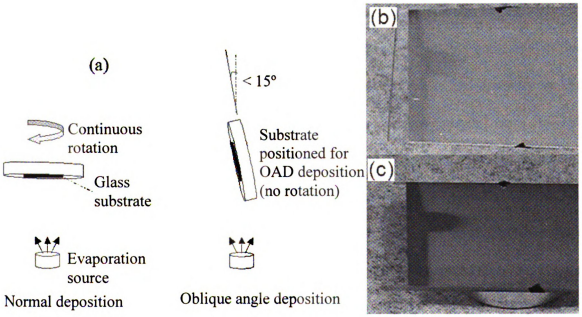

Figure 7-1. (a) OAD experimental set up schematic. (b) Optical image of Silver nanorods substrate (c) Optical image of copper nanorods substrate.

Figure 7-2 shows the SEM (accelerating voltage 15kV, 15mm working distance) image of the substrates with dense and well-aligned nanorods of different metals. As can be seen, the incidence flux was arriving from the bottom of the substrate and the shadowing effect is clearly visible in the form of black V-shape behind the white particulate towards the bottom-center of the image in **Figure 7-2** (c). It is envisaged that a combination of shadowing effect and high silver mobility even at low temperature is causing the incident flux to self-coalesce into small nanorods[40]. The aluminum nanorods show many sharp facets whereas copper and silver rods are mostly cylindrical. Typical length, diameter, and density of aluminum nanorods was found to be 652±96 nm, 217±66 nm, and 5-6 /μm^2 respectively from SEM studies. The silver nanorods were found to be more dense (10-11/μm^2) with length and diameter averaging 587±46 nm and 71±12 nm respectively. The copper nanorods were also dense (12-14/μm^2) like silver but exhibit greater bundling perpendicular to the direction of incident flux. The average length and diameter of copper nanorods was 523±58 nm and 64±8 nm respectively. It may be mentioned that the length of nanorods is the main controllable parameter in this synthesis technique whereas little or no control exists over density and diameter for the deposition conditions used in this work. The nanorods in length ranging from 500-700 nm, as shown in **Figure 7-2**, were found to yield good SERS signal. The diameters and lengths of the three types of nanorods were measured from SEM analysis. **Figure 7-3**, **Figure 7-4** and **Figure 7-5** show the distribution for diameters and lengths of aluminum, copper and silver nanorods respectively. The EDS analysis of the aluminum, copper and silver nanorods substrates is shown in **Figure 7-6**, **Figure 7-7** , and **Figure 7-8** respectively. The oxidation of nanorods is more severe for copper and aluminum than

silver as is evident from EDS quantization results. The silicon, sodium and calcium form a part of the underlying substrate glass. The underlying substrate shows up in the EDS because the electron beam penetrates few micron into the sample whereas the top layer of silver is only few hundred nm thick.

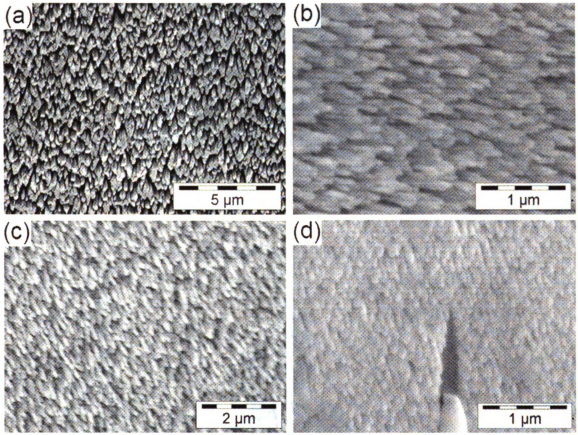

Figure 7-2. SEM images of nanorods synthesized on glass substrate. (a) Aluminum nanorods. (b) Copper nanorods. (c) Silver nanorods. (d) Silver nanorods showing shadowing effect.

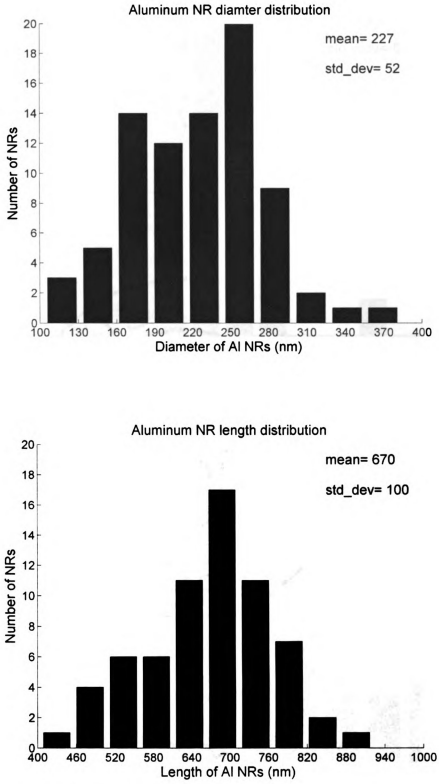

Figure 7-3. Aluminum NRs diameter and length distribution.

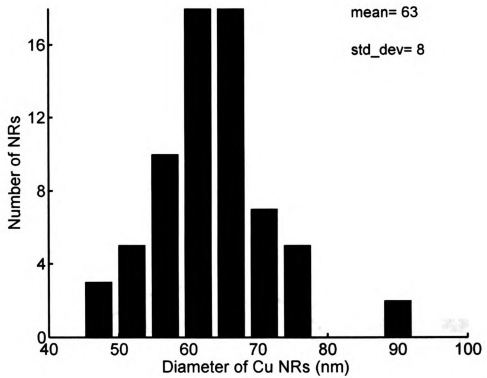

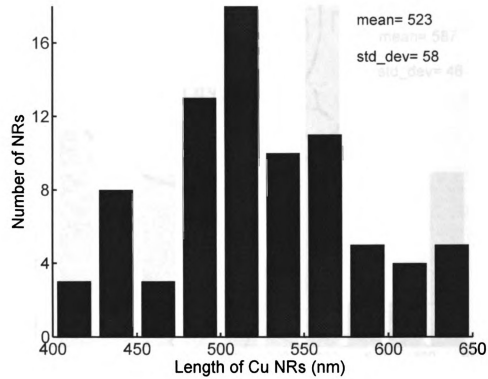

Figure 7-4. Copper NRs diameter and length distribution.

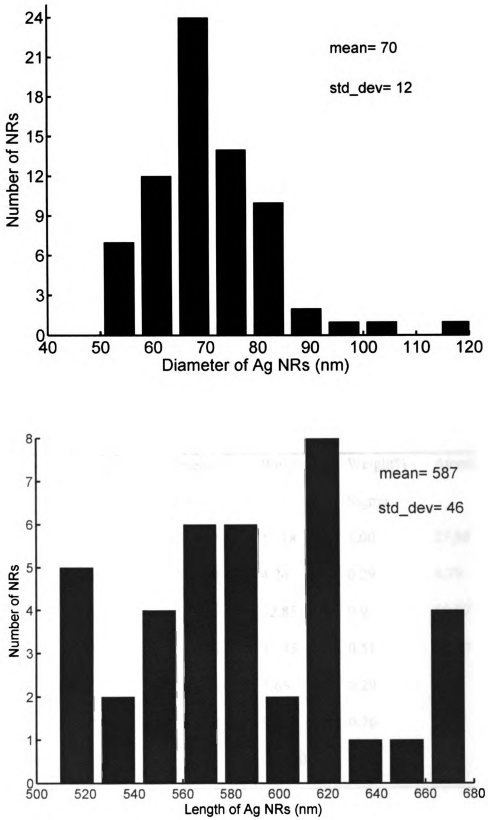

Figure 7-5. Silver NRs diameter and length distribution.

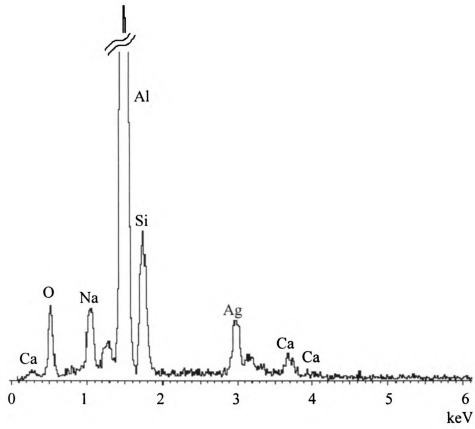

Element	App Conc.	Intensity Corrn.	Weight%	Weight% Sigma	Atomic%
O K	4.38	0.7629	17.18	1.00	27.88
Na K	1.94	1.3700	4.24	0.29	4.79
Al K	19.35	1.0946	52.85	0.9	50.87
Si K	3.10	0.6896	13.45	0.51	12.43
Ca K	0.85	0.9584	2.65	0.29	1.72
Ag L	2.34	0.7273	9.62	0.76	2.31
Totals			100.00		

Figure 7-6. EDS spectra and quantization results for aluminum nanorods substrate.

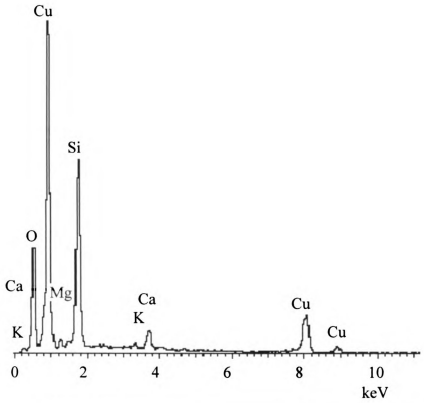

Element	Weight%	Atomic%
C K	3.30	8.81
O K	19.87	39.76
Mg K	1.12	1.48
Si K	17.06	19.44
K K	0.58	0.47
Ca K	2.67	2.13
Cu L	55.40	27.91
Totals	100.00	

Figure 7-7. EDS spectra and quantization results for copper nanorods substrate.

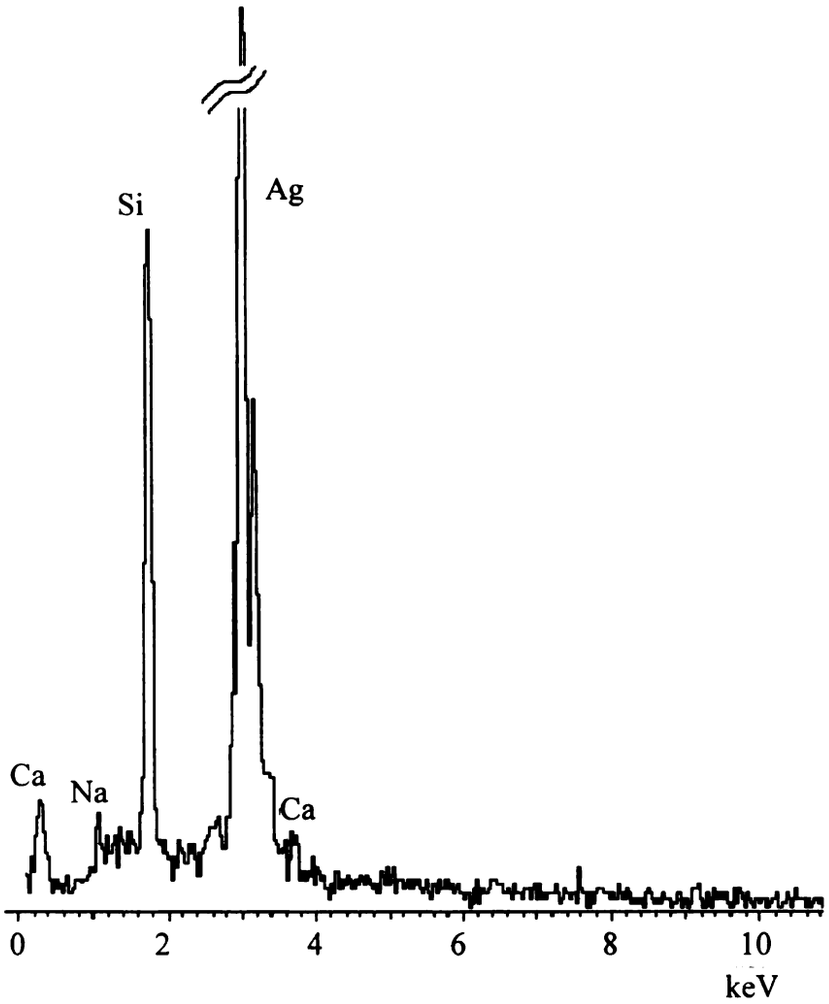

Element	App Conc.	Intensity Corrn.	Weight%	Weight% Sigma	Atomic%
Na K	0.18	0.8436	2.02	0.66	6.12
Si K	1.65	0.9923	15.37	0.95	38.06
Ca K	0.24	0.9365	2.35	0.65	4.08
Ag L	7.97	0.9202	80.26	1.26	51.74
Totals			100.00		

Figure 7-8. EDS spectra and quantization results for silver nanorods substrate.

There does not appear to be any specific requirement of having glass as the substrate for nanorods synthesis. The sample holding steel clips were also found to contain similar nanorods. For example, **Figure 7-9** shows the SEM image for one of the sample clips and the dense and aligned nanorods are covering the entire surface.

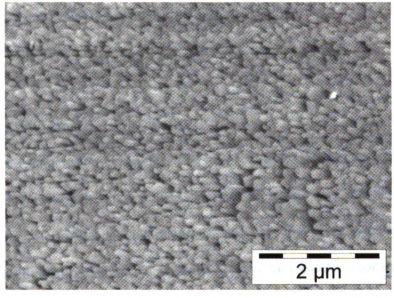

Figure 7-9. Silver nanorods that grew on sample clips (clips made of steel).

7.3 Oblique angle deposition kinetics

An excellent review of the different mechanism suggested to explain oblique angle deposition is given by Abelmann[183] and will not be repeated here. In summary, the shadowing effect is advanced as the most plausible argument for the formation of nanorods. In addition surface diffusion of adatoms also plays an important role. This can be random or directional due to oblique angle of incident which imparts them a lateral momentum[183]. For example, silver has high mobility even at room temperature and has been observed to self-coalesce from smooth film into small islands[40]. Other factors

such as presence of water or oxides on the surface also affect the process as these change the diffusion of adatoms[183]. Oxidation usually reduces whereas water increases surface diffusion of adatoms. So it may be a combination of shadowing and self-coalescing that is actually driving the growth of nanorods. The nano columns are tilted toward surface normal which is explained by the lateral momentum of incident flux[184]. Other operating parameters affecting growth are angle of incident flux, substrate temperature, and rate of deposition.

7.3.1 Incident flux angle

At increasing oblique angles, the vapor flux encounters enhanced atomic shadowing. This results in an increased porous structure of isolated grains that are inclined towards vapor source. This occurs because of atomic shadowing, which creates areas where incident flux cannot reach due to low adatom mobility for surface diffusion. Vick *et al.* reported that angle of greater than 80° is needed for any appreciable shadowing[185]. Similarly best results for germanium nanorods on Si were obtained for an angle of 87° with 0.2 – 1.5 A°/sec deposition rate[186].

7.3.2 Temperature

High temperature means greater mobility or surface diffusion of adatoms and this improves the crystallinity of the deposited material. However, for high temperatures the column cross-section tends to become elliptical and bundling results. As long as the increase in temperature is such that the bulk diffusion does not become dominant, the morphology will be still the columnar.

7.3.3 Rate of deposition

Low deposition rate gives the adatoms more time to diffuse on the substrate to form islands. It also ensures a larger spacing between nuclei in all directions, thus reducing bundling of growing nanorods. In fact there are two different types of diffusivities for the adatoms – one over the substrate and another over the growing film[187]. Better columnar structures are achieved for material having low diffusitivity over substrate but high over the growing film.

7.4 Raman characterization of substrates

The substrates were first characterized by acquiring Raman spectra without any analyte to establish the background reference. **Figure 7-10** shows the Raman spectra of silver nanorods without any probe molecule. The spectra contains broad background that peaks around 700 cm^{-1}. The exact source of this background is not known but has been commonly attributed to metal luminescence [188] or electronic Raman scattering from underlying metal[39, 73]. The spectra were also collected from uncoated part of glass slide and the shiny smooth silver film as shown in **Figure 7-11**. The smooth and shiny silver film did not yield any discernable spectra whereas broad fluorescence peak can be seen for glass slide. This fluorescence is strongly diminished for the silver coated part of the substrate.

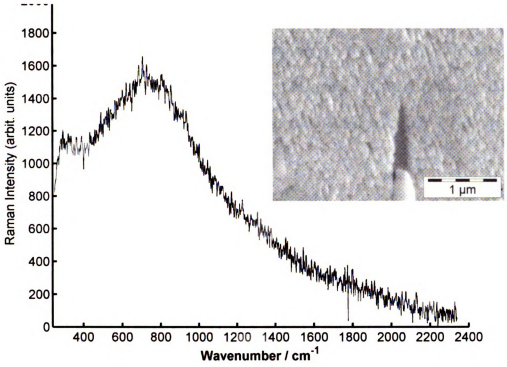

Figure 7-10. Raman spectra of silver nanorods, t_{acc} = 5 s. Insert shows SEM image of silver nanorods.

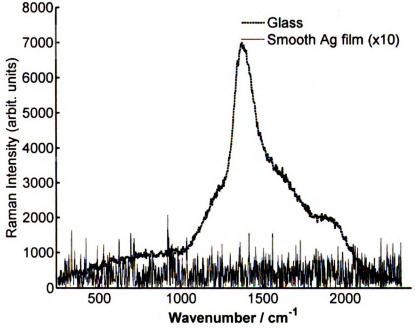

Figure 7-11. Raman spectra of smooth silver film and glass slide, t_{acc} =5 s.

Figure 7-12 shows the Raman spectra from silver tipped aluminum nanorods and copper nanorods. Just like case of silver nanorods, both types of substrates are characterized by broad background. The broad background is most probably due to electronic Raman scattering from underlying roughness of nanorods.

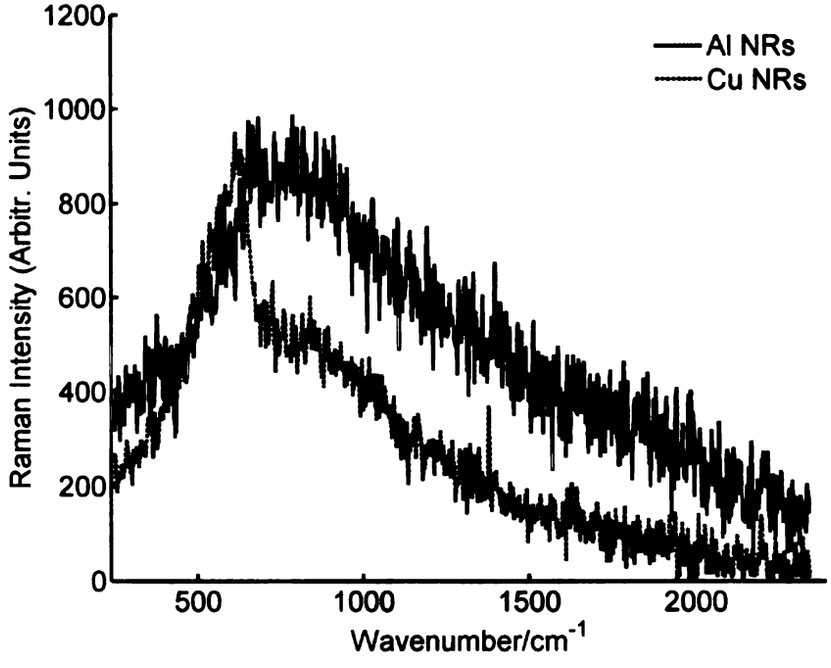

Figure 7-12. Raman spectra of copper and silver tipped aluminum nanorods, t_{acc} 5 s.

7.5 Detection of nile blue

Nile blue was the first analyte used for SERS evaluation of metallic nanorods. The probe solution was prepared by dissolving nile blue in 95% ethanol and then diluting this stock solution to get a concentration of ~ 5 μM. The samples for SERS measurement were prepared by applying nearly 3 μL drop of 5 μM solution to the substrate. The applied volume of analyte immediately spread to nearly 11 mm diameter spot on the substrate and was allowed to dry before acquisition of spectra. **Figure 7-13** shows

Raman spectra of substrate before and after application of 3 μL of 5 μM NB and all major peaks of NB are clearly distinguishable. The applied analyte volume/concentration and substrate coverage imply that nearly 1.24×10^{-15} moles of NB are contributing to SERS signal. The ordinary Raman spectra from 5 μMolar bulk solution of NB showed only the peaks for ethanol and did not yield any detectable NB spectra. This clearly confirms the enhancement from silver nanorods. It may be worth mentioning that no discernable ordinary Raman spectra could be observed even from highly concentrated (0.17 M ethanolic) NB solution due to strong fluorescence background as shown in the insert of **Figure 7-13**.

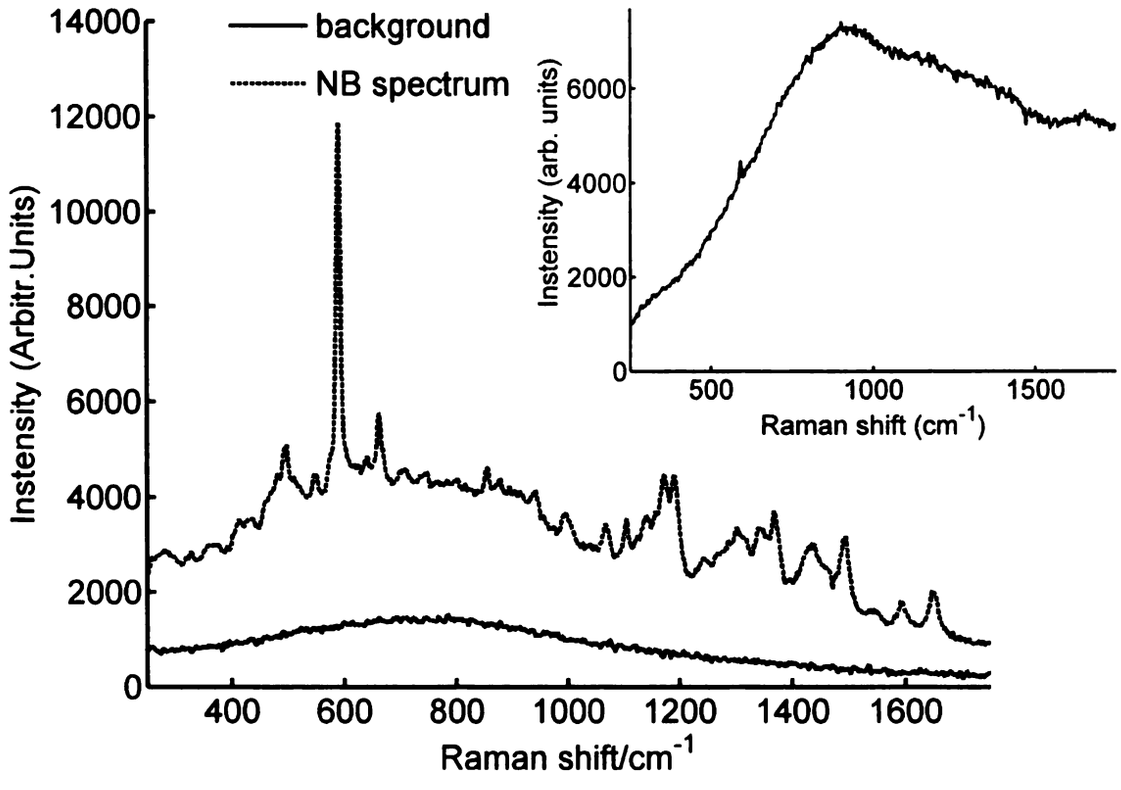

Figure 7-13. SERS spectra from Ag nanorods substrates before and after applying 3 μL of 5 μM ethanolic NB, t_{acc} 15 s. Insert shows ordinary Raman spectra of 170 mM NB in ethanol with only weak 582 cm^{-1} peak identifiable.

Figure 7-14 shows the successive SERS spectra of NB from nine different randomly selected points on the substrate. The major peaks of NB are clearly identifiable but some variation in signal intensity from different areas of the substrate is noticeable. Further investigation of substrate showed strong enhancement at most locations but some variation of Raman signal was observed across the substrate. These can be attributed to the non-uniform binding of the analyte on the substrate. For a more thorough study, another type of analyte that are known to strongly bind to the metal like thiols are investigated in the next section.

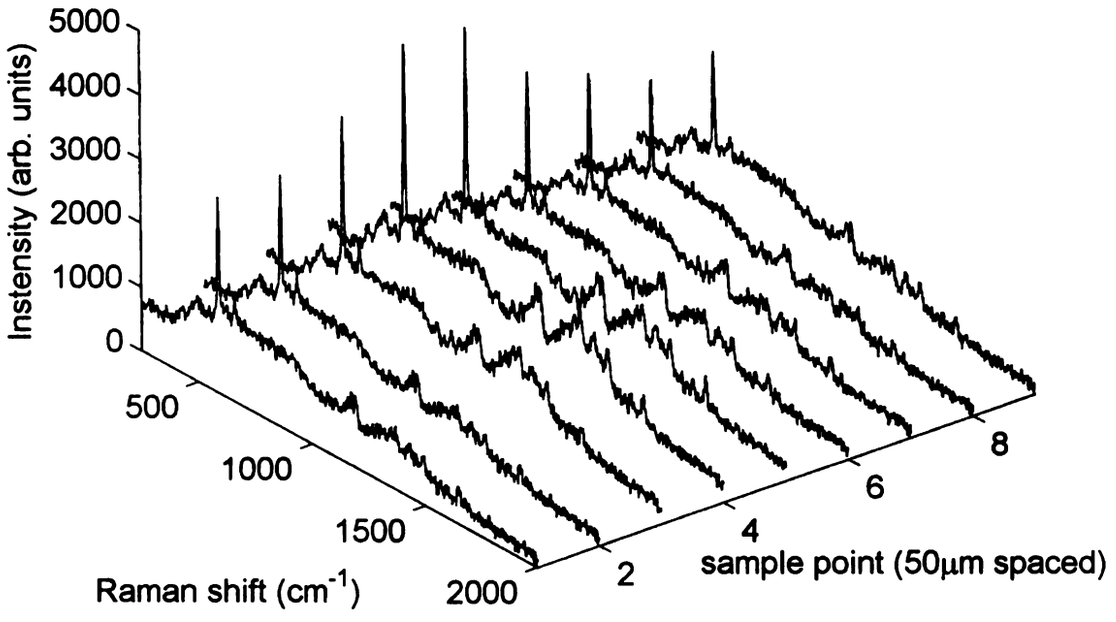

Figure 7-14. SERS spectra from Ag nanorods substrate from different spots for 5 μM ethanolic NB, t_{acc}= 5 s.

7.6 Detection of MBT

The 4-MBT, being an aromatic thiols, forms self-assembled monolayers (SAMs) on gold, silver, and copper[125]. The SAM forming analyte allows for easier and more accurate computation of the number of molecules contributing to SERS, and helps to obtain a better estimation of the Raman enhancement factor. Also such common probe molecules allow comparing the performance of the SERS substrates against others reported in the literature. The SAMs were prepared by soaking the silver tipped aluminum nanorods in a 100 μM methanolic solution of 4-MBT for 14 hrs. This concentration of 4-MBT is an order of magnitude smaller than the one reported for SAM[127, 189, 190] and is expected to yield sub-monolayer coverage. Actual coverage is expected to be even lower since silver tipped aluminum nanorods have substantial voids between adjacent rods. After the 4-MBT soak, the substrate was rinsed with methanol to remove multilayers and/or crystals that might have formed[127]. The substrate was then dried in the stream of nitrogen before acquiring the SERS spectra. **Figure 7-15** shows Raman spectra from silver tipped aluminum nanorods substrate and the characteristic peaks of 4-MBT are easily identifiable. Also shown is the Raman spectrum from the substrate alone, which shows a weak background continuum. A slightly enhanced continuum is also present in the SERS spectrum of 4-MBT monolayer. It has been almost a universal observation that the molecular SERS spectrum is accompanied by a broad background covering most of the normal 0-3000 cm^{-1} range[39, 73]. The precise origin of this continuum is still not clear and some researchers attribute this background to electronic Raman scattering from metal[116, 117] while others consider it luminescence[118]. However, it can be removed by the baseline correction.

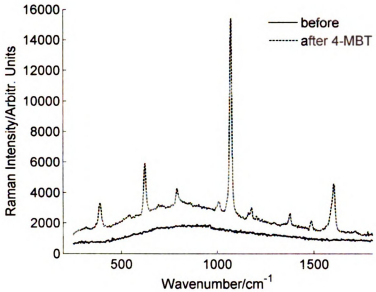

Figure 7-15. Raman spectra from silver tipped aluminum nanorods before and after application of 100 μM 4-MBT, t_{acc}= 15 s.

Figure 7-16 shows the successive spectra from different sample points lying along a line arbitrarily scanned on the substrate and the characteristic spectrum of 4-MBT is easily recognizable.

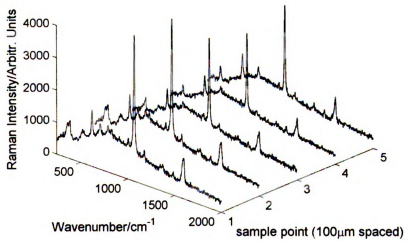

Figure 7-16. MBT SAM spectra before and after soaking aluminum nanorods in 0.1 mM methanolic for 14 hrs, t_{acc}= 5 s.

The spatial uniformity and repeatability of SERS measurement from substrate has been a challenging issue in SERS research. To investigate repeatability of the SERS signal, we acquired spectra from 100 raster-scanned locations covering an area of 1 mm × 1 mm. The 1071 cm^{-1} Raman peak intensity from each sample point is then plotted in **Figure 7-17** to give a spatial map of enhancement from the substrate. It can be seen that the substrate provides unambiguous and uniform SERS spectra for a monolayer of analyte over the tested area with only subtle variations.

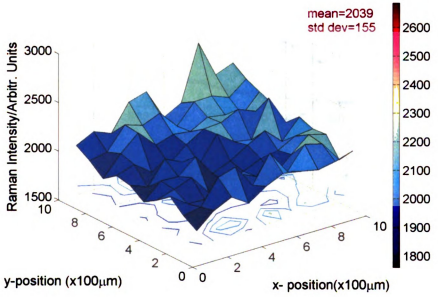

Figure 7-17. 4-MBT 1071 cm^{-1} Raman peak intensity distribution from silver tipped aluminum nanorods for randomly chosen area on substrate, t_{acc}= 5 s.

The copper nanorods were also evaluated for SERS using 4-MBT as probe molecule. The substrate was soaked in 1 mM 4-MBT solution for 15 hrs to form SAM[190]. After monolayer formation, substrate was rinsed with methanol to remove any physisorbed molecules and dried with nitrogen. The copper nanorods also yield

sufficient enhancement to detect main peaks of 4-MBT as shown in **Figure 7-18** but the signal intensity is low compared to silver tipped aluminum nanorods. This result is not unexpected given greater SERS activity of silver compared to copper.

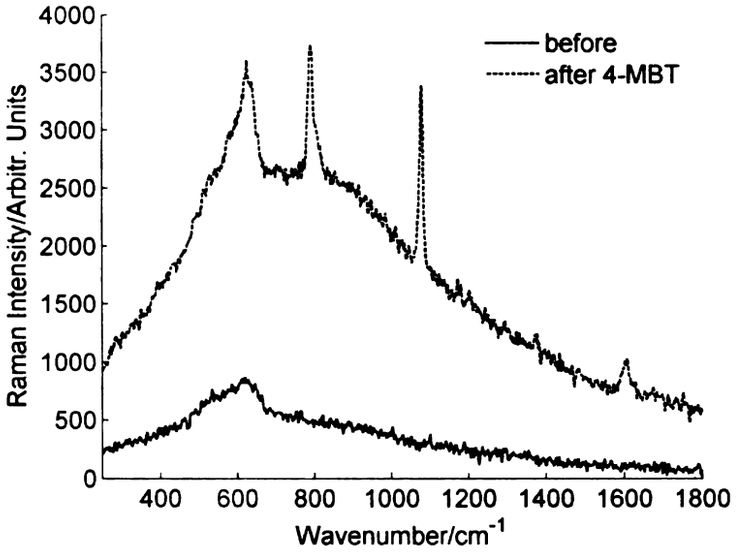

Figure 7-18. Raman spectra from copper nanorods before and after formation of SAM of MBT, t_{acc}= 15 s.

SERS from silver nanorods have been previously reported[36, 191] and hence it is reasonable to compare the SERS performance of aluminum and copper nanorods to that of silver. Hence, sliver nanorods were also synthesized using OAD and soaked in 100 μM methanolic MBT to compare their SERS performance with aluminum and copper nanorods. The silver nanorods also yield strong SERS spectrum of 4-MBT as shown in **Figure 7-19**. Quantitatively the intensity of main Raman peak at 1068 cm^{-1} is ~6 times stronger for silver nanorods than for aluminum nanorods.

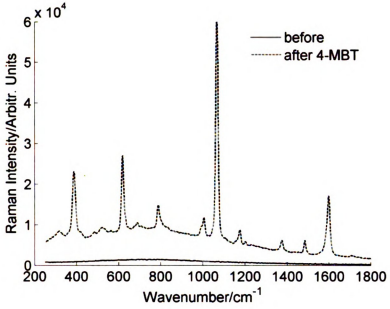

Figure 7-19. Raman spectra of from Silver nanorods substrate before and after formation of SAM of 4-MBT, t_{acc}= 15 s.

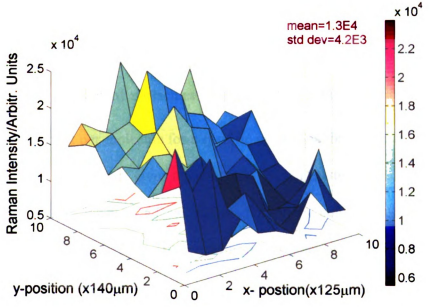

Figure 7-20. 4-MBT 1068 cm^{-1} Raman peak intensity distribution for a randomly chosen area on a silver nanorods substrate, t_{acc}= 5 s.

The spatial reproducibility of SERS signal form silver nanorods is again analyzed by acquiring spectra from 100 points covering a sample area of 1.4 ×1.25 mm^2. The spatial variation of 1068 cm^{-1} peak of 4-MBT from the tested area is shown in **Figure 7-20** and confirms good reproducibility of SERS signal.

The experimental Raman enhancement factor (*EF*) for the nanorods substrate was estimated using the equation

$$EF = \frac{I_{SERS}}{I_{ref}} \frac{N_{ref}}{N_{SERS}} \qquad (7.1)$$

where I_{SERS} is the intensity of some specific Raman band from the analyte adsorbed on a SERS active substrate and N_{SERS} is the number of molecules contributing to I_{SERS}. Similarly I_{ref} is the intensity of the same Raman band from the bulk analyte and N_{ref} is the number of molecules that yield I_{ref}. Thus equation (7.1) yields the Raman enhancement per molecule for a specific vibrational band of analyte. This specific band is typically the one that gives the strongest Raman scattering and hence we selected the 1068 cm^{-1} Raman band for *EF* calculation. For a more comprehensive estimate of *EF*, we utilized the average intensity from 100 sample points of substrate in equation (7.1). Taking 4.5×10^{14} molecules/cm^2 for a monolayer of 4-MBT on silver (we assume that the binding of 4-MBT on silver is similar to that of gold[130]), approximately 5.87×10^{-14} moles (or 3.53×10^{10} molecules) of 4-MBT were excited in the laser spot. The determination of N_{ref} is more involved and different methodologies have been

reported to estimate it. One obvious choice to estimate N_{ref} is by recording the Raman signal from a flat metal coated part of the same substrate but this method seldom yields any discernable spectra due to extremely weak Raman signal from just a monolayer of analyte in this configuration. Moreover, the Raman signal obtained in this configuration is not the true ordinary Raman spectra due to the presence of metal in the vicinity of the analyte[54]. Alternately one may use solid bulk form or higher concentration solution of analyte to get the approximate values of the reference parameters. Either of these techniques needs an estimate of laser interaction volume and that can be calculated from depth of field considerations. We did not detect any ordinary Raman spectra from ~20 mM 4-MBT methanolic bulk solution. Therefore, we used a solid crystal of 4-MBT to get values of I_{ref} and N_{ref}. The number of molecules excited in the bulk sample was determined by assuming the excitation volume to have the shape of a cylinder with waist diameter equal to the focused laser beam diameter and length equal to the depth of filed. The depth of field was determined by changing laser beam focus on sample and recording the 1/2 power points. The N_{SERS} was computed by taking the monolayer thickness of 4-MBT as 0.5 nm[127]. The average enhancement factor based on mean intensity from 100 sample points was estimated to be ~4.09×10^5 whereas the peak enhancement factor was found to be ~ 1.03×10^6. It may be mentioned that we ignore surface roughness in the *EF* calculations that can introduce a minor variation from the calculated value. However, the increased surface area due to roughness is largely offset by substantial voids between nanorods. The average *EF* for the copper and silver nanorods was found to be ~2.23×10^5 and ~2.51×10^6 respectively. The higher *EF* for silver nanorods is probably due to greater SERS activity of Ag. The Raman enhancement from copper nanorods is

not found to be very promising and the obvious reason is the rapid deterioration of the surface due to oxidation[127].

It is useful to compare the measured Raman *EF* with that predicted by theory. Theoretical enhancement factor for nanorods under quasi-static approximation can be calculated from relationship proposed by Wokaun *et al.*[192]

$$EF_{SERS} = \left| f(\omega_0).f(\omega_R) \right|^2 \tag{7.2}$$

where $f(\omega_0)$ and $f(\omega_R)$ are, respectively, the enhancement at laser and scattered Raman wavelengths. According to (7.2), the enhancement consists in two different factors: $f(\omega_0)$ from particle near-field enhancement at incident wavelength and $f(\omega_R)$ arising from the re-radiation of the molecule Raman near-field by the particle. The best enhancement should be located near average of two wavelengths. This also explains why the SERS enhancement decreases for higher Raman bands i.e., resonance width cannot effectively cover both incident and scattered radiation.

For an isolated metallic object of volume V and dielectric function $\varepsilon(\omega) = \varepsilon_1(\omega) + i\varepsilon_2(\omega)$ placed in an external electric field of frequency ω_0, the electric field enhancement $f(\omega)$ is given by[74]

$$\left| f(\omega) \right|^2 = \frac{\left| \varepsilon(\omega) \right|^2}{\left\{ 1 - \left[1 - \varepsilon_1 \right] A_j + \varepsilon_2 C \right\}^2 + \left\{ \varepsilon_2 A_j + \left[1 - \varepsilon_1 \right] C \right\}^2} \tag{7.3}$$

where $C = \frac{4\pi^2 V}{3\lambda^3}$ and the depolarization factor[193] $0 < A_j < 1$ characterizes particle eccentricity. For a spheroid with principal axes of length $2l_a$, $2l_b$, $2l_c$ and the laser field applied field applied along one of these axis, the depolarization factor is given by[192]

$$A_j = \frac{abc}{2} \int_0^\infty \frac{ds}{(s+l_j^2)\left\{(s+l_a^2)(s+l_b^2)(s+l_c^2)\right\}^{1/2}}, \qquad j = a, b, c.$$

The depolarization factors can be computed from above expression knowing only the geometry of the particle. **Table 7-1** lists some of these factors for some common particle shapes.

Table 7-1. Depolarization factors for some common geometries.

Shape	Depolarization factors		
	A_a	A_b	A_c
Sphere	1/3	1/3	1/3
Prolate spheroid with $a:b = 2:1$ and b=c	0.1736	0.4132	0.4132
Prolate spheroid with $a:b = 3:1$ and b=c	0.1087	0.4456	0.4456
Prolate spheroid with $a:b = 3:1$ and b=c	0.0754	0.4623	04623
Oblate spheroid with $a:b = 1:3$ and b=c	0.6354	0.1823	0.1823
Needle with $a:b \to \infty$ and b=c	0	0.5	0.5

Equation (7.3) can be used to predict theoretical SERS enhancement from the knowledge of dielectric function and depolarization factor of metal particle. The metallic nanorods synthesized here can be approximated as prolate spheroids with incident polarization along the long axis of the rods. The dielectric function of metals at the laser excitation wavelength can be approximated from the published values. For noble metals like silver, the imaginary part of the dielectric constant is small throughout the visible range and peak Raman enhancement $|f(\omega)|^2$ can be found by maximizing equation (7.3) with respect to $\varepsilon_1(\omega)$. The peak enhancement factor is obtained for $\varepsilon_1(\omega_{res}) \approx 1 - \frac{1}{A_j}$ assuming both $\varepsilon_2(\omega)$ and $\frac{V}{\lambda^3}$ are much smaller than unity. **Figure 7-21**(a) is a plot of bulk optical constants of silver as reported by Johnson and Christy[76]. We used cubic spline interpolation to get silver dielectric constants $\varepsilon_1 = -29.7841$ at 785 nm from reported values. This value of ε_1 will yield resonance in a prolate spheroid of aspect ratio nearly 6 ($A_j = 0.0481$) with laser excitation along long axis. **Figure 7-21**(b) shows the calculated Raman enhancement for 71 nm diameter silver nanorod (treated as prolate spheroid) as a function of aspect ratio. The SERS enhancement increases with increasing eccentricity of nanorod and becomes maximum ($\sim 7.605 \times 10^5$) for an aspect ratio of nearly 6. It may be reiterated that the theoretical model is valid for an isolated rod and does not take into account dipolar interactions between neighboring structures. The measured EF is higher than the predicted value due to contributions from neighboring nanorods.

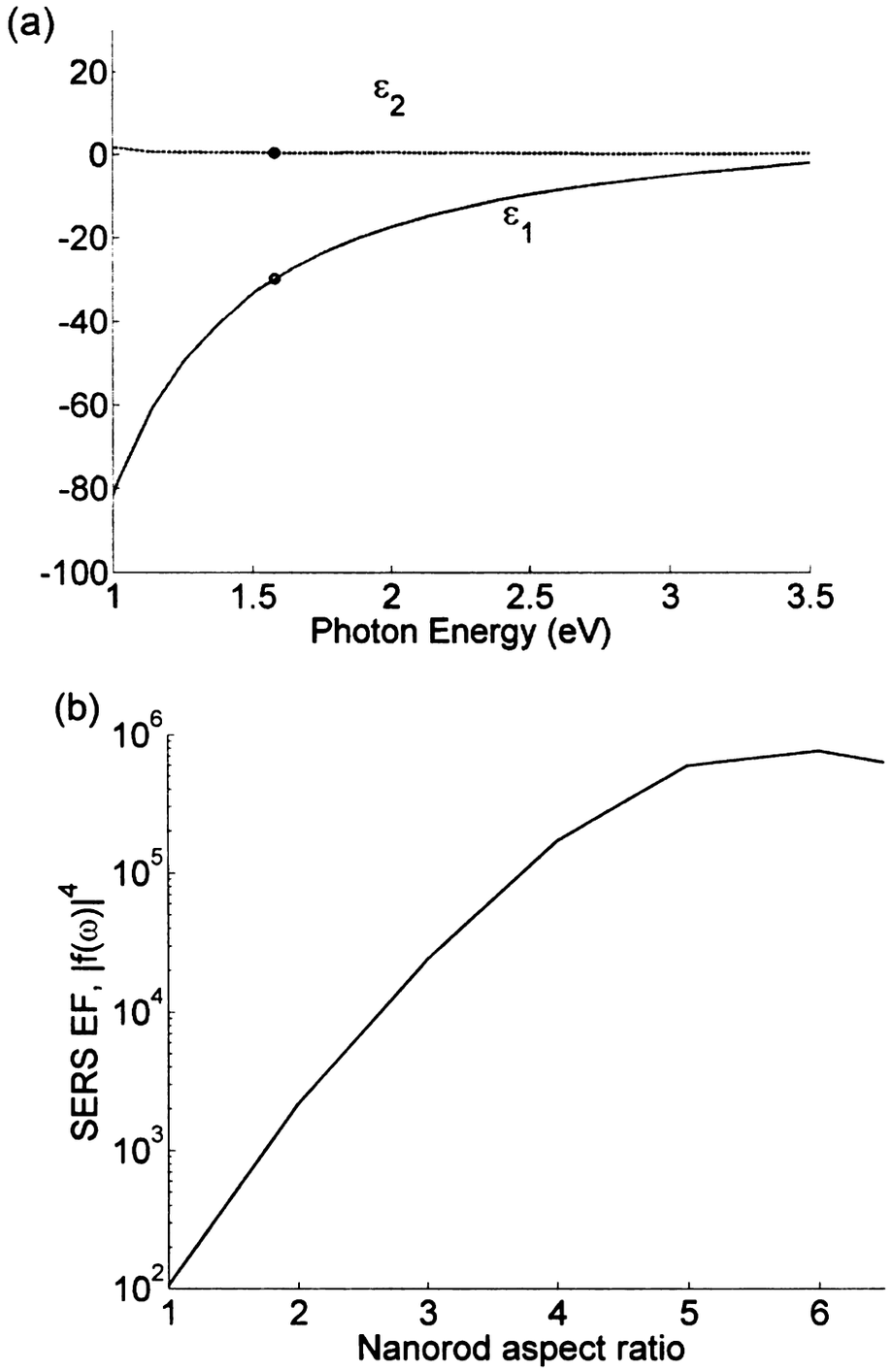

Figure 7-21. (a) Optical constants of silver as function of incident wavelength[76]. Circles correspond to laser wavelength used in this work. (b) Theoretical enhancement factor for an isolated silver nanorod as function of aspect ratio.

Similar theoretical analysis can be repeated for copper nanorods and is shown in **Figure 7-22**. The imaginary part of the dielectric function has larger value in case of copper and represents greater losses (absorption in material) compared to silver. On the other hand, the real part of dielectric function for copper has a lower magnitude than silver and this is reflected in resonance being excited for lower particle eccentricity (the maximum of SERS *EF* is predicted for an aspect ratio of 5 in case of copper as against 6 for silver). The predicted maximum *EF* is $\sim 5.88\times10^{5}$ for the copper nanorods. However, the measured value was smaller than the predicted and difference is probably due to oxidation of copper nanorods. The rapid oxidation of copper and aluminum was visually noticeable by the change of substrate color after removing it from deposition chamber. The EDS data also showed substantial presence of oxygen in case of aluminum and copper nanorods. The silver nanorods did not show any significant oxygen during EDS. This indicates the oxidation of silver is much slower compared to copper. The non-conductive top oxide layer on copper and aluminum not only changes the chemical binding of analyte but will also adversely affect the excitation of surface plasmons. On the other hand, silver oxide is a conductor and may still support surface plasmons.

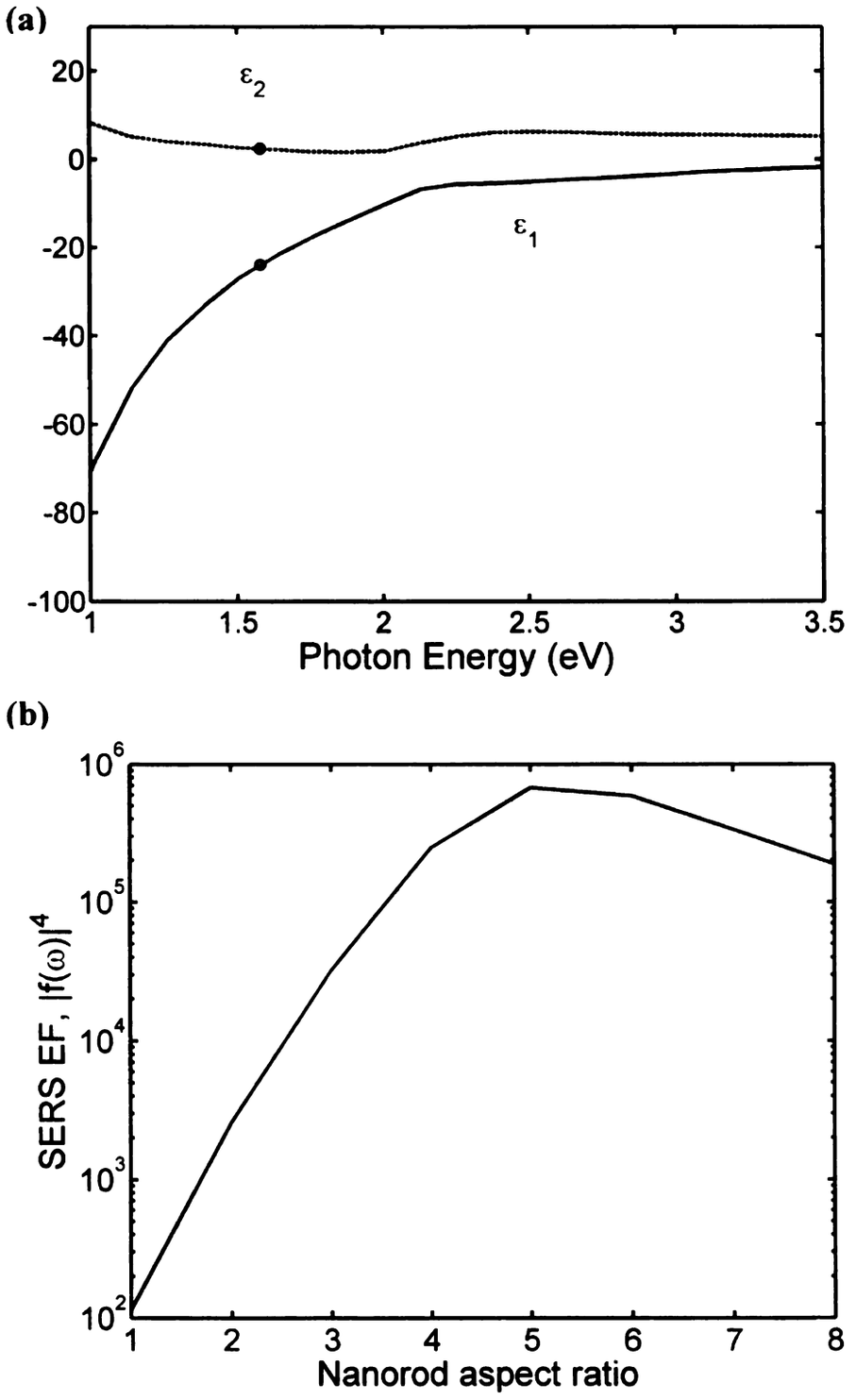

Figure 7-22. (a) Optical constants of copper as function of incident wavelength[76]. Circles correspond to laser wavelength used in this work. (b) Theoretical enhancement factor for an isolated copper nanorod as function of aspect ratio.

7.7 Detection of BDT

The SERS performance of the aluminum and silver nanorods was also evaluated using 1,2-BDT probe molecule. This molecule also forms self assembled monolayer (thickness of SAM ~0.49 nm) on silver by forming two sulfur-metal bonds[126]. For monolayer formation, the silver tipped aluminum nanorods substrate was soaked in 20 μM methanolic 1,2-BDT solution for 40 min. The sample was then rinsed with methanol and dried under dry nitrogen stream to ensure removal of any excess analyte. **Figure 7-23** shows the Raman spectrum of SAM of 1,2-BDT from silver tipped aluminum nanorods. It is evident that the substrate exhibits good enhancement to yield strong and unambiguous spectrum of 1,2-BDT superimposed on slowly varying broad background.

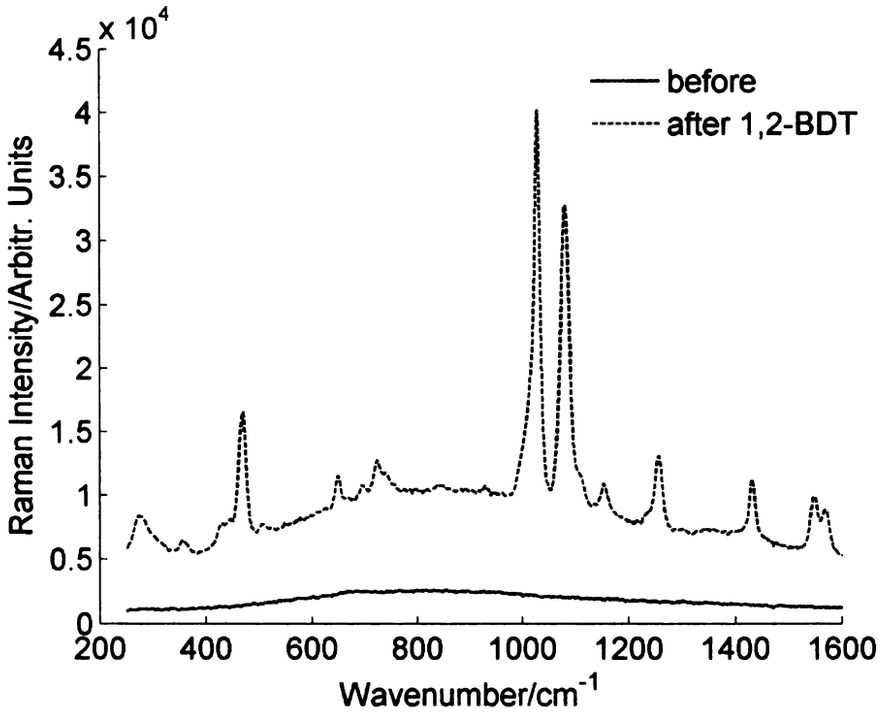

Figure 7-23. Raman spectra of aluminum nanorods before and after application of formation of SAM of 1,2-BDT, t_{acc}= 15 s.

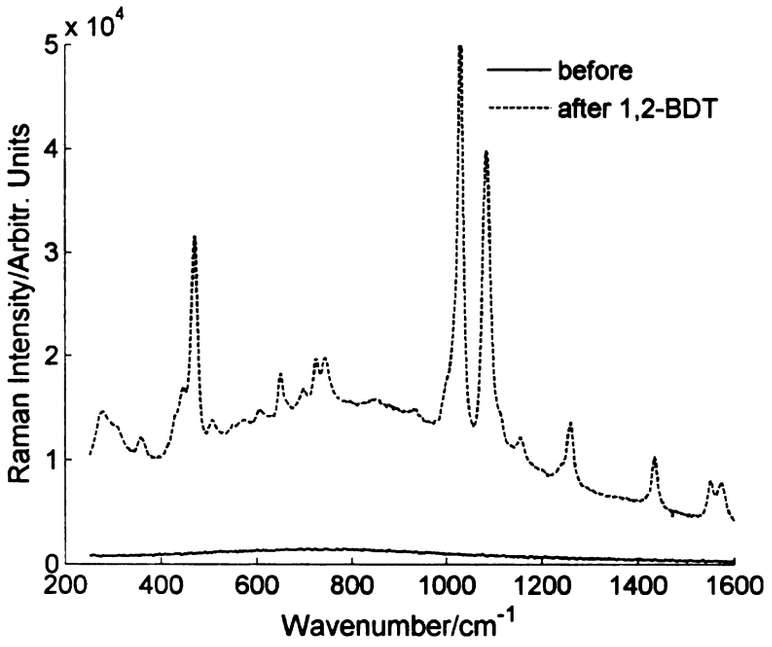

Figure 7-24. Raman spectra of silver nanorods before and after application of 20 μM 1,2-BDT, t_{acc}= 15 s.

For comparison we also acquired SERS spectra of 20 μM 1,2-BDT from silver nanorods substrate that was processed under similar conditions. **Figure 7-24** shows that the silver nanorods yield more intense spectra than aluminum nanorods as was observed in case of 4-MBT. To quantify the performance of these two substrates for 1,2-BDT, the SERS *EF* for 1,2-BDT was again calculated using equation (7.1) by utilizing the 1028 cm^{-1} Raman band. Assuming monolayer coverage of substrate with 1,2-BDT and each molecule binding to two silver atoms on surface, we get ca. 6.4×10^{14} molecules/cm^2 on the substrate. This implies that nearly 8.35×10^{-14} moles (5.03×10^{10} molecules) of 1,2-BDT contribute to the SERS signal for the laser spot size of 100 μm. The ordinary Raman spectrum of the bulk 1,2-BDT was used as a reference to calculate the Raman *EF*. The average intensity of 1028 cm^{-1} Raman band from 100 sample points

was employed to calculate Raman *EF*. The average enhancement factor from equation (7.1) was found to be $\sim 2.3 \times 10^5$ for aluminum nanorods and $\sim 8.1 \times 10^6$ for silver nanorods. These values are comparable to those obtained for 4-MBT and confirm strong enhancement from nanorods substrate.

7.8 Conclusion

Copper and aluminum nanorods were synthesized on glass substrates using OAD with e-beam evaporation. The tips of aluminum nanorods were coated with silver to make them SERS active. The EDS of the copper and aluminum nanorods showed presence of oxygen that was attributed to the oxidation of metal after exposure to atmosphere. The synthesized substrates were evaluated for SERS by using 4-MBT and 1,2-BDT as probe molecules. The substrates yielded an average enhancement factor of the order of 10^5 with good uniformity over the tested areas. The amount of analyte that yielded these strong SERS spectra was on the order of femto moles and confirmed the high sensitivity of these substrates. However, EDS analysis of both copper and aluminum nanorods showed existence of substantial amount of oxygen that was attributed to the corresponding metal oxide layer on nanorods. Silver nanorods on glass slides were also prepared and their SERS performance was compared with that of other two types of nanorods using same probe molecules. The pure silver nanorods substrates were found to have higher density of nanorods and larger enhancement factors of the order of $\sim 10^6$. The better SERS from silver nanorods was attributed to its greater SERS activity and absence of insulating top layer.

Chapter 8: Conclusions and Future Work

8.1 Conclusion

This dissertation deals with various types of nanowires and nanorods substrates for potential use in SERS. The initial SERS studies were done using germanium oxide nanowires synthesized at high temperature (> 800 °C). The high temperature synthesis scheme yielded very dense and long nanowires with little control over diameter and length. The nanowires were found to comprise of crystalline hexagonal phase of GeO_2 based on TEM, EDS and Raman studies. The as-synthesized nanowires did not yield any discernable Raman enhancement. Subsequently nanowires substrates were coated with thin film of gold to provide surface plasmon active surface. The gold was selected because of its good SERS activity, chemical stability and compatibility with biological species. The gold coating introduced a broad background in the SERS spectra of nanowires. The possible sources of background continuum due to contamination from metal deposition or processing of substrate were thoroughly investigated. The TEM study of gold-coated nanowires showed formation of nanoscale gold islands. It was concluded that the source of background is a characteristic of rough metal film over the substrate based on this study and previous reports in literature. The SERS performance of the substrates was evaluated using rhodamine 6G and nile blue probe molecules. Although strong SERS signal was obtained for micro molar concentration of these analytes, the issue of hot spots surfaced. It was hypothesized that the hot spots were due to selective adsorption of analyte over the substrate rather than the non-homogeneity of substrate. This hypothesis was tested by investigating thiol based analytes that are known to form self-assembled monolayers on gold under appropriate conditions. The 4-MBT, BPE and

1,2-BDT yielded strong and uniform SERS enhancement over tested area of the substrates. The average enhancement factor for GeO_2 nanowires based substrates was estimated to be of the order of 10^6 without any hot spots. The corresponding thickness of gold over smooth silicon surface did not yield any SERS enhancement after application of analyte alongside nanowire substrates. This showed the important role of nanowires in enhancing SERS signal. It was hypothesized that the nanowires framework served threefold purpose; (1) to provide a metal rough surface for plasmon activation, (2) to confine guide and couple the light between adjacent wires, and (3) to focus the light at the surface of the metal. The combined affect of these contributions of nanowires resulted in a strong and reproducible SERS signature from nanowires.

The lack of control over the diameter and length of the nanowires synthesized at high temperature necessitated further study of the synthesis process. The analysis of high temperature synthesis revealed very rapid reaction dumping lot of source material on the substrate in short time. It was hypothesized that the rate of reaction may be lowered by exploring temperate regime below the sublimation temperature of GeO. This led to the development of a new low temperature synthesis scheme that provided better control over the supply and condensation of source material on the substrate. The low temperature synthesis was carried out at a source temperature of ~650 °C while the substrate was located in the temperature region of 400-500 °C. This new synthesis employs the lowest temperature reported for germanium oxide nanowire growth using thermal evaporation. The technique yields good control over the diameter and length of nanowires. The Raman characterization of low temperature synthesized nanowires revealed a broad continuum with moderate strength. This was attributed to the existence of gold nanoparticles from

the initial gold film used to catalyze nanowires. However, the density of these gold particles was too low for any reasonable SERS enhancement and very weak Raman signal was detected for uncoated nanowires. The nanowires were coated with top gold layer to improve their SERS activity. Like the case of high temperature synthesized nanowires, gold coating resulted in substantial increase in the intensity of broad background. The SERS evaluation was done using 4-MBT and 1,2-BDT probe molecules. The substrates yielded strong and repeatable SERS signal for the two analytes over the tested area. The SERS performance of theses nanowire based substrates is also compared with that of commercially available SERS chip, Klarite from 3D Technologies Ltd. Our results indicate strong dependence of SERS on length of nanowires and thickness of gold coating. The average conservative estimates of enhancement factor for low temperature synthesized nanowire of nearly 1 μm length and coated with ~40 nm gold is approximately 6×10^6 with small standard deviation of nearly 4%. This enhancement was found to be better than from that of Klarite chip that yielded an enhancement of $\sim1.5\times10^6$ for same analyte at 785 nm laser excitation. This initial investigation confirms the potential of oxide nanowires for SERS applications aimed at developing a robust and sensitive detector platform.

Another type of substrate that was studied in this dissertation was the zinc oxide nanowires synthesized on silicon substrate. The synthesis was also based on simple thermal evaporation of zinc powder in an oxidizing environment. The same tube furnace set up used for germanium oxide nanowire synthesis was utilized to grow ZnO nanowires but with different reaction conditions. Unlike the case of germanium oxide that only grew at location of gold catalyst, the zinc oxide nanowires were also found at locations without

catalyst. However, the yield of catalyst-coated area was higher compared to uncoated area for the same experimental conditions. Another difference observed was in the morphology of the nanowires for the two materials. The germanium oxide nanowires almost always grew as long cylindrical wires whereas ZnO was found to yield a variety of morphologies including nanowires, hexagonal nanorods, nano-combs, nano-cages, nano-particles etc. However, the main morphologies were found to be nanowires and hexagonal nanorods. The hexagonal nanorods were usually partially aligned normal to the substrate and less dense compared to the randomly oriented nanowires. The SERS of both these morphologies of ZnO was also evaluated using 4-MBT and 1,2-BDT probe molecules. The gold thickness for optimal SERS enhancement was found to be ~40 nm. The average SERS enhancement of the order of 10^6 was obtained over the tested area of the substrate with small variations.

Metallic nanorods of aluminum and copper were also synthesized and evaluated for use as SERS substrates. The nanorods were fabricated over glass substrate using oblique angle deposition (OAD) technique. In OAD synthesis, the source material is evaporated from a point source and the resulting vapor arrives at a glancing angle on the substrate. The nanostructures are formed due to atomic shadowing of incident vapor on the substrate. The choice of aluminum and copper was based due to their low cost and ready availability in most research laboratories. The aluminum nanorods were synthesized with silver tips to make them SERS active. Silver nanorods have been previously reported to yield good SERS activity and were also synthesized to compare their performance against those of aluminum and copper. The synthesized nanorods were evaluated using NB, 4-MBT and 1,2-BDT probe molecules. The aluminum and copper

nanorods yielded average SERS enhancement factor of the order of 10^5 whereas silver nanorods showed stronger SERS enhancement of ~10^6. The stronger SERS enhancement for silver is not unexpected given the higher SERS activity of silver compared to other metals. However, an added issue with copper and aluminum nanorods is their tendency to form insulating surface oxide layer. Both aluminum and copper nanorods based substrates were found to change color after exposure to atmosphere. The EDS analysis confirmed existence of substantial quantity of oxide on the substrate. The insulating oxide layer not only changes the adsorption of analyte over the substrate but also affects the surface plasmon excitation in the top layer. Therefore, these two types were not considered competitive choices as SERS substrates unless surface stabilization can be achieved.

The list of major contributions of this dissertation is as follows:

1. Investigation of optimal conditions for high temperature synthesis of GeO_2 nanowires.
2. Demonstration of strong and reproducible SERS enhancement from gold coated GeO_2 nanowires synthesized at high temperature.
3. Development of novel technique for low temperature synthesis of GeO_2 nanowires.
4. Identification of optimal conditions for low temperature synthesis of GeO_2 nanowires.
5. Demonstration of good control over length and diameter of low temperature synthesis of GeO_2 nanowires.

6. Identification of optimal parameters for SERS from low temperature synthesized GeO_2 nanowires.
7. Demonstration of strong and uniform SERS enhancement from gold coated GeO_2 nanowires synthesized at low temperature.
8. Synthesis of two morphologies of ZnO nanowires.
9. Demonstration of strong and uniform SERS enhancement from two morphologies of ZnO nanowires.
10. Synthesis of aluminum, copper and silver nanorods and investigation of SERS performance.
11. Comparison of SERS performance of nanowires and nanorods with that of commercial Klarite SERS chip.

8.2 Future work

This dissertation forms the early work on the potential of using bulk synthesized oxide nanowires for use as SERS substrates. The results confirm that the nanowires have the potential to act as economical, scaleable and sensitive platform for detection of chemical species. The strength of these substrates lies in the good uniformity and repeatability of the SERS signal over the spatial extent of the substrate without the serious issue of hot spots that has plagued SERS research in case of random aggregates of metallic colloidals. However, caution has to be exercised in declaring these as the substrates of choice before further research. First of all, the most critical issue of analyte adsorption on the substrate needs be addressed. It is a universal agreement that gold and silver has high SERS sensitivity but the enhancement decays exponentially with

increasing distance from metal surface. The distances involved are of the order of few nanometers and can be reliably established for analytes that chemically bind to metal. This implies that the enhancement factors are strongly dependent upon type of analyte and the associated binding to the substrate. In fact, some sort of linker molecules may have to be used in order to immobilize non-binding target molecules on the substrate. A second issue relates to the change in the morphology of the substrate upon application of analyte solution. The resulting capillary forces during drying of the solution tend to pull nanowires together and leave behind bundled structures. There need to be more work done to increase robustness of the nanostructures so as to minimize distortion of nanostructures on the substrate. Thirdly nanowires of additional materials may be evaluated for use in SERS. Hence future work needs to focus on improving robustness of the nanowires, exploring additional nanowire materials, and investigating mechanism to immobilized analyte at close proximity to the substrate. Regarding metallic nanorods, only silver nanorods have exhibited the potential to yield high enhancement. Future work on silver nanorods may be focused towards achieving better control over the diameter of the nanorods to further enhance their SERS performance.

Appendix A: Operation of EzRaman-L system

A.1 Introduction

Following procedure gives a summary of EzRaman-L operation. For detailed description, please refer to system operation manual located alongside system.

A.2 Procedure

1. Power on the computer.
2. Login using Raman profile. Password is "raman".
3. Start the Enwave software by double clicking "Enwave application center" icon on desktop.
4. Start CCD camera software by double clicking "Logitech quickcam" icon on desktop. Start "Quick capture" to view sample image.
5. Make appropriate entry in Raman System log book.
6. Power on the Raman system by using Power ON/OFF switch located on front. The "SYSEM ON" green LED should lit.

A.3 Sample mounting

1. Set the sample on the sample stage.
2. Adjust distance between lens and sample to get sample at lens focus (~ 6 mm for 0.22 NA and ~3 mm 0.55 NA lens tube).
3. Position CCD camera such that it faces the sample
4. Place the cover in front of the Raman probe enclosure to ensure laser safety.
5. Put on laser safety goggle.

A.4 Acquiring Spectra

1. Set the Raman system parameters. Typical parameters are, "Integration :5, Average :1 and Boxcar :1". Use longer integration or higher average to get better signal in case of weak and noisy spectra.
2. Select X-axis as "cm^{-1}".
3. Select X-axis scale as minimum 250 maximum 2200.
4. Select Y-axis scale as minimum 0 maximum 60,000.
5. Switch on the laser by turning laser key clockwise from OFF to ON position. Wait for few seconds for red "LASER ON" LED to light.
6. Start desired type of scan by clicking corresponding icon. Typically continuous scan is used during focusing or spatial scanning of sample surface. Single scan will do one scan and then stop automatically whereas continuous scan needs be manually stopped using "Stop scan" button.

 Single scan

 Continuous scan

 Stop scan

7. Adjust fine focus by changing laser focus (use z-translation in quarter turn) and monitoring signal strength. The maximum signal intensity will be achieved when sample is in sharp focus. Stop scan if in continuous mode.
8. Obtain desired spectra by changing time and average settings if desired. Stop scan if in continuous scan mode.

9. Save Raman spectrum in desired file format (text, excel, jpg) by using save as option of "FILE" menu.

A.5 Shutdown

1. Make sure laser scan is OFF. If not, stop laser scan by pressing "Stop scan" icon.
2. Switch Off the laser by turning laser key clockwise from ON to OFF position. The red LASER ON LED should extinguish.
3. Shut down the Raman system by using Power ON/OFF switch located on front
4. Close Raman software.

A.6 System Calibration

1. System calibration is required to ensure correct pixel to wavenumber mapping. Please refer to chapter 5 of Raman system manual.

References

[1] G. L. Liu and L. P. Lee, "Nanowell surface enhanced Raman scattering arrays fabricated by soft-lithography for label-free biomolecular detections in integrated microfluidics," *Applied Physics Letters*, vol. 87, pp. 047101, 2005.

[2] A. Campion, "Raman Spectroscopy," in *Vibrational spectroscopy of molecules on surfaces*, J. T. Yates and T. E. Madey, Eds. New York and London: Plenum Press, 1987.

[3] E. Smith and G. Dent, *Modern Raman Spectroscopy - A practical approach*. West Sussex: John Wiley & Sons Ltd, 2005.

[4] C. L. Stevenson and T. Vo-Dinh, "Signal expressions in Raman Spectroscopy," in *Modern Techniques in Raman Spectroscopy*, J. J. Laserna, Ed. West Sussex: John Wiley and Sons, 1996, pp. 1-39.

[5] D. Porterfield and A. Campion, "Flourescence-free Ramam spectroscopy," *Journal of American Chemical society*, vol. 110, pp. 408-410, 1988.

[6] Fleischm.M, P. J. Hendra, and Mcquilla.Aj, "Raman-Spectra of Pyridine Adsorbed at a Silver Electrode," *Chemical Physics Letters*, vol. 26, pp. 163-166, 1974.

[7] M. Moskovits, "Surface roughness and the enhanced intesity of Raman scattering by molecules adsorbed on metals," *The Journal of Chemical Physics*, vol. 69, pp. 4159-4161, 1978.

[8] A. Otto, I. Mrozek, H. Grabhorn, and W. Akemann, "Surface-Enhanced Raman-Scattering," *Journal of Physics-Condensed Matter*, vol. 4, pp. 1143-1212, 1992.

[9] K. Kneipp, H. Kneipp, V. B. Kartha, R. Manoharan, G. Deinum, I. Itzkan, R. R. Dasari, and M. S. Feld, "Detection and identification of a single DNA base molecule using surface-enhanced Raman scattering (SERS)," *Physical Review E*, vol. 57, pp. R6281-R6284, 1998.

[10] K. Kneipp, H. Kneipp, G. Deinum, I. Itzkan, R. R. Dasari, and M. S. Feld, "Single-molecule detection of a cyanine dye in silver colloidal solution using near-infrared surface-enhanced Raman scattering," *Applied Spectroscopy*, vol. 52, pp. 175-178, 1998.

[11] K. Kneipp, H. Kneipp, I. Itzkan, R. R. Dasari, and M. S. Feld, "Surface-enhanced non-linear Raman scattering at the single-molecule level," *Chemical Physics*, vol. 247, pp. 155-162, 1999.

[12] K. Kneipp, H. Kneipp, R. Manoharan, I. Itzkan, R. R. Dasari, and M. S. Feld, "Near-infrared surface-enhanced Raman scattering can detect single molecules and observe 'hot' vibrational transitions," *Journal of Raman Spectroscopy*, vol. 29, pp. 743-747, 1998.

[13] K. Kneipp, Y. Wang, H. Kneipp, L. T. Perelman, I. Itzkan, R. Dasari, and M. S. Feld, "Single molecule detection using surface-enhanced Raman scattering (SERS)," *Physical Review Letters*, vol. 78, pp. 1667-1670, 1997.

[14] S. M. Nie and S. R. Emory, "Single-molecule detection and spectroscopy by surface-enhanced Raman scattering.," *Abstracts of Papers of the American Chemical Society*, vol. 213, pp. 177-Phys, 1997.

[15] S. Nie and S. R. Emory, "Probing Single Molecules and Single Nanoparticles by Surface-Enhanced Raman Scattering," *Science*, vol. 275, pp. 1102-1106, 1997.

[16] D. J. Maxwell, S. R. Emory, and S. M. Nie, "Nanostructured thin-film materials with surface-enhanced optical properties," *Chemistry of Materials*, vol. 13, pp. 1082-1088, 2001.

[17] W. A. Lyon and S. M. Nie, "Confinement and detection of single molecules in submicrometer channels," *Analytical Chemistry*, vol. 69, pp. 3400-3405, 1997.

[18] J. T. Krug, G. D. Wang, S. R. Emory, and S. M. Nie, "Efficient Raman enhancement and intermittent light emission observed in single gold nanocrystals," *Journal of the American Chemical Society*, vol. 121, pp. 9208-9214, 1999.

[19] K. Kneipp, Y. Wang, H. Kneipp, I. Itzkan, R. R. Dasari, and M. S. Feld, "Population pumping of excited vibrational states by spontaneous surface-enhanced Raman scattering," *Physical Review Letters*, vol. 76, pp. 2444-2447, 1996.

[20] J. Kneipp, "Nanosensors based on SERS for applications in living cells," *Surface-Enhanced Raman Scattering: Physics and Applications*, vol. 103, pp. 335-349, 2006.

[21] C. R. Yonzon, O. Lyandraes, N. C. Shah, J. A. Dieringer, and R. P. V. Duyne, "Glucose sensing with Surface-Enhanced Raman Spectroscopy," *Surface-Enhanced Raman Scattering: Physics and Applications*, vol. 103, pp. 367-379, 2006.

[22] T. Vo-Dinh, F. Yan, and M. B. Wabuyele, "Surface-Enhanced Raman Scattering for Biomedical Diagnostics and Molecular Imaging," *Surface-Enhanced Raman Scattering: Physics and Applications*, vol. 103, pp. 409-426, 2006.

[23] T. Vo-Dinh, N. Isola, J. P. Alarie, D. Landis, G. D. Griffin, and S. Allison, "Development of a multiarray biosensor for DNA diagnostics," *Instrumentation Science & Technology*, vol. 26, pp. 503-514, 1998.

[24] A. M. Alak and T. Vodinh, "Surface-Enhanced Raman-Spectrometry of Organophosphorus Chemical-Agents," *Analytical Chemistry*, vol. 59, pp. 2149-2153, 1987.

[25] S. Farquharson, F. E. Inscore, and S. Christesen, "Detecting Chemical Agents and their Hydrolysis Products in Water," *Surface-Enhanced Raman Scattering: Physics and Applications*, vol. 103, pp. 447-460, 2006.

[26] C. R. Y. Christy L. Haynes, Xiaoyu Zhang, Richard P. Van Duyne,, "Surface-enhanced Raman sensors: early history and the development of sensors for quantitative biowarfare agent and glucose detection," *Journal of Raman Spectroscopy*, vol. 36, pp. 471-484, 2005.

[27] X. Y. Zhang, N. C. Shah, and R. P. Van Duyne, "Sensitive and selective chem/biosensing based on surface-enhanced Raman spectroscopy (SERS)," *Vibrational Spectroscopy*, vol. 42, pp. 2-8, 2006.

[28] C. R. Yonzon, X. Zhang, J. Zhao, and R. P. Van Duyne, "Surface-enhanced nanosensors," *Spectroscopy*, vol. 22, pp. 42, 2007.

[29] S. Farquharson, A. D. Gift, P. Maksymiuk, and F. E. Inscore, "Rapid dipicolinic acid extraction from bacillus spores detected by surface-enhanced Raman spectroscopy," *Applied Spectroscopy*, vol. 58, pp. 351-354, 2004.

[30] A. Sengupta, M. Mujacic, and E. J. Davis, "Detection of bacteria by surface-enhanced Raman spectroscopy," *Analytical and Bioanalytical Chemistry*, vol. 386, pp. 1379-1386, 2006.

[31] K. T. Carron, X. Gi, and M. L. Lewis, "A Surface Enhanced Raman-Spectroscopy Study of the Corrosion-Inhibiting Properties of Benzimidazole and Benzotriazole on Copper," *Langmuir*, vol. 7, pp. 2-4, 1991.

[32] L. M. Sudnik, K. L. Norrod, and K. L. Rowlen, "SERS-active Ag films from photo reduction of Ag+ on TiO_2," *Applied Spectroscopy*, vol. 50, pp. 422-424, 1996.

[33] T. R. Jensen, M. D. Malinsky, C. L. Haynes, and R. P. Van Duyne, "Nanosphere lithography: Tunable localized surface plasmon resonance spectra of silver nanoparticles," *Journal of Physical Chemistry B*, vol. 104, pp. 10549-10556, 2000.

[34] G. Sauer, U. Nickel, and S. Schneider, "Preparation of SERS-active silver film electrodes via electrocrystallization of silver," *Journal of Raman Spectroscopy*, vol. 31, pp. 359-363, 2000.

[35] A. Tao, F. Kim, C. Hess, J. Goldberger, R. R. He, Y. G. Sun, Y. N. Xia, and P. D. Yang, "Langmuir-Blodgett silver nanowire monolayers for molecular sensing using surface-enhanced Raman spectroscopy," *Nano Letters*, vol. 3, pp. 1229-1233, 2003.

[36] S. B. Chaney, S. Shanmukh, R. A. Dluhy, and Y. P. Zhao, "Aligned silver nanorod arrays produce high sensitivity surface-enhanced Raman spectroscopy substrates," *Applied Physics Letters*, vol. 87, pp. 031908, 2005.

[37] H. Y. Chu, Y. J. Liu, Y. W. Huang, and Y. P. Zhao, "A high sensitive fiber SERS probe based on silver nanorod arrays," *Optics Express*, vol. 15, pp. 12230-12239, 2007.

[38] A. J. Haes, C. L. Haynes, A. D. McFarland, G. C. Schatz, R. R. Van Duyne, and S. L. Zou, "Plasmonic materials for surface-enhanced sensing and spectroscopy," *Mrs Bulletin*, vol. 30, pp. 368-375, 2005.

[39] J. Jiang, K. Bosnick, M. Maillard, and L. Brus, "Single molecule Raman spectroscopy at the junctions of large Ag nanocrystals," *Journal of Physical Chemistry B*, vol. 107, pp. 9964-9972, 2003.

[40] Z. Li, W. M. Tong, W. F. Stickle, D. L. Neiman, R. S. Williams, L. L. Hunter, A. A. Talin, D. Li, and S. R. J. Brueck, "Plasma-Induced Formation of Ag Nanodots for Ultra-High-Enhancement Surface-Enhanced Raman Scattering Substrates," *Langmuir*, vol. 23, pp. 5135-5138, 2007.

[41] J. P. Kottmann and O. J. F. Martin, "Plasmon resonant coupling in metallic nanowires," *Optics Express*, vol. 8, pp. 655-663, 2001.

[42] J. P. Kottmann, O. J. F. Martin, D. R. Smith, and S. Schultz, "Dramatic localized electromagnetic enhancement in plasmon resonant nanowires," *Chemical Physics Letters*, vol. 341, pp. 1-6, 2001.

[43] C. V. Raman and K. S. Krishnan, "A new type of secondary radiation," *Nature*, vol. 121, pp. 501-502, 1928.

[44] G. Mie, "Articles on the optical characteristics of turbid tubes, especially colloidal metal solutions.," *Annalen Der Physik*, vol. 25, pp. 377-445, 1908.

[45] D. A. Long, *Raman Spectroscopy*. New York: McGraw-Hill Inc, 1977.

[46] E. Gross, "Change of wave-length of light due to elastic heat waves at scattering in liquids," *Nature*, vol. 126, pp. 201-202, 1930.

[47] H. Skoog and Neiman, *Principles of Instrumental Analysis*, 5th ed. Philadelphia: Harcourt Brace College Pulbishers, 1998.

[48] H. A. Kramers and W. Heisenberg, "On the dispersal of radiation by atoms," *Zeitschrift Fur Physik*, vol. 31, pp. 681-708, 1925.

[49] P. A. M. Dirac, *Proc. R. Soc. London, Ser. A*, vol. 114, pp. 710, 1927.

[50] A. C. Albrecht, "Theory of Raman Intensities," *Journal of Chemical Physics*, vol. 34, pp. 1476-1484, 1961.

[51] A. Campion and P. Kambhampati, "Surface-enhanced Raman scattering," *Chemical Society Reviews*, vol. 27, pp. 241-250, 1998.

[52] A. Campion, J. E. Ivanecky, C. M. Child, and M. Foster, "On the Mechanism of Chemical Enhancement in Surface-Enhanced Raman-Scattering," *Journal of the American Chemical Society*, vol. 117, pp. 11807-11808, 1995.

[53] P. Kambhampati, C. M. Child, M. C. Foster, and A. Campion, "On the chemical mechanism of surface enhanced Raman scattering: Experiment and theory," *Journal of Chemical Physics*, vol. 108, pp. 5013-5026, 1998.

[54] M. Moskovits, "Surface-enhanced spectroscopy," *Reviews of Modern Physics*, vol. 57, pp. 783-826, 1985.

[55] R. W. Wood, "On a Remarkable case of Uneven Distribution of Light in a Diffraction Grating spectrum," *Proc. Phys. Soc. London*, vol. 18, pp. 269-275, 1902.

[56] H. Raether, "Surface-Plasmons on Smooth and Rough Surfaces and on Gratings," *Springer Tracts in Modern Physics*, vol. 111, pp. 1-133, 1988.

[57] J. A. Creighton, C. G. Blatchford, and M. G. Albrecht, "Plasma Resonance Enhancement of Raman-Scattering by Pyridine Adsorbed on Silver or Gold Sol Particles of Size Comparable to the Excitation Wavelength," *Journal of the Chemical Society-Faraday Transactions Ii*, vol. 75, pp. 790-798, 1979.

[58] J. Gersten and A. Nitzan, "Electromagnetic Theory of Enhanced Raman-Scattering by Molecules Adsorbed on Rough Surfaces," *Journal of Chemical Physics*, vol. 73, pp. 3023-3037, 1980.

[59] J. Gersten and A. Nitzan, "Spectroscopic Properties of Molecules Interacting with Small Dielectric Particles," *Journal of Chemical Physics*, vol. 75, pp. 1139-1152, 1981.

[60] J. I. Gersten, "The Effect of Surface-Roughness on Surface Enhanced Raman-Scattering," *Journal of Chemical Physics*, vol. 72, pp. 5779-5780, 1980.

[61] J. I. Gersten, "Rayleigh, Mie, and Raman-Scattering by Molecules Adsorbed on Rough Surfaces," *Journal of Chemical Physics*, vol. 72, pp. 5780-5781, 1980.

[62] S. L. Mccall and P. M. Platzman, "Raman-Scattering from Chemisorbed Molecules at Surfaces," *Physical Review B*, vol. 22, pp. 1660-1662, 1980.

[63] S. L. Mccall, P. M. Platzman, and P. A. Wolff, "Surface Enhanced Raman-Scattering," *Physics Letters A*, vol. 77, pp. 381-383, 1980.

[64] M. Kerker, O. Siiman, L. A. Bumm, and D. S. Wang, "Surface Enhanced Raman-Scattering (Sers) of Citrate Ion Adsorbed on Colloidal Silver," *Applied Optics*, vol. 19, pp. 3253-3255, 1980.

[65] M. Kerker, O. Siiman, and D. S. Wang, "Effect of Aggregates on Extinction and Surface-Enhanced Raman-Scattering Spectra of Colloidal Silver," *Journal of Physical Chemistry*, vol. 88, pp. 3168-3170, 1984.

[66] M. Kerker, D. S. Wang, and H. Chew, "Surface Enhanced Raman-Scattering (Sers) by Molecules Adsorbed at Spherical-Particles," *Applied Optics*, vol. 19, pp. 4159-4174, 1980.

[67] D. S. Wang, H. Chew, and M. Kerker, "Enhanced Raman-Scattering at the Surface (Sers) of a Spherical-Particle," *Applied Optics*, vol. 19, pp. 2256-2257, 1980.

[68] D. S. Wang and M. Kerker, "Enhanced Raman-Scattering by Molecules Adsorbed at the Surface of Colloidal Spheroids," *Physical Review B*, vol. 24, pp. 1777-1790, 1981.

[69] D. S. Wang and M. Kerker, "Absorption and Luminescence of Dye-Coated Silver and Gold Particles," *Physical Review B*, vol. 25, pp. 2433-2449, 1982.

[70] D. S. Wang, M. Kerker, and H. W. Chew, "Raman and Fluorescent Scattering by Molecules Embedded in Dielectric Spheroids," *Applied Optics*, vol. 19, pp. 2315-2328, 1980.

[71] H. Wang, C. S. Levin, and N. J. Halas, "Nanosphere arrays with controlled sub-10-nm gaps as surface-enhanced Raman spectroscopy substrates," *Journal of the American Chemical Society*, vol. 127, pp. 14992-14993, 2005.

[72] K. L. Kelly, E. Coronado, L. L. Zhao, and G. C. Schatz, "The optical properties of metal nanoparticles: The influence of size, shape, and dielectric environment," *Journal of Physical Chemistry B*, vol. 107, pp. 668-677, 2003.

[73] M. Moskovits, "Surface-enhanced Raman spectroscopy: a brief retrospective," *Journal of Raman Spectroscopy*, vol. 36, pp. 485-496, 2005.

[74] A. Wokaun, J. P. Gordon, and P. F. Liao, "Radiation Damping in Surface-Enhanced Raman-Scattering," *Physical Review Letters*, vol. 48, pp. 957-960, 1982.

[75] B. J. Messinger, K. U. Vonraben, R. K. Chang, and P. W. Barber, "Local-Fields at the Surface of Noble-Metal Microspheres," *Physical Review B*, vol. 24, pp. 649-657, 1981.

[76] P. B. Johnson and R. W. Christy, "Optical-Constants of Noble-Metals," *Physical Review B*, vol. 6, pp. 4370-4379, 1972.

[77] S. A. Maier, M. L. Brongersma, P. G. Kik, S. Meltzer, A. A. G. Requicha, and H. A. Atwater, "Plasmonics - A route to nanoscale optical devices," *Advanced Materials*, vol. 13, pp. 1501, 2001.

[78] C. J. F. Bottcher, *Theory of electric polarization*, vol. 1, 2nd ed. New York: Elsevier scientific publishing company, 1973.

[79] M. Moskovits, "Surface-enhanced Raman spectroscopy: a brief perspective," *Surface-Enhanced Raman Scattering: Physics and Applications*, vol. 103, pp. 1-17, 2006.

[80] A. M. Michaels, J. Jiang, and L. Brus, "Ag nanocrystal junctions as the site for surface-enhanced Raman scattering of single Rhodamine 6G molecules," *Journal of Physical Chemistry B*, vol. 104, pp. 11965-11971, 2000.

[81] R. S. Wagner and W. C. Ellis, "Vapor-Liquid-Solid Mechanism of Single Crystal Growth," *Applied Physics Letters*, vol. 4, pp. 89-90, 1964.

[82] M. Zacharias and P. M. Fauchet, "Light emission from Ge and GeO_2 nanocrystals," *Journal of Non-Crystalline Solids*, vol. 227-230, pp. 1058-1062, 1998.

[83] X. C. Wu, W. H. Song, B. Zhao, Y. P. Sun, and J. J. Du, "Preparation and photoluminescence properties of crystalline GeO_2 nanowires," *Chemical Physics Letters*, vol. 349, pp. 210-214, 2001.

[84] S. Sakaguchi and S. Todoroki, "Optical properties of GeO_2 glass and optical fibers," *Applied Optics*, vol. 36, pp. 6809-6814, 1997.

[85] Z. G. Bai, D. P. Yu, H. Z. Zhang, Y. Ding, Y. P. Wang, X. Z. Gal, Q. L. Hang, G. C. Xiong, and S. Q. Feng, "Nano-scale GeO_2 wires synthesized by physical evaporation," *Chemical Physics Letters*, vol. 303, pp. 311-314, 1999.

[86] Y. Zhang, J. Zhu, Q. Zhang, Y. Yan, N. Wang, and X. Zhang, "Synthesis of GeO_2 nanorods by carbon nanotubes template," *Chemical Physics Letters*, vol. 317, pp. 504-509, 2000.

[87] H. Y. Dang, J. Wang, and S. S. Fan, "The synthesis of metal oxide nanowires by directly heating metal samples in appropriate oxygen atmospheres," *Nanotechnology*, vol. 14, pp. 738-741, 2003.

[88] Q. L. J.-Q. Hu, X.-M. Meng, C.S. Lee, S.T. Lee,, "Synthesis and Nanostructuring of Patterned Wires of alpha-GeO_2 by Thermal Oxidation," *Advanced Materials*, vol. 14, pp. 1396-1399, 2002.

[89] Y. Su, X. Liang, S. Li, Y. Chen, Q. Zhou, S. Yin, X. Meng, and M. Kong, "Self-catalytic VLS growth and optical properties of single-crystalline GeO_2 nanowire arrays," *Materials Letters*, vol. 62, pp. 1010-1013, 2008.

[90] P. Hidalgo, B. Mendez, and J. Piqueras, "GeO_2 nanowires and nanoneedles grown by thermal deposition without a catalyst," *Nanotechnology*, vol. 16, pp. 2521-2524, 2005.

[91] Y. H. Tang, Y. F. Zhang, N. Wang, I. Bello, C. S. Lee, and S. T. Lee, "Germanium dioxide whiskers synthesized by laser ablation," *Applied Physics Letters*, vol. 74, pp. 3824-3826, 1999.

[92] C.-I. Wu and T. P. Hogan, "Growth of GeO_2 Nanowires by Thermal Annealing," presented at Mater. Res. Soc. Symp. Proc., San Francisco, 2006.

[93] Y. Cui, L. J. Lauhon, M. S. Gudiksen, J. F. Wang, and C. M. Lieber, "Diameter-controlled synthesis of single-crystal silicon nanowires," *Applied Physics Letters*, vol. 78, pp. 2214-2216, 2001.

[94] E. E. Crisman, Y. M. Ercil, J. J. Loferski, and P. J. Stiles, "The Oxidation of Germanium Surfaces at Pressures Much Greater Than One Atmosphere," *Journal of the Electrochemical Society*, vol. 129, pp. 1845-1848, 1982.

[95] V. A. Nazarenko, *Analytical chemistry of Germanium*. N. Y.: John Wiley & sons, 1974.

[96] J. Oh and J. C. Campbell, "Thermal desorption of Ge native oxides and the loss of Ge from the surface," *Journal of Electronic Materials*, vol. 33, pp. 364-367, 2004.

[97] K. Prabhakaran and T. Ogino, "Oxidation of Ge(100) and Ge(111) surfaces: an UPS and XPS study," *Surface Science*, vol. 325, pp. 263-271, 1995.

[98] V. I. Davydov, *Germanium*. New York, London, Paris: Gordon and Breach, Science publishers, 1966.

[99] P. J. Wolf, T. M. Christensen, N. G. Coit, and R. W. Swinford, "Thin film properties of germanium oxide synthesized by pulsed laser

sputtering in vacuum and oxygen environments," *Journal of Vacuum Science & Technology A: Vacuum, Surfaces, and Films*, vol. 11, pp. 2725-2732, 1993.

[100] Y. F. Zhang, Y. H. Tang, N. Wang, C. S. Lee, I. Bello, and S. T. Lee, "Germanium nanowires sheathed with an oxide layer," *Physical Review B*, vol. 61, pp. 4518-4521, 2000.

[101] A. Molle, M. N. K. Bhuiyan, G. Tallarida, and M. Fanciulli, "Formation and stability of germanium oxide induced by atomic oxygen exposure," *Materials Science in Semiconductor Processing poceedings of Symposium T E-MRS 2006 Spring Meeting on Germanium based semiconductors from materials to devices*, vol. 9, pp. 673-678, 2006.

[102] K. Prabhakaran, F. Maeda, Y. Watanabe, and T. Ogino, "Thermal decomposition pathway of Ge and Si oxides: observation of a distinct difference," *Thin Solid Films*, vol. 369, pp. 289-292, 2000.

[103] D. A. Hansen and J. B. Hudson, "The adsorption kinetics of molecular oxygen and the desorption kinetics of GeO on Ge(100)," *Surface Science*, vol. 292, pp. 17-32, 1993.

[104] A. W. Laubengayer and D. S. Morton, "Germanium. XXXIX. The polymorphism of germanium dioxide," *Journal of the American Chemical Society*, vol. 54, pp. 2303-2320, 1932.

[105] F. X. Hassion, C. D. Thurmond, and F. A. Trumbore, "On the Melting Point of Germanium," *Journal of Physical Chemistry*, vol. 59, pp. 1076-1078, 1955.

[106] E. S. Greiner and P. Breidt, "Melting Point of Germanium and the Constitution of Some Ge-Ga Alloys," *Transactions of the American Institute of Mining and Metallurgical Engineers*, vol. 203, pp. 187-188, 1955.

[107] L. M. Dennis and R. E. Hulse, "Germanium XXXV Germanium monoxide - Germanium monosulfide," *Journal of the American Chemical Society*, vol. 52, pp. 3553-3556, 1930.

[108] H. W. Kim, S. H. Shim, and J. W. Lee, "Cone-shaped structures of GeO_2 fabricated by a thermal evaporation process," *Applied Surface Science*, vol. 253, pp. 7207-7210, 2007.

[109] Z. Jiang, T. Xie, G. Z. Wang, X. Y. Yuan, C. H. Ye, W. P. Cai, G. W. Meng, G. H. Li, and L. D. Zhang, "GeO_2 nanotubes and nanorods synthesized by vapor phase reactions," *Materials Letters*, vol. 59, pp. 416-419, 2005.

[110] C.-I. Wu, "Fabrication and site specific growth of nanowires," Ph.D. dissertation, Michigan state university, East Lansing, MI, USA, 2006.

[111] D. P. Norton, J. D. Budai, and M. F. Chisholm, "Hydrogen-assisted pulsed-laser deposition of (001)CeO_2on (001) Ge," *Applied Physics Letters*, vol. 76, pp. 1677-1679, 2000.

[112] D. P. Norton, J. D. Budai, and M. F. Chisholm, "Epitaxial Electronic Oxides on Semiconductors using Pulsed-Laser Deposition," presented at Mat Res Soc, Fall 1999, 2000.

[113] S. Sharma, T. I. Kamins, and R. S. Williams, "Synthesis of thin silicon nanowires using gold-catalyzed chemical vapor deposition," *Applied Physics a-Materials Science & Processing*, vol. 80, pp. 1225-1229, 2005.

[114] M. Micoulaut, L. Cormier, and G. S. Henderson, "The structure of amorphous, crystalline and liquid GeO_2," *Journal of Physics-Condensed Matter*, vol. 18, pp. R753-R784, 2006.

[115] K. Kneipp, H. Kneipp, I. Itzkan, R. R. Dasari, and M. S. Feld, "Surface-enhanced Raman scattering and biophysics," *Journal of Physics-Condensed Matter*, vol. 14, pp. R597-R624, 2002.

[116] E. Burstein, Y. J. Chen, C. Y. Chen, S. Lundquist, and E. Tosatti, "Giant Raman-Scattering by Adsorbed Molecules on Metal-Surfaces," *Solid State Communications*, vol. 29, pp. 567-570, 1979.

[117] A. Otto, "Raman-Spectra of (Cn)- Adsorbed at a Silver Surface," *Surface Science*, vol. 75, pp. L392-L396, 1978.

[118] R. L. Birke, J. R. Lombardi, and J. I. Gersten, "Observation of a Continuum in Enhanced Raman-Scattering from a Metal-Solution Interface," *Physical Review Letters*, vol. 43, pp. 71-75, 1979.

[119] C. T. Campbell, "Ultrathin metal films and particles on oxide surfaces: Structural, electronic and chemisorptive properties," *Surface Science Reports*, vol. 27, pp. 1-111, 1997.

[120] L. Zhang, R. Persaud, and T. E. Madey, "Ultrathin metal films on a metal oxide surface: Growth of Au on TiO_2 (110)," *Physical Review B*, vol. 56, pp. 10549-10557, 1997.

[121] U. Diebold, J. M. Pan, and T. E. Madey, "Growth Mode of Ultrathin Copper Overlayers on Tio_2(110)," *Physical Review B*, vol. 47, pp. 3868-3876, 1993.

[122] Z. Zhou, F. Xiao, L. Liu, G. Wang, and Z. Xu, "Probing single-molecule by surface-enhanced resonance Raman scattering with linearly and circularly polarized laser," *Optics Communications*, vol. 251, pp. 209-215, 2005.

[123] M. Suzuki, Y. Niidome, and S. Yamada, "Heat-induced morphological control of gold nanoparticle films for surface-enhanced Raman scattering (SERS) measurements," *Colloids and Surfaces A: Physicochemical and Engineering Aspects A selection of papers from the 11th International Conference on Organized Molecular Films (LB11), June 26-30, 2005, Sapporo*, vol. 284-285, pp. 388-394, 2006.

[124] M. K. Lawless and R. A. Mathies, "Excited-State Structure and Electronic Dephasing Time of Nile Blue from Absolute Resonance Raman Intensities," *Journal of Chemical Physics*, vol. 96, pp. 8037-8045, 1992.

[125] A. Ulman, "Formation and structure of self-assembled monolayers," *Chemical Reviews*, vol. 96, pp. 1533-1554, 1996.

[126] Y. J. Lee, T. C. Jeon, W. K. Paik, and K. Kim, "Self-assembly of 1,2-benzenedithiol on gold and silver: Fourier transform infrared spectroscopy and quartz crystal microbalance study," *Langmuir*, vol. 12, pp. 5830-5837, 1996.

[127] G. Sauer, G. Brehm, and S. Schneider, "Preparation of SERS-active gold film electrodes via electrocrystallization: their characterization and application with NIR excitation," *Journal of Raman Spectroscopy*, vol. 35, pp. 568-576, 2004.

[128] S. H. Cho, Y. J. Lee, M. S. Kim, and K. Kim, "Infrared and Raman spectroscopic study of 1,2-benzenedithiol adsorbed on silver," *Vibrational Spectroscopy*, vol. 10, pp. 261-270, 1996.

[129] B. Nikoobakht, J. Wang, and M. A. El-Sayed, "Surface-enhanced Raman scattering of molecules adsorbed on gold nanorods: off-surface plasmon resonance condition," *Chemical Physics Letters*, vol. 366, pp. 17-23, 2002.

[130] K. Seo and E. Borguet, "Potential-Induced Structural Change in a Self-Assembled Monolayer of 4-Methylbenzenethiol on Au(111)," *J. Phys. Chem. C*, vol. 111, pp. 6335-6342, 2007.

[131] A. Ibrahim, P. B. Oldham, D. L. Stokes, and T. VoDinh, "Determination of enhancement factors for surface-enhanced FT-Raman spectroscopy on gold and silver surfaces," *Journal of Raman Spectroscopy*, vol. 27, pp. 887-891, 1996.

[132] G. Varsanyi, *Vibrational spectra of benzene derivatives*. New York: Academic press, 1969.

[133] F. R. Dollish, W. G. Gateley, and F. F. Bentley, *Characteristic Raman frequencies of organic compounds*. New York: Wiley Interscience, 1973.

[134] H. Kojima, T. Suzuki, T. Ichimura, A. Fujii, T. Ebata, and N. Mikami, "Laser-induced fluorescence of jet-cooled chlorotoluene molecules," *Journal of Photochemistry and Photobiology A: Chemistry*

3rd Japan-Sino Binational Symposium on Photochemistry, vol. 92, pp. 1-5, 1995.

[135] G. Varsanyi, *Assignments for vibrational spectra of seven hundred benzene derivatives*, vol. 1. New York: John Wiley & Sons, 1974.

[136] B. H. Jun, J. H. Kim, H. Park, J. S. Kim, K. N. Yu, S. M. Lee, H. Choi, S. Y. Kwak, Y. K. Kim, D. H. Jeong, M. H. Cho, and Y. S. Lee,

"Surface-enhanced Raman spectroscopic-encoded beads for multiplex immunoassay," *Journal of Combinatorial Chemistry*, vol. 9, pp. 237-244, 2007.

[137] Z. Ozhamam, M. Yurdakul, and S. Yurdakul, "DFT studies and vibrational spectra of trans 1,2-bis(4-pyridyl)ethylene and its zinc(II)halide complexes," *Journal of Molecular Structure-Theochem*, vol. 761, pp. 113-118, 2006.

[138] W. H. Yang, J. Hulteen, G. C. Schatz, and R. P. V. Duyne, "A surface-enhanced hyper-Raman and surface-enhanced Raman scattering study of trans-1,2-bis(4-pyridyl)ethylene adsorbed onto silver film over nanosphere electrodes. Vibrational assignments: Experiment and theory," *The Journal of Chemical Physics*, vol. 104, pp. 4313-4323, 1996.

[139] W. P. Griffith and T. Y. Koh, "Vibrational spectra of 1,2-benzenedithiol, 2-aminothiophenol and 2-aminophenol and their SER spectra," *Spectrochimica Acta Part A: Molecular and Biomolecular Spectroscopy*, vol. 51, pp. 253-267, 1995.

[140] J. T. Law and P. S. Meigs, "Rates of Oxidation of Germanium," *Journal of the Electrochemical Society*, vol. 104, pp. 154-159, 1957.

[141] E. B. Gorokhov, V. A. Volodin, D. V. Marin, D. A. Orekhov, A. G. Cherkov, A. K. Gutakovskii, V. A. Shvets, A. G. Borisov, and M. D. Efremov, "Effect of quantum confinement on optical properties of Ge nanocrystals in GeO2 films," *Semiconductors*, vol. 39, pp. 1168-1175, 2005.

[142] A. A. Borshch, M. S. Brodin, V. I. Volkov, V. P. Lyakhovetskii, and R. D. Fedorovich, "Giant nonlinear refraction in gold island films," *JETP Letters*, vol. 84, pp. 214-216, 2006.

[143] J. N. Chen, T. Martensson, K. A. Dick, K. Deppert, H. Q. Xu, L. Samuelson, and H. X. Xu, "Surface-enhanced Raman scattering of rhodamine 6G on nanowire arrays decorated with gold nanoparticles," *Nanotechnology*, vol. 19, pp. 275712, 2008.

[144] Z. L. Wang, "Zinc oxide nanostructures: growth, properties and applications," *Journal of Physics-Condensed Matter*, vol. 16, pp. R829-R858, 2004.

[145] M. H. Huang, S. Mao, H. Feick, H. Q. Yan, Y. Y. Wu, H. Kind, E. Weber, R. Russo, and P. D. Yang, "Room-temperature ultraviolet nanowire nanolasers," *Science*, vol. 292, pp. 1897-1899, 2001.

[146] M. H. Huang, Y. Y. Wu, H. Feick, N. Tran, E. Weber, and P. D. Yang, "Catalytic growth of zinc oxide nanowires by vapor transport," *Advanced Materials*, vol. 13, pp. 113-116, 2001.

[147] J. Y. Li, X. L. Chen, H. Li, M. He, and Z. Y. Qiao, "Fabrication of zinc oxide nanorods," *Journal of Crystal Growth*, vol. 233, pp. 5-7, 2001.

[148] Y. C. Kong, D. P. Yu, B. Zhang, W. Fang, and S. Q. Feng, "Ultraviolet-emitting ZnO nanowires synthesized by a physical vapor deposition approach," *Applied Physics Letters*, vol. 78, pp. 407-409, 2001.

[149] Y. J. Ma, Z. Zhang, F. Zhou, L. Lu, A. Z. Jin, and C. Z. Gu, "Hopping conduction in single ZnO nanowires," *Nanotechnology*, vol. 16, pp. 746-749, 2005.

[150] H. J. Son, K. A. Jeon, C. E. Kim, J. H. Kim, K. H. Yoo, and S. Y. Lee, "Synthesis of ZnO nanowires by pulsed laser deposition in furnace," *Applied Surface Science: Photon-Assisted Synthesis and Processing of Functional Materials - E-MRS-H Symposium*, vol. 253, pp. 7848-7850, 2007.

[151] W. I. Park, D. H. Kim, S. W. Jung, and G. C. Yi, "Metalorganic vapor-phase epitaxial growth of vertically well-aligned ZnO nanorods," *Applied Physics Letters*, vol. 80, pp. 4232-4234, 2002.

[152] W. I. Park, Y. H. Jun, S. W. Jung, and G. C. Yi, "Excitonic emissions observed in ZnO single crystal nanorods," *Applied Physics Letters*, vol. 82, pp. 964-966, 2003.

[153] M. J. Zheng, L. D. Zhang, G. H. Li, and W. Z. Shen, "Fabrication and optical properties of large-scale uniform zinc oxide nanowire arrays by one-step electrochemical deposition technique," *Chemical Physics Letters*, vol. 363, pp. 123-128, 2002.

[154] L. Vayssieres, "Growth of Arrayed Nanorods and Nanowires of ZnO from Aqueous Solutions," *Adv. Mater.*, vol. 15, pp. 464-466, 2003.

[155] C. Xu, Z. Liu, S. Liu, and G. Wang, "Growth of hexagonal ZnO nanowires and nanowhiskers," *Scripta Materialia*, vol. 48, pp. 1367-1371, 2003.

[156] H. E. Unalan, P. Hiralal, N. Rupesinghe, S. Dalal, W. I. Milne, and G. A. J. Amaratunga, "Rapid synthesis of aligned zinc oxide nanowires," *Nanotechnology*, vol. 19, pp. 255608, 2008.

[157] J. J. Wu and S. C. Liu, "Catalyst-free growth and characterization of ZnO nanorods," *Journal of Physical Chemistry B*, vol. 106, pp. 9546-9551, 2002.

[158] J. Yang, W. Z. Wang, Y. Ma, D. Z. Wang, D. Steeves, B. Kimball, and Z. F. Ren, "High throughput growth of zinc oxide nanowires from zinc powder with the assistance of sodium chloride," *Journal of Nanoscience and Nanotechnology*, vol. 6, pp. 2196-2199, 2006.

[159] H. Y. P. Yang, S. Mao, R. Russo, J. Johnson, R. Saykally, N. Morris, J. Pham, R. He, H.-J. Choi,, "Controlled Growth of ZnO Nanowires and Their Optical Properties," *Advanced Functional Materials*, vol. 12, pp. 323-331, 2002.

[160] J. Zhang, L.-D. Sun, X.-C. Jiang, C.-S. Liao, and C.-H. Yan, "Shape Evolution of One-Dimensional Single-Crystalline ZnO Nanostructures in a Microemulsion System," *Cryst. Growth Des.*, vol. 4, pp. 309-313, 2004.

[161] P. A. Hu, Y. Q. Liu, L. Fu, X. B. Wang, and D. B. Zhu, "Creation of novel ZnO nanostructures: self-assembled nanoribbon/nanoneedle junction networks and faceted nanoneedles on hexagonal microcrystals," *Applied Physics a-Materials Science & Processing*, vol. 78, pp. 15-19, 2004.

[162] M. Snure and A. Tiwari, "Synthesis, characterization, and green luminescence in ZnO nanocages," *Journal of Nanoscience and Nanotechnology*, vol. 7, pp. 481-485, 2007.

[163] Y. Hang Leung, A. B. Djurisic, J. Gao, M. H. Xie, and W. K. Chan, "Changing the shape of ZnO nanostructures by controlling Zn vapor release: from tetrapod to bone-like nanorods," *Chemical Physics Letters*, vol. 385, pp. 155-159, 2004.

[164] M. C. Newton and P. A. Warburton, "ZnO tetrapod nanocrystals," Materials Today, vol. 10, pp. 50-54, 2007.

[165] B. D. Yao, Y. F. Chan, and N. Wang, "Formation of ZnO nanostructures by a simple way of thermal evaporation," Applied Physics Letters, vol. 81, pp. 757-759, 2002.

[166] F. Z. Wang, Z. Z. Ye, D. W. Ma, L. P. Zhu, and F. Zhuge, "Novel morphologies of ZnO nanotetrapods," Materials Letters, vol. 59, pp. 560-563, 2005.

[167] L. E. Greene, M. Law, D. H. Tan, M. Montano, J. Goldberger, G. Somorjai, and P. D. Yang, "General route to vertical ZnO nanowire arrays using textured ZnO seeds," Nano Letters, vol. 5, pp. 1231-1236, 2005.

[168] M. Kitano, T. Hamabe, S. Maeda, and T. Okabe, "Growth of large tetrapod-like ZnO crystals : I. Experimental considerations on kinetics of growth," Journal of Crystal Growth, vol. 102, pp. 965-973, 1990.

[169] J. Park, H.-H. Choi, K. Siebein, and R. K. Singh, "Two-step evaporation process for formation of aligned zinc oxide nanowires," Journal of Crystal Growth, vol. 258, pp. 342-348, 2003.

[170] M. Rajalakshmi, A. K. Arora, B. S. Bendre, and S. Mahamuni, "Optical phonon confinement in zinc oxide nanoparticles," Journal of Applied Physics, vol. 87, pp. 2445-2448, 2000.

[171] M. A. Khan, T. P. Hogan, and B. Shanker, "Surface-enhanced Raman scattering from gold-coated germanium oxide nanowires," Journal of Raman Spectroscopy, vol. 39, pp. 893-900, 2008.

[172] J. Clarkson, C. Campbell, B. N. Rospendowski, and W. E. . Smith, "Molecular recognition using surface-enhanced Raman scattering from citrate-reduced silver colloids in non-aqueous solvents," Journal of Raman Spectroscopy, vol. 22, pp. 771-775, 1991.

[173] S. M. Prokes, O. J. Glembocki, R. W. Rendell, and M. G. Ancona, "Enhanced plasmon coupling in crossed dielectric/metal nanowire composite geometries and applications to surface-enhanced Raman spectroscopy," Applied Physics Letters, vol. 90, pp. 093105-1, 2007.

[174] T. G. Knorr and R. W. Hoffman, "Dependence of Geometric Magnetic Anisotropy in Thin Iron Films," Physical Review, vol. 113, pp. 1039-1046, 1959.

[175] D. O. Smith, "Anisotropy in Permalloy Films," Journal of Applied Physics, vol. 30, pp. 264S-265S, 1959.

[176] D. O. Smith, M. S. Cohen, and G. P. Weiss, "Oblique-Incidence Anisotropy in Evaporated Permalloy Films," Journal of Applied Physics, vol. 31, pp. 1755-1762, 1960.

[177] H. Konig and G. Helwig, "*Uber Die Struktur Schrag Aufgedampfter Schichten Und Ihr Einfluss Auf Die Entwicklung Submikroskopischer Oberflachenrauhigkeiten," Optik, vol. 6, pp. 111-124, 1950.

[178] J. P. Singh, T. Karabacak, D. X. Ye, D. L. Liu, C. Picu, T. M. Lu, and G. C. Wang, "Physical properties of nanostructures grown by oblique angle deposition," Journal of Vacuum Science & Technology B, vol. 23, pp. 2114-2121, 2005.

[179] M. Suzuki, W. Maekita, Y. Wada, K. Nakajima, K. Kimura, T. Fukuoka, and Y. Mori, "In-line aligned and bottom-up Ag nanorods for surface-enhanced Raman spectroscopy," Applied Physics Letters, vol. 88, pp. 203121, 2006.

[180] M. Suzuki, K. Nakajima, K. Kimura, T. Fukuoka, and Y. Mori, "Au Nanorod Arrays Tailored for Surface-Enhanced Raman Spectroscopy," Analytical Sciences, vol. 23, pp. 829-833, 2007.

[181] Y. Liu, J. Fan, Y.-P. Zhao, S. Shanmukh, and R. A. Dluhy, "Angle dependent surface enhanced Raman scattering obtained from a Ag nanorod array substrate," Applied Physics Letters, vol. 89, pp. 173134, 2006.

[182] K. Robbie, L. J. Friedrich, S. K. Dew, T. Smy, and M. J. Brett, "Fabrication of Thin-Films with Highly Porous Microstructures," Journal of Vacuum Science & Technology a-Vacuum Surfaces and Films, vol. 13, pp. 1032-1035, 1995.

[183] L. Abelmann and C. Lodder, "Oblique evaporation and surface diffusion," Thin Solid Films, vol. 305, pp. 1-21, 1997.

[184] K. Hara, M. Kamiya, T. Hashimoto, K. Okamoto, and H. Fujiwara, "Oblique-Incidence Anisotropy of the Iron Films Evaporated at Low Substrate Temperatures," Journal of Magnetism and Magnetic Materials, vol. 73, pp. 161-166, 1988.

[185] D. Vick, T. Smy, and M. J. Brett, "Growth behavior of evaporated porous thin films," Journal of Materials Research, vol. 17, pp. 2904-2911, 2002.

[186] W. K. Choi, L. Li, H. G. Chew, and F. Zheng, "Synthesis and structural characterization of germanium nanowires from glancing angle deposition," Nanotechnology, vol. 18, pp. 385301, 2007.

[187] A. G. Dirks and H. J. Leamy, "Columnar microstructure in vapor-deposited thin films," Thin Solid Films, vol. 47, pp. 219-233, 1977.

[188] C. K. Chen, A. R. B. Decastro, and Y. R. Shen, "Surface-Enchanced 2nd-Harmonic Generation," Physical Review Letters, vol. 46, pp. 145-148, 1981.

[189] J. Stropp, G. Trachta, G. Brehm, and S. Schneider, "A new version of AgFON substrates for high-throughput analytical SFRS applications," Journal of Raman Spectroscopy, vol. 34, pp. 26-32, 2003.

[190] Y. S. Tan, M. P. Srinivasan, S. O. Pehkonen, and S. Y. M. Chooi, "Effects of ring substituents on the protective properties of self-assembled benzenethiols on copper," Corrosion Science, vol. 48, pp. 840-862, 2006.

[191] Y. J. Liu, J. G. Fan, Y. P. Zhao, S. Shanmukh, and R. A. Dluhy, "Angle dependent surface enhanced Raman scattering obtained from a Ag nanorod array substrate," Applied Physics Letters, vol. 89, pp. 173134, 2006.

[192] A. Wokaun, Solid state physics, vol. 38. New York: Academic, 1984.

[193] C. J. F. Boettcher, Theory of Electric Polarization, 2nd ed. New York: Elsevier, 1973.